

CARBONATE CLUMPED ISOTOPE GEOCHEMISTRY OF MARINE
MOLLUSK AND BRACHIOPOD SHELLS AND ITS APPLICATION TO
DEEP-TIME PALEOCLIMATOLOGY

by

Gregory A. Henkes

A dissertation submitted to Johns Hopkins University in conformity with the
requirements for the degree of Doctor of Philosophy of Geochemistry

Baltimore, Maryland

September, 18th, 2014

© 2014 Gregory A. Henkes
All Rights Reserved

ABSTRACT

The main objective of this dissertation research was to study the carbonate clumped isotope compositions of marine mollusk and brachiopod shells, both modern and ancient, and to investigate critical problems with the preservation of isotope clumping in shell carbonate over the Phanerozoic Eon. This was accomplished through a series of empirical and laboratory studies detailed in each of the three chapters of this dissertation. This approach was aided by the knowledge gained from decades of previous research on the bulk carbon and oxygen isotope compositions of marine shells, but was novel in its application of modern methods for measuring carbonate clumped isotopes. Unlike conventional carbonate-water oxygen isotope thermometry, carbonate clumped isotope thermometry is independent of the isotopic composition of the precipitating fluid, which for shells growing in ancient seawater is largely unknown and the long-time subject of debate. Therefore, clumped isotopes, combined with bulk isotopic measurements of ancient shells, can provide an independent estimate of paleotemperature and the isotopic composition of paleoseawater. The first chapter of this dissertation describes a comprehensive calibration of the carbonate clumped isotope thermometer using modern mollusk and brachiopod shells collected worldwide from waters of known temperature and isotopic composition. The results are in accord with the temperature dependence of the thermometer predicted from theory, but are different from earlier empirical calibration attempts by other laboratories. The second chapter explores the phenomenon of carbonate clumped isotope reordering—that is closed-system alteration of ^{13}C - ^{18}O ‘clumped’ bonds—in Paleozoic brachiopod shells, finding that sedimentary burial temperatures above 100°C can alter primary clumped isotope compositions over geologic

timescales. The third chapter presents the emerging Phanerozoic clumped isotope record of seawater temperature and $\delta^{18}\text{O}$ from well-preserved marine mollusk and brachiopod fossils, and evaluates it with respect to clumped isotope bond reordering described in chapter two. Altogether, this research lays the groundwork for continued study of the clumped isotope geochemistry of marine shells, with future studies expected to shed insight into temperature calibration discrepancies between materials and laboratories, the limits and mechanism(s) of ^{13}C - ^{18}O bond reordering, and paleoclimatology of Paleozoic and Mesozoic worlds.

Primary Advisor:

Benjamin H. Passey, PhD, *Department of Earth and Planetary Sciences*

Second Reader:

John M. Ferry, PhD, *Department of Earth and Planetary Sciences*

ACKNOWLEDGEMENTS

I would first like to thank my PhD advisory committee: Profs. Benjamin Passey, John Ferry, and Dimitri Sverjensky. Over the years they have formally provided me with bi-annual support, even-handed criticism, and guidance, but in reality they were always willing and available for a quick drop-in conversation or chance hallway meeting. I will be proud of my graduate school association with each of these scholars for the remainder of my academic career. It has also been an honor to be part of the JHU stable isotope laboratory in its fledgling years. Ben Passey and Naomi Levin are consummate experimentalists and it has been a pleasure to learn from their constant attention to safety, detail, and data. Finally, I am grateful and humbled to be Ben Passey's first graduate student. It's a privilege to be the first in what will no doubt become a distinguished group of students from Ben's tutelage. For me, Ben has been the ideal advisor, giving room for me to explore and learn (and fail) when needed, but also having the foresight to know exactly when to pay close attention to my work in the laboratory or in writing manuscripts. He has lead his group of postdocs, graduate students, and visiting researchers in exemplary fashion, and it's my privilege to have learned by his example.

As a graduate student I have also been incredibly fortunate to work with a distinguished group of collaborators: Ethan Grossman, Thomas Yancey, Brock Shenton, Alberto Perez-Huerta, Alan Wanamaker, William Ambrose, and Michael Carroll. Ethan has truly been an 'advisor-from-another-university' and I will proudly carry this association throughout my career. Ethan and his wife have been incredibly hospitable during my visits to Texas A&M University and College Station, TX, as has Ethan's student (and now my friend

and colleague) Brock Shenton. Ethan has been my guide to the fossil record, particularly from Paleozoic rocks, and the history of stable isotope research of fossil shells. From Ethan, I have learned a great deal about other geochemical and petrographic laboratory methods, as well as skills in writing, professional communication, and the subtleties of successfully attending and presenting at conferences.

I also owe a great deal of my success and happiness as a graduate student to the JHU Department Earth and Planetary Sciences community; the faculty, researchers, and graduate students alike! In particular, my five-year officemate and fellow stable isotope aficionado, Shuning Li. Shuning and I have learned the ins and outs of isotope geochemistry together and she has been a consistent sounding board, whether she liked it or not, for my research and coursework. Our messy office chalkboards were a testament to the heated discussions, arguments, and “ah-ha” moments we enjoyed together. I was also fortunate to meet life-long friends and peers in Olin Hall: Erin Urquhart, Kial Stewart, Marcello Magaldi, Sophie Lehmann, Huanting Hu, Haoyuan Ji, Marina Suarez, Zelalem Bedaso, Rebecca Kraft, Scott Pitz, Sara Rivero-Calle, and Tiffany Smith. Collectively, this group kept the days in the department fun and light-hearted. They, among many others, were also perfect partners for blowing off steam at our weekly Friday beer hour!

Upon successfully graduating, I will have had two milestone moments in the last 5 years, the other being my marriage to Erin Compton (now Henkes). Erin and I met, dated, and

were engaged in the middle of my graduate studies and research. As such, she has been my rock (pun intended) at home, while traveling, and during grueling 24-hour, weeklong stints making measurements in the laboratory. I thank Erin for grounding me in Baltimore and introducing me to many lifelong friends. Her zeal for nursing and healthcare is matched by my own for earth science. We share many memories in the department and I thank EPS for welcoming her as one of their own. I would be remiss if I failed to also thank our dogs, Nepal, our newest addition, Onyx, and the late Ruby. Ruby's companionship during the early days of graduate school was unwavering and early on she taught me the importance of maintaining a responsible and appropriate work-life balance, even as a student. Nepal and Onyx have been wonderful additions to my life and provided daily love, entertainment, and comfort after long days in the lab.

Lastly, I thank my family: Amy, Kevin, and Emily Henkes. Only they truly know my journey to reach this point. Their support is never-ending and I lack the words to describe my appreciation of them. They moved me to Baltimore, guided me through my first experience of homeownership, put up with my (at times) scattered brain, and always knew when to coerce me away from the office and lab for a vacation, be it Peru, Panama, Napa Valley, or the Virgin Islands. It certainly takes a village to mint a new PhD, but in my case it also took a great family!

Each chapter of this dissertation owes its own set of personal and professional acknowledgements. For Chapter 2: The work has benefited from the generosity of several individuals who without which we would not have had the opportunity to analyze such a

wide range of specimens: C. Del Castillo collected shells from the La Parguera region of Puerto Rico, T. Moritaki provided deceased nautilus from the Toba Aquarium, J. Scourse provided the *A. islandica* shell from Iceland, and D. Merritt provided access to the aquaculture facilities at the Horn Point Laboratory. We would also like to thank H. Affek and P. Douglas at Yale University and R. Eagle and J. Eiler at Caltech for their participation in the inter-laboratory comparison exercise (Table 2.3). This manuscript has benefitted from numerous discussions with J. Ferry, D. Sverjensky, W. Guo, N. Levin, T. Haine, M. Suarez, and S. Li. We are also grateful to two anonymous reviewers, whose comments further improved the clarity of this manuscript for publication in *Geochimica et Cosmochimica Acta*. The research was supported by the Department of Earth and Planetary Sciences at Johns Hopkins University, and collection of the Barents Sea mollusks was supported by the Norwegian Research Council, under the International Polar Year program.

For Chapter 3: We would like to thank Arthur Mory and David Haig for their assistance with collection of shell fragment WA-CB-13 and for sharing their insights on Permian strata in Western Australia, and Ken Livi for electron microprobe analyses. Ray Guillemette is acknowledged for his advice and assistance on petrographic screening. We also thank Andreas Kronenberg for discussions and insights about solid-state diffusion in calcite, and three anonymous reviewers for comments that helped improve the manuscript for publication in *Geochimica et Cosmochimica Acta*. The research was funded by a grant from the United States National Science Foundation (EAR-1227076, and in part from EAR-1118713), the American Chemical Society Petroleum Research Fund, and The

Johns Hopkins University Department of Earth and Planetary Sciences. Samples were collected with prior support from the United States National Science Foundation (EAR-9304815, EAR-0003596, and EAR-0643309).

For Chapter 4: This research was funded by a grant from the United States National Science Foundation (EAR-1227076, and in part from EAR-1118713), and with support of the American Chemical Society Petroleum Research Fund and The Johns Hopkins University Department of Earth and Planetary Sciences. Carboniferous brachiopod samples were originally collected with prior support from the United States National Science Foundation (EAR-9304815, EAR-0003596, and EAR-0643309). We also acknowledge Naomi Levin and Dimitri Sverjensky for encouraging us to see the ‘bigger picture’ and Ray Guillemette for his assistance with sample preparation and petrographic screening.

TABLE OF CONTENTS

LIST OF TABLES.....	xiii
LIST OF FIGURES.....	xiv
1. INTRODUCTION.....	1
2. CARBONATE CLUMPED ISOTOPE COMPOSITIONS OF MODERN MARINE MOLLUSK AND BRACHIOPOD SHELLS.....	5
2.1 Introduction.....	6
2.2 Methods.....	11
2.2.1 Samples.....	11
2.2.1.1 Mollusk growth temperatures.....	17
2.2.1.2 Brachiopod growth temperatures.....	22
2.2.2 Stable isotope measurements.....	23
2.2.3 Data reduction and analysis.....	26
2.3 Results.....	28
2.4 Discussion.....	35
2.4.1 Methodological explanations.....	35
2.4.1.1 Intercalibration between different laboratories.....	35
2.4.1.2 Acid temperature.....	40
2.4.2 Biological explanations.....	43
2.4.2.1 Isotopic mixing.....	43
2.4.2.2 Amorphous calcium carbonate.....	44
2.4.2.3 Diffusion.....	46

2.4.2.4	pH and dissolve inorganic carbon speciation.....	51
2.4.2.5	DIC disequilibrium.....	52
2.5	Summary.....	56
3.	TEMPERATURE LIMITS FOR PRESERVATION OF PRIMARY CALCITE CLUMPED ISOTOPE PALEOTEMPERATURES.....	59
3.1	Introduction.....	60
3.2	Carboniferous brachiopods.....	64
3.2.1	Analytical methods.....	68
3.2.2	Results for Carboniferous brachiopods and associated cements.....	71
3.3	Experimental determination of reordering kinetics of brachiopod calcite.....	74
3.3.1	Experimental methods and observations.....	74
3.3.2	Heating experiment isotopic results.....	77
3.3.3	Carbonate clumped isotope reordering models.....	80
3.3.3.1	First-order approximation model.....	82
3.3.3.2	Transient defect/equilibrium defect model.....	85
3.3.4	General predictions of the models.....	86
3.4	Evaluation using the geological record.....	89
3.4.1	General approach and limitations.....	89
3.4.2	Compilation of burial-temperature histories.....	92
3.4.3	Results: predicted reordering during burial versus observed $T(\Delta_{47})$	93
3.5	Conclusions and an outlook for future research.....	103

4.	THE EMERGING RECORD OF PHANEROZOIC SEAWATER	
	TEMPERATURE AND $\delta^{18}\text{O}$ FROM CARBONATE CLUMPED ISOTOPES:	
	REAL OR REORDERED?	107
4.1	Introduction.....	108
4.2	Carbonate clumped isotope bond reordering.....	113
4.3	Results.....	114
4.3.1	Carboniferous brachiopods.....	114
4.3.2	Evaluation of clumped isotope reordering.....	115
4.4	The emerging Phanerozoic record.....	118
5.	SUMMARY AND CONCLUSIONS.....	123
	APPENDICIES.....	126
A2.1	X-ray diffraction data for mollusk shells.....	126
A2.2	Supplementary data table for modern mollusk and brachiopod analyses.....	127
A3.1	Derivation of the transient defect/equilibrium defect model.....	127
A3.2	Determination of rate constants in the transient defect/equilibrium defect model.....	130
A3.3	Brachiopod petrographic screening images and limestone isotopic data.....	138

A3.4	Supplementary data tables for Carboniferous brachiopod analyses and basin history compilations.....	150
A3.5	Supplementary data table for Carboniferous brachiopod analyses.....	156
A4.1	Brachiopod petrographic screening images.....	157
A4.2	Supplementary data tables for the Phanerozoic carbonate clumped isotope record from brachiopod and mollusk shells.....	168
REFERENCES.....		169
AUTHOR’S CURRICULUM VITEA.....		189

LIST OF TABLES

Table 2.1 Isotopic compositions of modern marine mollusks and brachiopods.....	12
Table 2.2 Mollusk and brachiopod calibration regression statistics.....	31
Table 2.3 Interlaboratory clumped isotope comparison.....	38
Table 2.4 Clumped isotope acid correction factors.....	41
Table 2.5 Stable isotope data for sample pretreatment experiments.....	46
Table 3.1 Stable isotope compositions of Carboniferous brachiopods.....	66
Table 3.2 Rate constants and Arrhenius parameters from the brachiopod heating experiments.....	83
Table 3.3 Temperature-time combinations predicted for clumped isotope reordering....	89
Table 4.1 Burial temperature information for the Phanerozoic clumped isotope record.	115

LIST OF FIGURES

Figure 2.1 Carbonate clumped isotope values from existing temperature calibrations.....	9
Figure 2.2 Carbon dioxide-water equilibration device schematic.....	25
Figure 2.3 Mollusk and brachiopod calibration curve.....	30
Figure 2.4 Calibration error histogram.....	34
Figure 2.5 Compilation of interlaboratory clumped isotope comparisons.....	39
Figure 2.6 Carbon vs. oxygen isotope crossplot for marine shells.....	50
Figure 2.7 Summary of theoretical predictions of Δ_{47} temperature dependence.....	53
Figure 3.1 Carboniferous brachiopod petrographic screening summary.....	69
Figure 3.2 Carboniferous brachiopod clumped isotope temperatures vs. their oxygen isotope compositions.....	72
Figure 3.3 Results of clumped isotope reordering experiments.....	79
Figure 3.4 Temperature-time predictions for clumped isotope reordering.....	87
Figure 3.5 A schematic of burial history and clumped isotope reordering circuits.....	94
Figure 3.6 Diagrams showing compiled burial histories and modeled clumped isotope compositions of the Carrara marble and Carboniferous brachiopods.....	96
Figure 3.7 Diagrams showing compiled burial histories and modeled clumped isotope compositions of Carboniferous brachiopods.....	98
Figure 3.8 Illustration of the threshold behavior of carbonate clumped isotope reordering for a simplified burial history.....	102
Figure 4.1 Compiled carbonate $\delta^{18}\text{O}$ and clumped isotope paleotemperatures from marine mollusks and brachiopods.....	112
Figure 4.2 Maximum burial temperatures and samples age for collection localities in the Phanerozoic clumped isotope record.....	117
Figure 4.3 The Phanerozoic seawater temperature and $\delta^{18}\text{O}$ record from carbonate clumped isotopes.....	119

1. INTRODUCTION

Stable isotope thermometry of sedimentary rocks, marine and terrestrial, is a cornerstone of modern paleoclimatological and paleoceanographic research (Grossman, 2012a). These applications have been recognized since the earliest days of stable isotope measurement, and the field of stable isotope thermometry has since expanded to the sub-surface, the cryosphere, and extraterrestrial materials. Mineral-water oxygen isotope thermometry, carbonate-water isotopic exchange in particular, is arguably one of the most widely used systems because of the relative ease of measuring ancient minerals, but has traditionally been limited by unknown oxygen isotope compositions of ancient precipitating waters (Kasting et al., 2006; Grossman, 2012b). Thus, mineral-water oxygen isotope thermometry is an underdetermined tool in most geological applications. This problem has, in part, motivated the calibration and study of alternative geochemical paleothermometers, including the temperature dependence of mineral-water cation distribution coefficients (e.g., Mg/Ca and Sr/Ca ratios in carbonates; Gentry et al., 2008) and the degree of organic molecule saturation (e.g., the alkenone unsaturation or “ U_{37}^k ” index; Müller et al., 1998). However, these other paleothermometers are not without complication and have also been found to depend on the geochemistry of the original precipitating fluids (e.g., Ries, 2004) and to be susceptible to alteration during diagenesis and sedimentary burial (e.g., Hedges and Prahl, 1993). An ideal (paleo)thermometer would therefore be solely dependent on the formation temperature of a given geologic archive and resistant to chemical or physical alteration during incorporation into the sedimentary rock record. A novel stable isotope thermometer, carbonate clumped isotope

thermometry, promises just that, although, like any new proxy, it requires detailed study to confirm its application across a range of geological materials and environments.

Carbonate clumped isotope thermometry is based on the temperature dependence of the equilibrium constant for the homogenous isotope exchange reaction for carbonate minerals which forms $^{13}\text{C}-^{18}\text{O}$ bonds by creation of the $^{13}\text{C}^{18}\text{O}^{16}\text{O}_2^{2-}$ ion group (Eiler, 2011). Statistical thermodynamics by Schauble et al. (2006) and Guo et al. (2009) predict that the equilibrium constant is slightly greater than 1 (thus favoring the creation of clumped bonds) at earth-surface temperatures, and asymptotically approaches 1 at high temperatures. This temperature dependence is independent of the ^{12}C , ^{13}C , ^{16}O , ^{17}O and ^{18}O content of the carbonate group and arises from the competing effects of lower vibrational energy of heavy isotope-heavy isotope bonds and configurationally entropy, which tends to randomize stable isotope distribution (Wang et al., 2004; Eiler, 2011). In practice, it is not possible to measure clumped isotopes in solid minerals, so the laboratory measurement relies on controlled phosphoric acid digestion of the carbonates, capture of the resultant CO_2 gas, and analysis of the $^{13}\text{C}-^{18}\text{O}$ containing isotopologue with a nominal mass of 47 ($^{13}\text{C}^{18}\text{O}^{16}\text{O}$) by gas source mass spectrometry. The abundance of this isotopologue is proportional to the abundance of clumped bonds in the mineral after accounting for stable isotope fractionation during the acid reaction (Guo et al., 2009).

Decades of carbonate-water oxygen isotope thermometry research have already identified many attractive paleoclimate questions and suitable sample sets for clumped isotope analysis. Among these are terrestrial carbonates, such as soil nodules, lacustrine marls,

and freshwater shells, used to reconstruct continental climate and topography (e.g., Ghosh et al., 2006a; Passey et al., 2010; Suarez et al., 2011) and marine carbonates, such as foraminifera tests, invertebrate shells, and early diagenetic cements, used to record zonal, meridional, and temporal trends in seawater temperature and oxygen isotope composition (e.g., Finnegan et al., 2011; Dennis et al., 2013; Price and Passey, 2013). The latter examples of biogenic carbonates from marine rocks are important archives because (1) their calcium carbonate shells are stable and resistant to post-depositional chemical alteration (i.e., recrystallization or ‘open-system’ diagenesis) over long timescales, (2) their geochemical and petrographic compositions are different from diagenetic fluids and therefore relatively easy to screen for recrystallization, and (3) they largely precipitate their shells in isotopic equilibrium with the surrounding seawater. These characteristics along with the scientific questions that can be answered by more clearly resolving their mineralization temperatures, such as the temperature and isotopic evolution of seawater over the Phanerozoic (Grossman, 2012), make mollusk and brachiopod shells natural targets for further carbonate clumped isotope study.

When I began work in 2010, there were several unknowns about clumped isotope thermometry that were ripe for further study: there was not yet a detailed temperature calibration for marine mollusks and brachiopod shells (important taxa for deep-time paleoclimate reconstructions), we knew of the effects of solid-state C-O bond reordering (largely from Dennis and Schrag, 2010), but had very little understanding of the kinetics and the temperature range where it becomes important, and the application of clumped isotopes to geological problems was still in its infancy. Thus, the following chapters

address several fundamental questions about mollusk and brachiopod shell carbonate clumped isotope thermometry, including development of a modern, empirical temperature calibration, a requisite for effective fossil analysis, an evaluation of cryptic alteration of primary clumped isotope compositions in the solid calcite, termed ‘clumped isotope reordering’, and presentation of the emerging Phanerozoic clumped isotope record from well-preserved fossil brachiopod and mollusk shells.

2. CARBONATE CLUMPED ISOTOPE COMPOSITIONS OF MODERN MARINE MOLLUSK AND BRACHIOPOD SHELLS¹

Abstract

We present an empirical calibration of the carbonate clumped isotope thermometer based on mollusk and brachiopod shells from natural and controlled environments spanning water temperatures of -1.0 to 29.5 °C. The clumped isotope data (Δ_{47}) are normalized to CO₂ gases with equilibrium distributions of clumped isotopologues at high temperature (1000 °C) and low temperature (27 or 30 °C), and thus the calibration is unique in being directly referenced to a carbon dioxide equilibrium reference frame (Dennis et al., 2011, Defining an absolute reference frame for clumped isotope studies of CO₂, *Geochimica et Cosmochimica Acta*, 75, 7117–7131). The shell clumped isotope data define the following relation as a function of temperature (in kelvin):

$$\Delta_{47} = 0.0327 \times 10^6 / T^2 + 0.3286 \quad (r^2 = 0.84)$$

The temperature sensitivity (slope) of this relation is lower than those based on corals, fish otoliths, foraminifera, and coccoliths, but is similar to theoretical predictions for calcite based on lattice dynamics calculations. We find no convincing methodological or biological explanations for the difference in temperature sensitivity between this calibration and the previous calibrations, and suggest that the discrepancy might represent real but unknown differences in mineral–DIC clumped isotope fractionation between mollusks/brachiopods and other taxa. Nevertheless, revised analytical methods similar to those used in this study are now in wide use, and it will be important to develop

¹ Henkes G.A., Passey B.H., Wanamaker A.D. Jr., Grossman E.L., Ambrose W.G. Jr., Carroll M.L. (2013) Carbonate clumped isotope compositions of modern marine mollusk and brachiopod shells. *Geochimica et Cosmochimica Acta*, 106: 307-325.

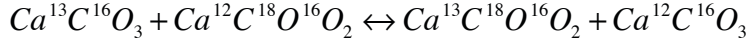
calibrations for other taxonomic groups using these updated methods, with analyses directly referenced to the carbon dioxide equilibrium reference frame.

2.1 Introduction

Traditional oxygen isotope thermometry is based on the temperature dependence of isotope exchange between fluid and mineral. The carbonate-water oxygen isotope thermometer, which is commonly used to infer paleotemperature from ancient carbonates, requires knowledge of both the oxygen isotope composition ($\delta^{18}\text{O}$) of the mineral and the precipitating fluid (e.g., Epstein et al., 1953). The difficulty of constraining both temperature and the oxygen isotope composition of the coeval water from a single carbonate $\delta^{18}\text{O}$ measurement is a long-standing dilemma in oxygen isotope paleothermometry. Except for fluid inclusions and pore fluids (e.g., Schrag and DePaolo, 1993) there are few direct $\delta^{18}\text{O}$ measurements of natural waters beyond the historical record, leaving the oxygen isotope paleothermometer underdetermined in most geologic applications. Reconstructing paleotemperature is the cornerstone of paleoclimatology and paleoceanography, but the absence of independent constraints on the isotopic composition of ancient waters has limited the application of the oxygen isotope paleothermometer. The ‘clumped’ isotope thermometer has emerged as an appealing alternative because, unlike carbonate $\delta^{18}\text{O}$ thermometry, it is independent of the bulk isotopic composition of water.

Clumped isotope thermometry examines the temperature dependence of bond formation between two rare, heavy isotopes within a single molecule (e.g., ^{13}C and ^{18}O forming the ^{13}C - ^{18}O isotopologue of carbon monoxide). This ‘clumping’ is based on homogeneous

isotope exchange reactions which are independent of the bulk isotopic composition (e.g., $\delta^{13}\text{C}$, $\delta^{18}\text{O}$) of the phase. The relevant exchange reaction for carbonate clumped isotope thermometry is:



This differs from traditional oxygen isotope thermometry, which is only concerned with ‘singly-substituted isotopologues’ of a molecule (e.g., $\text{Ca}^{12}\text{C}^{18}\text{O}^{16}\text{O}$). The carbonate clumped isotope thermometer is of particular interest because the temperature dependence of its enrichment has been predicted by theory (Schauble et al., 2006) and carbonate minerals are common in a range of natural environments. Precise measurement of multiple-substituted isotopologues in natural carbonates can therefore allow reconstructions of their formation temperatures. Additionally, clumped isotope-derived temperatures can be used in conjunction with the oxygen isotope thermometer to calculate the isotopic composition of the precipitating fluid. Because of these features, clumped isotope paleothermometry is becoming a widely used technique for reconstructing paleotemperature and the isotopic composition of ancient seawater (Came et al., 2007, Finnegan et al., 2011 and Keating-Bitonti et al., 2011). Meaningful application of the carbonate clumped isotope paleothermometer, however, is contingent on the development of calibration curves that relate Δ_{47} , a measure of ^{13}C – ^{18}O clumping in carbonate, with known temperatures of mineralization. Δ_{47} is a function of the abundance of the mass-47 ($^{13}\text{C}^{18}\text{O}^{16}\text{O}$) isotopologue of CO_2 produced by acid digestion of a carbonate mineral and is calculated as:

$$\Delta_{47} = \left[\left(R^{47} / R^{47*} \right) - \left(R^{46} / R^{46*} \right) - \left(R^{45} / R^{45*} \right) + 1 \right] \times 1000 \quad (2.1)$$

where

$$R^i = \text{mass } i / \text{mass } 44 \quad (2.2)$$

is the ratio for the each isotopologue of CO₂ generated from carbonate, and the asterisk superscript indicates ratios with stochastic isotopologue abundances.

Experimental calibrations of the clumped isotope thermometer have been generated by measuring the Δ_{47} of calcium carbonate precipitated at temperatures from 1 to ~70 °C (Ghosh et al., 2006 and Dennis and Schrag, 2010). Empirical calibrations have used biogenic carbonates produced by corals, foraminifera, coccolithophores, brachiopods, mollusks, and fishes from natural waters with known ambient growth temperatures (Ghosh et al., 2006, Ghosh et al., 2007, Came et al., 2007, Tripathi et al., 2010 and Thiagarajan et al., 2011). The majority of the calibration data have come from a laboratory at the California Institute of Technology (Caltech) and mostly conform to a single calibration line first described by Ghosh et al. (2006) (Fig. 2.1). Dennis and Schrag (2010), working at Harvard University and using slightly different analytical methods, developed an experimental (inorganic) calcite Δ_{47} –temperature calibration which deviated substantially from the Ghosh et al. (2006) calibration line at temperatures below ~20 °C. The Dennis and Schrag (2010) data, however, closely align with theoretical predictions of the temperature sensitivity of the carbonate clumped isotope thermometer for calcite minerals by Schauble et al. (2006) and Guo et al. (2009) (Fig. 2.1).

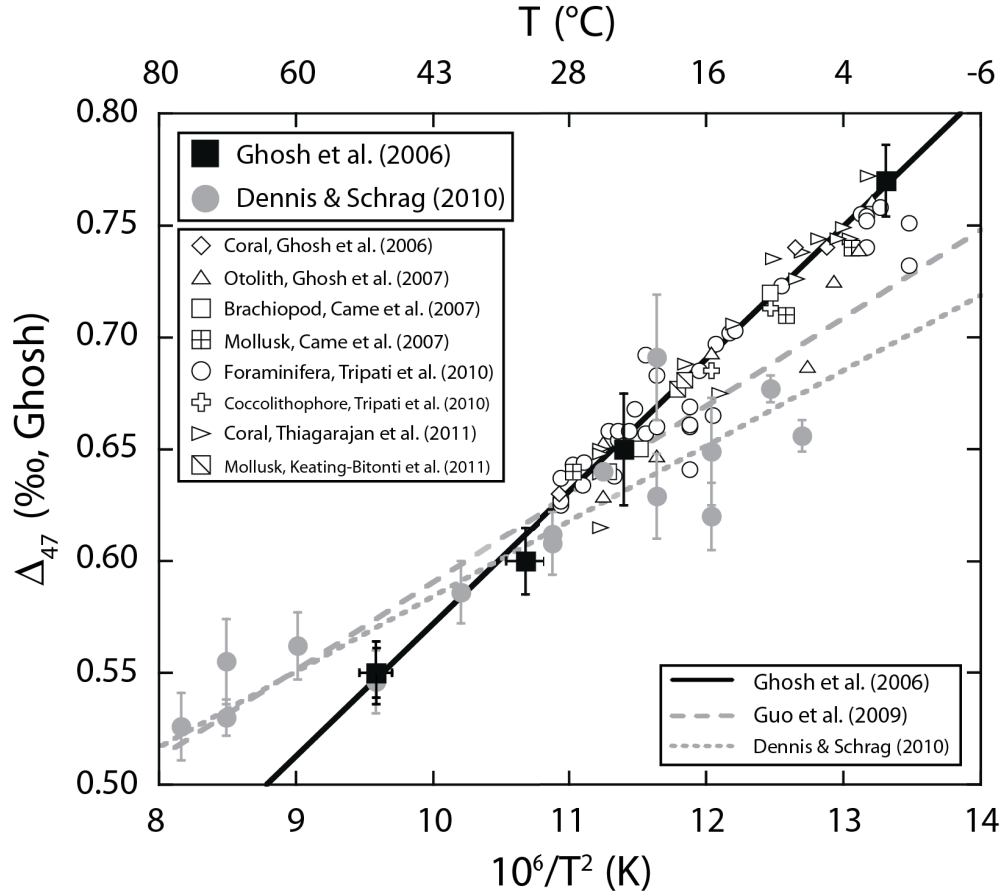


Figure 2.1 Carbonate clumped isotope values (Δ_{47}) from existing temperature (T) calibrations. The solid symbols are data from inorganic calcite precipitation experiments (Ghosh et al., 2006 and Dennis and Schrag, 2010) and the solid black and dotted gray lines are linear regressions through each dataset, respectively. The dashed gray curve is the theoretical Δ_{47} –temperature relationship for calcite from Guo et al. (2009). Open symbols are data from natural and cultured biogenic carbonates. Error bars on Δ_{47} represent the standard error from multiple analyses of a single sample, and error bars are not shown for the biogenic data to improve clarity. Clumped isotope data are reported on the heated gas or ‘Ghosh’ reference frame described by Ghosh et al. (2006) and Huntington et al. (2009). Error bars on $10^6/T^2$ represent the reported error for carbonate precipitation temperatures.

Unresolved differences between empirical calibrations have been a driving force behind interlaboratory comparisons designed to evaluate consistency between laboratories generating clumped isotope data (e.g., Dennis et al., 2011), as well as continued analysis of natural carbonates with well-constrained growth temperatures, such as modern land snails (Zaarur et al., 2011). Marine mollusks and brachiopods have so far escaped detailed calibration, although Came et al. (2007) report a limited dataset that conforms to the Caltech calibration line. A more comprehensive clumped isotope calibration, which spans a wider range of growth temperatures and a diversity of taxa, remains to be developed for these groups.

Additionally, few laboratories continue to utilize the analytical methods used to generate the Caltech calibrations reported in Ghosh et al., 2006, Ghosh et al., 2007, Came et al., 2007 and Tripathi et al., 2010, and Thiagarajan et al. (2011). These methods include 25 °C acid reactions in sealed vessels, use of a capillary gas chromatography (GC) column for purification of CO₂, and normalization of data to a single equilibrium CO₂ gas composition (1000 °C ‘heated gases’; see Huntington et al., 2009). Most laboratories, including Caltech, now use online extraction systems where carbonates are reacted in hot acid (typically 70–90 °C), CO₂ is continuously removed during the reaction by collection onto a cryogenic trap, and the CO₂ is purified by passage through traps or packed GC columns filled with a divinylbenzene polymer (Porapak Q™). In addition, an improved reference frame has recently been proposed (Dennis et al., 2011) whereby data are normalized to equilibrium CO₂ prepared at at least two temperatures, typically one high temperature (1000 °C) and one low temperature (~25 °C). As such, there is now

additional motivation to generate new calibrations, using the newer analytical methods, and within the framework of concurrent analyses of CO₂ gas in isotopologue equilibrium at two or more widely spaced temperatures.

In this paper we describe the results of a calibration of the carbonate clumped isotope thermometer for modern marine mollusks and brachiopods. The samples were obtained from natural marine environments or grown under monitored conditions in waters spanning a range of temperatures (−1.0 to 29.5 °C). Both of the major mineralogies of brachiopods and mollusks, calcite and aragonite, were examined. The Δ_{47} data are the first calibration data to be reported on a new reference frame for multiple isotopologue analyses of CO₂. Our study also employs laboratory methods similar to those now in wide usage.

2.2 Methods

2.2.1 Samples

The calibration was generated using shell material from 16 different mollusk and brachiopod species, spanning a range of growth environments and shell morphologies (Table 2.1). The majority of the organisms were collected live from the benthos, including shallow coastal areas, on the continental shelf, or in the deep-sea. Mollusks were collected from the northwestern Barents Sea (Spitsbergen Bank, Norway; Carroll et al., 2011), the northern Icelandic shelf (Grimsey Island, Iceland; Wanamaker et al., 2008), the northern Gulf of Mexico (Stetson Bank, USA; Gentry et al., 2008), and the coastal waters of southwest Puerto Rico. Other shells were grown in controlled

conditions that were monitored for changes in temperature and the oxygen isotopic composition of water. The temperate bivalve mollusks *Mytilus edulis* and *Mya arenaria* were grown in tanks at the Darling Marine Center (University of Maine, Walpole, ME, USA), located on the Gulf of Maine coast, using tidally-influenced water from the Damariscotta River (Wanamaker et al., 2007). Oysters, *Crassostrea virginica*, were grown in aquaculture cages at the Horn Point Marine Laboratory (University of Maryland, Cambridge, MD, USA) and nautiloids, *Nautilus pompilius*, were obtained from the Toba Aquarium (Toba, Japan). The brachiopods used in this study are from Antarctica (South Shetland Islands), the northern Gulf of Mexico, coastal California (Half Moon Bay, CA, USA), and the northern Caribbean Sea (Rio Bueno Harbor, Jamaica). Water temperatures at the collection locations ranged from 20 to 31 °C in the subtropics and tropics, to less than <0 °C in high-latitude seas.

Table 2.1 Carbon ($\delta^{13}\text{C}$), oxygen ($\delta^{18}\text{O}$), and clumped (Δ_{47}) isotope compositions of marine mollusks and brachiopods.

Sample ID	Depth (m)	Growth Temp. (°C)	Temp. Range (°C)	Salinity	Class ^a	Species
Mollusks						
<i>B-12, northwestern Barents Sea (Polar water), 75°39.80' N, 24°01.14' E</i>						
Ha-1	99	-1.0	2.0	34.5	Bivalvia (ar)	<i>Hiatella arctica</i>
Ha-2	99	-1.0	2.0	34.5	Bivalvia (ar)	<i>Hiatella arctica</i>
Ha-3	99	-1.0	2.0	34.5	Bivalvia (ar)	<i>Hiatella arctica</i>
Mt-1	99	-1.0	2.0	34.5	Bivalvia (ar)	<i>Mya truncata</i>
Mt-2	99	-1.0	2.0	34.5	Bivalvia (ar)	<i>Mya truncata</i>
Mt-3	99	-1.0	2.0	34.5	Bivalvia (ar)	<i>Mya truncata</i>
Ci-1	99	-1.0	2.0	34.5	Bivalvia (c)	<i>Chlayms islandica</i>
Ci-2	99	-1.0	2.0	34.5	Bivalvia (c)	<i>Chlayms islandica</i>
Ci-3	99	-1.0	2.0	34.5	Bivalvia (c)	<i>Chlayms islandica</i>
Ac-1	99	-1.0	2.0	34.5	Bivalvia (ar)	<i>Astarte crenata</i>
Ab-1	99	-1.0	2.0	34.5	Bivalvia (ar)	<i>Astarte borealis</i>
Ab-2	99	-1.0	2.0	34.5	Bivalvia (ar)	<i>Astarte borealis</i>
Ab-3	99	-1.0	2.0	34.5	Bivalvia (ar)	<i>Astarte borealis</i>
Cc-1	99	-1.0	2.0	34.5	Bivalvia (ar)	<i>Clinocardium ciliatum</i>
Cc-2	99	-1.0	2.0	34.5	Bivalvia (ar)	<i>Clinocardium ciliatum</i>

Table 2.1 (cont.)

Sample ID	Depth (m)	Growth Temp. (°C)	Temp. Range (°C)	Salinity	Class ^a	Species
<i>B-14, northwestern Barents Sea (Atlantic water), 75°00.06' N, 24°05.82' E</i>						
Ac-1	187	2.0	2.0	34.8	Bivalvia (ar)	<i>Asarte crenata</i>
Ac-2	187	2.0	2.0	34.8	Bivalvia (ar)	<i>Asarte crenata</i>
Cc-1	187	2.0	2.0	34.8	Bivalvia (ar)	<i>Clinocardium ciliatum</i>
Cc-2	187	2.0	2.0	34.8	Bivalvia (ar)	<i>Clinocardium ciliatum</i>
Cc-3	187	2.0	2.0	34.8	Bivalvia (ar)	<i>Clinocardium ciliatum</i>
<i>Grimsey Island, Icelandic Sea, 66°31.59' N, 18°11.74' E</i>						
WG06-1278	83	4.7	2.0	34.9	Bivalvia (ar)	<i>Arctica islandica</i>
<i>Stetson Bank, Gulf of Mexico, USA, 28°09.96' N, 94°17.82' W</i>						
FGS-1-1	24	27.5	2.2	≥34.0	Gastropoda (ar)	<i>Conus ermineus</i>
FGS-1-2	24	23.0	1.5	≥34.0	Gastropoda (ar)	<i>Conus ermineus</i>
FGS-1-3	24	19.8	0.8	≥34.0	Gastropoda (ar)	<i>Conus ermineus</i>
<i>La Parguera, Puerto Rico, USA, 17°95.00' N, 67°04.83' W</i>						
Pp-1	1	29.5	3.0	≥35.0	Bivalvia (ar)	<i>Phacoides pectinatus</i>
Pp-2	1	29.5	3.0	≥35.0	Bivalvia (ar)	<i>Phacoides pectinatus</i>
Pp-3	1	29.5	3.0	≥35.0	Bivalvia (ar)	<i>Phacoides pectinatus</i>
<i>University of Maine Darling Marine Center, Damariscotta River, Maine, USA, 43°51.75' N, 69°34.88' W</i>						
Mya-3.5	-	3.4	0.8	30.4	Bivalvia (ar)	<i>Mya arenaria</i>
Mya-8.5	-	8.6	2.2	29.9	Bivalvia (ar)	<i>Mya arenaria</i>
Mya-16	-	15.9	1.7	30.7	Bivalvia (ar)	<i>Mya arenaria</i>
Mytilus-4	-	4.0	0.5	32.0	Bivalvia (c)	<i>Mytilus edulis</i>
Mytilus-8	-	8.0	0.5	32.0	Bivalvia (c)	<i>Mytilus edulis</i>
Mytilus-12	-	12.0	0.5	32.0	Bivalvia (c)	<i>Mytilus edulis</i>
Mytilus-15	-	15.0	0.5	32.0	Bivalvia (c)	<i>Mytilus edulis</i>
<i>University of Maryland Horn Point Laboratory, Choptank River, Maryland, USA, 38°35.60' N, 76°07.74' W</i>						
HPL-1	-	14.4	0.5	13.5	Bivalvia (c)	<i>Crassostrea virginica</i>
HPL-2	-	27.3	0.2	11.6	Bivalvia (c)	<i>Crassostrea virginica</i>
HPL-3	-	23.7	0.1	13.2	Bivalvia (c)	<i>Crassostrea virginica</i>

Table 2.1 (cont.)

Sample ID	Depth (m)	Growth Temp. (°C)	Temp. Range (°C)	Salinity	Class ^a	Species
<i>Toba Aquarium, Toba, Japan, 34°29.00' N, 136°51.00' E</i>						
P8/30	-	24.5	0.5	-	Cephalopoda (ar)	<i>Nautilus pompilius</i>
P52	-	24.5	0.5	-	Cephalopoda (ar)	<i>Nautilus pompilius</i>
P132	-	24.5	0.5	-	Cephalopoda (ar)	<i>Nautilus pompilius</i>
P110	-	20	1.0	-	Cephalopoda (ar)	<i>Nautilus pompilius</i>
P95	-	20	1.0	-	Cephalopoda (ar)	<i>Nautilus pompilius</i>
P105	-	20	1.0	-	Cephalopoda (ar)	<i>Nautilus pompilius</i>
Brachiopods						
<i>Admiralty Bay, South Shetland Islands (Southern Ocean), 62°10.00' N, 58°25.00' W</i>						
GB4-3	250-300	-1.0	1.0	34.5	Rhynchonellata (c)	<i>Magellania</i> spp.
GB3-5	250-300	-1.0	1.0	34.5	Rhynchonellata (c)	<i>Magellania</i> spp.
<i>North Central Gulf of Mexico, USA, 27°09.96' N, 94°17.82' W</i>						
Brach-m1	742	5.5	-	-	Rhynchonellata (c)	<i>Ecnomiosa gerda</i>
Brach-m2	742	5.5	-	-	Rhynchonellata (c)	<i>Ecnomiosa gerda</i>
<i>Half Moon Bay, California, USA, 37°27.32' N, 122°26.13' W</i>						
HMB-3	55	10.5	1	33.2	Rhynchonellata (c)	<i>Terebratulina unguicula</i>
<i>Rio Bueno Harbor, Jamaica, 18°28.12' N, 77°27.50' W</i>						
RBJ-1-3	20	27.5	-	35.9	Rhynchonellata (c)	<i>Lacazella</i> spp.

Table 2.1 (cont.)

Sample ID	<i>n</i>	$\delta^{13}\text{C}_{\text{carb}}$ (‰, PDB)	$\delta^{18}\text{O}_{\text{carb}}$ (‰, PDB)	$\delta^{18}\text{O}_{\text{water}}$ (‰, SMOW) ^b	Δ_{47} (‰, Ghosh) ^c	Δ_{47} (‰, CDES) ^d
Mollusks						
<i>B-12, northwestern Barents Sea (Polar water), 75°39.80' N, 24°01.14' E</i>						
Ha-1	3	1.29 (±0.02)	5.08 (±0.02)	0.72	0.708	0.768 (±0.004)
Ha-2	3	1.42 (±0.06)	4.92 (±0.09)	0.72	0.726	0.783 (±0.006)
Ha-3	3	0.41 (±0.03)	5.05 (±0.04)	0.72	0.719	0.776 (±0.005)
Mt-1	3	1.71 (±0.01)	5.38 (±0.01)	0.72	0.707	0.772 (±0.006)
Mt-2	4	1.98 (±0.01)	5.49 (±0.03)	0.72	0.693	0.757 (±0.010)
Mt-3	3	2.07 (±0.01)	5.52 (±0.01)	0.72	0.709	0.775 (±0.007)
Ci-1	3	1.22 (±0.01)	4.43 (±0.02)	0.72	0.713	0.782 (±0.009)
Ci-2	3	1.02 (±0.01)	4.45 (±0.01)	0.72	0.697	0.763 (±0.005)
Ci-3	5	1.02 (±0.01)	4.56 (±0.02)	0.72	0.717	0.784 (±0.007)
Ac-1	3	1.50 (±0.04)	5.29 (±0.01)	0.72	0.711	0.781 (±0.003)
Ab-1	3	0.76 (±0.01)	5.35 (±0.02)	0.72	0.694	0.764 (±0.011)
Ab-2	3	1.03 (±0.02)	5.37 (±0.01)	0.72	0.707	0.773 (±0.004)
Ab-3	3	0.73 (±0.03)	5.27 (±0.01)	0.72	0.692	0.758 (±0.017)
Cc-1	3	0.27 (±0.01)	4.40 (±0.01)	0.72	0.686	0.753 (±0.007)
Cc-2	3	-0.96 (±0.02)	4.26 (±0.03)	0.72	0.682	0.745 ^e
<i>B-14, northwestern Barents Sea (Atlantic water), 75°00.06' N, 24°05.82' E</i>						
Ac-1	3	1.14 (±0.01)	4.88 (±0.01)	0.66	0.717	0.788 (±0.004) ^f
Ac-2	3	1.08 (±0.01)	4.89 (±0.02)	0.66	0.693	0.759 (±0.007)
Cc-1	3	-0.20 (±0.04)	4.19 (±0.01)	0.66	0.690	0.756 (±0.013)
Cc-2	3	-0.38 (±0.10)	4.12 (±0.01)	0.66	0.689	0.758 (±0.011)
Cc-3	3	-0.40 (±0.03)	4.19 (±0.03)	0.66	0.698	0.765 (±0.006)
<i>Grimsey Island, Icelandic Sea, 66°31.59' N, 18°11.74' E</i>						
WG06-1278	3	1.40 (±0.02)	3.62 (±0.02)	0.08	0.660	0.729 (±0.008)
<i>Stetson Bank, Gulf of Mexico, USA, 28°09.96' N, 94°17.82' W</i>						
FGS-1-1	3	-0.30 (±0.01)	-0.84 (±0.06)	1.34	0.593	0.656 (±0.007)
FGS-1-2	3	-0.04 (±0.01)	-0.22 (±0.02)	0.99	0.625	0.692 (±0.005)
FGS-1-3	3	-0.14 (±0.01)	0.60 (±0.01)	0.68	0.630	0.697 (±0.007)
<i>La Parguera, Puerto Rico, USA, 17°95.00' N, 67°04.83' W</i>						
Pp-1	3	0.90 (±0.07)	-0.55 (±0.07)	0.80	0.624	0.690 (±0.007)
Pp-2	3	0.77 (±0.01)	-0.70 (±0.02)	0.80	0.632	0.692 (±0.005)
Pp-3	3	1.07 (±0.02)	-0.72 (±0.04)	0.80	0.629	0.697 (±0.007)
<i>University of Maine Darling Marine Center, Damariscotta River, Maine, USA, 43°51.75' N, 69°34.88' W</i>						
Mya-3.5	2	1.42 (±0.01)	0.41 (±0.02)	-1.57	0.670	0.740 (±0.020)
Mya-8.5	3	1.34 (±0.01)	-0.45 (±0.04)	-1.66	0.649	0.718 (±0.007)
Mya-16	3	0.95 (±0.01)	-0.82 (±0.04)	-1.38	0.646	0.715 (±0.003)

Table 2.1 (cont.)

Sample ID	<i>n</i>	$\delta^{13}\text{C}_{\text{carb}}$ (‰, PDB)	$\delta^{18}\text{O}_{\text{carb}}$ (‰, PDB)	$\delta^{18}\text{O}_{\text{water}}$ (‰, SMOW)	Δ_{47} (‰, Ghosh)	Δ_{47} (‰, CDES)
<i>University of Maine Darling Marine Center, Damariscotta River, Maine, USA, 43°51.75' N, 69°34.88' W (cont.)</i>						
Mytilus-3.5	5	-6.47 (±0.03)	0.67 (±0.04)	-1.94	0.699	0.776 (±0.007) ^g
Mytilus-8.5	4	-7.89 (±0.02)	-1.40 (±0.03)	-3.07	0.680	0.757 (±0.009) ^g
Mytilus-12	2	-6.25 (±0.02)	-1.11 (±0.02)	-2.03	0.691	0.769 (±0.017) ^g
Mytilus-15	4	-6.82 (±0.01)	-1.34 (±0.04)	-1.37	0.665	0.741 (±0.005) ^g
<i>University of Maryland Horn Point Laboratory, Choptank River, Maryland, USA, 38°35.60' N, 76°07.74' W</i>						
HPL-1	3	-4.23 (±0.05)	-1.96 (±0.03)	-3.76	0.664	0.735 (±0.004)
HPL-2	2	-5.30 (±0.02)	-6.01 (±0.02)	-3.54	0.616	0.686 (±0.005)
HPL-3	3	-5.24 (±0.03)	-3.99 (±0.01)	-3.69	0.640	0.708 (±0.007)
<i>Toba Aquarium, Toba, Japan, 34°29.00' N, 136°51.00' E</i>						
P8/30	3	-0.43 (±0.02)	-1.10 (±0.05)	-0.34	0.661	0.726 (±0.005)
P52	3	-2.55 (±0.09)	-0.89 (±0.13)	-0.34	0.652	0.717 (±0.003)
P132	3	-3.63 (±0.03)	-0.71 (±0.04)	-0.34	0.661	0.726 (±0.008)
P110	3	-4.06 (±0.03)	-0.33 (±0.03)	-0.34	0.633	0.696 (±0.012)
P95	3	-3.82 (±0.01)	-0.06 (±0.01)	-0.34	0.634	0.706 (±0.009)
P105	3	-3.21 (±0.01)	-0.20 (±0.03)	-0.34	0.637	0.709 (±0.004)
Brachiopods						
<i>Admiralty Bay, South Shetland Islands (Southern Ocean), 62°10.00' N, 58°25.00' W</i>						
GB4-3	3	0.54 (±0.04)	3.50 (±0.03)	-0.20	0.709	0.784 (±0.007)
GB3-5	3	0.99 (±0.01)	3.48 (±0.02)	-0.20	0.693	0.773 (±0.013)
<i>North Central Gulf of Mexico, USA, 27°09.96' N, 94°17.82' W</i>						
Brach-m1	3	1.48 (±0.02)	3.02 (±0.02)	0.00	0.690	0.756 (±0.005)
Brach-m2	3	1.56 (±0.02)	3.48 (±0.02)	0.00	0.691	0.757 (±0.014)
<i>Half Moon Bay, California, USA, 37°27.32' N, 122°26.13' W</i>						
HMB-3	2	1.09 (±0.01)	1.22 (±0.01)	0.10	0.681	0.754 (±0.002)
<i>Rio Bueno Harbor, Jamaica, 18°28.12' N, 77°27.50' W</i>						
RBJ-1-3	3	2.07 (±0.04)	-1.00 (±0.07)	0.80	0.614	0.676 (±0.011)

Note: All \pm values are standard error of the mean ($=1\sigma/\sqrt{n}$), where 1σ is the standard deviation of the *n* analyses (each analysis consists of extraction of CO₂ from carbonate, purification of the CO₂, and analysis in the mass spectrometer over six ‘acquisitions’, as detailed in Section 2.2.).

^a(ar) = aragonite shell, (c) = calcite shell. In some cases this was confirmed by X-ray powder diffraction (Fig. A1.1).

^bWater oxygen isotope values were either measured directly or taken from the model of LeGrande and Schmidt (2006) using the sample coordinates and collection depths (model values are in italics).

^cValues reported on the heated gas or ‘Ghosh’ scale described by Ghosh et al. (2006) and Huntington et al. (2009).

^dValues reported on the carbon dioxide equilibrium scale or ‘CDES’ described by Dennis et al. (2011).

^eDuplicate and triplicate values were rejected because of high Δ_{48} values; possibly contaminated (Table A1.1).

^fHigh Δ_{47} value compared to other shells analyzed from this location. No methodological reason to reject data.

^gDivergent Δ_{47} values for carbonate standards run with these samples. The values of NBS-19 were greater than its working value (0.352‰) for JHU Sequence Numbers 382 and 409. Samples were rejected on these grounds.

The mineralogy of some mollusk shells was confirmed by powder X-ray diffraction using a Philips X’Pert Pro MPD diffractometer in the Department of Materials Science and Engineering at Johns Hopkins University, Baltimore, MD (Fig. A1.1). The shells of *N. pompilius* (Japan), *Hiatella arctica*, *Mya truncata*, *Astarte crenata*, *Astarte borealis*, *Clinocardium ciliatum* (all from the Barents Sea), *Phacoides pectinata* (Puerto Rico), and *M. arenaria* (Maine, USA) are all aragonite, whereas the shells of *Chlamys islandica* (Barents Sea) are calcite. *M. edulis* (Maine, USA) shells contain both calcite and aragonite, but only the calcitic component of these shells was sub-sampled for clumped isotope analysis (Wanamaker et al., 2007).

2.2.1.1 Mollusk growth temperatures

Generating this calibration required knowledge of the ambient shell growth temperatures of both natural and controlled environments. For shells collected in regions where long-term temperature records did not exist we relied on nearby records or direct temperature readings made during collections. In the northwestern Barents Sea mollusks were

collected at two sites in an area where Arctic and Atlantic water masses, each of different temperature, converge (see Carroll et al., 2011 for detailed collection information). The collection sites were located on either side of the Polar Front, an oceanographic boundary between the water masses. The position of the Polar Front may vary by kilometers annually, but is tightly constrained in the collection area by steep seafloor topography and regional circulation (Johannessen and Foster, 1978 and Harris et al., 1998). Bottom temperatures in Arctic waters north of the Polar Front at site ‘B-12’ were -1 ± 2 °C at a depth of 99 m, whereas bottom temperatures in the warmer Atlantic water south of the Polar Front at site ‘B-14’ were 2 ± 2 °C at 187 m (Harris et al., 1998 and Carroll et al., 2011). In summer 2007, live, undamaged bivalves were collected at each site, immediately shucked, and frozen aboard the R/V Lance (Norwegian Polar Institute, Tromsø, Norway). Using sclerochronological analyses of these same shells Carroll et al. (2011) demonstrated that *C. ciliatum* specimens collected at both sites were ≥ 25 years old. Because shell analyzed from all Arctic species represented a ‘bulk’ sample, which integrated across the entire shell, it is possible that decadal-scale variations in seawater temperature caused additional error in our growth temperature assignments for these sites. The longest instrumental temperature record from the Barents Sea along the Kola Transect shows that decadal variability in sea surface temperature (<200 m) did not exceeded ± 1 °C from ~1900 to 2000 (Skagseth et al., 2008). This implies that measured sub-annual temperature variability of ± 2 °C is greater than the annual and decadal variability over the last 100 years of shell growth in the Barents Sea.

One shell of the mollusk *Arctica islandica* was included in our calibration. This specimen was collected live from the northern Icelandic Shelf southwest of the island of Grimsey, Iceland at a depth of 83 m in June 2006 (Wanamaker et al., 2008). Based on counts of annual growth bands this organism lived from 1981 to 2006. Bottom temperatures on the northern Icelandic Shelf over this interval were estimated to be 4.7 ± 2 °C by averaging summer (JJA) measurements from 50 and 100 m depth along the Siglunes 3 profile, which is located ~25 km west of the collection location (data from the Marine Research Institute, Reykjavik, Iceland; see Knudsen et al., 2004). The average annual temperature range (1947–2006) is ~1.8 °C at Siglunes 3, which is greater than variability in the average monthly temperature (JJA, ± 0.9 °C). Because the *A. islandica* shell was subsampled across all growth years, we used ± 2 °C as a conservative estimate of the assigned temperature error.

A single specimen of the gastropod *Conus ermineus* was obtained for this study (see Gentry et al., 2008). This organism was collected live from the Stetson Bank in the northern Gulf of Mexico in 2003 at 24 m water depth, but died shortly after collection. Bottom growth temperatures were monitored from November 2002 to January 2004 using data loggers deployed at the collection site by Post, Buckley, Schuh & Jernigan, Inc. (PBS & J Inc.) under contract to the Flower Garden Banks National Marine Sanctuary. From 2002 to 2004, the bottom temperatures on the Stetson Bank ranged from 17 to 30 °C, with a mean temperature of 22.6 °C (Gentry et al., 2008). This relatively large seasonal temperature range precluded the use of ‘bulk’ shell from *C. ermineus* in our calibration. Instead, we sampled intra-annual shell material from within a single

growth year. By sub-sampling within 1 year we effectively decreased the temperature range associated with a single isotopic measurement. To do this we identified the most recent external growth band and sub-sampled from three divisions corresponding to the 2002 growth year using a Dremel[®] rotary drill. The sub-sampled areas were determined by scaling the sub-sampling intervals in Gentry et al. (2008) to another part of the shell. This sampling method allowed for direct comparison with the temperatures and seawater oxygen isotope measurements reported by Gentry et al. (2008).

Three shells of the bivalve mollusk *P. pectinatus* were collected in January 2010 from a mangrove lagoon located near the town of La Parguera, Puerto Rico. The bivalves were found buried in organic-rich sediment in 1 m of water. The ‘Pithahaya’ lagoon is subtidal and, because there are no significant local sources of freshwater, is fully marine with salinities in excess of 35‰ (Rooker and Dennis, 1991). Monthly sea surface temperatures (SST) recorded at a nearby coral reef over a 30 year period from 1966 to 1995 ranged from 25 to 30 °C with a mean of ~29.5 °C (Winter et al., 1998). Over 30 years the mean SST increased by 0.7 °C, which was significant but still smaller than the seasonal temperature range of 3 °C used as our estimate of growth temperature variability. *P. pectinatus* shell material used for clumped isotope analysis was sampled across all growth bands.

Shells from two species of temperate marine bivalves were used in this calibration. These organisms were grown under controlled and continuously monitored environmental conditions at the University of Maine, Darling Marine Center in Walpole, ME, USA.

Because seasonal temperature gradients in the Gulf of Maine can be large (16 °C) it was necessary to use ‘cultured’ shell grown at several constant, intermediate temperatures (~5 to 15 °C). We used shell material from the ventral margin of blue mussels, *M. edulis*, grown over intervals of 5–6 months at four temperatures (4, 8, 12, and 15 °C; reported in Wanamaker et al., 2007). Over these time periods only ~3 mm of new shell was grown. Because at least 30 mg of shell carbonate was required for replicate clumped isotope analyses (3×10 mg/analysis) we combined several individual shells from identical experimental conditions to obtain enough material for analysis. Water samples were collected weekly to monitor ambient changes in the seawater oxygen isotope value (Wanamaker et al., 2007). The soft shell clams, *M. arenaria*, used were also grown at the Darling Marine Center but the growth environments of these shells were not controlled. Instead, they lived in tanks fed with ambient water from the Damariscotta River. Shell growth was monitored from January to August 2010, over which time the water temperature warmed from ~2 to 18 °C. Calcein, a fluorescent dye which is commonly used for labeling shell, was used to mark three intervals in the shells which were later sub-sampled (see Beirne et al., 2012). This divided the 16 °C range in growth temperature into three periods: winter (average temp. = 3.39 ± 0.83 °C), spring (average temp. = 8.64 ± 2.18 °C), and summer (average temp. = 15.87 ± 1.65 °C).

Estuarine bivalves have traditionally been avoided in oxygen isotope thermometry because the temperature and oxygen isotope fluctuations (from meteoric water–seawater mixing) in mesohaline waters are covariable and therefore difficult to independently constrain. Because clumped isotope thermometry is independent of the isotopic

composition of the ambient fluid we included eastern oysters, *C. virginica*, from the Choptank River in the Chesapeake Bay in this calibration. These specimens were grown in natural waters at the University of Maryland, Horn Point Laboratory in Cambridge, MD, USA. Oyster growth temperatures were monitored from August to November 2010, and shell was sampled from three intervals within this period corresponding to August (average temp. = 27.3 ± 0.2 °C), August–September (average temp. = 23.7 ± 0.4 °C), and September–November (average temp. = 14.4 ± 0.5 °C). The oxygen isotope composition of the waters was also monitored periodically.

Lastly, several nautilus shells (*N. pompilius*) were obtained from the Toba Aquarium in Toba, Japan. Adult Nautili were maintained in recirculating aquaria which used natural seawater held at a constant temperature of 20 ± 1 °C. The Toba nautilus are one of the only broods in the world that successfully reproduce in captivity (T. Moritaki, personal communication). Deposited eggs are transferred to warmer recycled seawater held at 25 ± 0.5 °C in a smaller ‘incubation tank’ where they are allowed to hatch and grow for 1–2 months. We analyzed ‘bulk’ shell material from both juvenile and adult shells.

2.2.1.2 Brachiopod growth temperatures

The articulate brachiopods used in this study were all collected live from their natural habitats (Table 1). Two specimens identified as *Magellania* spp. were obtained from Admiralty Bay in the South Shetland Islands, Antarctica. Here the collection depth was 250–300 m with a mean annual temperature of -1 ± 1 °C. Two specimens of the species *Ecnomiosa gerda* were collected in 742 m of water at 5.5 °C in the north-central Gulf of

Mexico on the continental slope off of Texas, USA near site 83G3-6 in Grossman and Ku (1986). One specimen of *Terebratulina unguicula* was collected at 55 m depth in Half Moon Bay off the coast of California where waters were 10.5 ± 1.0 °C, and one specimen identified as *Lacazella* spp. was collected from Rio Bueno Harbor, Jamaica in 20 m of water which was ~ 27.5 °C (NODC World Ocean Atlas, <http://www.esrl.noaa.gov/psd/data/gridded/data.nodc.woa98.html>; Jackson and Winston, 1982). Brachiopod shell material came from the whole pedicle valve or was sub-sampled from one valve, perpendicular to the growth axis, across all growth bands.

2.2.2 Stable isotope measurements

Isotopic measurements were performed at John Hopkins University in the Department of Earth and Planetary Science using a Thermo Scientific MAT 253 mass spectrometer coupled to a custom-built, automated acid reaction and gas purification line. This line is nearly identical to the one described by Passey et al. (2010), and contains three coupled systems designed to generate high-purity CO₂ gas from carbonate samples and standards, and reference ‘equilibrium CO₂ gases’. In the first stage, ~ 10 mg of carbonate is reacted in vacuo for 10 min in a common acid bath containing phosphoric acid ($\rho = 1.91$ mg/ml) held at 90 °C. The CO₂ gas is collected in a liquid nitrogen (LN) trap after passing through a -78 °C water trap. In the second stage the sample CO₂ is transferred from the collection trap (warmed to -78 °C) to a second LN trap using a purified He carrier gas. During this transfer the sample and carrier gas pass through a second -78 °C trap, a getter containing silver wool (to remove sulfur-containing contaminants), and finally a 1.2 m gas chromatography (GC) column containing Porapak™ porous polymer absorbent held

at $-20\text{ }^{\circ}\text{C}$. Prior to August 2011 the system did not use a silver wool getter. The addition of the getter had no obvious impact on the isotopic compositions of samples or standards. The last stage consists of a final transfer from the post-GC LN collection trap (warmed to $-78\text{ }^{\circ}\text{C}$) to a smaller LN trap. This is done in vacuo after the He carrier gas is pumped away. The frozen sample CO_2 is then allowed to expand at room temperature for 3 min in the final trap before further expansion into the bellows of the MAT 253 dual inlet system. The other bellows contained a reference gas (Oztech Trading Corporation, Safford, AZ, USA) with a bulk isotopic composition of $\delta^{13}\text{C} = -3.61\text{‰}$ PDB and $\delta^{18}\text{O} = -15.81\text{‰}$ PDB.

Accurate carbonate clumped isotope measurements require a reference frame which corrects for changes in the ionization conditions inside of a gas source mass spectrometer and for ‘nonlinearities’ such as a dependence of the apparent Δ_{47} value on δ_{47} (where the latter is a measure of the ^{13}C and ^{18}O content of the sample; see Huntington et al., 2009 and Dennis et al., 2011). This also allows all laboratories measuring clumped isotopes to report their data on a common scale (Dennis et al., 2011). To construct this reference frame, we regularly analyzed CO_2 gases driven to isotopologue equilibrium at $1000\text{ }^{\circ}\text{C}$ and 30 or $27\text{ }^{\circ}\text{C}$. The former were prepared by heating aliquots of CO_2 in quartz tubes in a tube furnace held at $1000\text{ }^{\circ}\text{C}$. The latter were prepared by equilibrating CO_2 with water at a temperature of 30 or $27\text{ }^{\circ}\text{C}$ (Fig. 2.2). Prior to May 2010 the equilibrations were done at $27\text{ }^{\circ}\text{C}$; subsequently all equilibrations were done at $30\text{ }^{\circ}\text{C}$. For each of these temperatures, we used two different CO_2 (or H_2O) reservoirs of differing bulk composition, so that in total four different equilibrium gases were analyzed. We analyzed

one of these gases every 1–2 days, thus cycling through the four gases on a weekly or sub-weekly basis. These gases were introduced into a He carrier gas ‘upstream’ of the second stage of the purification line, and thus were treated in exactly the same manner as carbonates except for the initial acid extraction step.

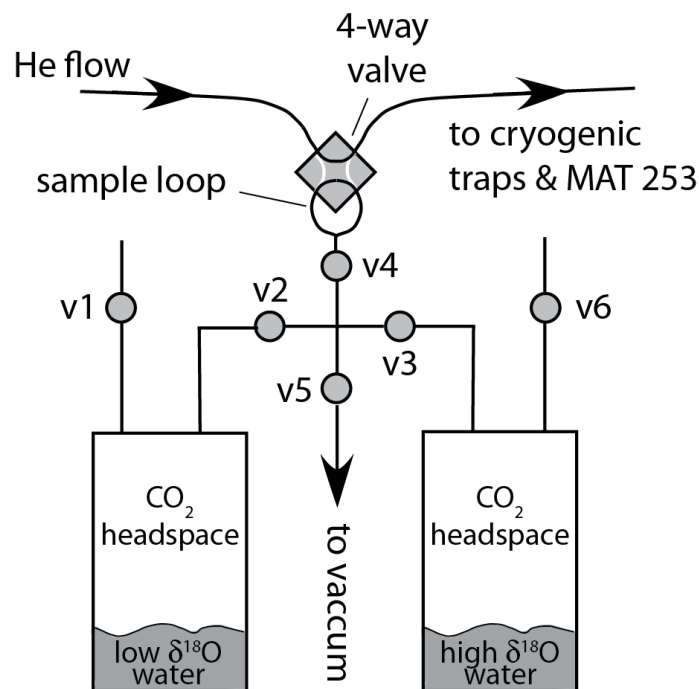


Figure 2.2 Carbon dioxide–water equilibration device used to generate ‘reference’ CO₂ gases in equilibrium with two isotopically different waters at controlled temperatures. Both reservoirs are submerged in a thermostatic water bath that maintains a constant temperature of 30 (or 27) ± 1 °C. The 4-port, 2-way valve is shown in the ‘standby’ position where the valve and lines to the automated extraction device (described in Section 2.2.2) are purged with a purified He carrier gas. During standby the sample loop is open to a rough pump via valves 4 and 5. During sample analysis, the sample loop is filled with CO₂ gas from either reservoir by closing valve 5 and opening valve 4, and then opening either valve 2 or 3. Valve 4 is then closed, and switching of the 4-port valve

introduces the CO₂ in the sample loop to the automated preparation device. The CO₂ immediately passes through a -78°C trap, and is treated in exactly the same manner as sample CO₂ (i.e., from carbonate) except that it bypasses the phosphoric acid/autosampler volume.

Each sample, standard, or reference gas was analyzed at a bellows pressure corresponding to a signal of 12 V on the Faraday cup measuring mass 44 CO₂. The measurement sequence consisted of six repetitions of nine cycles, each with 26 s of integration time for a total combined integration of 1404 s per gas. The long-term internal standard deviation for Δ_{47} on the six repetitions of nine cycles was approximately 0.030‰. Most of the mollusk and brachiopod shells were run in triplicate, in which case the combined integration time approached the asymptotic portion of the shot noise curve predicted for carbonate clumped isotope analyses (Thiagarajan et al., 2011). The reported isotope ratios were calculated from these measurements. In some cases replicate measurements for a single sample (e.g., Ha-2) were all made during a single analytical session. It is possible that the reported error for these samples is artificially small because all analyses were corrected using the same reference frame. However, most samples used for this calibration were analyzed (replicated) over several analytical sessions.

2.2.3 Data reduction and analysis

Post-analysis data reduction was done according to the scheme outlined by Dennis et al. (2011) in which the equilibrium CO₂ gases are used to construct an empirical transfer function (ETF) that maps the measured sample Δ_{47} values onto a reference frame

anchored to theoretical predictions of Δ_{47} of CO₂ gas at two different equilibration temperatures: 27 or 30 °C, and 1000 °C. It has been observed that the raw Δ_{47} values of the equilibrium CO₂ gases may drift over time due to changes in the physical state of mass spectrometers (Huntington et al., 2009 and Passey et al., 2010), causing the slope and intercept of the ETF to drift. To correct for this drift we used a MATLAB[®] script that models changes in the slope and intercept of the equilibrium gas lines as low-order polynomial functions of time using a least squares approximation (Passey et al., 2010). Occasionally, there was no discernible drift in the reference gas lines. When this was the case a static correction was used, where the equilibrium gas data were simply linearly regressed, not modeled. The ETF scheme also differs from previous attempts to establish a Δ_{47} reference frame (e.g., the heated gas line) because it does not depend on assumptions about (or calibration of) the Δ_{47} value of the dual inlet reference gas CO₂ (Ghosh et al., 2006, Huntington et al., 2009 and Dennis et al., 2011). An acid temperature correction factor was applied to all data to normalize values to acid extractions performed at 25 °C. For the values reported on the original ‘Ghosh’ scale, we used an acid correction factor of 0.081‰ (Passey et al., 2010). For values reported on the new ‘carbon dioxide equilibrium scale’, we used a value of 0.092‰, a value that was determined by analyzing three different shells using both 25 and 90 °C acid reactions (see Section 4.1.2.).

We analyzed NBS-19 and two internal carbonate standards (UU-Carrara and 102-GC-AZ01) at regular intervals to monitor system stability and precision, with the following results (reported on the ‘carbon dioxide equilibrium scale’): NBS-19 (n = 23) Δ_{47} = 0.414

$\pm 0.018\text{‰}$ (mean $\pm 1\sigma$ standard deviation); UU-Carrara ($n = 93$) $\Delta_{47} = 0.403 \pm 0.015\text{‰}$; 102-GC-AZ01 ($n = 102$) $\Delta_{47} = 0.710 \pm 0.015$. The $\delta^{13}\text{C}$ and $\delta^{18}\text{O}$ values of the samples were normalized to concurrent analyses of NBS-19 ($\delta^{13}\text{C} = 1.95\text{‰ PDB}$, $\delta^{18}\text{O} = -2.20\text{‰ PDB}$) or an in-house Carrara marble standard calibrated to NBS-19. Statistical treatment of corrected isotopic data (e.g., comparing Δ_{47} means) was done using Kaleidagraph 4 (Synergy Software) and JMP 9 (SAS Institute Inc.). The Electronic Annex reports all isotopic data for samples, carbonate standards, and equilibrium gases, as well as information on the models, the slopes, and intercepts of equilibrium gas lines and ETFs. Thus the Section A1.2 contains all of the data necessary to recalculate Δ_{47} values and reconstruct the calibration. We present all data from all of the analytical sessions that we attempted for modern mollusks and brachiopods, including data that were judged to be poor analyses and subsequently were excluded from the final dataset.

2.3 Results

The isotopic compositions ($\delta^{13}\text{C}$, $\delta^{18}\text{O}$, and Δ_{47}) of the mollusk and brachiopod shells are presented in Table 1 and the mean Δ_{47} value for each shell is plotted against its assigned growth temperature in Fig. 2.3a. A salient feature of this calibration data is the difference in Δ_{47} , at growth temperatures below $\sim 25^\circ\text{C}$, relative to the previous biogenic calibrations. Note that these previous calibrations have been converted to the ‘carbon dioxide equilibrium scale’ using the equation given in Table 4 of Dennis et al. (2011) (Fig. 2.3a). Bivalve mollusks from the Barents Sea have the highest Δ_{47} values, ranging from 0.788‰ to 0.745‰ , and sub-sampled shell from the 27.5°C interval of the *C. ermineus* shell from the Gulf of Mexico has the lowest Δ_{47} value of 0.656‰ (Table 2.1,

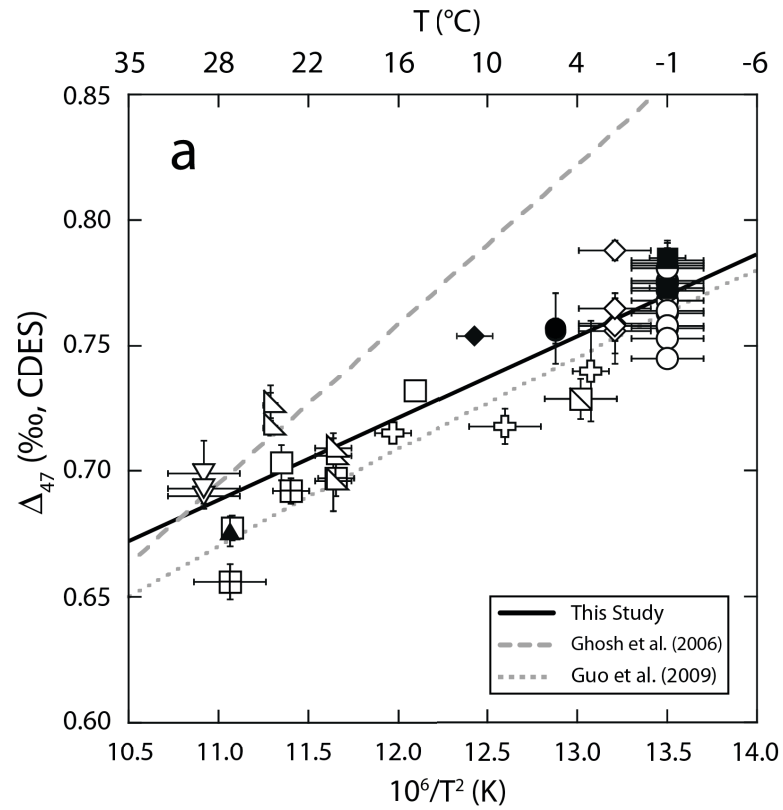
Fig. 2.3). The six brachiopod Δ_{47} values plot within the range of mollusk values.

Additionally, there is no clear difference in Δ_{47} between aragonitic mollusks and calcitic mollusks or brachiopods, despite the theoretical prediction of $\sim 0.02\text{‰}$ enrichment in Δ_{47} of aragonite relative to calcite in this temperature range (Schauble et al., 2006 and Guo et al., 2009). The absence of aragonite–calcite fractionation is consistent with Caltech datasets for calcitic and aragonitic biogenic carbonates (e.g., Tripathi et al., 2010 and Thiagarajan et al., 2011), which fall on a single line that agrees well with the inorganic calcite calibration line of Ghosh et al. (2006). A least squares linear regression of the mollusk and brachiopod Δ_{47} data versus the inverse squared growth temperatures results in a calibration line ($r^2 = 0.84$):

$$\Delta_{47} = 0.0327 \times 10^6 / T^2 + 0.3286 \quad (2.3)$$

that crosses the Ghosh et al. (2006) calibration line at 31.1 °C. The statistical details of Eq. (2.3) are presented in Table 2.2. The theoretical calibration for calcite (Schauble et al., 2006) is within the error of Eq. (2.3) over the temperature range of the shell data.

Note that this calibration is adapted to the carbon dioxide equilibrium scale via conversion of the mineral- CO_2 Δ_{47} ‘acid’ fractionation reported by Guo et al. (2009) ($=0.232\text{‰}$) to the carbon dioxide equilibrium scale ($=0.268\text{‰}$; Dennis et al., 2011, Table 2.4). The slope and intercept of Eq. (2.3) are also similar to the re-calculated Dennis and Schrag (2010) calibration within the reported errors of each regression (Dennis et al., 2011).



- | | |
|--|---|
| ○ Molluscs, Barents Sea (B-12) | ◇ Molluscs, Barents Sea (B-14) |
| ▢ <i>Arctica islandica</i> , Iceland | ⊕ <i>Mya arenaria</i> , ME, USA |
| □ <i>Crassostrea virginica</i> , MD, USA | ⊞ <i>Conus ermineus</i> , Gulf of Mexico |
| ▵ <i>Nautilus pompilius</i> , Japan | ▽ <i>Phacoides pectinatus</i> , Puerto Rico |
| ■ <i>Magellania</i> spp., Antarctica | ● <i>Ecnomosa gerda</i> , Gulf of Mexico |
| ◆ <i>T. unguicula</i> , CA, USA | ▲ <i>Lacazella</i> spp., Jamaica |

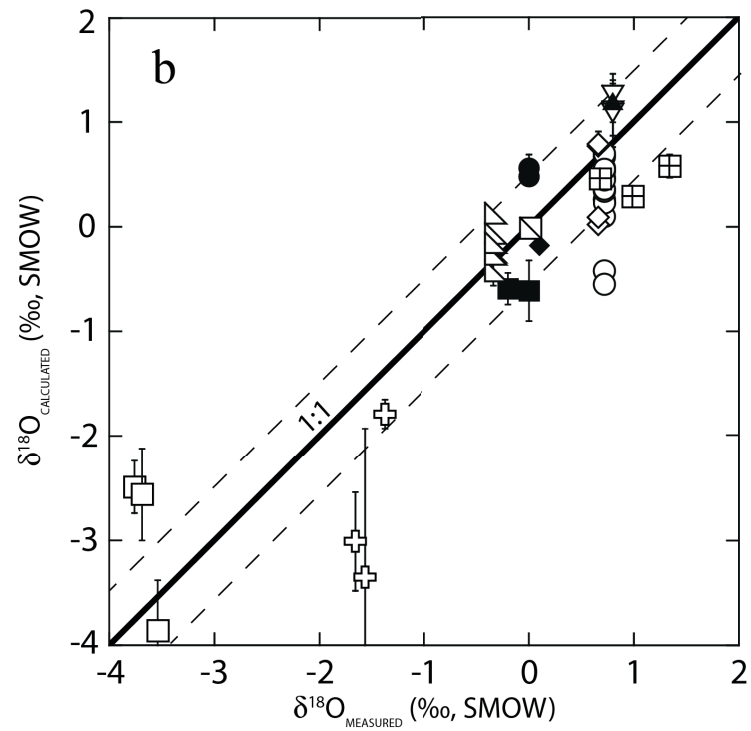


Figure 2.3 (*previous page*) (a) All Δ_{47} measurements of mollusk and brachiopod shells versus their growth temperatures. The solid black line is a linear regression through the mollusk and brachiopod data and the dashed and dotted grey lines are the empirical (Ghosh et al., 2006) and theoretical (Guo et al., 2009) calibrations for calcite, respectively. Clumped isotope data are reported on the carbon dioxide equilibrium scale or ‘CDES’ (Dennis et al., 2011), whereas data in Fig. 1 are reported on the ‘Ghosh’ scale (Ghosh et al., 2006). Error bars on Δ_{47} represent the standard error of the mean from multiple analyses of a single shell, and error bars on $10^6/T^2$ are the temperature ranges from Table 1. (b) Calculated $\delta^{18}\text{O}$ of seawater (using the measured carbonate $\delta^{18}\text{O}$ and the apparent clumped isotope temperatures from mollusks and brachiopods) versus the measured $\delta^{18}\text{O}$ of seawater at each collection location. For aragonitic mollusks the inorganic aragonite equilibrium oxygen isotope fractionation equation of Kim et al. (2007) was used to calculate seawater $\delta^{18}\text{O}$. For calcitic brachiopods and mollusks the inorganic calcite oxygen isotope equilibrium equation of Kim and O’Neil (1997) was used instead. The dashed lines are $\pm 0.5\text{‰}$ deviation from the 1:1 line and are shown only for reference.

Table 2.2 Linear regression of mollusk and brachiopod Δ_{47} values versus their growth temperatures.

Linear regression	$\Delta_{47} = 0.0327 \times 10^6/T^2 + 0.3286$
Shells used	45
R^2	0.84
RMSE ^a	0.15
Intercept standard error (‰)	0.0278
Intercept t ratio ^b	11.83
Slope standard error (‰/ $10^6/T^2$)	0.0022
Slope t ratio ^b	14.83

^aThe square root of the mean squared error.

^bThe ratio of the linear regression parameters to their respective standard errors. For example, a value greater than 2 is significant at the 0.05 significance interval.

For comparison with previous and contemporary data cast on the ‘Ghosh’ scale (e.g., Ghosh et al., 2006 and Huntington et al., 2009), we also report a least squares regression of the mollusk and brachiopod inverse squared growth temperatures and clumped isotope data reported in the ‘older’ reference frame:

$$\Delta_{47} = 0.0318 \times 10^6 / T^2 + 0.2737 \quad (2.4)$$

It should be noted that isotopic data from the *M. edulis* shells were excluded from this calibration. During the short interval in the January–May, 2010 analytical session when these shells were analyzed (Table A1.1) the Δ_{47} value of the carbonate standard NBS-19 was offset by $0.031 \pm 0.005\text{‰}$ (mean \pm standard error of the mean) from the accepted value, which was several times greater than the offsets for other working standards run during this analytical session. This offset persisted despite our efforts to correct for temporal variability in carbonate standard Δ_{47} residuals during this analytical session, thus precluding the use of the *M. edulis* data in the Δ_{47} –temperature calibration. We note, however, that these *M. edulis* Δ_{47} values, when plotted against their assigned growth temperatures, appear to agree with the trend of the mollusk and brachiopod data in Fig. 2.3a.

We also evaluated the ability of paired carbonate $\delta^{18}\text{O}$ and Δ_{47} analyses to predict the $\delta^{18}\text{O}$ of water in which each shell grew (Fig. 2.3b). This is done by converting the Δ_{47} value to an apparent temperature using Eq. (2.3), and then calculating the temperature dependent oxygen isotope fractionation factor between carbonate and water using the equations of Kim and O’Neil (1997) or Kim et al. (2007) for calcite or aragonite,

respectively. The standard error of the calculated $\delta^{18}\text{O}_{\text{water}}$ was determined by the propagation of error from the Δ_{47} -derived temperature and measured shell $\delta^{18}\text{O}$ through the equilibrium oxygen isotope thermometry equations. In general, these comparisons revealed that seawater compositions are predicted within about 0.5‰ of measured/modeled $\delta^{18}\text{O}_{\text{water}}$, although larger deviations are not uncommon (Fig. 2.3b). For some localities we relied on modeled $\delta^{18}\text{O}_{\text{water}}$ values (LeGrande and Schmidt, 2006) and apparent oxygen isotope disequilibrium could be caused, in part, by error in these estimates (Table 2.1).

In Fig. 2.3a, it is apparent that a range of Δ_{47} values for mollusk and brachiopod shells are observed for a given growth temperature. This is demonstrated most clearly where there is a high density of data, for example at the Polar site B-12 in the Barents Sea where 15 shells spanning six bivalve mollusk species were analyzed. The Δ_{47} values at B-12 ranged from 0.753‰ for *C. ciliatum* to 0.784‰ for *C. islandica*, within which there appear to be real differences between individuals and perhaps between species (Table 2.1). One way to evaluate the ‘spread’ of data around the linear regression (Eq. (2.3)) is to evaluate if it could be created by the analytical error of Δ_{47} measurements alone. Fig. 2.4 plots distribution of all mollusk and brachiopod Δ_{47} measurements (i.e., not ‘grouped’ by means of replicate analyses), normalized by the linear regression (Eq. 2.3), along with a Gaussian probability density function that has a mean equal to zero and a standard deviation equivalent to long-term, repeat analyses of our in-house Carrara marble standard (=0.015‰). This comparison shows that the standard deviation of all measurements of mollusks and brachiopods (=0.018‰) is slightly greater than the

measurement error of a homogeneous carbonate standard. The standard deviation for only the Arctic shells from site B-12 ($n = 46$) is 0.016‰, only slightly greater than the measurement error for our internal standards. It is conceivable that this poorer precision is an artifact of sample heterogeneity and errors in our estimates of the growth temperatures. However, the data are also consistent with a small degree of ‘vital effect’ disequilibrium, or simply reduced precision for analyses of natural biogenic carbonates containing complex organic matrices, relative to the precision obtained for very pure laboratory standards.

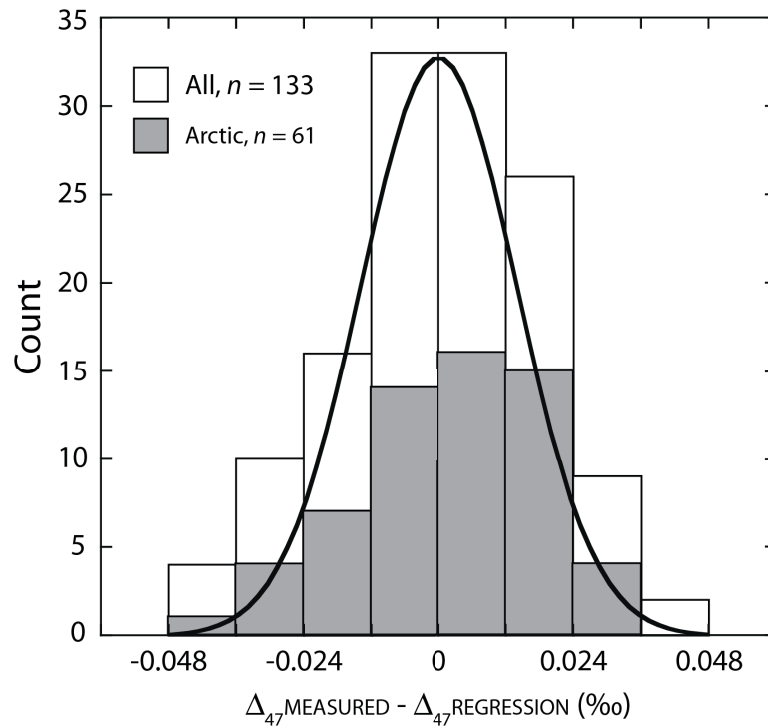


Figure 4.2 Distribution of all Δ_{47} measurements plotted as the difference between the measured Δ_{47} and the growth temperature-equivalent Δ_{47} predicted by Eq. (2.3). The distribution of Δ_{47} values for only the Arctic bivalves (sites B-12 and B-14) is shown in grey. The black line represents a Gaussian distribution of Δ_{47} data around a mean of 0‰ with a standard deviation of 0.015‰, which is the long-term standard deviation of our in-

house Carrara marble standard. The Δ_{47} data used to create the ‘All’ and ‘Arctic’ histograms are from individual analysis of mollusk and brachiopod shell material. This differs from Fig. 2.2, which presents the Δ_{47} data as the mean of replicate analyses on a single specimen.

2.4 Discussion

The clumped isotope calibration in this study was generated by analyzing mollusks and brachiopods across the virtual totality of ambient temperatures that they inhabit (-1.0 to 29.5 °C), as well as a number of different habitats. In the following discussion we seek explanations for why the calibration slopes of our study and Dennis and Schrag (2010) differ from those of Ghosh et al., 2006, Ghosh et al., 2007, Came et al., 2007 and Tripathi et al., 2010, and Thiagarajan et al. (2011). Section 2.4.1. explores methodological explanations and Section 2.4.2. explores ‘biological’ explanations relating to possible differences in isotopic fractionation during biomineralization in different taxonomic groups.

2.4.1 Methodological explanations

2.4.1.1 Intercalibration between different laboratories

A simple explanation for the observed differences in calibrations is that different laboratories are poorly intercalibrated. Prior to 2011, published carbonate clumped isotope data were reported on a ‘heated gas’ reference frame, which used CO₂ heated to 1000 °C to create a stochastic distribution of ¹³C–¹⁸O bonds (Ghosh et al., 2006 and Huntington et al., 2009). These gases were analyzed along with samples and used to

construct a reference line to which measured Δ_{47} values could be compared. A problem with this method was that the Δ_{47} value of the heated gases was defined as 0‰, effectively assuming that the reference line represented a completely disordered state after spending a sufficient amount of time (~ 2 h) at a high temperature (~ 1000 °C). However, theoretical predictions of Δ_{47} by Wang et al. (2004) suggested that CO₂ heated to 1000 °C has an equilibrium Δ_{47} value of 0.027‰. The heated gas reference frame also relied on an empirically-derived correction factor to account for CO₂ fragmentation and/or recombination reactions in the ionization source which may ‘scramble’ or reorder the ¹³C–¹⁸O bonds in the analyte gas (Huntington et al., 2009). Use of this ‘scale compression’ or ‘stretching’ factor requires the assumption that different tanks of Oztech reference CO₂ used in different laboratories have the same Δ_{47} value, or alternatively it requires calibration of a reference gas to gases previously analyzed relative to the original Oztech reference gas at the California Institute of Technology (Caltech) used in the Ghosh et al. (2006) calibration study. NBS-19 served as the only widely available reference material for evaluating the soundness of the correction scheme through time, and indeed most laboratories reported broadly similar Δ_{47} values for this material. However, its Δ_{47} value, ~ 0.35 ‰, is far outside of the range of low temperature calibrations (0.55–0.78‰ on the ‘Ghosh’ scale).

Dennis et al. (2011) readdressed the issue of interlaboratory standardization of clumped isotope measurements by establishing an empirical reference frame that tied measured Δ_{47} values of CO₂ to theoretical predictions of Δ_{47} of CO₂ at given equilibration temperatures. They showed that by using this revised reference frame, which we refer to

as the carbon dioxide equilibrium scale (CDES), interlaboratory agreement on a set of natural carbonates was at least 0.017‰ (1σ standard deviation), and as good as 0.008‰ (1σ standard deviation). These differences are too small to account for the greatest difference ($\sim 0.08\%$) observed between Δ_{47} –temperature calibrations at the coldest mollusk and brachiopod growth temperatures.

We directly tested for interlaboratory agreement by distributing an aliquot of aragonitic shell from specimen Ha-3 (*H. arctica*, site B-12, western Barents Sea) for analysis at Yale University and Caltech. Ha-3 was chosen for this comparison because the Δ_{47} values of shells from the Arctic site B-12 are the most different from the Δ_{47} value predicted by the Ghosh et al. (2006) calibration. Of the 15 individual shells analyzed from B-12, Ha-3 had abundant material and a Δ_{47} value (0.776‰) that was close to the group mean of 0.770‰. The raw clumped isotope data (δ_{47} , Δ_{47}) from Yale and Caltech were corrected using a static heated gas line and compared to our measured value for Ha-3 on the ‘Ghosh’ scale (Table 2.3). Unfortunately, these analyses were made before all laboratories were routinely reporting Δ_{47} data on the carbon dioxide equilibrium scale, thus precluding the use of the revised reference frame in these comparisons. The reported Δ_{47} value from Yale is 0.021‰ higher than our measurement and the Caltech value is 0.008‰ higher, but neither was high enough to account for the difference between the Caltech calibrations and the JHU + Harvard calibrations (Table 2.3, Fig. 2.5). However, these differences do highlight the importance of reporting Δ_{47} values on the CDES reference frame, as it was designed to empirically account for source fragmentation or recombination reactions during carbonate sample, standard, and equilibrium reference

gas analysis. Given these results and those of the interlaboratory calibration presented by Dennis et al. (2011), it seems that the different slopes of the Caltech and JHU + Harvard calibrations cannot be explained by poor interlaboratory calibration. However, these intercalibration exercises are imperfect for addressing this question, because the methodologies used at Caltech for these exercises are not the same as those used for the Caltech calibration studies. The former utilized the newer 90 °C acid reaction, packed GC column, online technique, whereas the latter utilized the original 25 °C acid reaction, capillary GC column, offline method. However, the methodology used at Yale for the interlaboratory calibration exercises are similar to the original methods used for the Caltech calibrations.

Table 2.3 Interlaboratory Δ_{47} comparison using shell Ha-3 (Site B-12, Barents Sea)

Laboratory	<i>n</i>	$\delta^{13}\text{C}$ (‰, PDB)	$\delta^{18}\text{O}$ (‰, PDB)	Δ_{47} (‰, Ghosh)	$ q ^a$	<i>P</i> -value ^b	Null ($\alpha=0.1$)
Johns Hopkins University	3	0.41 (± 0.03)	5.05 (± 0.04)	0.719 (± 0.005)	-	-	-
Yale University	4	0.68 (± 0.02)	4.93 (± 0.03)	0.741 (± 0.015)	1.55	0.60	Cannot reject
California Institute of Technology	3	0.47 (± 0.03)	5.03 (± 0.07)	0.727 (± 0.013)	0.66	0.89	Cannot reject

Notes: All \pm values are standard error of the mean ($=1\sigma/\sqrt{n}$), where 1σ is the standard deviation of the *n* analyses. Yale Δ_{47} data were corrected using a source fragmentation/recombination scaling factor of -0.87‰ . JHU and Caltech data were corrected using a -0.8453‰ scaling factor (Huntington et al. 2009). If -0.8453‰ is used in the Yale correction then the Yale Δ_{47} becomes 0.720‰ .

^aAnalysis of variance (ANOVA) Tukey HSD post hoc test *q* statistic. A large value (approximately an order of magnitude greater than the reported values) indicates statistical significance.

^bThe *P*-value associated with the *q* statistic. If the value is below a threshold ($\alpha = 0.1$) the conclusion would be that there is a difference between groups.

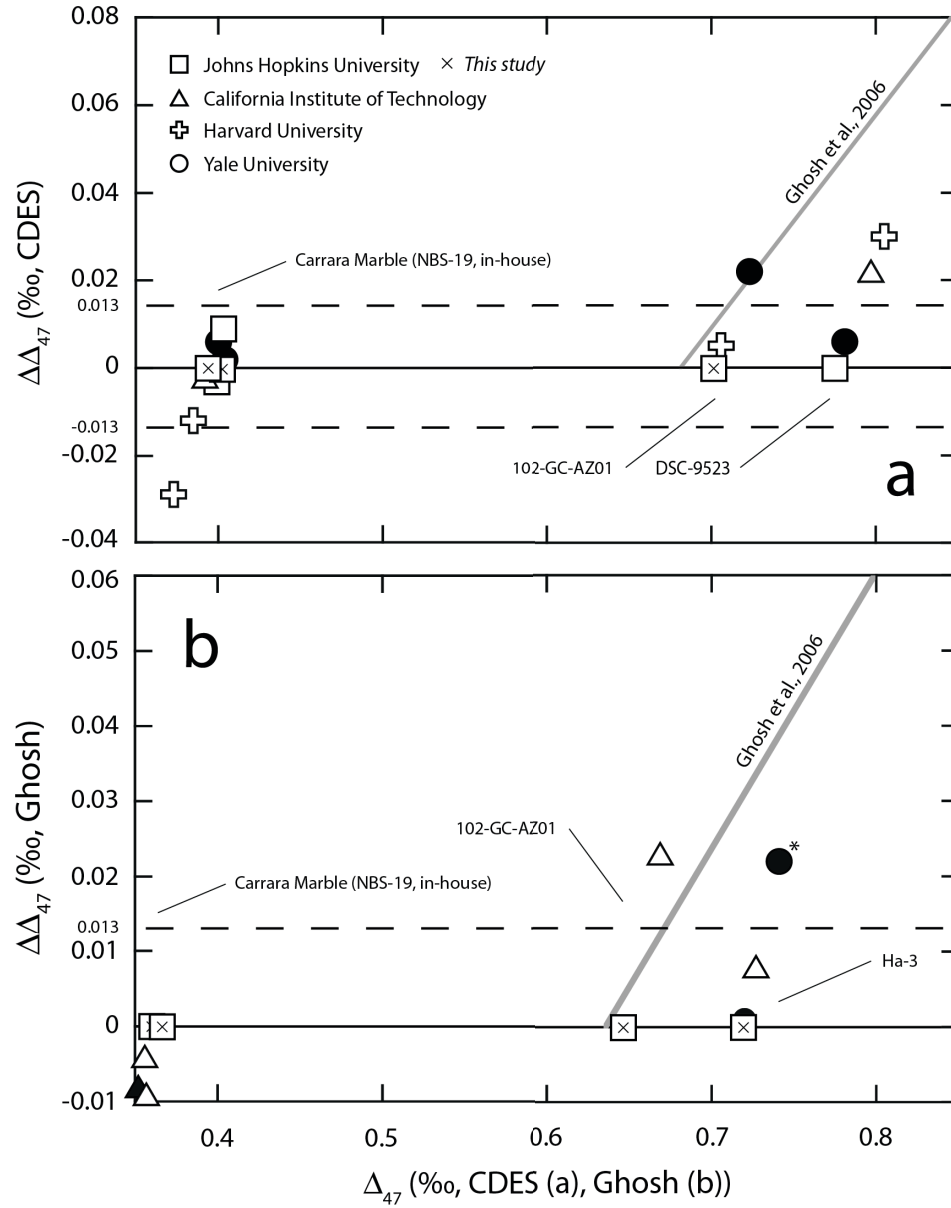


Figure 2.5 A compilation of interlaboratory clumped isotope comparisons. $\Delta\Delta_{47}$ is the clumped isotope difference between measurements at Johns Hopkins University and other laboratories ($\Delta\Delta_{47} = \Delta_{47,\text{JHU}} - \Delta_{47,\text{other}}$). Open symbols represent data generated using a 90 °C phosphoric acid reaction, whereas the solid symbols represent those done at 25 °C. The dashed lines in (a) and (b) are the long-term precision ($\pm 1\sigma$ standard deviation) of Δ_{47} measurements made on an in-house Carrara marble at JHU. The asterisk

in (b) identifies the Yale University measurement of Ha-3 corrected using their preferred source fragmentation/recombination scaling factor of -0.87‰ , instead of the -0.8453‰ used at JHU and Caltech (Table 2.3; Huntington et al., 2009). Data for the Carrara marbles, 102-GC-AZ01, and DSC-9253 on the CDES scale are from Dennis et al. (2011) and this study. Data for the Carrara marbles, 102-GC-AZ01, and Ha-3 on the ‘Ghosh’ scale are from Passey et al., 2010 and Csank et al., 2011, and this study (Table 2.3). In (a) the grey line labeled (Ghosh et al., 2006) represents the difference between the Ghosh et al. (2006) calibration and the mollusk and brachiopod calibration (Eq. (2.3)). In (b) the grey line labeled (Ghosh et al., 2006) represents the difference between the Ghosh et al. (2006) calibration the theoretical calibration for calcite from Guo et al. (2009).

2.4.1.2 Acid temperature

The Caltech calibrations (Ghosh et al., 2006, Ghosh et al., 2007, Came et al., 2007, Tripathi et al., 2010 and Thiagarajan et al., 2011) utilized 25 °C phosphoric acid reactions, whereas this study and Dennis and Schrag (2010) utilized 90 °C reactions. Thus it is critical that the difference in acid fractionation factor between 90 and 25 °C is accurately known, where the acid fractionation factor $\Delta^* = \Delta_{47,\text{CO}_2} - \Delta_{63,\text{CaCO}_3}$ (Guo et al., 2009). Δ_{47,CO_2} is the composition of CO_2 generated by phosphoric acid reaction of carbonate, and $\Delta_{63,\text{CaCO}_3}$ is the composition of the carbonate mineral. Passey et al. (2010) estimated the difference in Δ^* between 25 and 90 °C reactions, Δ^*_{25-90} , by analyzing homogenous carbonates using both a 90 °C , packed GC column, online extraction line, as well as by 25 °C , capillary GC column, offline extractions. All analyses were conducted at Caltech, but using two different mass spectrometers. The observed value for Δ^*_{25-90} , 0.081‰ , is

not a pure estimate of the acid temperature effect, because the approach convolved acid temperature, extraction method, and different mass spectrometers. Likewise, the interlaboratory calibrations of Dennis et al. (2011) and those reported in Section 2.4.2. convolve several methodological aspects, only one of which is acid temperature.

Therefore we undertook an experiment to measure Δ^*_{25-90} using a single extraction line and mass spectrometer. We studied three mollusk shells, two from the Arctic collection site B-12 and one from Puerto Rico (Table 2.4). The 25 °C reactions were conducted in McCrea-type vessels for ~12 h, with the vessels immersed in a constant temperature water bath. The vessels were then attached to our automatic gas preparation line and the CO₂ was extracted in the same way as our regular 90 °C analyses. The same materials were also analyzed using 90 °C reactions. The mean Δ^*_{25-90} source was $0.076 \pm 0.007\text{‰}$ (1σ standard deviation; on the ‘Ghosh’ scale), similar to the 0.081‰ offset determined by Passey et al. (2010). The mean Δ^*_{25-90} for the carbon dioxide equilibrium scale is $0.092 \pm 0.012\text{‰}$ (1σ standard deviation). The differences among these values are not large enough to explain discrepancies between calibrations (Fig. 2.3a).

Table 2.4 Δ_{47} acid correction factors based on acid reactions at 90 and 25 °C using mollusk shells

Sample ID	Sample species /type	n	Δ_{47} (‰, Ghosh) autoline, 90 °C	Δ_{47} (‰, CDES) autoline, 90 °C	Δ_{47} (‰, Ghosh) offline ^a , 25 °C	Δ_{47} (‰, CDES) offline ^a , 25 °C
Ha-3 (B-12)	<i>Hiatella arctica</i>	3	0.638	0.684	0.714	0.783
Ac-1 (B-12)	<i>Astarte crenata</i>	3	0.630	0.689	0.699	0.767
Pp-3	<i>Phacoides pectinatus</i>	3	0.548	0.601	0.630	0.700
			Acid correction (‰, Ghosh)	Acid correction (‰, CDES)		
Ha-3 (B-12)	<i>Hiatella arctica</i>		0.076	0.099		
Ac-1 (B-12)	<i>Astarte crenata</i>		0.69	0.078		
Pp-3	<i>Phacoides pectinatus</i>		0.082	0.099		
	Mollusk average		0.076	0.092		
	1 σ SD		0.007	0.012		
	Passey et al. (2010) ^b		0.081	-		
	Guo et al. (2009) ^c		0.069	-		

^a‘Offline’ reactions done in vacuo for ~12 h at 25 °C using $\rho = 1.91$ phosphoric acid. Evolved CO₂ was cleaned by cryogenic trapping and gas chromatography using the same sample purification as the automated preparation device acid reactions at 90 °C. See Section 2.2.2.

^bEmpirically derived.

^cTheoretically derived.

In summary, we find no convincing explanation for why the carbonate clumped isotope calibration for mollusks and brachiopods should be different than the existing inorganic and biogenic calibration data (e.g., Ghosh et al., 2006). Our interlaboratory Δ_{47} comparisons of shell Ha-3 add to previous comparisons, which have now been completed on a suite of natural carbonates (Fig. 2.5). These data should be viewed as the most

realistic comparisons of interlaboratory reproducibility because they make no effort to evaluate any single aspect of making a carbonate clumped isotope measurement. If Δ_{47} calibration measurements made at Johns Hopkins were dramatically different from measurements currently being made at Caltech, Yale, or Harvard, it should be apparent in a comparison such as Fig. 2.5.

2.4.2 Biological explanations

It is conceivable that mollusks and brachiopods have a unique response of Δ_{47} to temperature, possibly owing to differences in biomineralization mechanisms. In the biological systems relevant to this discussion, carbonate formation occurs in semi-isolated volumes which have varying degrees of connectivity with the ambient environment (Weiner and Dove, 2003). The chemical composition and mineral precipitation kinetics within these volumes is therefore a function of some combination of (a) the biological influence on the chemistry of the precipitating fluid (e.g., ionic transport or metabolic activity) and (b) the ambient seawater chemistry. While the design of our study does not allow us to evaluate the isotopic interplay between biology and seawater directly, we can discuss isotopic effects associated with the chemical and physical conditions of marine carbonate biomineralization.

2.4.2.1 Isotopic mixing

The non-linear effect on Δ_{47} resulting from mixing carbonates with different bulk isotopic compositions has been predicted from theory and demonstrated by experiment (Eiler and Schauble, 2004). In our study, this effect is a concern when two or more regions of a shell

with different $\delta^{13}\text{C}$ and $\delta^{18}\text{O}$ may be combined for analysis or during biomineralization when the shell itself may be formed from two isotopically distinct reservoirs of dissolved inorganic carbon (DIC). In either case, mixing will cause the resultant Δ_{47} to be greater than the weighted sum of the end member Δ_{47} values (Eiler and Schauble, 2004). Mollusk and brachiopod shell $\delta^{13}\text{C}$ and $\delta^{18}\text{O}$ vary in accordance with seasonal environmental conditions such as productivity, temperature, and the isotopic composition of water (e.g., Mii and Grossman, 1994, Buening and Spero, 1996, Goodwin et al., 2003, Gentry et al., 2008, McConnaughey and Gillikin, 2008, Wanamaker et al., 2011 and Beirne et al., 2012). The clumped isotopic composition of shells used in this calibration that were sub-sampled indiscriminately across all growth bands could therefore incorporate a pronounced mixing effect. To evaluate this effect we consider a 50/50 mixing of end-member $\delta^{13}\text{C}$ and $\delta^{18}\text{O}$ values for shell grown during a hypothetical mid-latitude summer ($\delta^{13}\text{C} = 0\text{‰}$, $\delta^{18}\text{O} = -2\text{‰}$) and winter ($\delta^{13}\text{C} = 1.5\text{‰}$, $\delta^{18}\text{O} = 1.5\text{‰}$). The result is a Δ_{47} mixing effect of 0.0014‰. If the Ghosh et al. (2006) calibration represents the Δ_{47} –temperature relationship that all biocarbonates (including mollusks and brachiopods) should have, then mixing isotopically different parts of a shell would cause a shift in the wrong direction (positive) with a magnitude that would be too small to explain the difference between calibrations.

2.4.2.2 *Amorphous calcium carbonate*

An alternative to the mixing effect caused by combination of shell regions with different isotopic compositions is a different kind of mixing effect due to the presence of multiple phases of calcium carbonate. When material for this calibration was sub-sampled from

mollusk shells containing both aragonite and calcite, we carefully selected one over the other (e.g., calcite from *M. edulis*). Recent analysis of mollusk shells, however, has demonstrated that amorphous calcium carbonate (ACC) may be a component of juvenile and adult mollusk shell as a precursory phase (Weiss et al., 2002 and Jacob et al., 2011) that is unresolvable by traditional methods for mineralogical identification (e.g., X-ray diffraction). The physical and thermochemical properties of ACC have been described (Radha et al., 2010), but the stable isotopic composition of ACC relative to non-amorphous phases of calcium carbonate (calcite or aragonite) is unknown. Therefore, it is impossible to speculate on the effect of incorporating residual molluscan (or brachiopod) ACC in our carbonate clumped isotope measurements. In an effort to reduce any putative contribution of ACC to our analyte CO₂, we pretreated two shells in a pH-buffered calcium acetic acid solution (1 M, pH = 4.6) at 4 °C for 24 h. This pretreatment was expected to preferentially dissolve ACC over aragonite. We observed no effect of this pretreatment on the Δ_{47} value of the shells (Table 2.5), implying that either no appreciable ACC was present initially, pretreatment was ineffective at removing ACC, or ACC did not significantly affect the isotopic composition of untreated shell. Regardless, the paucity of isotopic data from amorphous phases of calcium carbonate highlights an important avenue for further research as it has been suggested to be an important transitional phase during carbonate biomineralization in mollusks, echinoderms, and arthropods (Adaddi et al., 2003).

Table 2.5 Stable isotope data from sample pretreatment experiments using pH-buffered acetic acid.

Sample ID	Species	n	Pretreatment ^a	$\delta^{13}\text{C}_{\text{carb}}$ (‰, PDB)	$\delta^{18}\text{O}_{\text{carb}}$ (‰, PDB)	Δ_{47} (‰, Ghosh)	Δ_{47} (‰, CDES)	<i>P</i> -value ^b
Ha-4 (B-12)	<i>Hiatella arctica</i>	2	0.1 M pH-buffered acetic acid	1.03 (±0.03)	4.98 (±0.02)	0.680	0.751 (±0.002)	0.33
Ha-4 (B-12)	<i>Hiatella arctica</i>	2	Deionized water (control)	0.99 (±0.08)	4.98 (±0.01)	0.672	0.741 (±0.006)	-
Pp-2	<i>Phacoides pectinatus</i>	2	0.1 M pH-buffered acetic acid	0.82 (±0.02)	-0.70 (±0.01)	0.620	0.688 (±0.028)	0.80
Pp-2	<i>Phacoides pectinatus</i>	3	None	0.77 (±0.03)	-0.70 (±0.02)	0.632	0.699 (±0.013)	-

Note: All ± values are standard deviation (1σ).

^aThe pretreatment was for 12 h at room temperature after sonicating twice for 5 min each.

^b*P*-values from a Wilcoxon–Mann–Whitney rank sum test. Values greater than $\alpha = 0.1$ indicate no significant differences between treatments and control values.

2.4.2.3 Diffusion

Extensional molluskan shell growth occurs directly along the ventral margin from the extrapallial fluid (EPF), which is enclosed in a cavity between the inner shell surface and the mantle. The ionic and organic composition of the EPF distinguishes it from seawater and suggests active biological control over the conditions of shell precipitation (Crenshaw, 1972). It has been hypothesized that at least some of the calcium ions and DIC in the EPF is supplied by the hemolymph to the outermost mantle cells (Lowenstam and Weiner, 1989), which is supported by recent studies on the carbon isotope composition of ambient DIC and coeval shell (e.g., Beirne et al., 2012). Thus, isotope effects from the diffusion of dissolved CO₂ across cellular membranes or through body fluids should be considered in light of the observed discrepancies between clumped isotope calibrations.

Isotopic fractionation due to diffusion of CO₂ through the phospholipid bilayer is often invoked in ‘vital effect’ models for carbonate biomineralization (Erez, 2003 and Cohen and McConnaughey, 2003). As Thiagarajan et al. (2011) point out in their discussion of clumped isotope compositions of corals, Knudsen diffusion, in which gas passes through a pore with a diameter that is less than the mean free path of the diffusing molecule, predicts that the diffused gas will be depleted in heavy isotopes relative to the residual gas according to the equation:

$$R_{diffused} / R_{residual} = \sqrt{m_1 / m_2} \quad (2.5)$$

where $R_{diffused}$ and $R_{residual}$ are the isotope ratios of the diffused and residual gases and m_1 and m_2 are masses of isotopologues 1 and 2. For an aliquot of CO₂ gas that has undergone Knudsen diffusion the diffused gas will be lower in $\delta^{13}\text{C}$ and $\delta^{18}\text{O}$ by 11.3‰ and 22.5‰, respectively, but 0.5‰ higher in Δ_{47} (Eiler and Schauble, 2004). A nonstochastic value of Δ_{47} in the diffused gas results from the non-linear dependence of Δ_{47} on the bulk isotopic composition of the gas (Eiler and Schauble, 2004 and Thiagarajan et al., 2011).

The isotopic fractionation associated with diffusion of CO₂ through a different gas (e.g., air) can be calculated using the following equation:

$$R_{diffused} / R_{residual} = \sqrt{\left(\frac{(M_2 + M_{air})}{(M_2 M_{air})} \right) \times \left(\frac{(M_1 M_{air})}{(M_1 + M_{air})} \right)} \quad (2.6)$$

where, again, $R_{diffused}$ and $R_{residual}$ are the isotope ratios of the diffused and residual gases, M_1 and M_2 are masses of isotopologues 1 and 2, and M_{air} is the average atomic mass of air. The gas-phase diffusion of CO₂ through air results in decreases for $\delta^{13}\text{C}$ and $\delta^{18}\text{O}$ in the diffused gas by 4.4‰ and 8.7‰, respectively, and a positive fractionation of 0.3‰

for Δ_{47} . However, Thiagarajan et al. (2011) point out that while illustrative of the magnitude and direction of isotope effects associated with pin-hole and gaseous diffusion, the fractionations determined by Eqs. (2.5) and (2.6) are clearly not applicable to aqueous systems at relatively low temperatures where the behavior of fluids deviates strongly from that of ideal gases. O’Leary (1984) experimentally determined a -0.7‰ carbon isotope fractionation associated with diffusion of CO_2 through water, which was less than what is predicted by solving Eq. (2.6) using the atomic mass of water as “ M_{air} ”. Thiagarajan et al. (2011) extrapolated this result using a power law relationship between the magnitude of fractionation and the ratio of isotopologue masses to determine the isotope fractionation associated with CO_2 diffusion through water for $\delta^{18}\text{O}$, -1.6‰ , and Δ_{47} , 0.036‰ .

Based on this information, we examine two different scenarios.

- (i) The carbonates studied in the Caltech calibrations have greater isotopic contributions from diffused DIC, leading to elevated Δ_{47} values, and this contribution increases with decreasing temperature, leading to a steeper Δ_{47} – T slope. If this scenario is correct, then it is fortuitous that the methods used to precipitate calcite in the laboratory (Ghosh et al., 2006) contributed similar amounts of ‘diffused’ DIC to the site of mineralization as reaches the sites of mineralization in natural corals, foraminifera, and coccoliths (Tripathi et al., 2010 and Thiagarajan et al., 2011). Furthermore, if this scenario were correct, we would expect to see corresponding depletions in $\delta^{13}\text{C}$ and $\delta^{18}\text{O}$. While there is certainly evidence of this in the coral dataset (Thiagarajan et al., 2011,

Fig. 2.6), there is no clear evidence of such in the inorganic data (Ghosh et al., 2006) or the foraminifera and coccolith data (Tripathi et al., 2010). We therefore regard this scenario as an unsatisfactory explanation for the differences between the Caltech calibrations and the JHU or Harvard calibrations.

- (ii) Mollusks and brachiopods, and the inorganic carbonates precipitated by Dennis and Schrag (2010), incorporate DIC from reservoirs out of which DIC has diffused. Thus these carbonates incorporate residual DIC with low Δ_{47} that is left over after part of the DIC has diffused from the mineralization environment. If this scenario is correct, then we should observe corresponding enrichments in $\delta^{13}\text{C}$ and $\delta^{18}\text{O}$ in mollusk and brachiopod carbonate. Fig. 2.3b shows that, at least for $\delta^{18}\text{O}$, there is no consistent enrichment over expected values. Additionally, this scenario is unsatisfactory because DIC should be diffusing into, not out of, the extrapallial fluid environment during mineralization, because mineralization itself consumes DIC.

In summary, diffusive mechanisms do not explain all of the observed data, and cannot be the sole reason for the observed differences in calibration.

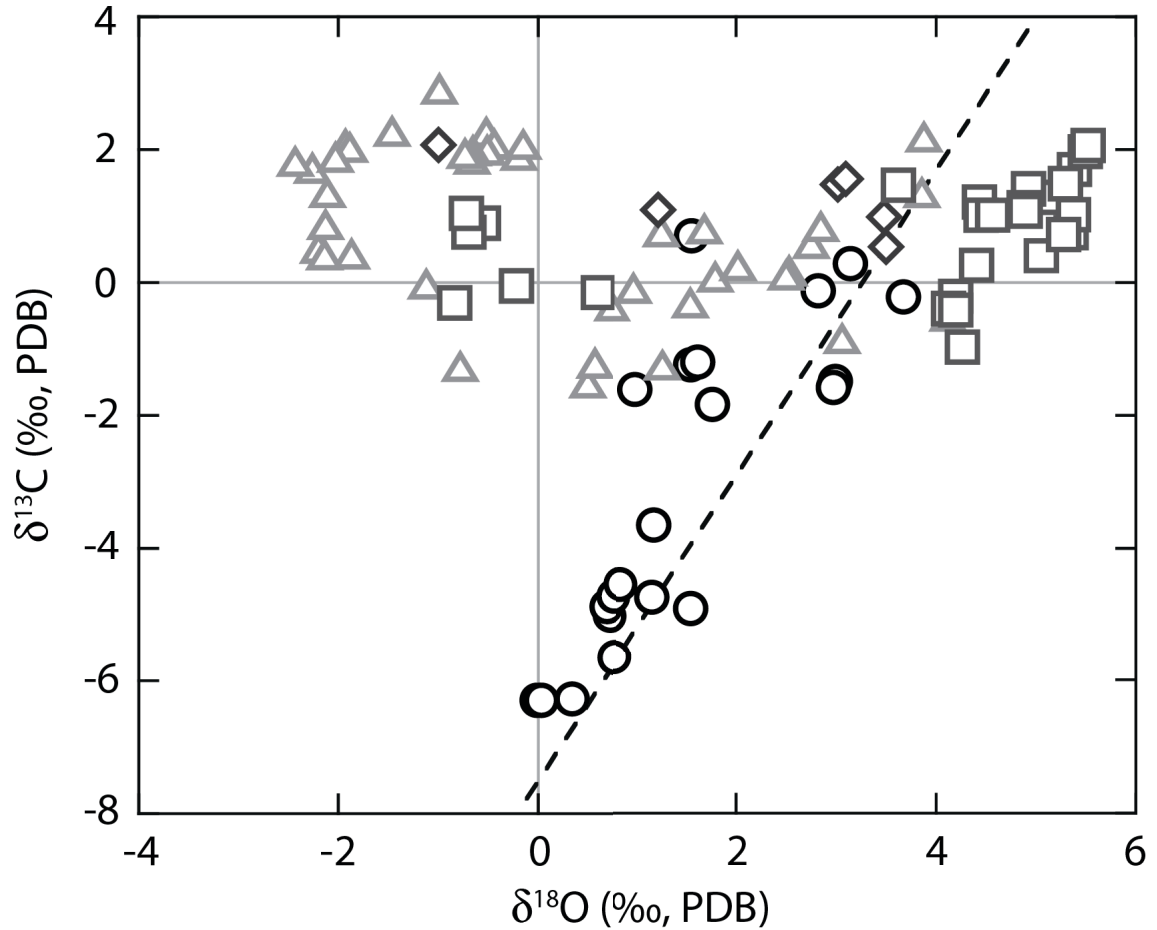


Figure 2.6 Carbon isotope versus oxygen isotope crossplot for mollusk, brachiopod, coral, and foraminifera samples used in empirical carbonate clumped isotope calibrations. Mollusk (dark gray squares) and brachiopod (dark gray diamonds) shells from this study; deep-sea corals from Thiagarajan et al. (2011; black circles), and foraminifera from Tripathi et al. (2010; gray triangles). The dashed line is the average linear regression of deep-sea coral stable isotope compositions in Adkins et al. (2003): $\delta^{13}\text{C} = 2.3 \times \delta^{18}\text{O} - 7.5$. Agreement between the Thiagarajan et al. (2011) data and the average regression confirms the presence of an Adkins et al. (2003)-type vital effect in these samples. There is no clear relationship between $\delta^{13}\text{C}$ and $\delta^{18}\text{O}$ for mollusks, brachiopods, and foraminifera.

2.4.2.4 pH and dissolved inorganic carbon speciation

It has been demonstrated that the equilibrium oxygen isotope fractionation between the sum of the DIC species and water decreases with increasing pH (Usdowski et al., 1991). This effect arises because the equilibrium oxygen isotope fractionations between DIC and water decrease in the order $\text{CO}_2\text{--H}_2\text{O}$; $\text{HCO}_3^-\text{--H}_2\text{O}$; and $\text{CO}_3^{2-}\text{--H}_2\text{O}$. Therefore, because the relative concentrations of DIC species change strongly as a function of pH, so too will the oxygen isotope difference between total DIC and water (see Zeebe and Wolf-Gladrow, 2001 for review). Beck et al. (2005) determined equilibrium oxygen isotope fractionation factors between CO_2 and H_2O , HCO_3^- and H_2O , and CO_3^{2-} and H_2O , and showed that $\delta^{18}\text{O}$ of total DIC can vary with pH by as much as 17‰ at a single temperature. The pH isotope effect is an important consideration because there is a large range of pH values observed in body fluids of carbonate mineralizing marine organisms. Among these taxa mollusks are unique in that their extrapallial fluid (EPF) has a pH value that is slightly lower than seawater and 0.5–1.5 pH units less than the precipitating fluids of foraminifera, surface corals, and fishes ($\text{pH} \geq 8$; Crenshaw, 1972).

Currently, only theoretical predictions of the equilibrium clumped isotope compositions of different inorganic carbon species are available (Guo, 2009 and Guo et al., 2012). At 300 K, HCO_3^- is predicted to be 0.018‰ enriched in $^{13}\text{C}\text{--}^{18}\text{O}$ bonds relative to CO_3^{2-} , but may be as large as 0.04‰ (Guo et al., 2012). As an end-member scenario, if mollusk shells derive carbonate only from HCO_3^- , and corals and foraminifera only from CO_3^{2-} , then mollusks may be ~0.04‰ higher in Δ_{47} than corals and foraminifera. This offset is of insufficient magnitude, and more importantly of the wrong sign, to explain the

difference in the Δ_{47} versus temperature relationships between these taxa. However, experimental observations of the effects of pH and DIC speciation on Δ_{47} have not yet been described, and given the importance of DIC speciation to the isotopic composition of carbonate and the nearly 2 unit range of pH values observed in biomineralizing organisms, it will be important to characterize these effects.

2.4.2.5 DIC disequilibrium

For the temperature range 0–50 °C, CO_2 has significantly higher Δ_{47} values than does carbonate at the same temperature (Fig. 7.2.). The equilibrium clumped isotopic compositions of CO_2 and CO_3^{2-} over a range of temperatures define the end-member values of a domain that may be useful for evaluating the differences between clumped isotope calibrations. We consider a hypothetical system where CO_2 , which has a higher equilibrium Δ_{47} than CO_3^{2-} at a given temperature, is incorporated into the biomineral through the DIC system without fully re-equilibrating to Δ_{47} compositions of CO_3^{2-} . Thus the mineral ‘inherits’ some of the high Δ_{47} of the original CO_2 . Because of longer timescales of equilibration at lower temperatures, the ^{13}C – ^{18}O inheritance from CO_2 would be enhanced at low temperatures, leading to an artificially steep Δ_{47} versus T slope. Several scenarios may be envisioned where these kinetics would be relevant, including the incorporation of diffused CO_2 into fast growing biogenic carbonate (e.g., Adkins et al., 2003) or rapid biochemical pH change to induce mineralization from invaginated seawater (e.g., foraminifera; Bentov et al., 2009).

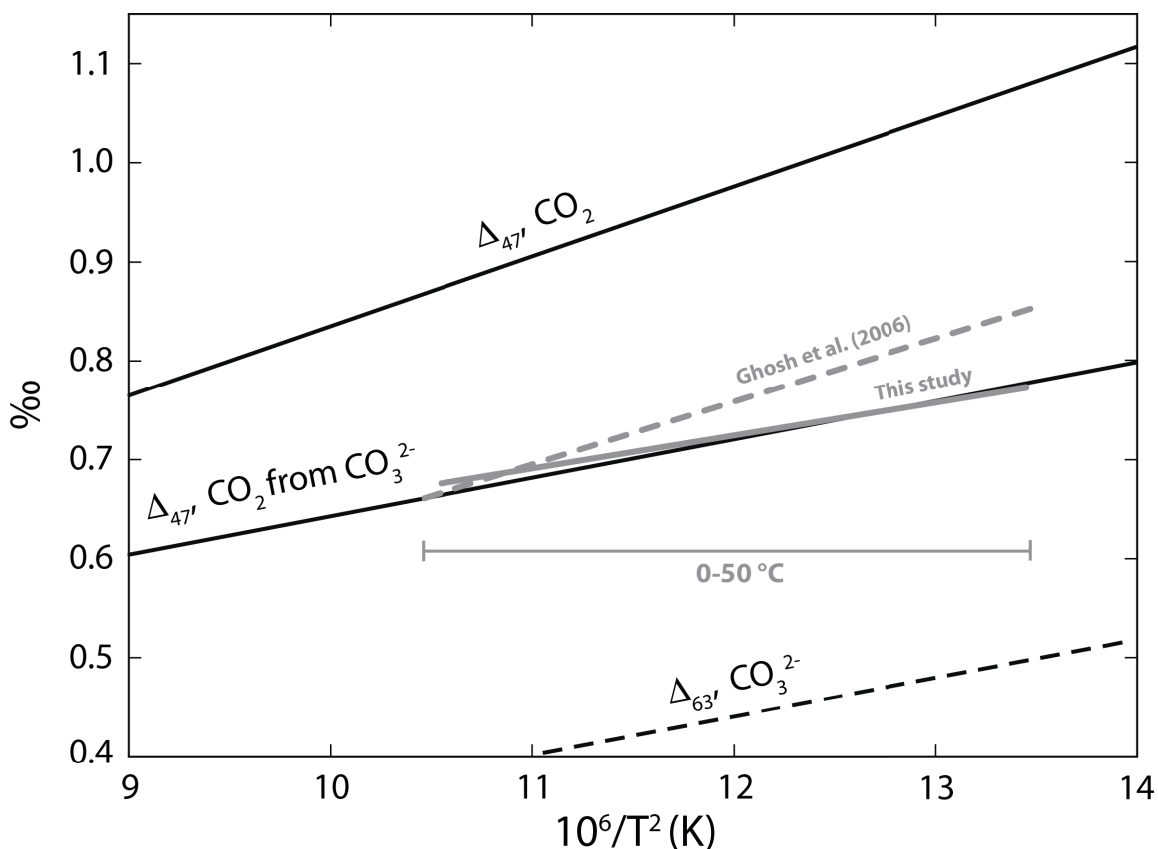
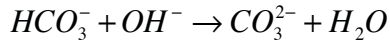


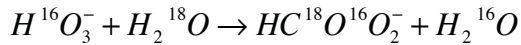
Figure 2.7 Theoretical predictions of the temperature dependence of Δ_{47} of CO_2 (solid black line; Wang et al., 2004), Δ_{47} of CO_2 liberated from calcite by phosphoric acid digestion at 25 °C (solid black line; Guo et al., 2009), and of Δ_{63} for View the MathML source (dashed black line; Schauble et al., 2006). These curves illustrate the $\sim 0.3\%$ difference between CO_2 and CO_2 generated from calcite at earth surface temperatures (~ 0 to 50 °C). The empirical Δ_{47} –temperature calibration of Ghosh et al. (2006) and Eq. (2.3) from this study are shown as grey dashed and solid lines, respectively.

Additionally, a complicated interplay of chemical and isotope exchange kinetics of DIC ultimately determines the isotopic composition of biogenic carbonates. The rate constants of the carbonate system are not well understood relative to the equilibrium constants, but

they may be used to compare with equivalent isotope exchange reaction rates (Zeebe and Wolf-Gladrow, 2001). For example, the forward reaction rate constant for the hydrolysis reaction:



is $k = 6 \times 10^9 \text{ kg mol}^{-1} \text{ s}^{-1}$ at 20 °C, which for $\sim 2.5 \text{ mmol kg}^{-1}$ of HCO_3^- is practically instantaneous (Eigen, 1964). In contrast, the oxygen isotope exchange reaction between bicarbonate and water:



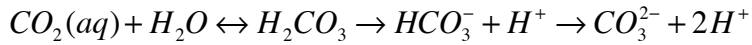
can take hours to tens of hours (depending on the ambient temperature and pH) to reach equilibrium, implying comparatively slow reaction kinetics (Beck et al., 2005). Thus in a closed system with a rapid precipitation rate it is possible to rapidly dissociate bicarbonate into carbonate without establishing isotopic equilibrium prior to precipitation in the mineral phase. This kinetic effect has been invoked to explain carbonate ion effects on the oxygen isotope compositions of synthetic and natural carbonates (Usdowski et al., 1991, Spero et al., 1997 and Adkins et al., 2003).

Dissolved CO_2 plays an important role in coral and foraminifera mineralization, and is involved in Kim and O'Neil-type laboratory precipitation experiments similar to those used by Ghosh et al. (2006). Thus it is conceivable that the clumped isotope composition of CO_2 could be imprinted on synthetic calcium carbonates. In scleractinian corals it has been hypothesized that the enzyme Ca^{2+} ATPase drives calcification by pumping calcium ions across cellular membranes, causing aragonite supersaturation in the precipitating fluid (Adkins et al., 2003 and Cohen and McConnaughey, 2003). The currency of

extracellular ion exchange by Ca^{2+} ATPase is the proton, whose removal from the precipitating fluid causes the pH to increase, thereby dissociating HCO_3^- to CO_3^{2-} . Carbonate precipitation results in a net CO_2 diffusion across the cellular membrane to the calcification site. Carbon dioxide diffusion could also be caused by CO_2 removal by photosynthesis (this would not be the case for non-symbiotic corals) or CO_2 hydration reactions that fail to keep pace with CaCO_3 precipitation. The presence of another enzyme, carbonic anhydrase, may accelerate the CO_2 hydration reaction when the growth of the biogenic carbonate is limited by carbonate ion supply (Cohen and McConnaughey, 2003), but we feel that this would only strengthen our hypothetical scenario where CO_2 carries at least part of its equilibrium clumped isotopic composition to the mineral phase.

Marine foraminifera also manipulate pH to control the calcite or aragonite saturation state of their precipitating fluids, which are small-volumes of endocytosed seawater (Erez, 2003). Like corals, a pH change in the precipitating vacuole of a foraminifera causes the enclosed DIC (i.e., ambient seawater) to shift to mostly CO_3^{2-} , and if the internal pH is higher than the external pH this causes CO_2 diffusion into the endocytosing vacuole. It is possible that metabolic CO_2 also diffuses into these vacuoles. Regardless, for both corals and foraminifera, it seems plausible that some of the C–O bonds in carbonate could be inherited from CO_2 without equilibration as CO_3^{2-} . The superficial similarities between the modern coral and foraminifera clumped isotope data are linked by a similar mechanism for inducing calcium carbonate supersaturation in their calcifying fluids (Cohen and McConnaughey, 2003 and Erez, 2003).

To evaluate this ‘CO₂ inheritance’ hypothesis, we may again turn to carbon and oxygen isotopes. For low temperature conditions (0–30 °C), the $\delta^{13}\text{C}$ of dissolved CO₂ is approximately 10‰ lower than that of carbonate, and $\delta^{18}\text{O}$ is approximately 20‰ higher than carbonate (Mook, 1986, Zhang et al., 1995 and Beck et al., 2005). It is impossible for a DIC species to reach carbon and oxygen isotope equilibrium without also reaching clumped isotopologue equilibrium, so any disequilibrium isotope effect seen in Δ_{47} should also be reflected in $\delta^{13}\text{C}$ and $\delta^{18}\text{O}$. As an end-member scenario, we assume that no isotopic fractionation is associated with the initial conversion of CO₂ to CO₃²⁻:



Thus the initial (unequilibrated) CO₃²⁻ will have a Δ_{47} value ~0.3‰ higher than equilibrated CO₃²⁻, $\delta^{13}\text{C}$ –10‰ lower, and $\delta^{18}\text{O}$ 20‰ higher. The offset between the Caltech calibrations and the theoretical calibrations at 0 °C is about 0.08‰. Under this scenario about 25% of the carbonate ions in the final carbonate mineral would have to inherit their Δ_{47} value from unequilibrated CO₂. The corresponding fractionations in $\delta^{13}\text{C}$ and $\delta^{18}\text{O}$ should be about –2.5‰, and +5‰, respectively. Such large fractionations are not observed. This implies that either the overall scenario of ‘inherited’ CO₂ clumping is incorrect, or that the assumption of zero isotope fractionation during the initial synthesis of CO₃²⁻ from CO₂ + H₂O is grossly in error. Both of these possibilities can presumably be addressed by additional theoretical and experimental work.

2.5 Summary

This paper presents the results of carbonate clumped isotope analyses performed on modern marine mollusk and brachiopod shells, which spanned virtually the entire range

of growth temperatures found in modern oceans. Regressed against the inverse squared shell growth temperature, these data form a calibration line, $\Delta_{47} = 0.0327 \times 10^6/T^2 + 0.3286$, whose temperature sensitivity (slope) is approximately half that of similar calibrations done on biogenic carbonates and inorganic laboratory precipitates (Fig. 2.3a; Ghosh et al., 2006, Ghosh et al., 2007, Tripathi et al., 2010 and Thiagarajan et al., 2011). This study is unique in that it is the only clumped isotope calibration to date that uses newer analytical methods (i.e., ‘hot’ phosphoric acid reaction, polymer-packed gas chromatography column, and automated sample preparation), and is fully referenced to the ‘carbon dioxide equilibrium scale’ reference frame (Dennis et al., 2011). Potential methodological causes for discrepancies between calibrations, including poor interlaboratory calibration and error in the acid temperature correction, were found to be relatively minor compared to the magnitude of calibration disagreement. Biological explanations for the different temperature sensitivity of the mollusk and brachiopod calibration were also addressed. The isotopic effects associated with mechanical mixing and diffusion, as they pertain to biomineralization, were predicted to have small effects on the clumped isotope composition of shell. We addressed some of the physical and chemical aspects of shells and the chemical conditions of their formation, such as the potential incorporation of amorphous calcium carbonate into the analyzed material and the isotopic consequences of taxonomic differences in precipitating fluid pH. These effects are predicted to not affect shell clumped isotope compositions, although more data are needed to fully understand the effects of pH and ACC on the isotopic composition of biogenic carbonate. Finally, we used a simple kinetic model for clumped isotopic disequilibrium in biogenic carbonates to evaluate the possibility of CO_2 , whose clumped

isotope composition is $\sim 0.3\text{‰}$ higher than CO_3^{2-} at a given temperature, ‘imprinting’ its composition on carbonate ions incorporated into rapidly growing carbonate. This is an attractive explanation for the differences between calibrations because of the superficial similarities of coral and foraminifera biomineralization, but is untenable given the bulk isotopic compositions (e.g., $\delta^{13}\text{C}$, $\delta^{18}\text{O}$) of these carbonates.

Despite differences in calibration, the clumped isotope thermometer remains an alluring technique for carbonate paleothermometry and reconstruction of the oxygen isotopic composition of precipitating fluids. Clumped isotope thermometry is an emerging method – only a handful of laboratories currently make the measurement, the field has just recently been introduced to a normalization scheme that can be reliably reproduced in different laboratories (Dennis et al., 2011), and experimental and empirical calibrations continue to emerge. There are many aspects of carbonate isotopologue systematics that remain to be described, such as equilibrium fractionations between coexisting species of DIC, kinetic fractionations during transformations of DIC species, and temperature and pH-dependent rates of exchange among coexisting isotopologues. This kind of knowledge, combined with improved analytical techniques and standardized methods of data normalization, will continue to improve our ability to interpret clumped isotope compositions of natural carbonates in terms of temperature and other parameters.

3. TEMPERATURE LIMITS FOR PRESERVATION OF PRIMARY CALCITE CLUMPED ISOTOPE PALEOTEMPERATURES²

Abstract

Solid-state reordering of C–O bonds in the calcite lattice can alter the clumped isotope composition of paleotemperature archives such as fossil brachiopod shells without inducing significant changes in shell microstructure and trace element concentrations, metrics commonly used to gauge preservation quality. To correctly interpret the paleoenvironmental significance of clumped isotope-derived paleotemperatures, it is necessary to understand the temperature–time domain in which solid-state C–O bond reordering is important. We address this question using a combination of laboratory and natural geological experiments on Paleozoic brachiopod shells. The laboratory experiments involve heating fossil brachiopod calcite at different temperatures and times to directly observe rates of ^{13}C – ^{18}O bond reordering. The resulting Arrhenius parameters are indistinguishable from values previously determined for an optical calcite with similar trace element compositions. We develop an alternative kinetic model for reordering that accounts for non-first-order reaction progress observed during the initial several hundred minutes of laboratory heating experiments, and show that the simplified first-order approximation model (Passey and Henkes, 2012) predicts reaction progress equally well for temperatures and timescales relevant to sedimentary basins. We evaluate our laboratory-based rate predictions by studying brachiopod calcite from several sedimentary basins with independently constrained burial temperature histories.

² Henkes G.A., Passey B.H., Grossman E.L., Shenton B.J., Pérez-Huerta A., Yancey T.E. (2014) Temperature limits for preservation of primary calcite clumped isotope paleotemperatures. *Geochimica et Cosmochimica Acta*, 139: 362-382.

Specifically, we use the laboratory-derived Arrhenius parameters to predict the evolution of brachiopod calcite clumped isotope compositions during successive one million-year time steps reflecting the burial and exhumation temperature paths of each basin. While this exercise is limited by the relatively large uncertainties in the temperature histories of these basins, we find general correspondence, within error, between predicted and observed clumped isotope values. We present simplified temperature–time diagrams for calcite showing domains where primary clumped isotope compositions will be preserved, partially reordered, and fully reordered. In conclusion, calcite samples dwelling at ~ 100 °C or lower for 10^6 – 10^8 year timescales should not be affected by solid-state C–O bond reordering.

3.1 Introduction

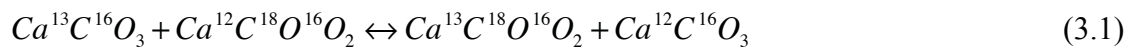
Clumped isotope thermometry of fossil marine carbonates has provided new insight into the paleotemperatures and oxygen isotope compositions of ancient seawaters (Came et al., 2007, Keating-Bitonti et al., 2011 and Price and Passey, 2013), revealed evidence for large global climatic shifts (e.g., the Late Ordovician-Early Silurian glaciation; Finnegan et al., 2011), and differentiated estuarine from marine paleoenvironments (e.g., in the Cretaceous Western Interior Seaway; Dennis et al., 2013). Undoubtedly, deep-time paleoceanography using the skeletons of marine organisms will continue to be a major application of this relatively new paleothermometer, in part because of the fundamental questions that can be addressed, such as the possibility of hot Early Paleozoic oceans (Joachimski et al., 2009, Finnegan et al., 2011 and Grossman, 2012a), the role of cooling in Ordovician biodiversification (Sheehan, 2001 and Trotter et al., 2008), and the isotopic

evolution of seawater (Veizer et al., 1999 and Eiler, 2011). This technique has also been applied to reconstructions of ancient terrestrial paleotemperatures and meteoric water $\delta^{18}\text{O}$ (e.g., Ghosh et al., 2006a and Passey et al., 2010). Despite the apparent success of this new method, relatively little is known about the physical conditions required for long-term ($\sim 10^6$ – 10^9 years) preservation of primary carbonate clumped isotope paleotemperatures. The goal of this study is to establish a quantitative basis for defining those conditions through analysis of fossil brachiopod shells, which have become a de facto standard for pre-Mesozoic stable isotope paleothermometry (Veizer et al., 1999 and Grossman, 2012a).

Brachiopod shells have been the preferred material for deep-time isotopic paleotemperature studies because of their widespread occurrence in space and time, relatively large size, and stable mineralogy and chemistry (low-Mg calcite). However, preservation of shell chemistry for hundreds of millions of years has long been a concern (e.g., Land, 1995 and Veizer, 1995). This has led to a variety of analytical approaches to evaluate preservation of fossil shells, including petrographic and cathodoluminescence microscopy, scanning electron microscopy, trace and minor element analysis, and X-ray powder diffraction (e.g., Compston, 1960, Popp et al., 1986, Veizer et al., 1986, Grossman et al., 1996 and Mii et al., 1997). In addition, cements and replacement calcites associated with fossils have also been studied to understand isotopic and chemical trends associated with diagenesis. The net result of applying various combinations of these techniques is highly screened stable isotope records that are believed to represent conditions at the ancient Earth surface (Grossman, 2012b). All of the recent carbonate

clumped isotope studies of marine fossils have used some combination of these diagenetic screening techniques (Came et al., 2007, Finnegan et al., 2011, Keating-Bitonti et al., 2011, Brand et al., 2012, Dennis et al., 2013 and Price and Passey, 2013). Therefore, these clumped isotope paleotemperature records are thought to be devoid of major diagenetic imprints, at least to limits of detection for the most common screening tests.

However, clumped isotope paleotemperatures from primary carbonates are susceptible to alteration via C–O bond reordering in the solid mineral lattice. Specifically, such ‘reordering’ must involve the breakage of existing C–O bonds, and reforming the C–O bonds with allochthonous C or O originating from, for example, neighboring carbonate groups, or interstitial positions. Such reordering is likely related to solid-state diffusion of C and O atoms through the mineral lattice. Regardless of the exact mechanism(s), the net result is a change in the abundance of ^{13}C – ^{18}O bonds (and other isotope-specific bonds), as illustrated by the following isotope exchange reaction (for the case of calcium carbonate):



This process can reset primary clumped isotope compositions without changing the texture, $^{18}\text{O}/^{16}\text{O}$, $^{13}\text{C}/^{12}\text{C}$, or trace element composition of the calcite. Because the process involves reordering of C–O bonds at the molecular to unit-cell scale, it does not require mass exchange with external fluids or gases, as would be required to alter $^{18}\text{O}/^{16}\text{O}$ and $^{13}\text{C}/^{12}\text{C}$ via self-diffusion (e.g., Anderson, 1969, Kronenberg et al., 1984 and Farver, 1994). Studies of marbles and carbonatites suggest ‘closure temperatures’ for this process

of approximately 150–250 °C (Dennis and Schrag, 2010). However, these closure temperatures are cooling-rate dependent (Passey and Henkes, 2012), and knowledge of the clumped isotope compositions of marbles and carbonatites does not provide a basis for accurate prediction of reordering rates at lower temperatures that might be experienced during burial and exhumation of paleoclimate archives.

The kinetics of C–O bond reordering have recently been investigated via timed heating experiments on two natural calcites (Passey and Henkes, 2012). Arrhenius parameters derived from these experiments predict that for timescales of 10^6 – 10^8 years, burial temperatures of ~100–150 °C may lead to measurable alteration of primary clumped isotope paleotemperatures. Thus, it is possible that the marine carbonate clumped isotope paleotemperature record includes data from samples that were at least partially reordered. This is problematic because unlike dissolution/reprecipitation-type diagenesis of fossil calcite, purely reordered samples are not identifiable by existing chemical and textural approaches.

In this study, we present carbonate clumped isotope results from 12 Carboniferous brachiopod shells collected from five ancient sedimentary basins now exposed in the United States and Russia. These samples are ‘well-preserved’ from the viewpoint of texture (thin sections) and trace element geochemistry (i.e., cathodoluminescence), but their clumped isotope paleotemperatures range from 35 to 165 °C, with the higher temperatures clearly pointing to alteration. We then present results of a set of laboratory heating experiments, similar to those of Passey and Henkes (2012), performed on aliquots

of calcite from a Permian brachiopod shell. We evaluate these data in the context of first-order reaction progress (Passey and Henkes, 2012), as well as a new non-first-order kinetic model, and determine Arrhenius parameters that allow for prediction of reordering over temperatures and timescales relevant to sedimentary basins. Predictions based on the experimental data are evaluated against brachiopod clumped isotope data from the five Carboniferous basins, and calcite data from the Carrara marble (a deep-burial, high-temperature end-member). Brachiopod calcite is ideal for such tests because, unlike calcite in micritic limestones or sedimentary cements, it provides constraints on primary texture, chemistry, and temperature of mineralization (probably less than 40 °C, and certainly less than 50 °C, given the current understanding of thermal limits for complex animal life; e.g., Ravaux et al., 2013). Thus, for brachiopods we have a basis for determining whether or not calcite has been extensively altered (chemically or physically), and can therefore avoid such samples in our analysis (since we are studying solid-state diffusion processes, and not recrystallization processes such as dissolution/reprecipitation, authigenic carbonate overgrowths or infillings of porosity, and other non-primary mineralization). Our experiments help place new constraints on the timescales and burial conditions most likely to afford preservation of original shell clumped isotope paleotemperatures.

3.2. Carboniferous brachiopods

We studied several pristine Carboniferous brachiopod shells from the United States and Russia (Table 3.1). The samples come from the Bird Spring Formation, Nevada (Early Pennsylvanian; Jones et al., 2003), the Grove Church Formation, Illinois (Late

Mississippian; Flake, 2011), the Glenshaw Formation, West Virginia (Late Pennsylvanian; Flake, 2011), the Fern Glen Formation, Missouri (Early Mississippian; Mii et al., 1999) and from the Cheremchanskian and Krasnopolyanskian Horizons exposed in the Ural Mountains, Russia (Early Pennsylvanian; Mii et al., 2001). The tectonic setting of these basins include active arc-continent and continent–continent convergent margin tectonics (Nevada and the Ural Mountains, respectively), and relatively stable intra-plate basins (Illinois, West Virginia, and Missouri) with sediment supplied by adjacent mountain building resulting from convergent tectonics. The burial histories of these basins are discussed in detail in Section 3.4.

Table 3.1 Stable isotope compositions of Carboniferous brachiopods from North America and Western Russia.

Sample ID	Taxonomic information	CL Character	<i>n</i>	$\delta^{13}\text{C}_c$ (‰, VPDB)	$\delta^{18}\text{O}_c$ (‰, VPDB)
North America					
<i>Fern Glen Fm. (upper Mississippi Valley, Missouri, USA), Early Mississippian (348-340 Ma)</i>					
MO074	<i>Prospira vernonensis</i>	NL	3	3.60 ± 0.36	-1.93 ± 0.14
MO076	<i>Prospira vernonensis</i>	NL	3	3.16 ± 0.05	-1.75 ± 0.05
MO077	<i>Prospira vernonensis</i>	NL/SL	3	4.14 ± 0.08	-1.97 ± 0.07
<i>Bird Spring Fm. (eastern Great Basin province, Nevada, USA), Late Mississippian (323 Ma)</i>					
NV007	productid	NL	3	2.66 ± 0.05	-1.06 ± 0.04
NV008	productid	NL/SL	3	2.84 ± 0.03	-1.04 ± 0.03
NV014	productid	NL	3	1.55 ± 0.04	-0.78 ± 0.07
NV021	productid	NL/SL	3	2.32 ± 0.45	-0.40 ± 0.04
<i>Grove Church Fm. (southern Illinois Basin, Illinois, USA), Late Mississippian (333-318 Ma)</i>					
WP58 Inf-1	<i>Inflatia</i>	NL	3	1.26 ± 0.03	-3.33 ± 0.03
<i>Glenshaw Fm. (Appalachian Basin, West Virginia, USA), Late Pennsylvanian (305-299 Ma)</i>					
WP50b NS-1	<i>Neospirifer</i>	NL/SL	3	2.72 ± 0.03	-3.66 ± 0.06
WP53 NS-1	<i>Neospirifer</i>	NL/SL	3	1.92 ± 0.03	-3.70 ± 0.05
Western Russia					
<i>Cherem. & Krasno. Hrzs. (Urals Mountains, Russia), Early Pennsylvanian (318 Ma)</i>					
RU124	<i>Choristites</i>	NL	3	4.84 ± 0.02	-1.02 ± 0.18
RU129A	<i>Choristites</i>	NL	3	4.66 ± 0.06	-2.48 ± 0.11

Table 3.1 (cont.)

Sample ID	Δ_{47} (‰, CDES) ^a	T(Δ_{47}) (°C) ^b	$\delta^{18}\text{O}_w$ (‰, VSMOW) ^c
North America			
<i>Fern Glen Fm. (upper Mississippi Valley, Missouri, USA), Early Mississippian (348-340 Ma)</i>			
MO074	0.708 ± 0.013	20 ± 5	-1.5
MO076	0.686 ± 0.016	29 ± 7	0.6
MO077	0.695 ± 0.011	25 ± 4	-0.4
<i>Bird Spring Fm. (eastern Great Basin province, Nevada, USA), Late Mississippian (323 Ma)</i>			
NV007	0.439 ± 0.012	157 ± 12	17.2
NV008	0.430 ± 0.013	166 ± 13	17.8
NV014	0.448 ± 0.005	148 ± 4	16.9
NV021	0.461 ± 0.013	137 ± 11	16.4
<i>Grove Church Fm. (southern Illinois Basin, Illinois, USA), Late Mississippian (333-318 Ma)</i>			
WP58	0.621 ± 0.004	48 ± 2	2.4
Inf-1			
<i>Glenshaw Fm. (Appalachian Basin, West Virginia, USA), Late Pennsylvanian (305-299 Ma)</i>			
WP50b	0.652 ± 0.002	35 ± 1	-0.3
NS-1			
WP53	0.633 ± 0.008	42 ± 4	1.1
NS-1			
Western Russia			
<i>Cheremchanskian & Krasnopolyanskian Horizons (Urals Mountains, Russia), Early Pennsylvanian (318 Ma)</i>			
RU124	0.448 ± 0.016	149 ± 14	16.6
RU129A	0.450 ± 0.015	147 ± 13	15.0

Note: Error values are standard error of the mean ($= \pm 1 \sigma / \sqrt{n}$), where 1σ is the standard deviation of n analyses. When $n = 2$ the error value is 1σ (standard deviation).

^aValues relative to the ‘carbon dioxide equilibrium scale’ or CDES. An acid correction factor of 0.092‰ was applied to normalize these data to the 25 °C phosphoric acid reaction scale.

^bPaleotemperatures calculated using linear regressions through the theoretical Δ_{47} -temperature relationship from Schauble et al. (2006) adjusted for the kinetic effects of calcite phosphoric acid reaction (Guo et al., 2009). A regression of model predictions from 0 to 50 °C ($\Delta_{47} = 38455/T^2 + 0.258$) was used for ‘WP’ samples and a regression from 50–250 °C ($\Delta_{47} = 41746/T^2 + 0.213$) was used for ‘NV’ and ‘RU’ samples. The modern calibration from Henkes et al. (2013) was used for ‘MO’ samples. Error was calculated by propagating the analytical error for Δ_{47} through these linear equations.

^cWater isotope compositions calculated using clumped isotope derived paleotemperatures and the calcite oxygen isotope thermometry equation of O’Neil et al. (1969): $1000\ln\alpha = 2.78 \times 10^6/T^2 - 3.39$ for temperatures > 50 °C. For temperature < 50 °C the equation of Kim and O’Neil (1997): $1000\ln\alpha = 18.03 \times 10^3/T - 32.42$ was used.

3.2.1 Analytical methods

Prior to stable isotope analysis, we characterized the preservation of brachiopods using plane-polarized light and cathodoluminescence (CL) microscopy. An example of results is shown in Fig. 3.1, and results for other specimens are provided in Section A3.3 (Figs. A3.3–A3.13). Some of this screening was done by referencing previous characterizations of these specimens by Mii et al. (1999) and Mii et al. (2001). New or more detailed imaging was performed at Texas A&M University using a Technosyn 8200 MKII CL stage mounted on a petrographic microscope. Based on these images, each shell was assigned a qualitative CL character (Table 3.1). Non-luminescent (NL) and semi-luminescent (SL) shells are considered pristine and near-pristine, respectively, whereas luminescent shells reflect uptake of trace elements (primarily Mn) and hence are not considered in this study. The prismatic secondary or tertiary shell layers were sampled, with care taken to avoid material from the primary shell layer, which is commonly observed to be recrystallized (e.g., Adlis et al., 1998) and exhibit vital effects (e.g., Carpenter and Lohmann, 1995).

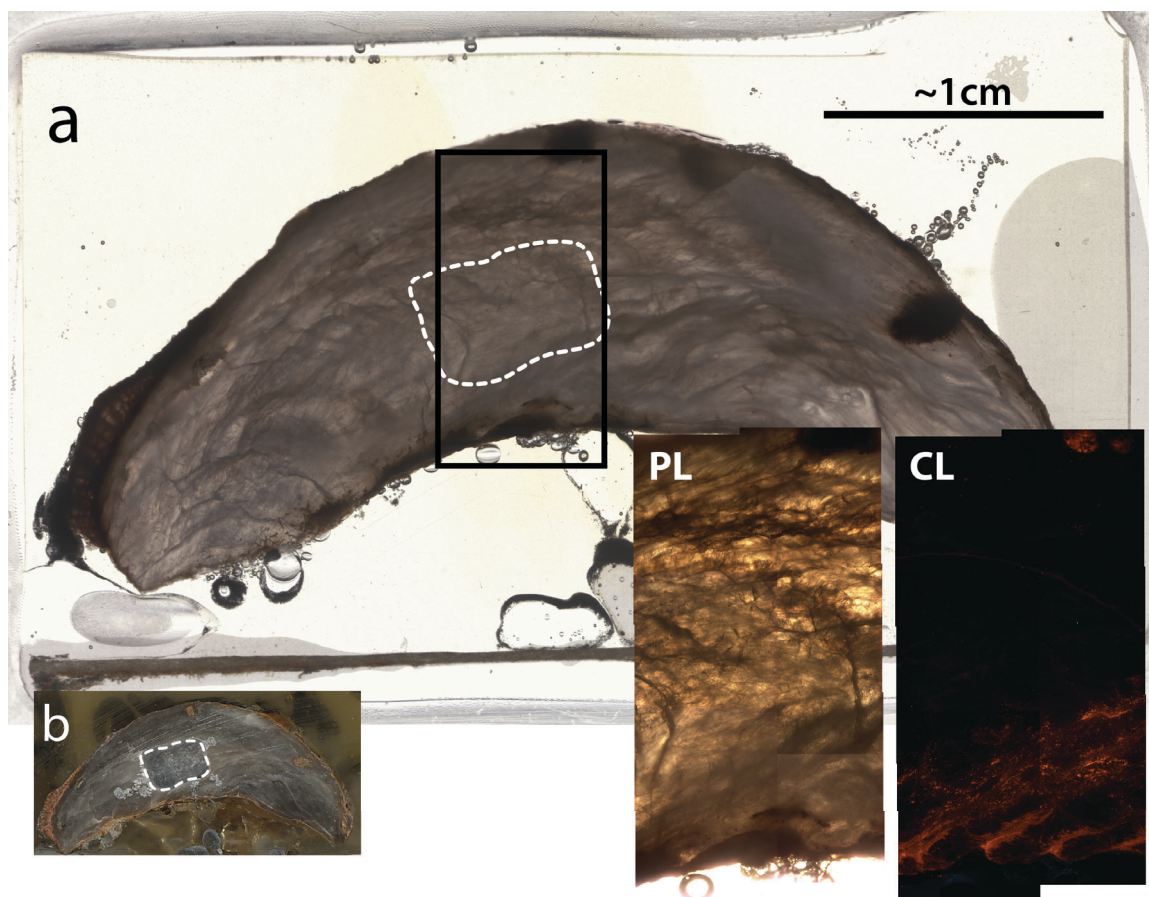


Figure 3.1 Scanned sample thin section (a) and billet (b), and plane-light (PL) and cathodoluminescence (CL) photomicrograph mosaics for a Carboniferous productid brachiopod (NV007) from the Bird Spring Formation, Arrow Canyon, NV, USA. The black box in (a) corresponds to the area covered by the photomicrograph images. This sample represents a typical nonluminescent (NL) brachiopod shell (Table 3.1). The sample billet (b) was scanned after sub-sampling from the area inside the white dashed line (also shown in 3.1a).

Stable isotope compositions of the fossil shells and their associated limestone matrices were determined at Johns Hopkins University (JHU) using methods described in Henkes et al. (2013). Carbonate clumped isotope compositions are expressed in Δ notation:

$$\Delta_{47} = \left[\left(\frac{R^{47}}{R^{47*}} - 1 \right) - \left(\frac{R^{46}}{R^{46*}} - 1 \right) - \left(\frac{R^{45}}{R^{45*}} - 1 \right) \right] \times 1000 \quad (3.2)$$

where R^i = mass i /mass 44 and the asterisk indicates ratios for isotopologues at stochastic abundance levels (Affek and Eiler, 2006). Mass 47 CO₂ contains the ¹³C–¹⁸O bond on which the thermometer is based (Ghosh et al., 2006b). Oxygen and carbon isotope values are expressed in δ notation, on either the VPDB (mineral) or VSMOW (water) scales. All carbonate clumped isotope values in this study are presented on an absolute reference frame, herein referred to as the ‘carbon dioxide equilibrium scale’ or CDES, which empirically corrects for instrumental nonlinearities and changes in the ionization environment during mass spectrometry (Dennis et al., 2011). This reference frame was established by periodically analyzing aliquots of CO₂ that were isotopically equilibrated at 30 or 1000 °C (for details see Henkes et al., 2013). We analyzed at least one of these equilibrium CO₂ reference gases every 1–2 days, thus cycling through four isotopically distinct gases weekly or sub-weekly.

The international standard NBS-19 and two internal carbonate standards, UU-Carrara and 102-GC-AZ01, were regularly analyzed alongside samples to monitor system stability and precision, with the following long-term averages: NBS-19 ($n = 9$) $\Delta_{47} = 0.404 \pm 0.009\text{‰}$ (CDES, mean $\pm 1\sigma$ standard deviation); UU-Carrara ($n = 27$) $\Delta_{47} = 0.402 \pm 0.017\text{‰}$; 102-GC-AZ01 ($n = 36$) $\Delta_{47} = 0.713 \pm 0.012\text{‰}$. The $\delta^{13}\text{C}$ and $\delta^{18}\text{O}$ values of samples were corrected using concurrent analyses of NBS-19. An effort was made to analyze each sample in triplicate during different analytical sessions to minimize session-

specific bias, although for some samples replicate measurements were made during a single session (Table A3.12).

Temperatures were calculated from Δ_{47} using the theoretical Δ_{47} -temperature relationship from Schauble et al. (2006), adjusted for the kinetic effects of calcite phosphoric acid digestion (Guo et al., 2009). The theoretical Δ_{47} temperature calibration was used because of the lack of empirical calibrations in the range of temperatures corresponding to the Carboniferous brachiopod clumped isotope compositions (up to ~ 150 °C) and our experimental temperatures. For brachiopod samples thought to have retained their primary clumped isotope compositions, we used the modern mollusk and brachiopod temperature calibration from Henkes et al. (2013) to calculate paleotemperatures.

3.2.2. Results for Carboniferous brachiopods and associated cements

Carbonate clumped isotope paleotemperatures ($T(\Delta_{47})$) of fossil brachiopod shells ranged from 20 ± 5 °C to 166 ± 13 °C (Fig. 3.2, Table 3.1, Table A3.12). The higher temperatures are clearly incompatible with shell growth, whereas the lower temperatures seem plausible for the low-paleolatitude tropical seas from which they originated (Mii et al., 1999; Mii et al., 2001). Measured brachiopod shell $\delta^{18}\text{O}$ values were used with $T(\Delta_{47})$ to solve calcite–water oxygen isotope thermometry equations (e.g., O’Neil et al., 1969 and Kim and O’Neil, 1997) for the oxygen isotope composition of the waters ($\delta^{18}\text{O}_w$) that would have been in equilibrium with these shells. Calculated $\delta^{18}\text{O}_w$ values ranged from -0.4‰ to 17.8‰ (Table 3.1). Again, the higher-end values in this range are incompatible with primary shell growth in ancient seawater. Note that the data in Fig. 3.2

generally plot along ‘closed-system pathways’ defined by solutions to the calcite-water $\delta^{18}\text{O}$ thermometry equations for constant calcite $\delta^{18}\text{O}$. In other words, the drastically altered clumped isotope compositions are not accompanied by obvious changes in calcite $\delta^{18}\text{O}$, a pattern consistent with solid-state reordering or low water/rock ratio recrystallization. The most extreme examples of this behavior are brachiopods from Arrow Canyon, NV, USA and the Ural Mountains in Russia (Fig. 3.2). Associated carbonate matrix from Arrow Canyon and the Ural Mountains (Fig. A3.12, Table A3.3) have $T(\Delta_{47})$ values that range from 89 to 127 °C, which are cooler than each of the associated brachiopods, but warmer than expected for early diagenetic cements.

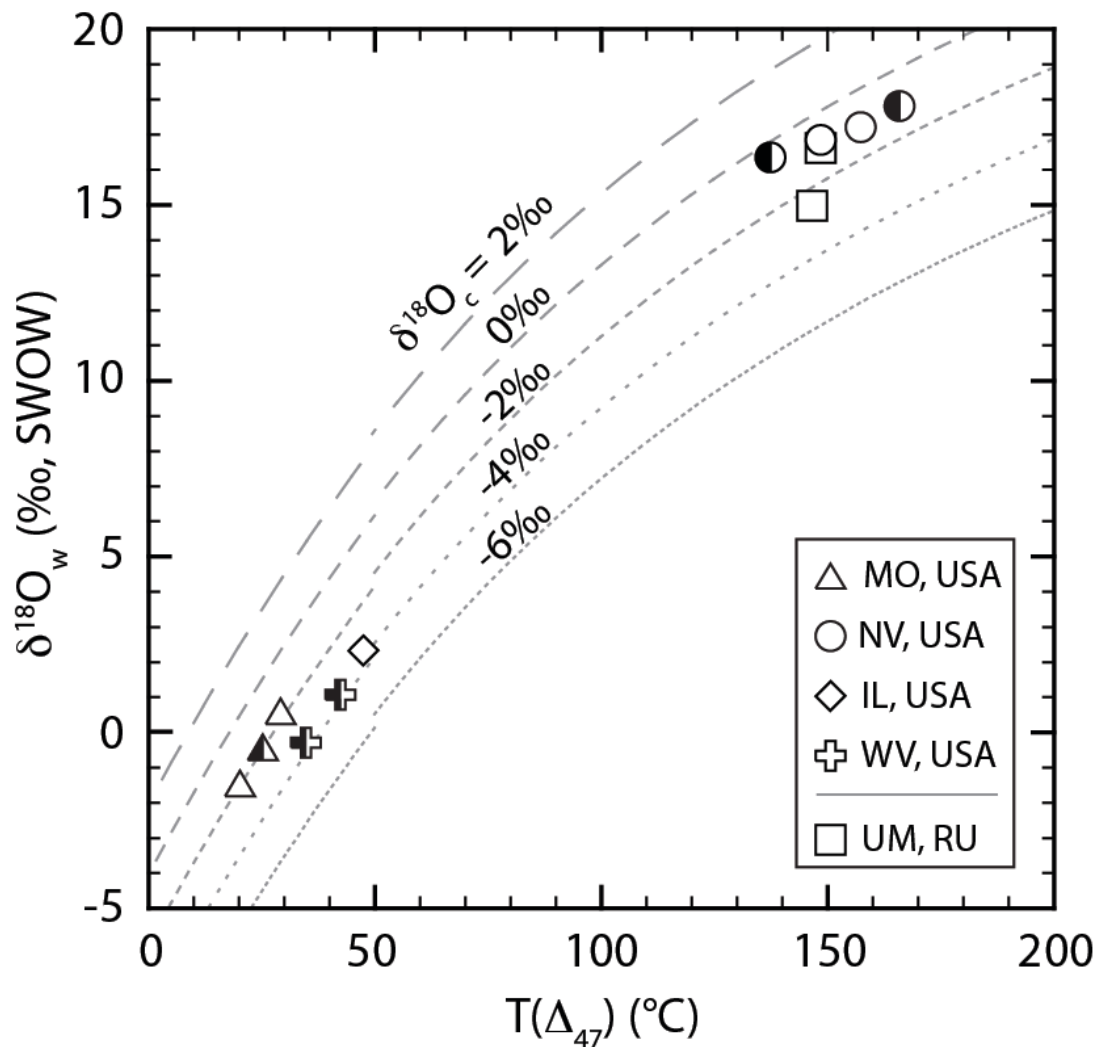


Figure 3.2 (*previous page*) Carboniferous brachiopod carbonate clumped isotope temperatures ($T(\Delta_{47})$) versus apparent water oxygen isotope compositions of the precipitating waters ($\delta^{18}\text{O}_w$). Water oxygen isotope values were determined from measured carbonate $\delta^{18}\text{O}$ and $T(\Delta_{47})$ using the calcite-water oxygen isotope thermometry equation of Kim and O’Neil (1997). For paleotemperatures greater than 50 °C, the equation of O’Neil et al. (1969) was used. Details on the Δ_{47} -temperature relationships used to determine the temperatures are in Table 3.1. Open symbols represent non-luminescent (NL) shells, whereas half-filled symbols represent semi-luminescent (SL) shells. The gray dashed and dotted lines represent solutions to the calcite–water oxygen isotope thermometry equations for constant carbonate $\delta^{18}\text{O}_c$ values, as noted above the figure.

The $T(\Delta_{47})$ data in Fig. 3.2 pose a problem: How can primary paleotemperatures be identified when analyses of brachiopods of similar textural and chemical preservation yield a ~150 °C apparent temperature range? Given the elevated clumped isotope temperatures, the lack of evidence for extensive recrystallization, and the apparently primary calcite $\delta^{18}\text{O}$ values we conclude that much of this temperature range results from solid-state reordering of C–O bonds at elevated burial temperatures experienced by some of these samples. An understanding of the temperatures and timescales over which such reordering becomes important will aid in identification of sedimentary strata and fossils most capable of preserving primary clumped isotope compositions.

3.3. Experimental determination of reordering kinetics in brachiopod calcite

3.3.1. Experimental methods and observations

Timed heating experiments were conducted on a fossil brachiopod shell fragment (WA-CB-13) collected from the Lower Permian Callytharra Formation in the Carnarvon Basin of Western Australia (Sakmarian-Artinskian Stage, ~290 mya). This formation contains the oldest Permian sediments in the region free of Late Paleozoic glacial influence (Dixon and Haig, 2004 and Mory and Haig, 2011). This shell was selected over the lower-temperature Carboniferous shells shown in Fig. 3.2 because of the large sample size requirements (see below) for heating experiments run at several temperatures. The design of the heating experiments closely follows the methods of Passey and Henkes (2012). The shell fragment ($3.4 \times 2.4 \times 0.8$ cm) was crushed in a mortar and pestle and sieved through 125 and 251 μm mesh. This size fraction was then rinsed and ultrasonicated in deionized water to remove smaller adhered particles. The cleaned material was dried at 60 °C for 24 h and stored in a desiccator. Approximately 30 mg aliquots of the crushed shell material were loaded into fused silica tubes, dried in vacuo at 100 °C for 1 h, and then torch-sealed along with ~80 μmol of dry CO_2 . The isotopic composition of the CO_2 was $\delta^{13}\text{C} = -39\text{‰}$ (VPDB) and $\delta^{18}\text{O} = -31\text{‰}$ (VPDB), which was significantly different than the shell ($\delta^{13}\text{C} = 3.75\text{‰}$; $\delta^{18}\text{O} = -0.66\text{‰}$), allowing for monitoring of isotopic exchange between the mineral and CO_2 as might result from unintended dissolution/precipitation reactions.

The silica tubes containing aliquots of WA-CB-13 were held at temperatures ranging from 385–475 °C inside tube furnaces for time periods of 30 min to 4 days. Each tube

was quickly removed from the furnace at prescribed intervals and quenched to room temperature (<30 s) with compressed air. Calibration curves between thermocouple-indicated furnace temperature and actual temperature were generated regularly by observation of in vacuo melting points for Sn, Zn, and Al using their ITS 90 reference values (Preston-Thomas, 1990), and the uncertainty in absolute temperature was less than 3 °C.

The average Δ_{47} value of unreacted shell material was $0.669 \pm 0.010\text{‰}$ (CDES), which corresponds to a growth temperature of 37 ± 5 °C (using the mollusk- and brachiopod-specific calibration reported by Henkes et al., 2013). Electron microprobe analyses of unreacted and reacted WA-CB-13 grains revealed low Mn and Fe contents (128–216 $\mu\text{mol/mol}$ Mn/Ca, 36–110 $\mu\text{mol/mol}$ Fe/Ca; Table A3.4), suggesting that the shell fragment did not undergo obvious natural meteoric diagenesis, and did not change in minor element composition during experimental heating (Popp et al., 1986). Heated grains of WA-CB-13 appeared similar to unheated grains in terms of size, shape, surface luster, and color. However, in some longer experiments, a slight darkening of the grains was observed. This may have been caused by pyrolyzation of trace amounts of organic carbon, or reduction of calcite to graphite, or calcite decomposition, and is similar to observations for heated optical and spar calcite studied by Passey and Henkes (2012).

In several reactions at 425–475 °C, a small amount of condensation was observed on the inside of the silica tubes following the quench to room temperature (noted in Table A3.5). The source of this fluid is unknown, but it is possible that it came from decrepitation of

fluid inclusions or hydrolysis of organic carbon occluded in the shells. Of relevance as to whether the presence of such water might affect reordering rates, Passey and Henkes (2012) conducted both dry (CO_2 , ~ 0.1 MPa) and wet (H_2O , ~ 0.1 and ~ 100 MPa) reordering experiments on calcite at 425°C , and observed no difference in reordering rates between these treatments. Thus we do not expect this fluid to have a large influence on the reordering behavior of our current experiments. As discussed in Passey and Henkes (2012), the apparent insensitivity of clumped isotope reordering rates on $f_{\text{H}_2\text{O}}$ is consistent with recent evidence (Labotka et al., 2011) that the mechanism of increased apparent rates of O diffusion in calcite at elevated $f_{\text{H}_2\text{O}}$ relates to reactions between water and calcite at the mineral surface, and not to changes in the diffusivity of the bulk mineral.

However, we did observe systematic $0.2\text{--}0.4\text{‰}$ decreases in $\delta^{18}\text{O}$ of reacted samples (Table A3.5), and we also observed that the samples did not approach equilibrium Δ_{47} values as closely as was observed in previous experiments with optical calcite (Passey and Henkes, 2012). Complete oxygen isotope exchange between CO_2 and calcite in our experiments would result in a lowering of the calcite $\delta^{18}\text{O}$ by about 6‰ (calculated using CO_2 -calcite fractionation factors from Chacko et al., 1991), and hence an observed change of 0.3‰ represents an approach to equilibrium of about 5% . At the same time, we observed no change in $\delta^{13}\text{C}$ values of reacted samples, despite an equilibrium value for complete C exchange between CO_2 and calcite about 10‰ lower than the initial composition of the mineral. These findings suggest that the observed change in $\delta^{18}\text{O}$ probably does not reflect dissolution and reprecipitation of mineral lattice (which we

expect would result in decreases of mineral $\delta^{13}\text{C}$ values). Perhaps the change in $\delta^{18}\text{O}$ is a result of solid-state O diffusion (which is significantly faster than C diffusion; e.g., Labotka et al., 2011), or some intrinsic change in the acid fractionation factor related to dewatering of the samples, or other unknown factors. With this caveat, we proceed with interpreting the observed clumped isotope changes as reflecting solid-state reordering only.

3.3.2. Heating experiment isotopic results

The isotopic compositions ($\delta^{13}\text{C}$, $\delta^{18}\text{O}$, and Δ_{47}) of our heating experiment samples are presented in Table A3.5 and illustrated (Δ_{47} only) in Figs. 3.3a–c. For comparison, we plot these data alongside results for optical calcite (Fig. 3.3d–f) from Passey and Henkes (2012). These two materials show similar Δ_{47} changes with time, including (1) progressive decrease throughout the reaction, (2) higher rates of decline at higher temperature, (3) an initial, rapid decline followed by a less rapid decrease after several hundred minutes, and (4) an asymptotic approach towards high temperature equilibrium Δ_{47} values of 0.30–0.35‰ for higher temperature reactions. Fig. 3.3b and e plot the data in terms of first-order reaction progress (Passey and Henkes, 2012):

$$\ln(1 - F) = -kt = \ln \left[\frac{\Delta_{47}^t - \Delta_{47}^{eq}}{\Delta_{47}^{init} - \Delta_{47}^{eq}} \right] \quad (3.3)$$

where Δ_{47}^t is the value of the sample at a time duration t , and Δ_{47}^{init} and Δ_{47}^{eq} are the initial and equilibrium Δ_{47} values, respectively, F is the fractional approach to equilibrium, and k is the reaction rate constant. The temperature-dependent Δ_{47}^{eq} values used in this study are the same as reported by Passey and Henkes (2012), but adjusted by +0.011‰ to

account for the difference in acid fractionation factors used in this study (0.092‰; see Henkes et al., 2013) versus the previous study (0.081‰). Fig. 3.3b and e clearly show that the reaction is not strictly first-order since the data for a given reaction temperature do not plot along straight lines (except for data from samples closely approaching equilibrium), and do not have intercepts at the origin. Instead, the data show early, rapid reordering followed by slower reordering.

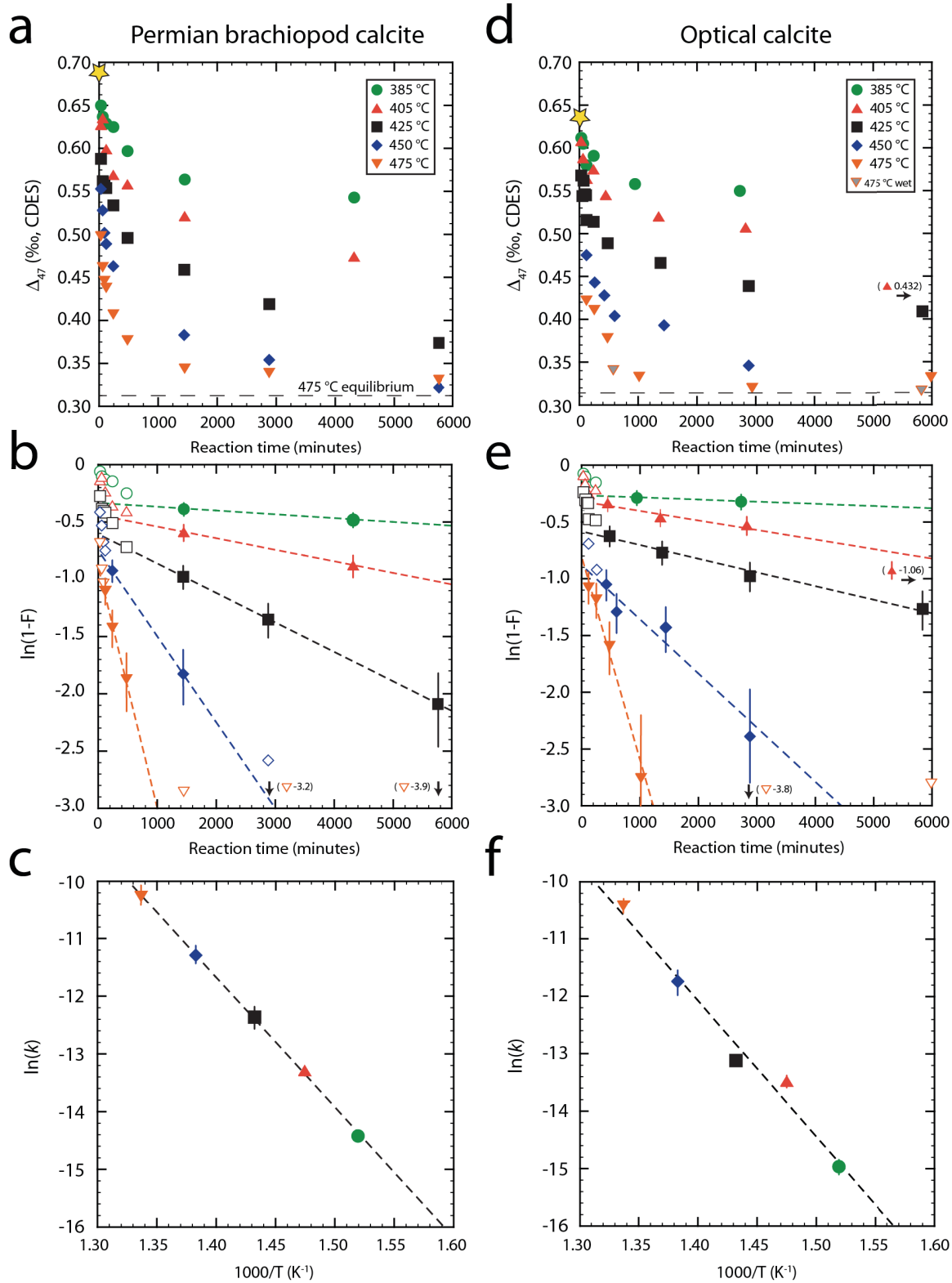


Figure 3.3 (*previous page*) Results of the reordering experiments on the Permian brachiopod shell WA-CB-13, and for comparison the results of analogous experiments performed on an optical calcite, MGB-CC-1, from Passey and Henkes (2012). (a,d) Measured Δ_{47} values as a function of time. The temperatures of each heating experiment are indicated in the legend. The yellow stars denote the initial compositions of the materials and the dashed line marks the theoretical equilibrium value for 475 °C, shifted by +0.092‰ to account for the acid fractionation for 90 °C reactions (Henkes et al., 2013). (b,e) Reordering reaction progress, plotted as $\ln(1-F)$, as a function of time. The dashed lines represent best-fit linear regressions to the data identified as having first-order behavior, whose slopes are equivalent to the reaction rate constant k (Eq. (3.3), Table 3.2). Unfilled symbols at times <1000 min correspond to non-first-order reaction and thus are not included in the linear regressions. Unfilled symbols at times >1000 min correspond to data that closely approach equilibrium for the respective reaction temperatures and are also not included in the linear regressions (see Section A3.1). (c,f) Arrhenius plots for determining the activation energies (E_a) and frequency factors (K_0) for the first-order approximation model. The slopes of the regressions equal $-E_a/R$, where R is the universal gas constant, and the intercepts equal $\ln(K_0)$.

3.3.3. Carbonate clumped isotope reordering models

We consider two alternative kinetic models for the data. The first model treats the data in terms of first-order kinetics (‘first-order approximation’ model; Passey and Henkes, 2012), whereas the second, a new ‘transient defect/equilibrium defect’ model, accounts for all parts of the reaction progress curve. Both models are based on the hypothesis that

crystallographic defects, particularly point defects, are the vehicle by which solid-state diffusion occurs (Lasaga, 1998, Cole and Chakraborty, 2001, Kittel, 2005 and Zhang, 2010). Defects can be classified as intrinsic, extrinsic, or “structural”. Intrinsic defects have concentrations that are a function of temperature and exist as a consequence of the thermodynamic battle between order and energy. In contrast, extrinsic defects arise from ionic impurities with radii and charges similar to or different from those of native ions, as well as other non-intrinsic point defects generated during crystal growth. Lastly, structural defects are those associated with dislocations, low and high angle grain boundaries, surfaces, radiation damage zones, and macroscale inclusions. For example, a Frenkel defect is a type of intrinsic defect consisting of a vacancy-interstitial pair created by migration of an atom from a lattice position to an interstitial position. The number of Frenkel defects increases with temperature according to $n \approx N \exp(-E_p/2k_B T)$ where N is the total number of atoms, E_p is the energy required to create a vacancy-interstitial pair, k_B is Boltzmann’s constant, and T is temperature in Kelvin (Kittel, 2005). Of these defect types, intrinsic defects can be considered to be ‘unannealable’: their concentrations are not reduced or changed during prolonged heating at elevated temperature (but note that with the onset of heating, the concentration of intrinsic defects will adjust to the new thermodynamic equilibrium). In contrast, certain types of extrinsic and structural defects are ‘annealable’: prolonged heating can act to eliminate (‘annihilate’ or ‘heal’) or otherwise immobilize these defects (i.e., the defect becomes fixed in its spatial coordinate and is no longer able to effect C–O bond reordering). The models presented below are based on the dichotomy of annealable defects, here termed ‘transient’ defects, and unannealable defects, here termed ‘equilibrium’ defects. Note that the latter is not strictly

limited to intrinsic defects; for example, it is generally not possible to remove ionic impurities simply by heating samples under closed-system conditions.

3.3.3.1. First-order approximation model

As described in Passey and Henkes (2012), this model assumes that the initial rapid reaction observed in our experiments (first several hundred minutes; Fig. 3.3a and c) is influenced by ‘transient’ defects. The existence of annealable defects in calcite and their promotion of rapid rates of solid-state diffusion have previously been observed in studies of O self-diffusion in calcite (Kronenberg et al., 1984 and Farver, 1994), although the nature of these defects has not been resolved. We further define a transient defect as any defect whose role in promoting C–O bond reordering is deactivated by prolonged heating. The transient defects are deactivated early in the experiment after effecting a finite amount of ^{13}C – ^{18}O reordering, while equilibrium defects persist indefinitely, with constant, temperature-dependent concentrations. Thus, equilibrium defects give rise to the first-order reaction progress observed during the latter part of the reactions (see Passey and Henkes, 2012, for further justification for applying first-order rate laws to ^{13}C – ^{18}O bond reordering).

For determination of first-order rate constant regressions and Arrhenius parameters (Fig. 3.3c and f) we will exclude the early transient defect-related data (unfilled data in Fig. 3.3b and e) from consideration. The justification for this exclusion is given by Passey and Henkes (2012), who argue that transient defects anneal early in the thermal evolution of carbonates previously residing at high temperatures (e.g., marbles and carbonatites). The

general purpose of the present study, however, is to constrain reordering rates at elevated temperatures for samples initially residing at surface temperatures. Therefore, we cannot assume that transient defects have been annealed, and we must make the assumption that the annealable defects are mostly inactive (in terms of effecting C–O bond reordering) at temperatures relevant to burial of paleoclimate archives (~200 °C or lower). This assumption is evaluated in our development of the extended ‘transient defect/equilibrium defect’ model (Section 3.3.3.2), and indirectly in Section 3.4, where we compare predicted clumped isotope compositions of Carboniferous brachiopods (based on the Arrhenius parameters applied to known burial temperature histories) to measured clumped isotope compositions.

The slope of linear regressions through the data exhibiting apparent first-order behavior (filled symbols in Fig. 3.3b and e) provide values for the reaction rate constant k (Fig. 3.3b, Table 3.2). Section A3.2 discusses the criteria used to include or exclude data from rate constant regressions; in short, the included data are from reaction durations longer than the period in which the transient reordering is active, but shorter than the period when clumped isotope compositions closely approach their equilibrium values.

Table 3.2 Rate constant regressions and Arrhenius parameters for the first-order approximation model for Permian brachiopod calcite WA-CB-13 and an optical calcite from Passey and Henkes (2012), for comparison.

Reaction T (°C)	Slope ($=-k$) (s ⁻¹)	Intercept	R^2	SRX Points Used*
<i>WA-CB-13</i>				
385	-5.52×10^{-7}	-0.34	-	037, 042
405	-1.68×10^{-6}	-0.44	0.98	033, 041, 044
425	-4.29×10^{-6}	-0.61	1.00	012, 013, 014
450	-1.25×10^{-5}	-0.75	-	020, 031
475	-3.50×10^{-5}	-0.88	1.00	017, 021, 029
Arrhenius parameters: $E_a = 188 \pm 6$ kJ/molm $K_0 = 4.45 \times 10^8$ [$\{+27.14/-1.05\} \times 10^9$] s ⁻¹				

Table 3.2 (cont.)

Reaction T (°C)	Slope ($=-k$) (s^{-1})	Intercept	R^2	‘RDX’ Points Used
<i>MGB-CC-1</i> (from Passey and Henkes, 2012)				
385	-3.18×10^{-7}	-0.27	-	181, 189
405	-1.39×10^{-6}	-0.32	0.99	169, 173, 177
425	-2.01×10^{-6}	-0.59	0.97	149, 150, 151, 153
450	-7.95×10^{-6}	-0.88	0.91	144, 145, 147, 148
475	-2.98×10^{-5}	-0.79	0.97	112, 113, 114, 115
Arrhenius parameters: $E_a = 197 \pm 19$ kJ/molm $K_0 = 1.39 \times 10^9$ [$\{+36.0/-1.34\} \times 10^9$] s^{-1}				

Note: Regressions are best-fit, least-squares regressions calculated using the statistical software package JMP.

*Isotope data provided in Table A3.5.

According to the Arrhenius relation:

$$k = K_0 e^{\left(\frac{-E_a}{RT}\right)} \quad (3.4)$$

where K_0 is a constant referred to as the frequency factor. A plot of $\ln(k)$ versus $1/T$ for each experiment will have a slope of $-E_a/R$, where E_a is the activation energy and R is the universal gas constant, and an intercept of $\ln(K_0)$ (Fig. 3.3c and f). The Arrhenius parameters for WA-CB-13 are presented in Table 3.2, along with the data and calculated Arrhenius parameters for the optical calcite (MGB-CC-1, from Passey and Henkes, 2012). We find that the activation energies of the brachiopod calcite and the optical calcite are identical within error, and that their frequency factors are marginally distinguishable. Note that for two experimental temperatures for WA-CB-13, only two points are used for the Arrhenius regressions (Table 3.2). This was unavoidable given the criteria used for selecting points to define the equilibrium defect behavior (Section A3.2) and the lack of sufficient sample for additional experiments.

3.3.3.2. Transient defect/equilibrium defect model

This model, developed fully in Section A3.1, accounts for C–O bond reordering due to both transient defects and equilibrium defects. The first step in this analysis is to quantify the reordering kinetics due to equilibrium defects, which is procedurally and mathematically equivalent to quantifying rate constants in the ‘first-order approximation’ model discussed above, and hence yields the same Arrhenius parameters. We then mathematically subtract the influence of the equilibrium defect pool on the overall reaction progress, leaving a reaction progress that is solely attributable to transient defects (the ‘curve-stripping’ procedure is described in Section A3.2). The resulting reaction progress is non-first-order, reflecting the fact that the rate constant is a function both of defect concentration and the efficacy of those defects at promoting C–O reordering. Since the concentration of transient defects decreases with time, the rate “constant” k is not actually constant. We therefore model k as a function of time (elapsed since initiation of heating), and for simplicity assume that the concentration of defects decreases proportional to the number of defects (a first-order rate law). The integrated rate equation for this model is (Section A3.1):

$$\ln\left(\frac{\Delta_{47}^t - \Delta_{47}^{eq}}{\Delta_{47}^{init} - \Delta_{47}^{eq}}\right) = k_c t + \frac{k_d}{k_2}(e^{-k_2 t} - 1) \quad (3.5)$$

Note that this equation features three rate constants, and hence three Arrhenius equations. The constant k_c is identical to the first-order rate constant in the first-order approximation model (Section 3.3.3.1), and describes the reordering behavior due to equilibrium defects. The constant k_d describes the efficacy of transient defects at effecting reordering, whereas the constant k_2 describes the rate at which these defects are annealed (the time-evolving concentration of defects). Regressions for determining these constants for WA-CB-13,

and their Arrhenius parameters, are given in Table A3.1. The results of these regressions for the optical calcite from Passey and Henkes (2012) are also given in Table A3.2.

3.3.4. General predictions of the models

In this section we evaluate the extent of ^{13}C – ^{18}O reordering predicted by each model as a function of time and temperature. For the first-order approximation model, Eqs. (3.3) and (3.4) can be combined, resulting in the following relationship:

$$\ln \left[\frac{\Delta_{47}^t - \Delta_{47}^{eq}}{\Delta_{47}^{init} - \Delta_{47}^{eq}} \right] = tK_0 \exp \left[\frac{-E_a}{RT} \right] \quad (3.6)$$

This equation allows the prediction of reaction progress (i.e., the change in Δ_{47}^t) as a function of temperature T , time spent at that temperature t , and the mineral- and material-specific Arrhenius parameters E_a and K_0 . The solid lines in Fig. 3.4 show equation 3.6 evaluated over a wide range of temperatures and time durations for the Arrhenius parameters of brachiopod calcite (WA-CB-13, Fig. 3.4a) and optical calcite (MGB-CC-1, Fig. 4b). Lines are given for T - t combinations that would result in 1% approach to isotopic equilibrium (minimal reordering) and 99% approach to isotopic equilibrium (nearly complete reordering). This figure predicts that solid-state reordering will be negligible for samples held at ~ 100 °C or lower for $\sim 10^8$ year timescales. The close correspondence between the lines for brachiopod calcite and optical calcite reflects the similarity in Arrhenius parameters observed for these materials.

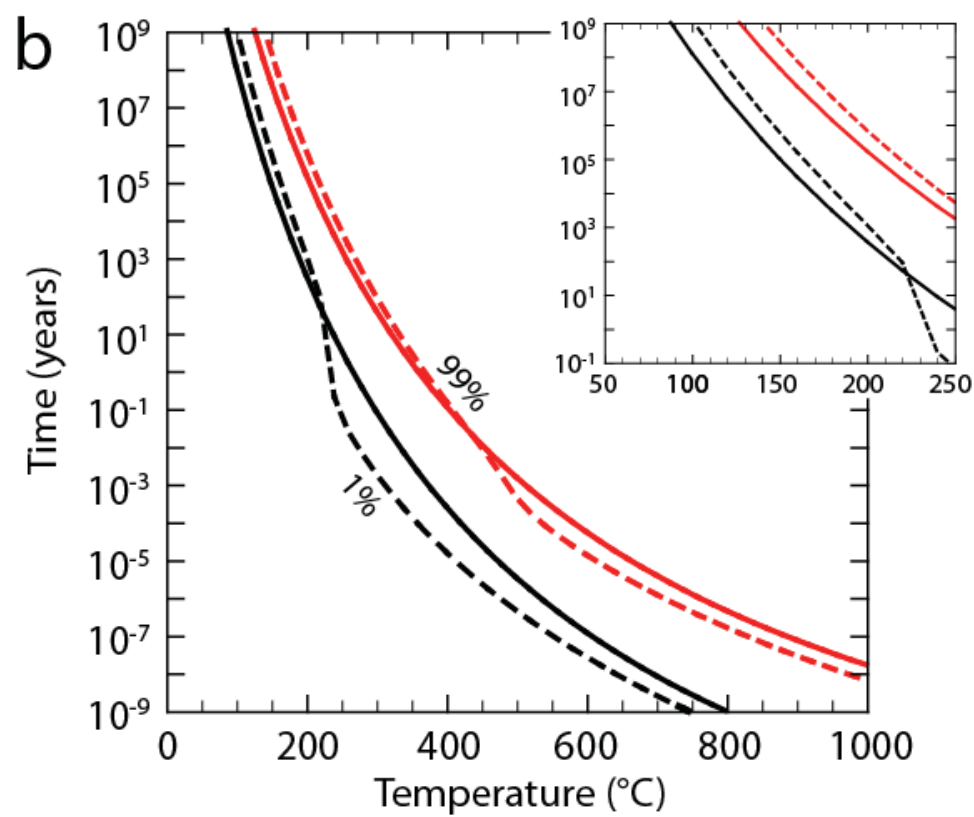
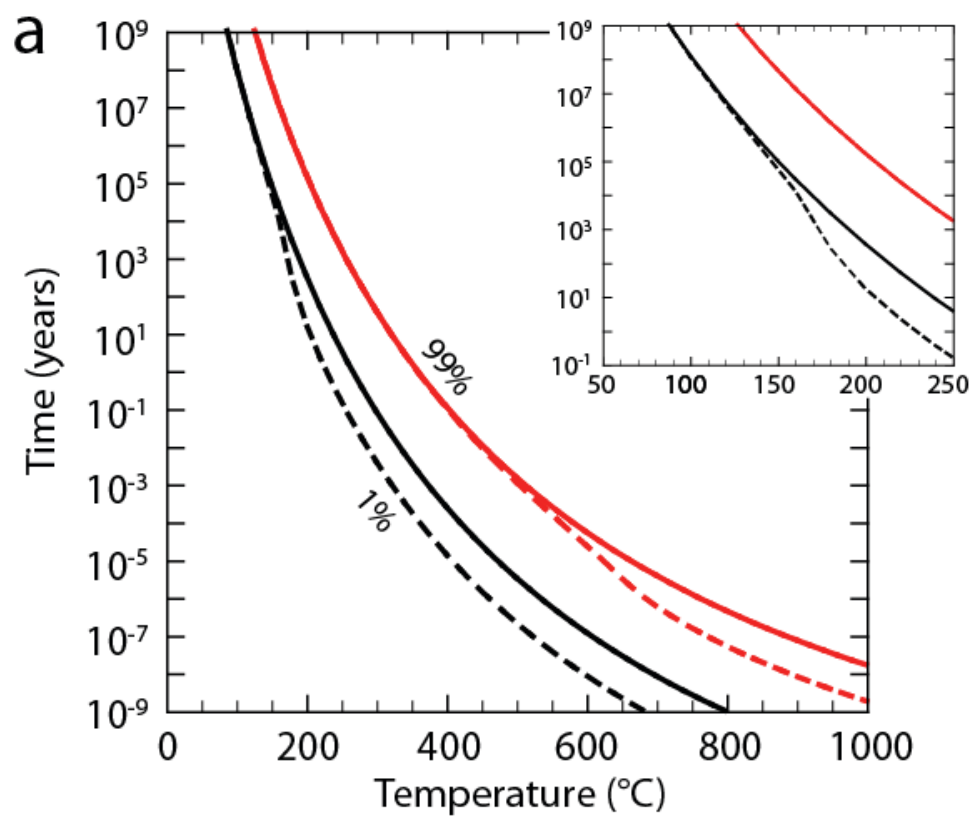


Figure 3.4 (*previous page*) Temperature-time predictions for incipient (1%) and near-complete (99%) reordering calculated using Arrhenius parameters for (a) WA-CB-13, well-preserved Permian brachiopod calcite, and (b) MGB-CC-1, an optical calcite (Passey and Henkes, 2012). The lower, black lines correspond to 1% reordering and the upper, red lines correspond to 99% reordered. The region to the left of these curves are the conditions necessary for preservation of primary carbonate clumped isotope compositions from brachiopods. The dashed lines show the ‘transient defect/equilibrium defect’ model and the solid lines show the ‘first-order approximation’ model. The inset figures focus on the conditions relevant to sedimentary burial and demonstrate that below temperatures of ~150 °C both models have similar behavior.

For the transient defect/equilibrium defect model, equation 3.5 can be combined with Arrhenius equations for each of the three rate constants (i.e., as Eq. (3.4)) to give an equation analogous to equation 3.6 allowing prediction of reaction progress as a function of temperature and time:

$$\ln\left(\frac{\Delta_{47}^t - \Delta_{47}^{eq}}{\Delta_{47}^{init} - \Delta_{47}^{eq}}\right) = -tK_c \exp(E_c / RT) + \frac{K_d \exp(E_d / RT)}{K_2 \exp(E_2 / RT)} \left\{ \exp[-tK_2 \exp(E_2 / RT)] - 1 \right\}$$

(3.7)

where K_c , E_c ; K_d , E_d ; and K_2 , E_2 are the frequency factors and activation energies for the equilibrium defect component (c), transient defect component (d), and rate of annealing of the transient defect component (2). The temperature–time predictions from this model are shown as dashed lines in Fig. 3.4. A key finding illustrated by this figure is that reordering rates are nearly identical to those predicted by the first-order approximation

model for temperatures below 150–200 °C. Thus, the transient defects are inefficient at effecting C–O bond reordering at temperatures below this range, and hence are predicted to be important only for samples experiencing higher burial temperatures. Geologically relevant temperature–time combinations for incipient and near-complete reordering as predicted by both of the models are listed in Table 3.3.

Table 3.3 Temperature–time combinations for incipient (1%) and near-complete (99%) carbonate clumped isotope reordering calculated using Arrhenius parameters for Permian brachiopod calcite (WA-CB-13) and optical calcite (MGB-CC-1).

Time	Permian brachiopod calcite				Optical calcite			
	First-order approx. model		Transient defect/ equil. defect model		First-order approx. model		Transient defect/ equil. defect model	
	1% (°C)	99% (°C)	1% (°C)	99% (°C)	1% (°C)	99% (°C)	1% (°C)	99% (°C)
1 Ga	88	127	87	127	98	138	98	138
100 Ma	102	144	101	144	112	155	112	155
10 Ma	116	163	115	163	127	174	127	174
1 Ma	133	183	131	183	144	194	144	194
100 ka	150	205	146	205	161	216	161	216
10 ka	169	230	162	230	180	241	180	241
1 ka	190	257	174	257	201	268	201	268
1000 y	213	287	186	287	224	298	223	298
100 y	239	321	205	321	250	332	245	331
10 y	267	360	229	359	278	370	263	369
1 y	301	407	258	405	312	416	273	414
1 m	323	438	278	435	334	447	274	443
1 d	356	485	306	479	366	492	289	481
1 h	417	576	359	559	426	580	349	546
1 m	515	730	445	665	522	728	462	705
1 s	647	954	557	826	649	938	614	928

3.4. Evaluation using the geological record

3.4.1. General approach and limitations

In this section we evaluate the laboratory-derived reordering kinetics against our observations from the geological record (Section 3.2). Our approach is straightforward: we examine sedimentary strata that have reasonably good independent constraints on

thermal history (e.g., from the study of fluid inclusions, conodont color alteration index, vitrinite reflectance, overburden reconstruction, and low-temperature thermochronology). For each Carboniferous basin we construct a thermal history that begins at the time of deposition, proceeds to maximum burial and through exhumation, and ends with the sample residing in outcrop at the present day. We divide the thermal history into uniform time-steps, typically one million years, which we find to be sufficiently short for accurate modeling of reordering progress. For each time-step, we use Eq. (3.6) to predict the extent of solid state C–O reordering that would be experienced by brachiopod calcite. This allows calculation of a new calcite Δ_{47} value that can be used as the Δ_{47}^{init} value in the next time-step of the model (this approach is functionally equivalent to using equation 13 of Passey and Henkes, 2012). We model changes in brachiopod Δ_{47} at million year time-steps, and the final result is a prediction of the final Δ_{47} value of the brachiopod after the final step (after exposure at the surface). We then compare this modeled Δ_{47} value (or equivalent $T(\Delta_{47})$) with the measured Δ_{47} values (or equivalent $T(\Delta_{47})$) of the brachiopod(s) collected from the same basin. If our laboratory-derived kinetics are valid for geological temperatures and timescales and if the burial temperature reconstructions are correct, then we should observe general correspondence between modeled and measured Δ_{47} values.

The main limitation of this approach is gaps or uncertainties in the thermal histories of the basins. As will be seen below, for many basins these uncertainties lead to large differences in the extents of predicted ^{13}C – ^{18}O reordering, in some cases ranging from no reordering to ‘complete’ reordering. As yet we have no remedy for this problem, but

point out that other simple geological heating events such as contact metamorphism from emplacement of dikes and sills also have wide error margins due to uncertainties in the thermal properties of magmas and rocks and the nature of heat transfer (e.g., conductive versus convective). Despite these uncertainties, we can still examine whether laboratory-derived rate predictions are consistent with observations from the geological record.

Also, we can in part work around these uncertainties by studying several basins that collectively have a wide range of thermal histories, from shallow burial of no more than ~1 km (mid-continental U.S.) to burial in a metamorphic core complex (Carrara marble).

Additionally, an irony exists in that we are treating methods like conodont color alteration, vitrinite reflectance, and fission-track annealing as yielding “correct” thermal history estimates against which our estimates of C–O reordering kinetics can be tested, whereas these burial temperature proxies arguably have more complicated and uncertain kinetics than solid-state C–O bond reordering (e.g., Castroño and Sparks, 1974, Epstein et al., 1977 and Donelick et al., 2005). For example, no simple chemical reactions can be written to describe the processes of conodont color alteration or bitumen maturation.

These processes undoubtedly involve vast suites of high molecular weight organic molecules, and in the case of vitrinite reflectance may also involve physical changes such as consolidation and compaction. Thus, while we test the estimates of C–O reordering kinetics versus these more established methods, in the future C–O reordering may become a measure against which other methods are compared.

3.4.2. Compilation of burial-temperature histories

We compiled burial temperature histories for strata from five sedimentary basins, ranging (roughly) from high-temperature to low-temperature: the Bird Spring Formation, Arrow Canyon, Nevada (Late Mississippian); the Cheremchanskian and Krasnopolyanskian Horizons, Ural Mountains, Russia (Early Pennsylvanian); the Grove Church Formation, Illinois (Late Mississippian); the Glenshaw Formation, West Virginia (Late Pennsylvanian); and the Fern Glen Formation, Missouri (Early Mississippian).

Additionally, as a high-temperature end-member, we modeled the rapid burial and exhumation of the Carrara marble, initially comprised of marine carbonate rocks that were buried deeply enough to become part of a metamorphic core complex and metamorphosed to marble (Kligfield et al., 1986, Carmignani and Kligfield, 1990 and Fellin et al., 2007). When possible we used complete thermal histories determined by previous studies, for example a numerical hydrothermal fluid-flow model for the southern Illinois Basin in Rowan et al. (2002) and an apatite fission track and (U–Th)/He thermochronology record for the central Appalachian Basin in Reed et al. (2005). However, this was not possible for other basins and therefore we compiled basic thermal histories using published data from conodont color alteration, vitrinite reflectance, sediment decompaction, and geochemistry. Temperatures, times, uncertainties, and citations for all burial temperature histories are given in Tables A3.6–A3.11.

As part of this empirical comparison it is important to consider the range of uncertainty for each point used to construct thermal histories. The commonly used indices for burial temperature have errors arising from analytical methods (e.g., (U–Th)/He

thermochronology; see Reed et al., 2005) and natural variability (e.g., conodont color alteration; see Epstein et al., 1977). Because of the relatively narrow band between ‘unaltered’ and ‘reordered’ states apparent in Fig. 3.4, a slight shift (within error) to warmer or cooler temperatures in the compiled burial histories could result in drastically different model predictions of apparent $T(\Delta_{47})$. This threshold behavior is discussed further in Section 3.4.3, but to give a sense of this feature in complex, natural systems we have modeled both ‘shallow’ and ‘deep’ scenarios. These represent the lower and upper bounds of uncertainty in our compilations and expose a limitation of these empirical data-model comparisons, as the scenarios often yield extreme $T(\Delta_{47})$ predictions (i.e., no reordering at the lower bound and ‘complete’ reordering at the higher bound). It should also be noted that uncertainty in the chronology of the thermal histories is as important in the models as uncertainty in burial temperatures, but for simplicity we only consider the latter.

3.4.3. Results: predicted reordering during burial versus observed $T(\Delta_{47})$

A schematic diagram demonstrating the behavior of the first-order approximation model in response to a simple, hypothetical burial and exhumation history is shown in Fig. 3.5. There are several distinct features of the burial trajectory predicted by the model. First, there is a period where clumped isotope reordering is ‘inactive’, coinciding with early burial, and original $T(\Delta_{47})$ values do not change. For a sample buried to sufficiently high temperatures this initial inactivity is followed by a period of rapid activation of reordering when the apparent $T(\Delta_{47})$ approaches equilibrium with the burial environment. With increasing temperature, $T(\Delta_{47})$ reaches equilibrium with the ambient temperature

($T(\Delta_{47}) = T$). Once the sample reaches this point of apparent thermal equilibrium it will continue to remain in equilibrium at all higher burial temperatures. During retrograde cooling the sample will again pass through the burial temperature equilibrium point and enter a phase where reordering is still active, but is ‘closing’ (i.e., apparent $T(\Delta_{47}) >$ burial temperature). Eventually the sample will cool to a point where reordering is effectively closed and the mineral ‘locks in’ an apparent $T(\Delta_{47})$ value.

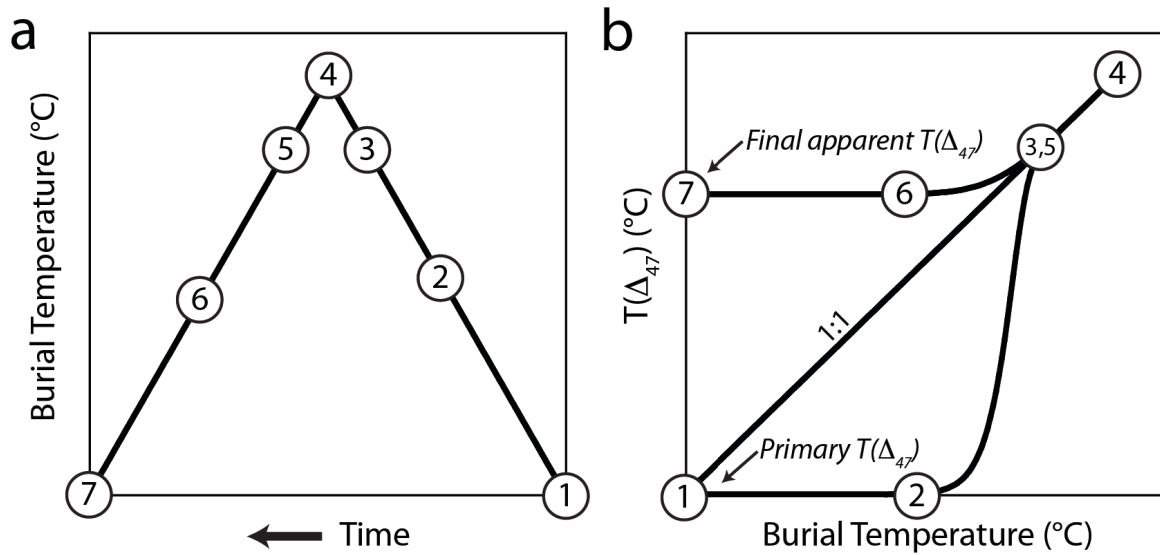


Figure 3.5 A schematic guide to the features of the burial history (a) and $T(\Delta_{47})$ -burial T trajectories (b) predicted by the first-order approximation model for carbonate clumped isotope reordering. Points 1→2: Reordering ‘inactive’ during early burial. No change in $T(\Delta_{47})$ is predicted by the model. Points 2→3: Reordering becomes ‘active’ during further burial. Points 3→4: Reordering remains active, and the clumped isotope temperature of the sample is in equilibrium with the burial temperature. Points 4→5: The sample remains in equilibrium with the burial environment during retrograde cooling. Points 5→6: Reordering remains active during further cooling but is ‘closing’ with

respect to the burial environment. Points 6→7: Reordering becomes inactive during late exhumation and apparent $T(\Delta_{47})$ is ‘locked in’. It should be noted that if a buried sample only reaches point 2 (that is, if burial temperatures do not reach the active region of the reordering curve) then the first-order approximation model predicts no change in original $T(\Delta_{47})$.

Modeled changes in brachiopod (and marble) clumped isotope compositions, expressed as apparent $T(\Delta_{47})$, are presented in Fig. 3.6 and Fig. 3.7 along with estimated burial temperature histories used in each of the models (from Tables A3.5–A3.11). The panels in each figure are arranged in order of highest $T(\Delta_{47})$ to lowest. Fig. 3.6 shows scenarios for the three highest $T(\Delta_{47})$ values, including the marble, and Fig. 3.7 shows the scenarios for the three lowest. In most cases three ‘burial trajectories’ are shown for each basin, with the upper and lower curves reflecting the uncertainty in the burial temperature estimates in our compilations. The yellow stars indicate the measured $T(\Delta_{47})$ from each basin and allow for direct comparison with the final model predictions.

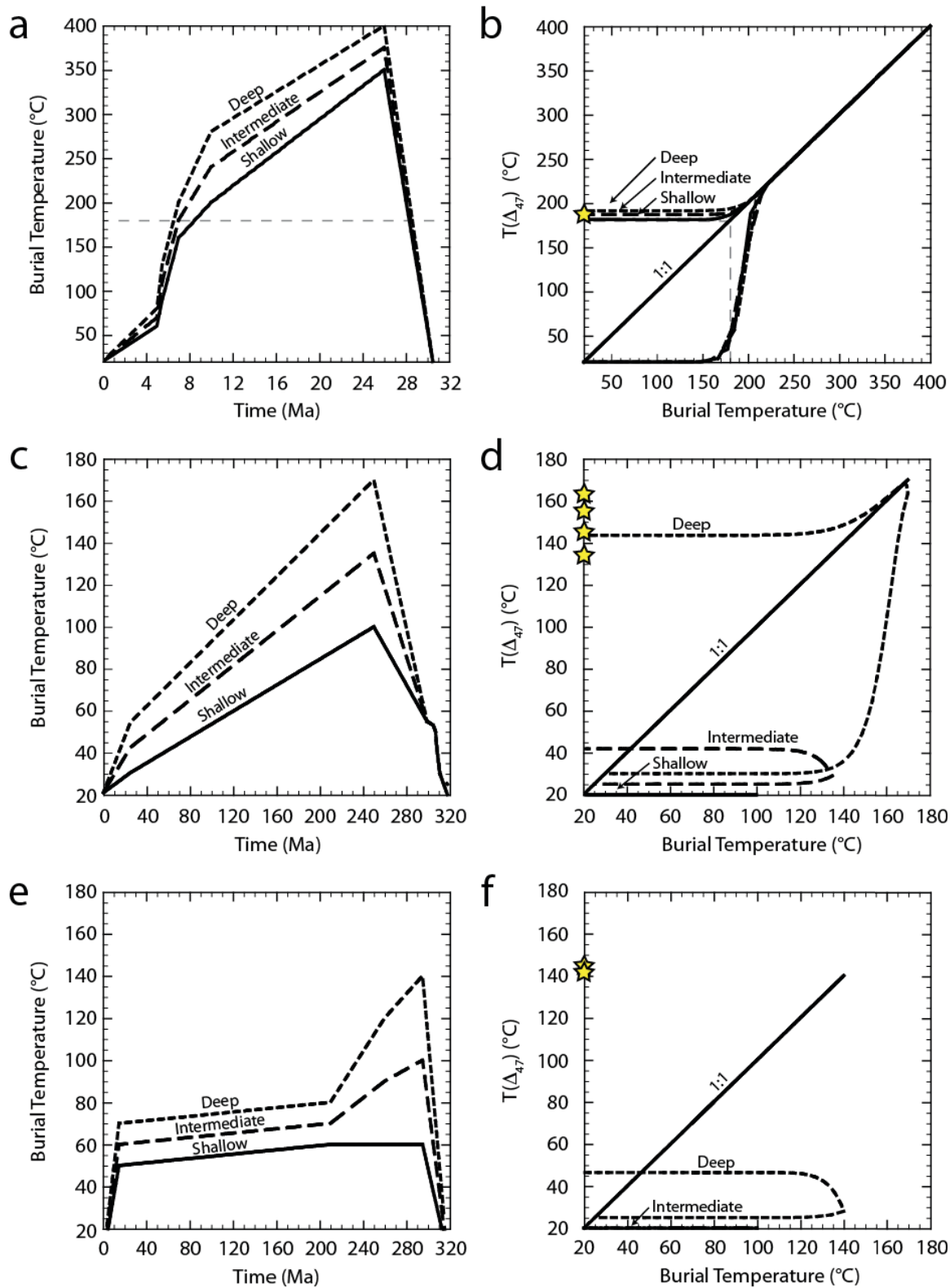


Figure 3.6 (*previous page*) Diagrams showing the compiled burial histories for samples with apparent $T(\Delta_{47})$ greater than 100 °C, including Carrara marble, and the modeled evolution of $T(\Delta_{47})$ during burial. Supporting data for burial temperature histories are presented in Tables A3.6–A3.8 for the Carrara marble (a,b), brachiopods from Arrow Canyon, NV (c,d), and brachiopods from the Ural Mountains, Russia (e,f). For each location three curves are shown: an ‘intermediate’ curve representing published values, and ‘deep’ and ‘shallow’ curves representing uncertainty in the burial temperature estimates. The grayed lines in (d) and (f) are the model predictions that are invalidated by the measured $T(\Delta_{47})$ values (i.e., the values represent minimum burial temperatures). The clumped isotope reordering model for the Carrara marble used kinetic parameters from Passey and Henkes (2012) for the optical calcite, whereas the brachiopod models used parameters for the ‘first-order approximation model’ determined in this study. The gray dashed lines in (a) and (b) mark the axis boundaries in (c) through (f). Yellow stars in (b), (d), and (f) indicate measured clumped isotope temperatures (Table 3.1).

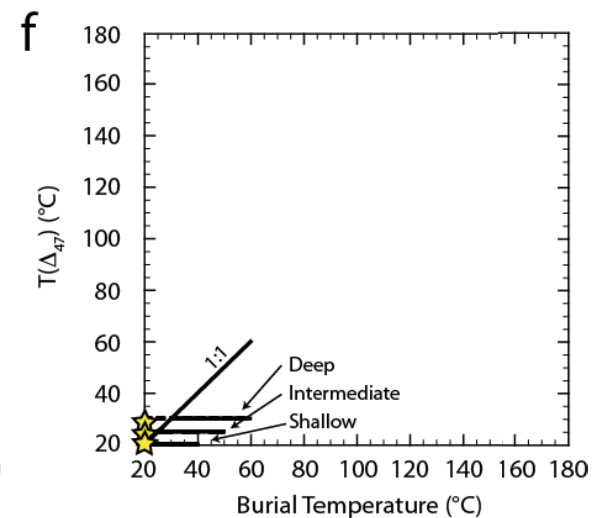
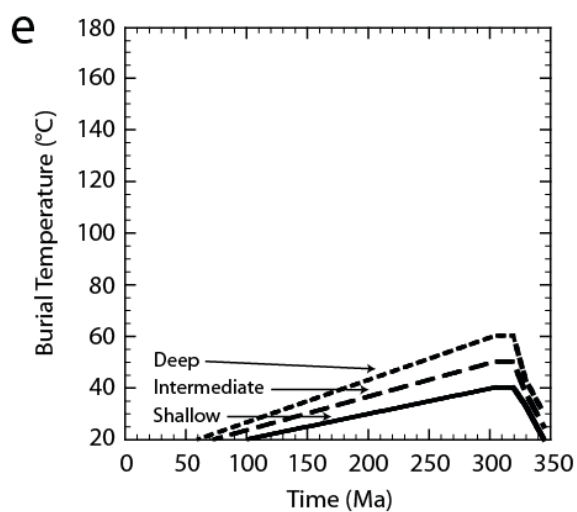
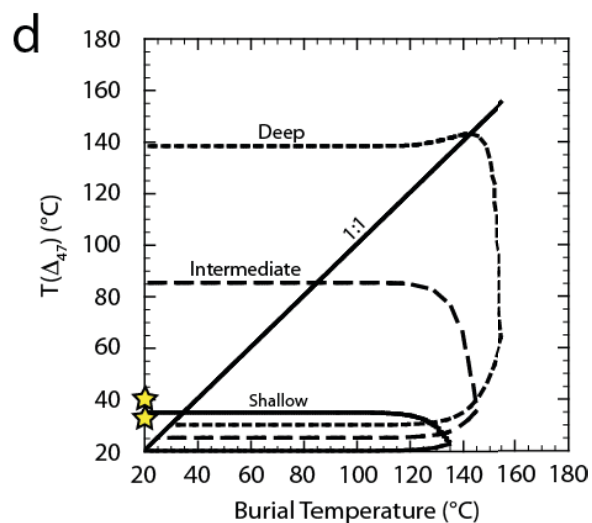
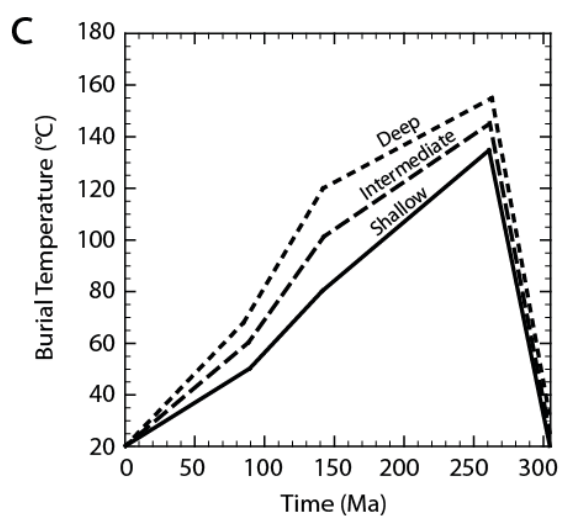
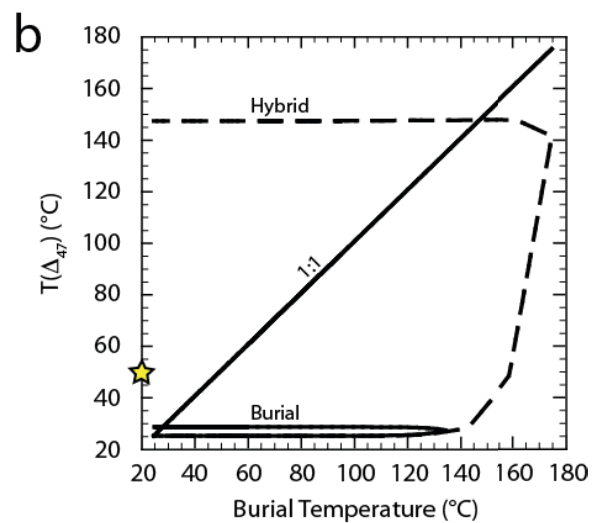
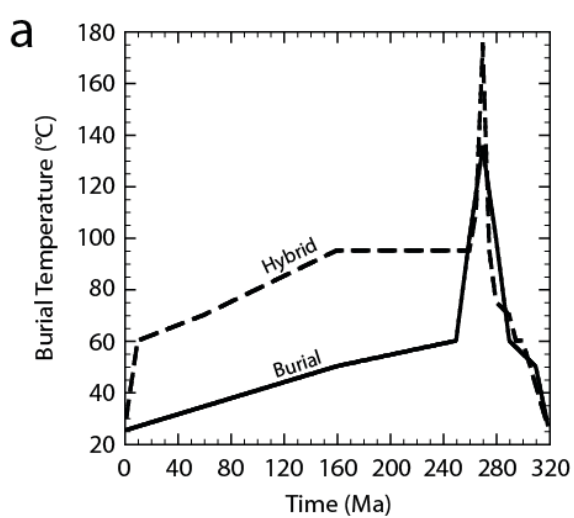


Figure 3.7 (*previous page*) Diagrams showing the compiled burial histories for samples with apparent $T(\Delta_{47})$ less than 100 °C and the modeled evolution of $T(\Delta_{47})$ during burial. Supporting data for burial temperature histories are presented in Tables A3.9–A3.11 for brachiopods from the Illinois Basin (a,b), the Appalachian Basin, WV (c,d), and the U.S. midcontinent, MO (e,f). For each location three curves are shown: an ‘intermediate’ curve representing published values, and ‘deep’ and ‘shallow’ curves representing uncertainty in the burial temperature estimates. Yellow stars in (b), (d), and (f) indicate measured clumped isotope temperatures (Table 3.1). For the Illinois Basin we relied exclusively on modeled burial temperature histories of Rowan et al. (2002), who considered (1) a thermal history using sedimentary burial only (“burial”) and (2) a hybrid thermal history using burial depth and simulated hydrothermal fluid flow (“hybrid”). An intermediate burial scenario was not considered for this locality.

In the six comparisons in Fig. 3.6 and Fig. 3.7 the models demonstrate at least one or more of the features described in Fig. 3.5, thereby capturing a range of responses from the reordering model. Overall, we observe a general (albeit inexact) correspondence between the measured $T(\Delta_{47})$ and the reordering model predictions. In the U.S. midcontinent, which has the coolest reconstructed burial temperatures, burial trajectories never reach the aforementioned activation period (Fig. 3.7f), whereas basins with high peak burial temperatures approach thermal equilibrium with the burial environment, with final Δ_{47} values possibly determined by retrograde reordering and cooling rate during exhumation (Fig. 3.6d). The burial trajectory for the Carrara marble also shows this

cooling rate dependence, and close correspondence between all of the modeled scenarios and the measured $T(\Delta_{47})$ (Fig. 3.6b).

This empirical test, however, is not without complications. Observed clumped isotope temperature from Arrow Canyon, NV are only compatible with the ‘deep’ burial scenario (Fig. 3.6c and d)—that is, the upper bound of the temperatures estimated from measured conodont color alteration index values of 2.0–2.5 (Martin et al., 2012)—and all of the model predictions from the Ural Mountains are cooler than the measured $T(\Delta_{47})$ (Fig. 3.6e and f). In Arrow Canyon these results suggest that carbonate clumped isotope studies may complement and refine existing maximum burial temperature estimates in the region as reordered brachiopod clumped isotope thermometry indicates at least a minimum burial temperature, thereby invalidating shallower burial histories (Fig. 3.6c and d). In the Ural Mountains the data-model mismatch highlights the lack of reliable burial information in the middle Uralian foredeep where our brachiopods were collected (Fig. 3.6e and f; Mii et al., 2001). However, it is also possible that data-model differences are the result of these brachiopod shells having different and thus far unrecognized clumped isotope reordering kinetics. We are continuing to conduct timed heating experiments on other brachiopod calcites to probe whether there are a range of susceptibilities to carbonate clumped isotope reordering, but the observation that two vastly different calcite samples (Permian brachiopod and hydrothermal optical calcite) have nearly identical kinetics (i.e., Fig. 3.3) suggests that compositionally similar minerals may have similar kinetics.

The wide range of possible trajectories predicted by the reordering model using published burial histories is best demonstrated by the data-model comparisons in the Illinois and Appalachian Basins. In both cases the measured $T(\Delta_{47})$ values are only consistent with the cooler burial temperature histories (Fig. 3.7a–c). In the Illinois Basin there is good geologic and model-based evidence of late Paleozoic hydrothermal fluid flow, as shown by the thermal ‘pulse’ in Fig. 3.7a. Because this pulse is relatively short-lived, the modeled $T(\Delta_{47})$ is highly dependent on the maximum temperature of the fluid, and hence the wide range of predictions in Fig. 3.7b. In this case, additional clumped isotope measurements could help constrain the duration, geographic range, and peak temperature of this event due to the wide temperature–time sensitivity of clumped isotope reordering (Fig. 3.4).

To summarize, these data-model comparisons highlight a relationship between the burial temperature history of fossil brachiopod shell calcite and its measured carbonate clumped isotope composition. From the perspective of preservation of primary brachiopod paleotemperatures, these results suggest that Δ_{47} values are preserved at burial temperatures of less than $\sim 100\text{--}120\text{ }^{\circ}\text{C}$; above those temperatures C–O bond reordering begins altering Δ_{47} values. This is illustrated in Fig. 3.8 where we used a simple ‘box car’ heating event lasting 60 million years and the first-order approximation model for WA-CB-13 to solve for the evolution of $T(\Delta_{47})$ at simulated burial temperatures from 100 to $160\text{ }^{\circ}\text{C}$. At $160\text{ }^{\circ}\text{C}$, the apparent $T(\Delta_{47})$ altered to $160\text{ }^{\circ}\text{C}$ in ~ 15 million years, whereas at $100\text{ }^{\circ}\text{C}$ there is no apparent change in $T(\Delta_{47})$. Intermediate burial temperatures show a range of final $T(\Delta_{47})$ between 28 and $137\text{ }^{\circ}\text{C}$, none of which reach apparent thermal

equilibrium with the artificial burial environment after 60 million years. Translated to the geologic record, this behavior implies that carbonate fossils with burial temperature histories that fall within this intermediate temperature range may be expected to have a wide range of measured Δ_{47} values. In contrast, primary carbonate with burial temperatures that are lower or higher than this range are expected to show, respectively, either no evidence of reordering or essentially complete reordering to higher $T(\Delta_{47})$ values, the latter reflecting cooling rate dependent ‘closure’ temperatures (e.g., Passey and Henkes, 2012). In the future, these observations may be exploited by measurement of natural brachiopod shells spanning a range of stratigraphic positions in a single basin as a tool for refining the dynamics of burial.

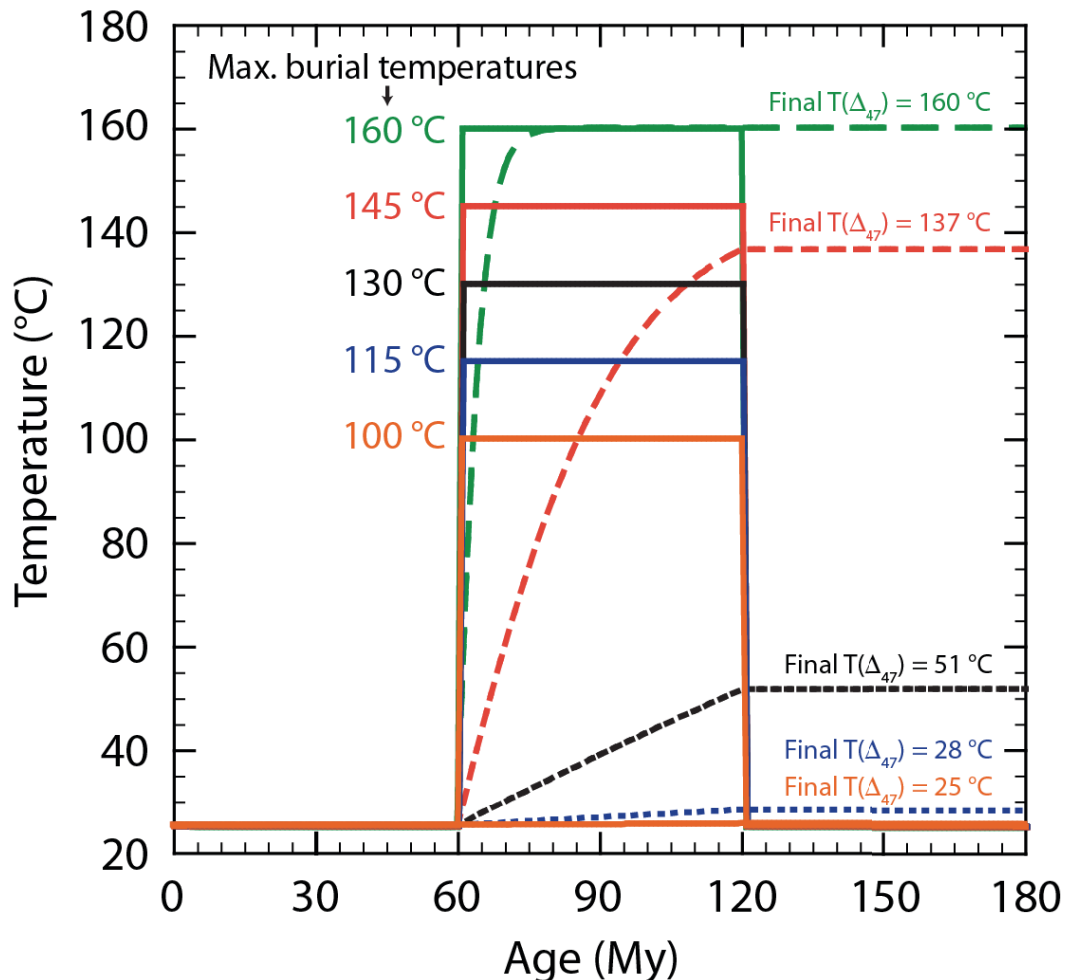


Figure 3.8 (*previous page*) Illustration of the threshold behavior of carbonate clumped isotope reordering for simple ‘box-car’ heating scenarios lasting 60 million years. The solid lines represent the temperature forcing used to solve the first-order approximation model and are in 15 °C increments from 100 to 160 °C. The dashed and dotted lines represent the model response at each time step, with the final indicated temperature (at 180 My) equivalent to a measured Δ_{47} temperature. At 100 °C maximum burial temperature there is no apparent change from the initial $T(\Delta_{47})$ (25 °C) whereas at 160 °C maximum burial temperature the model predicts complete reordering.

3.5 Conclusions and an outlook for future research

A key conclusion from the laboratory reordering data and empirical comparisons presented in this study is constraining the burial temperatures capable of preserving of primary brachiopod paleotemperatures to less than ~100 °C for 10^6 – 10^8 year timescales. Also remarkable is the nearly identical carbonate clumped isotope reordering kinetics for two different types of calcite, well-preserved Permian brachiopod calcite and an optical calcite. The similar trace element content of these materials (Table A3.4; Fig. 1, Passey and Henkes, 2012) and the implication of ionic impurities in the creation of extrinsic crystallographic defects suggest that the bulk chemistry of calcite may, in part, determine its susceptibility or resistance to reordering. A positive relationship between trace element (Mn) content and the rate of O diffusion into the calcite lattice has been identified (Kronenberg et al., 1984), but similar effects on self-diffusion of C and O within a carbonate mineral are largely unknown. We note, however, that an experimentally heated calcite spar sample from Passey and Henkes (2012; NE-CC-1 had

very different Mg and Mn contents and distinctly different reordering kinetics. A combination of future experiments and identification of naturally reordered samples will likely shed new light on the relationship between trace elements and reordering, and on the nature of C–O bond reordering itself.

This conclusion limits meaningful clumped isotope paleoclimate records to sedimentary basins with relatively shallow burial histories. Fortunately, we can screen the stratigraphic record for suitable burial histories prior to analysis. Thermal maturity index data and thermochronology studies exist for most basins throughout the world due to the economic importance of oil, gas, and coal resources, particularly (and fortuitously) in pre-Cenozoic strata. As was attempted in Section 3.4 of this study, compilations of these data prior to sampling for deep-time paleoclimate studies should allow for a ‘first-pass’ evaluation of primary $T(\Delta_{47})$ preservation with respect to clumped isotope reordering. Additionally, an understanding of the reordering reaction kinetics for other minerals commonly targeted for carbonate clumped isotope analysis – for example soil carbonates, mollusk shells, biogenic apatite, and dolomite – will further constrain the burial environments capable of preserving primary paleoclimate information over a range of timescales.

Finally, the clumped isotope composition of pristine, yet reordered brachiopod shells may be exploited and utilized as a low-temperature geothermometer, provided brachiopod calcite reordering kinetics are universal and appropriate constraints can be placed on their geological context (e.g., age and stratigraphy). This approach would be similar to the

inversion of low-temperature thermochronology data resulting in a set of temperature–time ‘paths’ or a single, best-fit path representing some statistical evaluation of the numerical models presented in this paper and measured $T(\Delta_{47})$ (Ketcham, 2005). Of course, this approach would require that the variation observed in Δ_{47} values would be solely determined by clumped isotope reordering processes and not simultaneously influenced by cryptic dissolution/precipitation diagenesis, which cannot be definitively ruled out for the natural and experimental brachiopods in this study.

Electron backscatter diffraction (EBSD) is a relatively new technique with increasing use in the study of diagenesis of fossil biocarbonates, including brachiopods. EBSD has been used to detect loss of primary crystallographic orientation with no apparent alteration of microstructures (Pérez-Huerta et al., 2007 and Pérez-Huerta et al., 2012), presence of secondary mineralization and recrystallization not detected with other techniques (such as XRD; Cusack et al., 2008), and the presence of primary crystallographic information for paleoecological and phylogenetic applications (Grellet-Tinner et al., 2012 and Dietrich et al., 2013). Ongoing analyses are expected to provide information on how EBSD observations of extant brachiopod shells compare with samples from the geologic record, and will probe micro-scale calcite dissolution/precipitation and diagenetic reorientation of otherwise ‘well-preserved’ calcite crystals. In the context of carbonate clumped isotope reordering, EBSD may be well-suited as a complementary method used to rule out the contribution of chemical diagenesis to apparent $T(\Delta_{47})$ changes. It may also be able to constrain the spatial scales over which C–O bond reordering occurs, to the extent that crystallite size may exert control over the maximum domain size of defect

propagation. In future applied and experimental clumped isotope studies we envision ‘next generation’ sample screening techniques such as EBSD to be used in conjunction with traditional petrographic screening, as each method has equivalent trade-offs between analysis time and resolution.

4. THE EMERGING RECORD OF PHANEROZOIC SEAWATER TEMPERATURE AND $\delta^{18}\text{O}$ FROM CARBONATE CLUMPED ISOTOPES: REAL OR REORDERED?

Abstract

The 5-6‰ increase in marine carbonate $\delta^{18}\text{O}$ from past to present over the Phanerozoic is one of the most prominent and yet poorly-understood features of the geological record. The correct interpretation of the increase has broad implications for the evolution of climate, metazoan life, and water-rock interactions at oceanic spreading centers. Competing explanations for the increase in $\delta^{18}\text{O}$ over this interval include decreasing ocean temperatures, increasing seawater $\delta^{18}\text{O}$, and the influence of diagenesis on older samples. Carbonate clumped isotope thermometry has the potential to address these possibilities because unlike $\delta^{18}\text{O}$ thermometry, it can uniquely resolve the temperature and $\delta^{18}\text{O}$ value of ancient seawater. However, also unlike $\delta^{18}\text{O}$, clumped isotope bonds (e.g., $^{13}\text{C}-^{18}\text{O}$) are susceptible to alteration by closed-system recrystallization and solid-state diffusion. Here we present a long-term paleotemperature and seawater $\delta^{18}\text{O}$ record from new and previously published clumped isotope data, screened for chemical diagenesis (recrystallization) and evaluated for the effects of solid-state diffusive reordering of $^{13}\text{C}-^{18}\text{O}$ bonds. To accomplish the latter, we used newly determined kinetic parameters for C-O bond reordering in brachiopod and optical calcite, combined with the reconstructed maximum burial temperature of each basin from which biogenic calcite and aragonite were analyzed, to predict the degree of preservation of the original clumped isotope ordering. In general, shallowly-buried brachiopod and mollusk shells comprising much of the Phanerozoic clumped isotope record are unaffected by solid-state reordering.

The emerging Phanerozoic clumped isotope record shows no evidence of a long-term trend in seawater $\delta^{18}\text{O}$ over the last ~450 million years, and indicates that tropical seawater temperatures exceeded 30 °C during intervals of the early and latest Paleozoic.

4.1. Introduction

Since its inception, carbonate clumped isotope thermometry has been poised to shed new light on the interpretation of the Phanerozoic marine carbonate oxygen isotope record (Came et al., 2007; Eiler, 2011). The technique holds this promise because, unlike conventional carbonate-water oxygen isotope thermometry, it is independent of the bulk isotopic composition of the mineral and fluid from which the analyzed mineral precipitated (Eiler and Schauble, 2004; Schauble et al., 2006; Ghosh et al., 2006). In addition to the paleoclimatological value of reconstructing temperature, simultaneous knowledge of both the clumped and oxygen isotope compositions of carbonates allows for calculation of the isotopic composition of ancient seawater. In the context of the long-term marine carbonate $\delta^{18}\text{O}$ record, deconvolving the paleotemperature and seawater $\delta^{18}\text{O}$ signals has broad biological, geochemical, and geophysical implications (Muehlenbachs, 1998; Kasting et al., 2006; Jaffrés et al., 2011).

Three explanations have been proposed for the observed 5-6‰ increase in carbonate $\delta^{18}\text{O}$ from past to present over the Phanerozoic: (1) cooling of low-latitude seawater temperatures towards present-day values from 35-40 °C during the early to middle Paleozoic (e.g., Bassett et al., 2007; Trotter et al., 2008; Joachimski et al., 2009 (after correcting for differences in standardization [Puceat et al., 2010; M. Joachimski, pers.

comm., 2013]; Grossman, 2012), (2) a secular increase of seawater $\delta^{18}\text{O}$ (Veizer et al., 1999; Kasting et al., 2006; Jaffrés et al., 2011), and (3) progressively increased oxygen isotope exchange between older carbonate rocks and diagenetic fluids (Land et al. 1995; Veizer et al., 1995; Land and Lynch, 1996). The third possibility has been largely discounted for the Phanerozoic record from well-preserved and carefully screened marine invertebrate fossils (e.g., brachiopods, mollusks, and foraminifera; Grossman, 2012a), although diagenesis remains a problem for the interpretation of Proterozoic and Archean oxygen isotope records from non-biogenic sedimentary carbonates and cherts.

The temperatures proffered in the first hypothesis assume an ice-free world with a constant seawater $\delta^{18}\text{O}$ value of -1‰ (VSMOW). Such high paleotemperatures for early to middle Paleozoic ocean (~35°C or higher) challenge our understanding of the thermal limits of metazoan life and of greenhouse climate dynamics. It has long been assumed that metazoan life has upper temperature limits near that of maximum seawater temperatures today (~30 °C), but recent findings on the thermal tolerances of organisms at hydrothermal vents show that metazoans can survive at temperatures warmer than 40 °C, but not more than 55 °C, thus challenging traditional assumptions about the environmental limits imposed by biology (Ravaux et al., 2013). While many common extant marine bivalve species have thermal limits exceeding 30 °C (summarized by Hicks and McMahon, 2002). It seems unlikely, however, that these organisms can spend their entire lives at such high temperatures, and it is questionable whether they are able to actively precipitate shell material under such conditions.

Hot seawater paleotemperatures also have provocative implications for the existence or absence of a climate thermostat (Huber, 2012). Tropical temperatures in excess of 30 °C may be inconsistent with the strict physical mechanisms thought to maintain the modern tropical climate and meridional temperature gradient, although data-model mismatch could be reduced on either end: models require better constraints for different climate modes (e.g., super-greenhouses) and paleotemperature proxies require refinements their degrees of uncertainty.

If instead early Phanerozoic temperatures were relatively clement, then seawater $\delta^{18}\text{O}$ values must have increased significantly over the last ~450 million years, indicating either a decrease in low-temperature water-rock interaction (as occurs on continents and in the shallow oceanic crust), and increase in high-temperature water-rock interaction (as occurs at mid-ocean ridges and deep within the oceanic crust), or both. However, it has been argued that this is inconsistent with oxygen isotope measurements of oceanic crust silicates and typical rates of water-rock interaction at mid-ocean ridges (Muehlenbachs and Clayton, 1976; Gregory and Taylor, 1981; Muehlenbachs, 1998). Nevertheless, compelling predictions of changing seawater $\delta^{18}\text{O}$ have come from geophysical models of seafloor spreading and hydrothermal circulation (e.g., Kasting et al., 2006; Jaffrés et al., 2011).

New geochemical constraints from carbonate clumped isotope thermometry are clearly needed. Published carbonate clumped isotope datasets from marine fossils now collectively span the greater part of the Phanerozoic (Fig. 4.1; Table 4.1). All of these

studies have employed some combination of chemical and petrographic methods to identify and omit altered samples (Popp et al., 1986; Grossman, 1994; Veizer et al., 1999). Therefore, a Phanerozoic record representing the best-preserved samples is at hand (Fig. 4.1). Despite this screening, anomalous clumped isotope temperatures persist. Henkes et al. (2014) have attributed the highest of these altered paleotemperatures, including $T(\Delta_{47})$ as high as ~ 150 °C, to solid-state reordering of C-O bonds at elevated temperatures following sedimentation during deep sedimentary burial. Paleotemperatures from well-preserved Carboniferous brachiopods with very warm (40-50°C), but not extreme clumped isotope temperatures may also be eliminated from the Phanerozoic record based on burial temperature histories that exceeded 100 °C (Henkes et al., 2014). However, it is not known whether other samples in Figure 4.1 may have also been affected by C-O bond reordering during burial.

Here we present new brachiopod clumped isotope data from the Carboniferous of the U.S. mid-continent and the Moscow Basin in Russia, and combine these data with published results to critically evaluate the emerging Phanerozoic clumped isotope record with respect to the effects of solid-state reordering. Such evaluation has recently been made possible by the availability of kinetic data for C-O reordering in calcites (Passey and Henkes, 2012; Henkes et al., 2014).

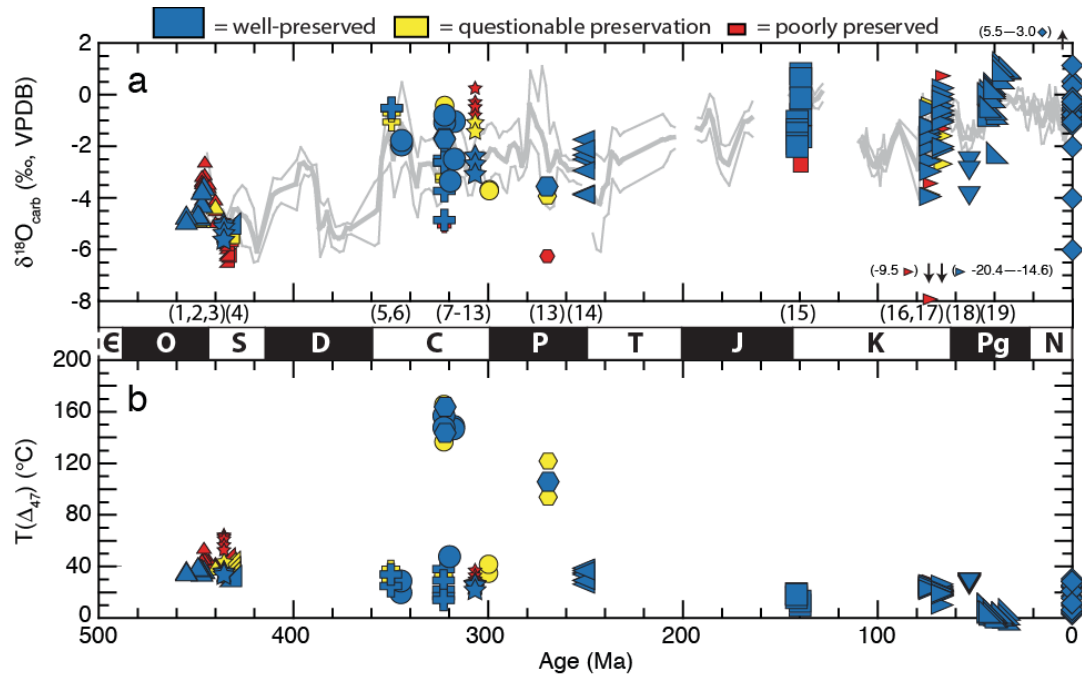


Figure 4.1 Compiled (a) carbonate $\delta^{18}\text{O}$ and (b) clumped isotope paleotemperatures ($T(\Delta_{47})$) from marine brachiopod and mollusk fossils. The thick gray line in (a) is a running average of $\delta^{18}\text{O}$ from tropical/sub-tropical foraminifera, belemnites, and brachiopods from Grossman (2012), with $\pm 1\sigma$ standard deviation indicated by the thin lines. Large blue symbols refer to samples that pass geochemical tests for good preservation. Medium red symbol are of questionable/intermediate preservation based on geochemical tests but still may have been effected by solid state reordering of clumped isotopes following burial, and small yellow symbols represent poorly preserved samples. In some cases smaller symbols are obscured by larger symbols. Individual studies are represented by different symbols: equilateral triangle, Finnegan et al. (2011); star, Came et al. (2007); cross, this study; half-square (diagonal), Cummins et al., (2014); circle, Henkes et al. (2014); polygon, Shenton et al. (*submitted*); left-facing triangle, Brand et al. (2012); square, Price and Passey (2013); right-facing triangle, Dennis et al. (2013); inverted equilateral triangle, Keating-Bitonti et al. (2011); half-square (diagonal),

Douglas et al., (2014); diamonds, Henkes et al. (2013). $T(\Delta_{47})$ precision is typically the width of the blue symbols ($\sim 5\text{-}7\text{ }^{\circ}\text{C}$). The numbers in parentheses underneath (a) correspond to collection localities in Table 4.1.

4.2. Carbonate clumped isotope reordering

Carbonate clumped isotope reordering is a process whereby solid-state diffusion of C and O atoms through the carbonate mineral lattice alters the abundance of $^{13}\text{C}\text{-}^{18}\text{O}$ ‘clumped’ bonds (Dennis and Schrag, 2010; Passey & Henkes, 2012). Although the exact mechanism(s) of reordering is (are) unknown, the process must involve the breakage of existing $^{13}\text{C}\text{-}^{18}\text{O}$ bonds and subsequent formation of $^{12}\text{C}\text{-}^{18}\text{O}$ and $^{13}\text{C}\text{-}^{16}\text{O}$ bonds, with ^{12}C or ^{16}O swapped from neighboring carbonate ions or interstitial spaces. Based on data from laboratory heating experiments Passey and Henkes (2012) determined reordering rates in abiogenic calcite and used a first-order kinetic model to predict these rates as a function of temperature. Henkes et al. (2014) applied the same experimental approach to the study of Late Paleozoic brachiopod calcite, explored alternative kinetic models for the reordering reaction, and used a numerical modeling scheme to predict clumped isotope reordering during the burial and exhumation of brachiopods from several sedimentary basins worldwide. General agreement between predictions of the clumped isotope reordering model and the measured values of Carboniferous brachiopods demonstrate that laboratory-derived kinetics reasonably predict the progress of reordering over geological timescales (Henkes et al., 2014). A similar approach is used here to evaluate the Phanerozoic carbonate clumped isotope record with respect to carbonate clumped isotope reordering.

4.3. Results

4.3.1. Carboniferous brachiopods

New stable isotope data for Carboniferous brachiopods and their limestone matrices are presented in Table A4.1 and shown in Figure 4.1 as part of the Phanerozoic record.

These fossils are from the Kinderhookian-age Gilmore City Formation (~350 Ma) in Iowa, USA (Mii et al., 1999) and the Chesterian-age Tarruskian Horizon (~320 Ma) in the Moscow Basin south of Moscow, Russia (Mii et al., 2001). The average clumped isotope paleotemperatures from well-preserved specimens are 32 °C from the Gilmore City Fm. and 27 °C from the Tarruskian Horizon, with average calculated seawater $\delta^{18}\text{O}$ values of 2.1‰ and -1.7‰, respectively. Their calcite oxygen isotope compositions fall along a running-mean curve representing well-preserved subtropical fossils and thus agree with measured brachiopod values globally for the Carboniferous (Fig. 4.1a; from Grossman, 2012). In general, these shells have excellent petrographic and chemical preservation, as indicated by cathodoluminescence microscopy (i.e., little to no diagenetic uptake of Mn^{2+} from reduced pore waters) and previous trace element analyses (Figs. A4.1-A4.12; Mii et al., 1999, 2001); however, some shells show slight luminescence and are therefore shown as small, yellow symbols in Figure 4.1. While these shells likely have some diagenetic overprinting, their isotopic compositions are within the range of values for nominally pristine samples during the Carboniferous.

4.3.2. Evaluation of clumped isotope reordering

We compiled maximum burial temperature estimates from the literature for each collection locality represented in the Phanerozoic marine carbonate clumped isotope record (Table 4.1). Based on the sample age (t) and maximum burial temperature (T) each sample can be plotted on a diagram (Fig. 4.2) showing the t - T domains where samples will be completely reordered, not reordered (i.e., pristine), and partially reordered (Henkes et al., 2014). By using the maximum burial temperatures and sample ages in Figure 4.2, we are effectively assuming a ‘boxcar’ burial history, where the box width is the sample age and the box height is the maximum burial temperature. This then makes the most restrictive use of the dataset as samples likely did not reside at maximum depth for the entire time since sedimentation until present. This is a conservative approach because it assumes instantaneous rates of burial and exhumation rather than relying on poorly constrained estimates, and because rates and extents of reordering are the greatest at maximum burial temperatures. Using this approach, we discard data from samples from the Phanerozoic record that plot to the right of the 1% curve in Figure 4.2. Importantly, the majority of samples included in the geochemically and physically-screened Phanerozoic record fall well within the domain of no reordering.

Table 4.1 Burial temperature information for the Phanerozoic clumped isotope record

#	Collection Locality (<i>reference</i>)	Age (Ma)	Max. Burial Temp. (°C)	Burial Temperature Reference*	Clumped isotope reordering?
1	Minnesota, USA (<i>Finnegan et al., 2011</i>)	455	<50	Hay et al. (1988) ¹	No
2	Kentucky and Indiana, USA (<i>Finnegan et al., 2011</i>)	447-449	<90	Epstein et al. (1977) ²	No
3	Anticosti Island, Canada (<i>Finnegan et al., 2011; Came et al., 2007</i>)	447-440	<90	Mcracken and Barnes (1981) ²	No

Table 4.1 (cont.)

#	Collection Locality (<i>reference</i>)	Age (Ma)	Max. Burial Temp. (°C)	Burial Temperature Reference*	Clumped isotope reordering?
4	Gotland Island, Sweden (<i>Cummins et al., 2014</i>)	434-430	<50-80	Jeppsson (1983) ²	No
5	Iowa, USA (<i>this study</i>)	350	~50	Kaufmann et al. (1988), Banner and Kaufman (1994) ³	No
6	Missouri, USA (<i>Henkes et al., 2014</i>)	345	~50	Kaufmann et al. (1988), Banner and Kaufman (1994) ³	No
7	Nevada, USA (<i>Henkes et al., 2014</i>)	323	170-180	Martin et al. (2012), Shenton et al. (<i>submitted</i>) ^{2,4}	Yes
8	Moscow Basin, Russia (<i>this study</i>)	320	<80	Alekseev et al. (1996) ²	No
9	Illinois, USA (<i>Henkes et al., 2014</i>)	320	135, 175	Rowan et al. (2002) ⁵	Yes
10	Ural Mountains, Russia (<i>Henkes et al., 2014</i>)	318	>100	Matenaar et al. (2005) ^{2,6}	Yes
11	Oklahoma, USA (<i>Came et al., 2007</i>)	307	<70	Cardott et al. (1990) ⁶	No
12	West Virginia, USA (<i>Henkes et al., 2014</i>)	300	145	Reed et al. (2005) ^{4,6}	Yes
13	Andes, Venezuela (<i>Shenton et al., submitted</i>)	270	150	Callejon et al. (2003) ^{7,8}	Yes
14	Southern Alps, Italy (<i>Brand et al., 2012</i>)	251	100, but ?	Zattin et al. (2006) ⁶	No [†]
15	Siberia, Russia (<i>Price and Passey, 2013</i>)	140	50	Price and Passey (2013) ⁷	No
16	South Dakota, USA (<i>Dennis et al., 2013</i>)	73.5, 67	60-80	Gerhard et al. (1982) ⁷	No
17	Maryland, USA (<i>Dennis et al., 2013</i>)	67	50	Hansen (1969), Minard et al. (1974)	No
18	Alabama, USA (<i>Keating-Bitonti et al., 2011</i>)	53	65	Carroll (1999) ⁶	No
19	Seymour Island, Antarctic Peninsula (<i>Douglas et al., 2014</i>)	45-37.4	<80	Pirrie et al. (1994) ^{6,8}	No

(previous page) *Numbers indicate burial depth/temperature proxy used in each reference: 1=K/Ar dating of authigenic K-feldspar formation (timing of maximum burial), 2=conodont color alteration index, 3=unpublished coal grade and burial history curve cited by these authors, 4=secondary fluid inclusions, 5=predictions from hydrothermal fluid flow model, 6=vitrinite reflectance, 7=sedimentary overburden with assumed geothermal gradient (~25 °C/km), 8=apatite fission track thermochronology. †Conclusion of no clumped isotope reordering is tentative given the collection locality information in Brand et al. (2012) and the complex structure of Permian sediments in the Italian Alps. According to Zattin et al. (2006), vitrinite reflectance values vary from 0.95 to 2.63% within 20 km.

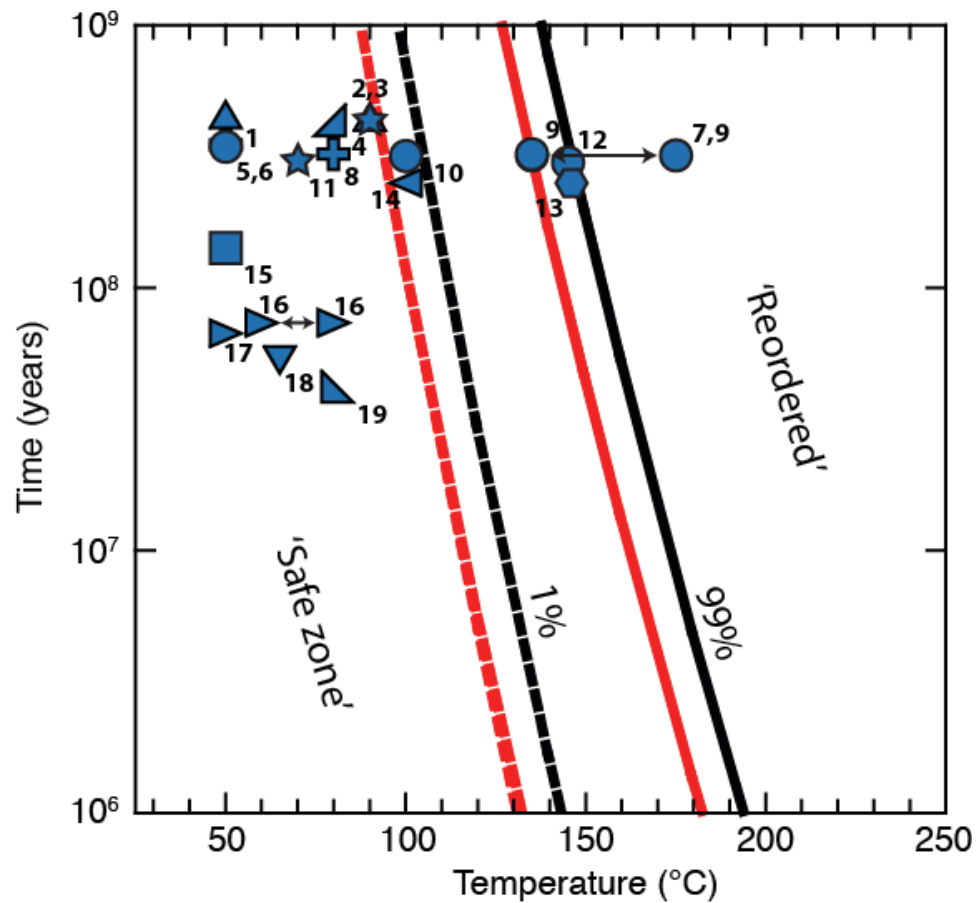


Figure 4.2 (*previous page*) Maximum burial temperature and sample age for each collection locality in the Phanerozoic clumped isotope record. The data symbols are identical to Fig. 4.1 and the numbers (to the lower right of each symbol) correspond to localities in Table 4.1. The lines represent predictions of carbonate clumped isotope reordering using experimentally-derived reaction kinetics for a low-temperature, hydrothermal, optically-pure calcite (black, Passey and Henkes, 2012) and a pristine Permian brachiopod (red, Henkes et al., 2014). The dashed lines represent 1% ‘reordered’ and the solid lines represent 99% reordering. The area between the lines is the zone of partial clumped isotope reordering. For some localities the arrows connecting two points indicate a range of estimated maximum burial temperatures.

4.4. The emerging Phanerozoic record

The screened Phanerozoic clumped isotope paleotemperature record from fossil brachiopods and mollusks is presented in Figure 4.3, as are calculated seawater oxygen isotope compositions from these samples. Note that low-latitude seawater paleotemperatures during some intervals of the Paleozoic were extremely warm (≥ 30 °C), for example across the Ordovician-Silurian boundary and during the early Carboniferous. Most of these brachiopod fossils come from shallow, epicontinental seas and therefore may be best compared with modern analog environments in the western tropical Pacific and the Arabian Peninsula, where summer seawater temperatures regularly reach 28-30 °C and higher (e.g., Boely et al., 1990; Pohl et al., 2014). Paleozoic samples primarily come from low-paleolatitudes, whereas Mesozoic and Cenozoic shells are from temperate and high paleolatitudes. Only when the clumped

isotope temperature record from marine invertebrate shells has been filled out both spatially and temporally, as is approached by the carbonate $\delta^{18}\text{O}$ record (Grossman, 2012), will we be able to fully evaluate the long-term seawater temperature evolution of the oceans. Despite this, the clumped isotope record screened for both chemical alteration and the effects of carbonate clumped isotope reordering nevertheless suggests paleotemperatures approaching 40 °C.

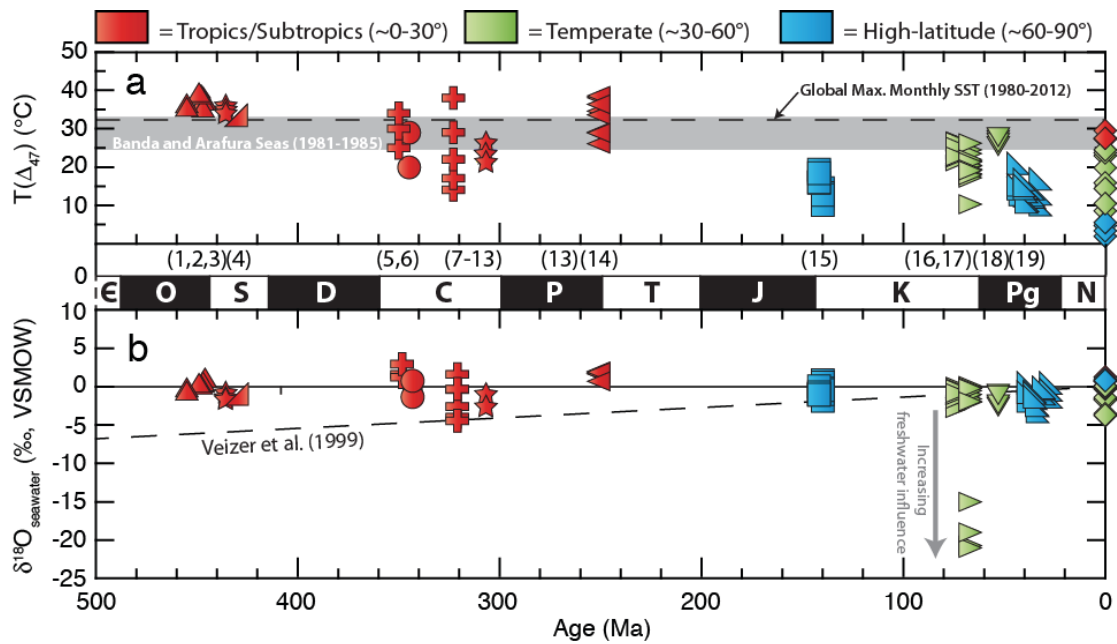


Figure 4.3 Paleotemperatures ($T(\Delta_{47})$) and calculated seawater oxygen isotope compositions ($\delta^{18}\text{O}_{\text{seawater}}$) from clumped isotope and $\delta^{18}\text{O}$ measurements of fossil brachiopod and mollusk shells, after screening for variable chemical and petrographic preservation (Table A4.2, Fig. 4.1) and for carbonate clumped isotope reordering (Table A4.3, Fig. 4.2). Data symbols correspond to studies referenced in Fig. 4.1 and are colored according to the paleolatitudes of each collection locality. For reference in (a) the average global monthly maximum sea surface temperature for the tropics between 1980 and 2012 is shown (dashed line), as well as the range in modern maximum sea

surface temperature in the Banda and Arafura Seas (gray band, modern analogs for ancient epicontinental seas; Boely et al., 1990). In (b) the trend of $\delta^{18}\text{O}$ of seawater proposed by Veizer et al. (1999) is shown by the dashed line. The numbers in parentheses underneath (a) correspond to collection localities in Table 4.1.

One issue of note in these paleotemperature determinations is the temperature range for which the carbonate clumped isotope paleothermometer was defined. For mollusk and brachiopod shells, the modern calibration data do not exceed 30 °C (Henkes et al., 2013; Eagle et al., 2013; Came et al., 2014), which may lead to larger uncertainty in calculated temperatures from relatively low Δ_{47} values ($<0.70\text{‰}$, but $>0.65\text{‰}$) corresponding to hot paleotemperatures in the Paleozoic. The problem of extrapolating paleothermometers outside their modern calibration temperature ranges is not unique to clumped isotopes. The proxy data suggesting extremely hot tropical temperatures during the Eocene (Pearson et al., 2007), mid-Cretaceous (Forster et al., 2007), and Paleozoic (Joachimski et al., 2009) raises similar concerns (Huber and Caballero, 2011), and together with these clumped isotope data highlight the need to refine calibrations for interpreting controversial paleotemperature proxy data.

Perhaps more striking than the emerging Phanerozoic seawater temperature trend is the nearly constant seawater $\delta^{18}\text{O}$ values calculated from these samples, notably the clustering of values around 0‰ since the Late Ordovician-Early Silurian (~450 million years ago). This observation disregards the Cretaceous Western Interior Seaway samples from Dennis et al. (2013) that exhibit possible freshwater influence (Fig. 4.3b).

Interpretation of this long-term $\delta^{18}\text{O}$ record simultaneously requires a congruent explanation for the observed range of the data clustered around near-modern seawater $\delta^{18}\text{O}$ values ($\pm 2\text{-}3\text{‰}$). We believe that this could reflect the influence of climatological or local environmental changes, which occur at timescales well below our sampling resolution. For example, to explain high $\delta^{18}\text{O}$ values for Early Carboniferous brachiopods from the North American midcontinental seas, Grossman et al. (2008) argue for intense evaporation as evidenced by laterally extensive evaporate deposits in the region (Iowa and Missouri samples in Fig. 4.3; this study and Henkes et al., 2014). This is a tenable scenario for seawater $\delta^{18}\text{O}$ variation in Figure 4.3 considering observed enrichments in modern, low-latitude closed basin seawaters (e.g., $\sim +2\text{‰}$ in the Mediterranean Sea; LeGrande and Schmidt, 2006). The waxing and waning of continental glaciers, especially across at the Ordovician-Silurian boundary and during the Late Paleozoic greenhouse-icehouse transition, is also a suspected driver of 1-2‰ changes in global seawater $\delta^{18}\text{O}$ values at both high and low frequencies (Grossman et al., 2008; Finnegan et al., 2011), and finally, we cannot rule out the effects of fluid-rock oxygen exchange in oceanic crust causing $\pm 1\text{‰}$ changes on million year timescales (Muehlenbachs and Clayton, 1976).

In conclusion, there are now a sufficient number of published carbonate clumped isotope datasets from marine biogenic carbonates to piece together a preliminary revision of the Phanerozoic paleotemperature and seawater $\delta^{18}\text{O}$ record. While uncertainties in clumped isotope temperature calibration and questions about the interpretation of extremely warm paleotropical seas remain, we believe we are now able to effectively remove from the

overall record (Fig. 4.1b) the effects of (1) chemical diagenesis, from geochemical and petrographic tests, and (2) carbonate clumped isotope reordering, given the recent evaluations of the controls on clumped isotope reordering (Passey and Henkes, 2012; Henkes et al., 2014). Future paleoclimate studies using fossil carbonates must carefully consider the effects of bond reordering on the preservation of primary clumped isotope temperatures, and continued analysis of texturally- and chemically-preserved Paleozoic and Mesozoic mollusks and brachiopods will further test the fidelity of our conclusion that seawater oxygen isotope compositions have not changed, on average, over the last 450 million years.

5. SUMMARY AND CONCLUSIONS

This research, along with the growing body of literature and datasets produced from other carbonate clumped isotope laboratories, serves to improve our understanding of mollusk and brachiopod shell-based clumped isotope thermometry. As emphasized throughout this dissertation, this method of determining ancient seawater temperatures and oxygen isotope compositions shows promise for resolving the deep-time paleoclimate record, notably in the Paleozoic and Mesozoic, where the hypothesized temperature changes are commensurate with the current precision of the measurement ($\sim\pm 3\text{-}5^\circ\text{C}$) and the isotopic composition of seawater is largely unconstrained. As documented in each chapter, successful application of carbonate clumped isotope thermometry is contingent on 1) empirical and experimental temperature calibration using modern carbonates, biogenic and inorganic, with universal interlaboratory agreement, 2) a working understanding of C-O bond reordering constrained by laboratory-derived kinetics and predictive models for geologic samples, and 3) reconciling the emerging Phanerozoic record with our current understanding of the thermal structure of Earth's ancient oceans, especially the tropics, and the geochemical processes which control the oxygen isotope values of the ocean over long timescales.

In Chapter 2 a carbonate clumped isotope temperature calibration using modern mollusk and brachiopod shell carbonate is presented. The observed calibration line is striking in that it has a slope approximately half of previous clumped isotope calibrations using modern biogenic and inorganic carbonates. The discussion of the mollusk and brachiopod data included evaluating some of the aspects of shell formation, such as

incorporation of amorphous calcium carbonate and taxonomic differences in the chemistry of the precipitating fluids, none of which are concluded to have a significant effect on clumped isotopes in these samples. Differences in clumped isotope composition between dissolved inorganic carbon species in body fluids are also explored as a possible explanation for the shallower calibration slope, but are untenable given the bulk carbon and oxygen isotope composition of these shells. Since the completion of this research and its publication, differences among various clumped isotope calibrations has received much attention in the clumped isotope research community. Methodological differences are a compelling explanation for calibration discrepancies. Newer laboratory methods and data standardization schemes indicated that the slope of the Δ_{47} -temperature relationship appears to be dependent on the temperature and manner of carbonate acid digestion (e.g., Wacker et al., 2013; Fernandez et al., 2014). Future studies and interlaboratory tests of carbonate standards should provide further clarity on these issues. Nevertheless, problems with proxy calibration and establishing laboratory best practices are not challenges unique to clumped isotopes, and will co-evolve with application of this thermometer to scientific questions.

Chapter 3 presented a laboratory and empirical study of carbonate clumped isotope bond reordering in brachiopod shell calcite, following the methods and theory developed in Passey and Henkes (2012). There are now experimental constraints on C-O bond reordering kinetics for several calcites and two models for the observed Δ_{47} changes during the laboratory heating experiments, one that assumes first-order reaction kinetics and one that does not. Regardless of the kinetic models used, the predictions from the

data are the nearly same: the effects of clumped isotope reordering are insignificant below temperatures of ~ 100 °C on geologic timescales. This conclusion bears on the preservation of primary paleotemperatures from carbonates precipitated at Earth surface conditions (e.g., shells), but perhaps more importantly allows prediction of the extent of reordering when minerals experience temperatures above 100 °C during deep sedimentary burial. Results demonstrate the potential of carbonate clumped isotope thermometry in quantitatively constraining burial histories of sedimentary basins at >2 -3 km in the continental crust. This application may be seen as an improvement on existing semi-quantitative thermal maturity proxies commonly used to constrain the formation of oil, gas, and coal. The predictive clumped isotope reordering models may also be employed to screen the sedimentary record for collection localities suitable (or not) for paleoclimate studies. Future research on C-O bond reordering in carbonates should focus on whether or not calcites have a universal ‘susceptibility’ to this phenomenon, as well as elucidating the mechanism(s) that control the breakage and reforming of ^{13}C - ^{18}O clumped bonds in the solid mineral lattice.

Finally, in Chapter 4 a compiled and critically evaluated the Phanerozoic clumped isotope record for reconstructing global seawater paleotemperatures and oxygen isotope compositions. The emerging record suggests trends that are contrary to convention (e.g., Paleozoic temperatures as high as 35 °C in the tropics) and supports the hypothesis that seawater $\delta^{18}\text{O}$ has, on average, not varied from modern values of $\sim 0 \pm 2$ -3‰ over the last ~ 450 million years. Future studies of samples that are well preserved both chemically and with respect to clumped isotope reordering, shells test and refine these observations.

APPENDICES

A2.1 X-ray diffraction data for mollusk shells

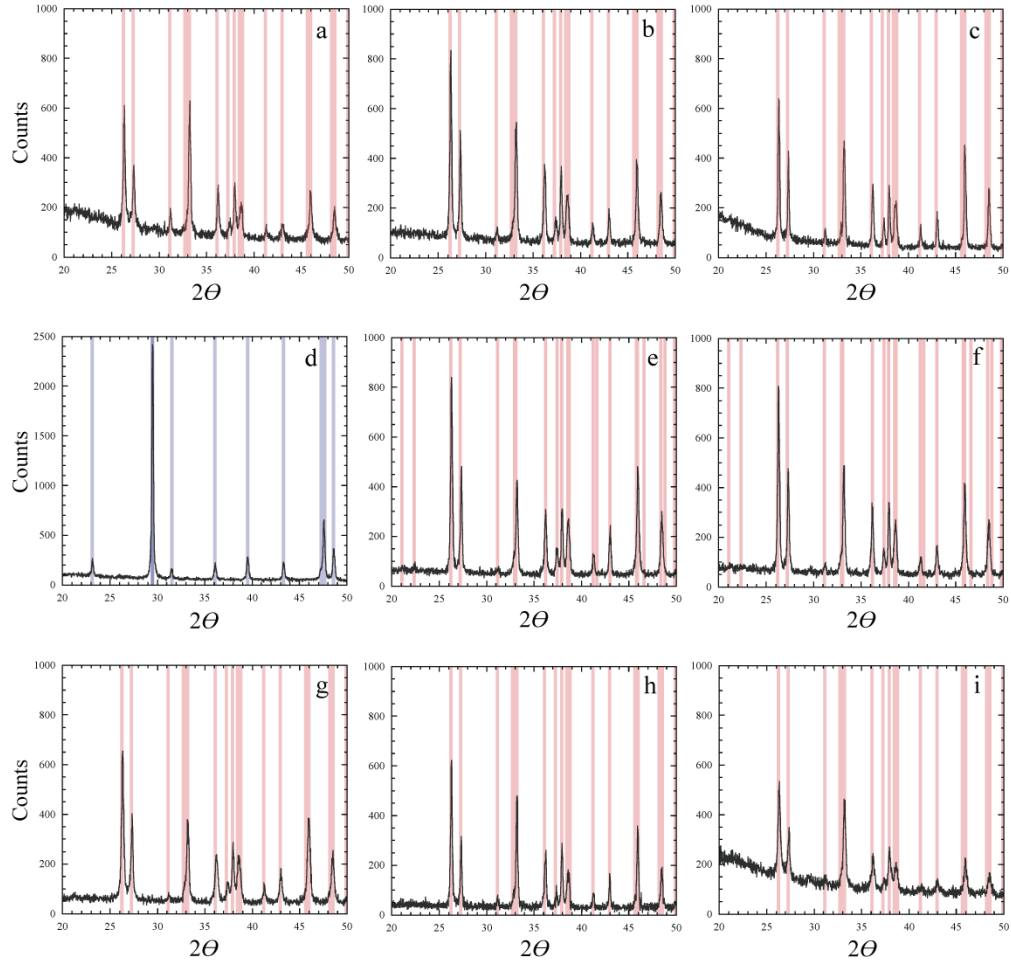


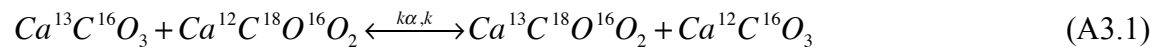
Figure A1.1 X-ray diffraction spectra generated from the shells of a) *Nautilus pompilius*, b) *Hiatella arctica*, c) *Mya truncata*, d) *Chlamys islandica*, e) *Astarte crenata*, f) *Astarte borealis*, g) *Clinocardium ciliatum*, h) *Phacoides pectinata*, and i) *Mya arenaria*. Peaks were qualitatively identified using the Phillips X'Pert Highscore software references for aragonite (red, #24-0025 for a-c, g-i and #76-0606 for e,f) and calcite (blue, #89-1304 for d).

A2.2 Supplementary data table for modern mollusk and brachiopod analyses

(Table A2.2, *see supplemental files*)

A3.1 Derivation of the transient defect/equilibrium defect model

Here we provide a full derivation of the ‘transient defect/equilibrium defect’ model for carbonate clumped isotope reordering as an alternative explanation (to the ‘first-order approximation’ model in Section 3.3.3) for the experimental observations in Fig. 3.3a and d. We can start with a more complete form of Eq. (3.1) to describe the reordering reaction:



where the reaction from left to right corresponds to the ordering reaction, and from right to left is the disordering reaction. For simplicity, we denote the species in Eq. (A3.1) as (from left to right) 61, 62, 63, and 60, in reference to the mass numbers of the carbonate ion in each species. Also, for simplicity we do not explicitly include ^{17}O and the isotopologues $Ca^{12}C^{17}O^{18}O^{16}O$, $Ca^{13}C^{16}O^{17}O_2$, and $Ca^{12}C^{17}O_3$, which together comprise only about 6.5% of mass 63 isotopologues (Ghosh et al. 2006a). The following derivation is based largely on Criss’ (1999, p. 140–142) treatment for the kinetics of isotopic exchange. The rate of change of the clumped species (mass 63) can be written as:

$$\frac{d63}{dt} = k\alpha[61][62] - k[63][60] \quad (A3.2)$$

where the brackets denote fractional abundances ($[60] + [61] + [62] + [63] \approx 1$). Note that at equilibrium, the left term becomes zero, and α is the equilibrium constant:

$$\alpha_{eq} = \frac{[63]_{eq}[60]_{eq}}{[61]_{eq}[62]_{eq}} \quad (A3.3)$$

The isotopologue ratios normalized to mass 60 are:

$$R^{63} = \frac{[63]}{[60]}, R^{62} = \frac{[62]}{[60]}, R^{61} = \frac{[61]}{[60]} \quad (\text{A3.4})$$

Combining (A3.2) and (A3.4) yields:

$$\frac{d63}{dt} = k\alpha R^{61} R^{62} [60]^2 - kR^{63} [60]^2 \quad (\text{A3.5a})$$

Since the concentration of mass 60 is essentially constant, $[60]^2$ is constant and can be subsumed into k , so:

$$\frac{d63}{dt} = k(\alpha R^{61} R^{62} - R^{63}) \quad (\text{A3.5b})$$

Differentiation of R^{63} yields:

$$dR^{63} = \frac{d[63]}{[60]} - \frac{[63]d[60]}{[60]^2} \quad (\text{A3.6a})$$

Because $[63]$ is very small ($\sim 6.5 \times 10^{-5}$), and $d[60] = d[63]$ (from Eq. (A3.1)) and $[60]$ is close to 1, the second term on the right side is negligible compared to the first term on the right side. Thus:

$$dR^{63} = \frac{d[63]}{[60]} \quad (\text{A3.6b})$$

Combining (A3.5b) and (A3.6b), and subsuming $[60]$ into the rate constant, yields:

$$dR^{63} = -k(R^{63} - \alpha R^{61} R^{62})dt \quad (\text{A3.7})$$

In a closed system, variation in R^{63} is due solely to deviation of R^{63} from the stochastic prediction. The natural range of this deviation is on the order of 1.5‰ (Eiler and Schauble, 2004), which corresponds to a change of 0.0001‰ (0.1 ppm) in the absolute abundance of mass 63 carbonate. According to Eq. (A3.1), the corresponding change in

mass 61 and 62 carbonate is the same (~ 0.1 ppm), which amounts to $\sim 0.009\%$ and $\sim 0.016\%$ changes in R^{61} and R^{62} , respectively. Thus, compared to changes in R^{63} , changes in R^{61} and R^{62} due to reordering reactions are negligible, and we can approximate these ratios as their equilibrium values. Combining (A3.7) and (A3.3) thus yields:

$$dR^{63} = -k(R^{63} - R_{eq}^{63})dt \quad (\text{A3.8})$$

where R_{eq}^{63} is the R^{63} ratio at thermodynamic equilibrium, and is therefore constant at any given temperature.

To account for the rapid initial reaction observed in the experimental data, we propose that the rate constant k is related to (1) a time-invariant pool of equilibrium defects of concentration D_c with an ability to effect C–O bond reordering (represented by k_c), and (2) a pool of transient defects of concentration D_d that decreases with time due to defect annealing, trapping, or other means of deactivation, with an ability to effect C–O bond reordering indicated by k_d . Thus equation A3.8 can be recast as:

$$\frac{dR^{63}}{R^{63} - R_{eq}^{63}} = -(k_c D_c + k_d D_d)dt \quad (\text{A3.9})$$

Since D_c is constant, it can be subsumed into the rate constant k_c of the equilibrium defect pool. D_d is not constant, and although other models are imaginable, we assume that the rate of defect disappearance is proportional to the concentration of defects:

$$D_d = D_0 e^{-k_2 t} \quad (\text{A3.10})$$

where D_0 is the initial defect concentration, and k_2 is a rate constant describing the loss of defects with time. Since D_0 is constant, it can be subsumed into k_d , and therefore:

$$\frac{dR^{63}}{R^{63} - R_{eq}^{63}} = -(k_c + k_d e^{-k_2 t}) dt \quad (A3.11)$$

Integration yields:

$$\ln(R_t^{63} - R_{eq}^{63}) = -k_c t + \frac{k_d}{k_c} e^{-k_2 t} + C \quad (A3.12)$$

At $t = 0$, $R_t^{63} = R_{init}^{63}$, the initial R^{63} of the sample, and therefore:

$$\ln(R_{init}^{63} - R_{eq}^{63}) = \frac{k_d}{k_c} e^{-k_2 t} + C \quad (A3.13)$$

Combining Eqs. (A3.12) and (A3.13) yields:

$$\ln\left(\frac{R_t^{63} - R_{eq}^{63}}{R_{init}^{63} - R_{eq}^{63}}\right) = -k_c t + \frac{k_d}{k_c} (e^{-k_2 t} - 1) \quad (A3.14)$$

which is approximately equivalent to (see Passey and Henkes, 2012, Appendix A):

$$\ln\left(\frac{\Delta_{47}^t - \Delta_{47}^{eq}}{\Delta_{47}^{init} - \Delta_{47}^{eq}}\right) = -k_c t + \frac{k_d}{k_c} (e^{-k_2 t} - 1) \quad (A3.15)$$

All of the parameters on the left side of the equation can be determined by mass spectrometry (or provisionally inferred from theory in the case of Δ_{47}^{eq}), leaving the parameters k_c , k_d , and k_2 as unknowns.

A3.2 Determination of rate constants in the transient defect/equilibrium defect model

As shown by Eq. (A3.15), the carbonate clumped isotope reordering reaction progress for any temperature is related to three rates constants: k_c , k_d , and k_2 . Here we describe an inverse ‘curve-stripping’ procedure for determining these rate constants that is analogous to the approach used to identify different half-lives in mixtures of radioisotopes

(Friedlander et al., 1981; see also Appendix B of Passey and Henkes, 2012). For convenience, we define a reaction progress term $\ln(1 - F)$ as:

$$\ln(1 - F) = \ln\left(\frac{\Delta_{47}^t - \Delta_{47}^{eq}}{\Delta_{47}^{init} - \Delta_{47}^{eq}}\right) = -k_c t + \frac{k_d}{k_c} (e^{-k_2 t} - 1) \quad (\text{A3.16})$$

In the case where $k_2 \gg k_c$, the term $e^{-k_2 t}$ becomes negligible at long times t , and Eq.

(A3.1) reduces to:

$$\ln(1 - F) = -k_c t + \frac{k_d}{k_c} \quad (\text{A3.17})$$

Therefore a plot of $\ln(1 - F)$ versus t will produce straight line arrays whose slope correspond to the temperature-dependent values of $-k_c$, and whose intercepts equal $-k_d/k_2$. Fig. A3.1a shows that this is true for WA-CB-13 at the experimental temperatures, indicating that $k_2 \gg k_c$ for this material. Note that while the mathematics differ, procedurally this is equivalent to the regressions in the first-order approximation model (Fig. 3.3a and b; see also Passey and Henkes, 2012).

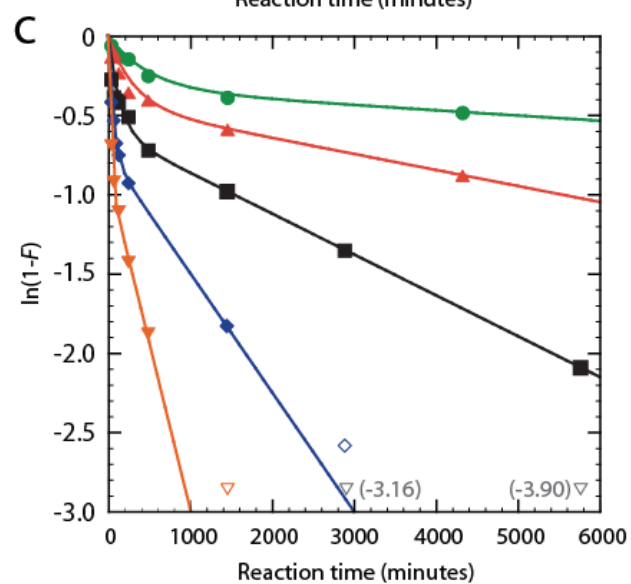
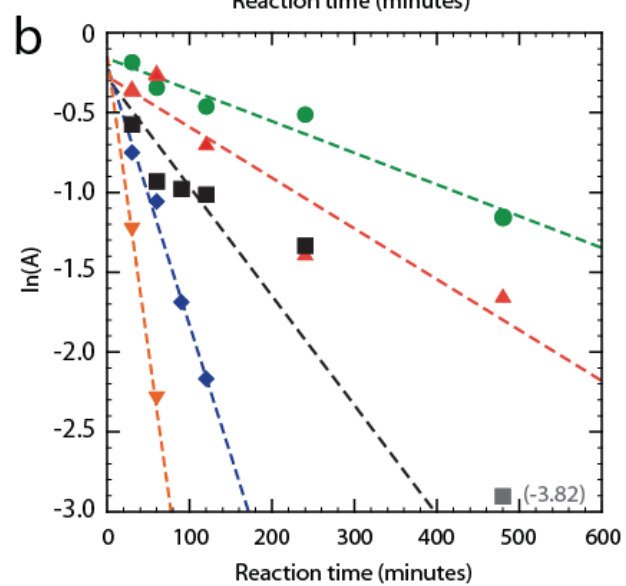
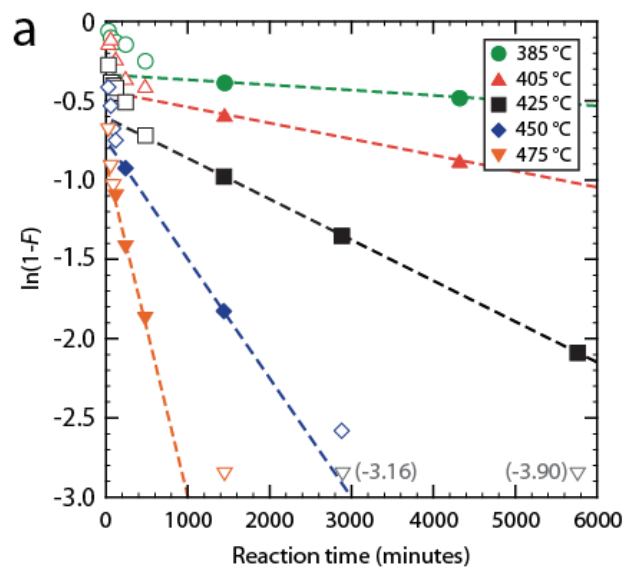


Figure A3.1 (*previous page*) The scheme for determining reaction rates constants for the transient defect/equilibrium defect model. (a) First-order reaction progress (i.e., equilibrium defect pool) and best-fit linear regressions plotted as a function of time. Empty symbols, which mostly represent early, non-first-order samples, are not included in the regressions. The temperatures of the heating experiments are indicated. Gray inverted triangle symbols for the 475 °C reaction plot off-axis and closely approach equilibrium, and thus are not suitable for inclusion in the regression. (b) Reaction progress of the early, non-first order data that represent the annealable transient defect pool. (c) Reaction progress data plotted with the full solutions to the transient defect/equilibrium defect model (Eq. (3.15), solid lines) for each experimental temperature.

In practice, when selecting the points to define the equilibrium defect (linear) behavior, it is important to consider that some points at earlier times t may still reflect the evolving contribution of the transient pool of defects (i.e., when the transient pool is active), and thus should not be included in the regression (Fig. A3.1a). Conversely, at very long experimental times t and high temperatures T the Δ_{47} values may approach the equilibrium Δ_{47} composition, where analytical error has an increasingly large influence in the error of calculated $\ln(1-F)$ values (gray data in Fig. A3.1a). Thus, it is important to establish a cut-off value for $\ln(1 - F)$ below which values are excluded from the regression. Admittedly, selection of a cut-off value is somewhat arbitrary, but here we use a value of -2.5 , which corresponds to the approximate $\ln(1 - F)$ for a sample with $\Delta_{47} = \Delta_{47}^{equil} + 1\sigma$ (where 1σ is the analytical precision). We note that the exact value of

Δ_{47}^{equil} used is dependent on the experimental temperature, so the exact $\ln(1 - F)$ value will vary slightly.

With values of k_c and k_d/k_2 determined, the influence of the k_c pool is then added back to each data point, resulting in the quantity $\ln(1 - F)'$:

$$\ln(1 - F)' = \ln(1 - F) + k_c t = \frac{k_d}{k_c} (e^{-k_2 t} - 1) \quad (A3.18)$$

Simply stated, $\ln(1 - F)'$ represents the progress of reordering due only to the transient defect pool. Eq. (A3.3) can be rearranged to solve for k_2 in terms of $\ln(1 - F)'$ and the ratio k_d/k_2 :

$$k_2 t = -\ln \left[\frac{k_2}{k_d} \left(\ln(1 - F)' + \frac{k_d}{k_2} \right) \right] = -\ln(A) \quad (A3.19)$$

where A is substituted for the terms inside the brackets. Therefore, a plot of $\ln(A)$ versus t will produce straight line arrays whose slopes correspond to the temperature-dependent values of $-k_2$ (Fig. A3.1b). Values of k_d are calculated using k_2 values and the ratio k_d/k_2 . Finally, the Arrhenius relation (Eq. (3.3)) is used to determine the activation energies and frequency factors of each component. Table A3.1 summarizes the rate constants and Arrhenius parameters determined for WA-CB-13, the Permian brachiopod calcite, and Table A3.2 summarizes the rate constants and Arrhenius parameter determined for MGB-CC-1, an optical calcite from Passey and Henkes (2012).

Table A3.1 Rate constants and Arrhenius parameters determined for the transient defect/equilibrium defect model using the Permian brachiopod calcite WA-CB-13.

Reaction T (°C)	Slope ($=-k_c$) (s^{-1})	Intercept	R^2	SRX Points Used
<i>Equilibrium defect component</i>				
385	-5.48×10^{-7}	-0.34	-	037, 042
405	-1.68×10^{-6}	-0.44	-	041, 044
425	-4.29×10^{-6}	-0.61	1.00	012, 013, 014
450	-1.25×10^{-5}	-0.74	-	020, 031
475	-3.50×10^{-5}	-0.87	0.99	017, 021, 029
k_c Arrhenius parameters: $E_a = 187.6 \pm 2.7$ kJ/mol $K_0 = 4.5 \times 10^8$ [$\{+27.14/-1.1\} \times 10^9$] s^{-1} , $R^2=0.999$				
<i>Transient defect component</i>				
385	-3.30×10^{-5}	-0.16	0.95	034, 036, 040, 043, 047
405	-5.30×10^{-5}	-0.27	0.88	033, 035, 038, 045, 046
425	-1.14×10^{-4}	-0.28	0.93	006, 007, 008, 009, 010, 011
450	-2.71×10^{-4}	-0.19	0.98	019, 023, 025, 032
475	-6.14×10^{-4}	-0.11	1.00	016, 026, 027
k_d Arrhenius parameters: $E_a = 180.0 \pm 5.7$ kJ/mol $K_0 = 2.0 \times 10^9$ [$\{+34.5/-8.1\} \times 10^8$] s^{-1} , $R^2=0.997$				
k_2 Arrhenius parameters: $E_a = 136.1 \pm 3.7$ kJ/mol $K_0 = 1.8 \times 10^6$ [$\{+13.1/-7.2\} \times 10^8$] s^{-1} , $R^2=0.993$				
<i>Note:</i> \pm values are the standard errors of error weighted, best-fit linear regressions using the statistical software package JMP.				

Table A3.2 Rate constants and Arrhenius parameters determined for the transient defect/equilibrium defect model using the optical calcite MGB-CC-1.

Reaction T (°C)	Slope ($=-k_c$) (s^{-1})	Intercept	R^2	'RDX' Points Used*
<i>Equilibrium defect component</i>				
385	-3.18×10^{-7}	-0.27	-	037, 042
405	-1.40×10^{-6}	-0.32	0.99	169, 173, 177
425	-2.00×10^{-6}	-0.59	0.97	149, 150, 151, 153
450	-7.95×10^{-6}	-0.88	0.91	144, 145, 147, 148
475	-2.98×10^{-5}	-0.79	0.97	112, 113, 114, 115
k_c Arrhenius parameters: $E_a = 196.6 \pm 19.1$ kJ/mol $K_0 = 1.4 \times 10^9$ [$\{+37/-1.3\} \times 10^9$] s^{-1} , $R^2=0.97$				
<i>Transient defect component</i>				
385	-4.43×10^{-5}	-0.31	0.47	182, 183, 185, 187
405	-7.68×10^{-5}	-0.30	0.76	168, 171, 175, 176, 178, 179
425	-7.07×10^{-5}	-0.46	0.55	152, 154, 166, 167, 170, 172, 174
450	-1.29×10^{-4}	-0.33	-	143, 146
k_d Arrhenius parameters: $E_a = 133.3 \pm 11.9$ kJ/mol $K_0 = 4.5 \times 10^5$ [$\{+30.8/-3.9\} \times 10^5$] s^{-1} , $R^2=0.999$				
k_2 Arrhenius parameters: $E_a = 47.9 \pm 21.2$ kJ/mol $K_0 = 3.2 \times 10^{-1}$ [$\{+1.3/-0.3\} \times 10^1$] s^{-1} , $R^2=0.940$				

Note: \pm values are the standard errors of error weighted, best-fit linear regressions using the statistical software package JMP.

*Stable isotope data from Passey and Henkes (2012).

From Table A3.1 and Table A3.2 it can be seen that the regressions for the k_c component are generally good, however, for WA-CB-13 many of the regressions are only defined by two points. Regressions for the k_2 component are excellent for WA-CB-13, but much less so for MGB-CC-1. In future experiments these uncertainties may be remedied by further experimentation, particularly in the early and late t range, and greater analytical replication (i.e., $n > 1-2$, Table A3.5). Also troubling is the fact that while equation ?.4 predicts that the intercept of $\ln(A)$ versus t should be zero, we observe intercepts as low as -0.5 (Table A3.1 and Table A3.2, Fig. A3.1b). This may indicate the presence of an additional, unrecognized reordering component accounting for $\sim 5-10\%$ of the total reordering signal.

Finally, Fig. A3.1c shows that the forward model based on the derived Arrhenius parameters (Eq. (A3.15)) closely reproduces the observed data for WA-CB-13, with the exception of some data-model mismatch in the earliest reaction. This may be related to the non-zero intercept in the $\ln(A)$ versus t regressions. Nevertheless, we view the model as being successful at predicting the observed reordering behavior.

A3.3 Brachiopod petrographic screening images and limestone matrix isotopic data

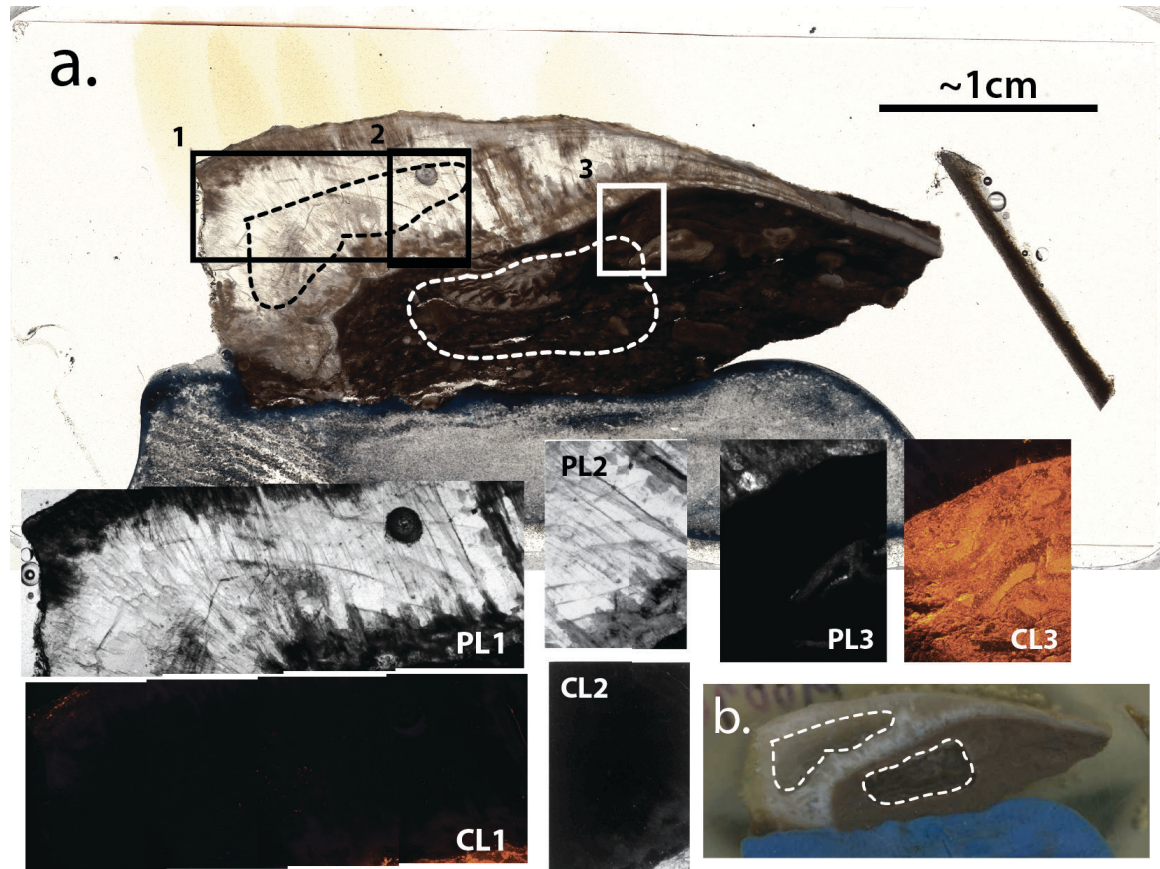


Figure A3.2. Scanned thin section (a.) and billet (b.) of brachiopod sample MO074 (cross-sectional view). Collection and taxonomic information is listed in Table 3.1. In a. and b. the areas inside the dashed lines are the regions of shell (translucent material) and limestone matrix (opaque material) sub-sampled for carbonate clumped isotope analysis. The white and black outlined boxes in a. correspond to the plane polarized light (‘PL’) and cathodoluminescence (‘CL’) photomicrographs from Mii et al. (1999) (PL2 & CL2) and this study (PL1 & CL1, PL3 & CL3). PL1 and CL1 are photomicrograph mosaics each composed of 4 overlapping images. The dark, circular area inside the black outlined boxes in a. and in PL1 is the sub-sampled region of Mii et al. (1999).

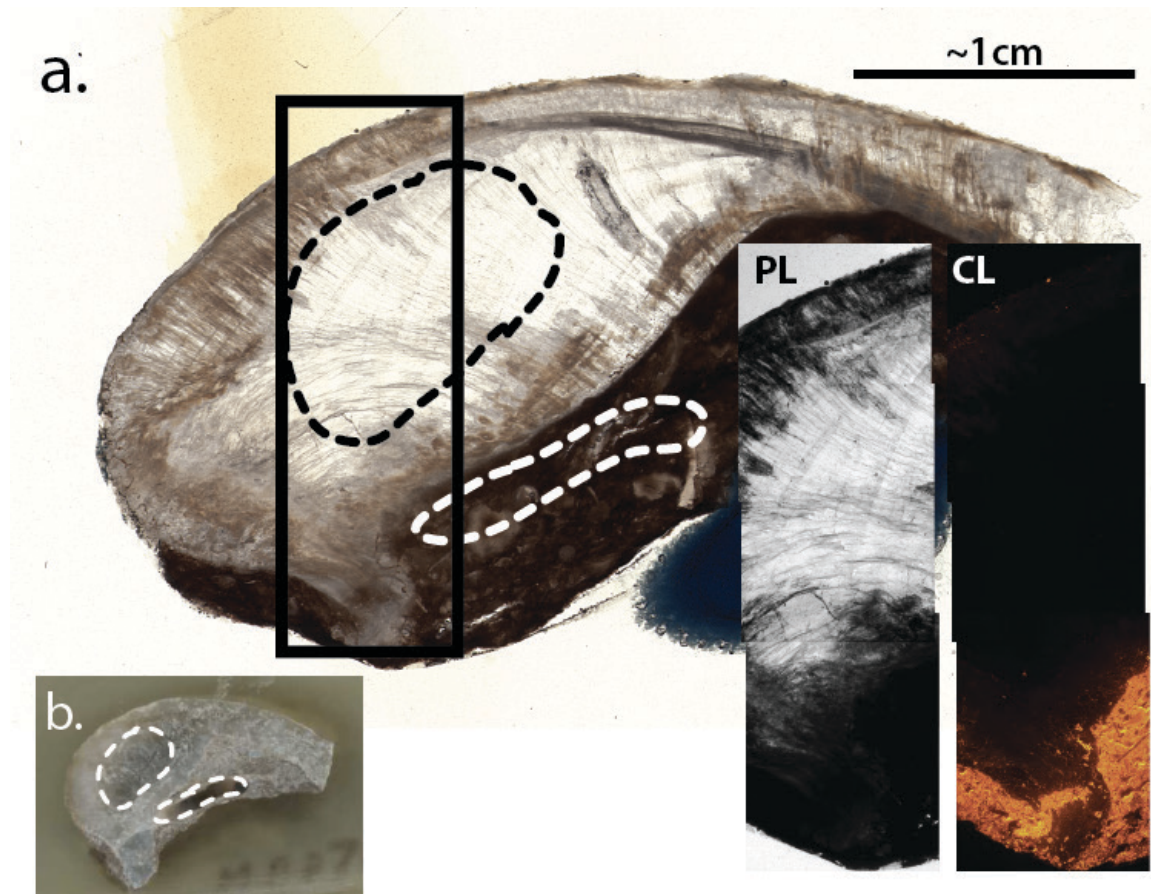


Figure A3.3. Scanned thin section (a.), sample billet (b.), and photomicrograph mosaics for brachiopod shell MO076 (cross-sectional view). Collection and taxonomic information is listed in Table 3.1. The black box in a. corresponds to the photomicrograph images in the lower right corner. “PL” stands for plane-polarized light and “CL” for cathodoluminescence microscopy. MO076 represents a typical non-luminescent shell (Table 3.1). The sample billet (b.) was scanned after sub-sampling from the areas highlighted by the dotted lines. Both shell and micritic limestone matrix were sampled.

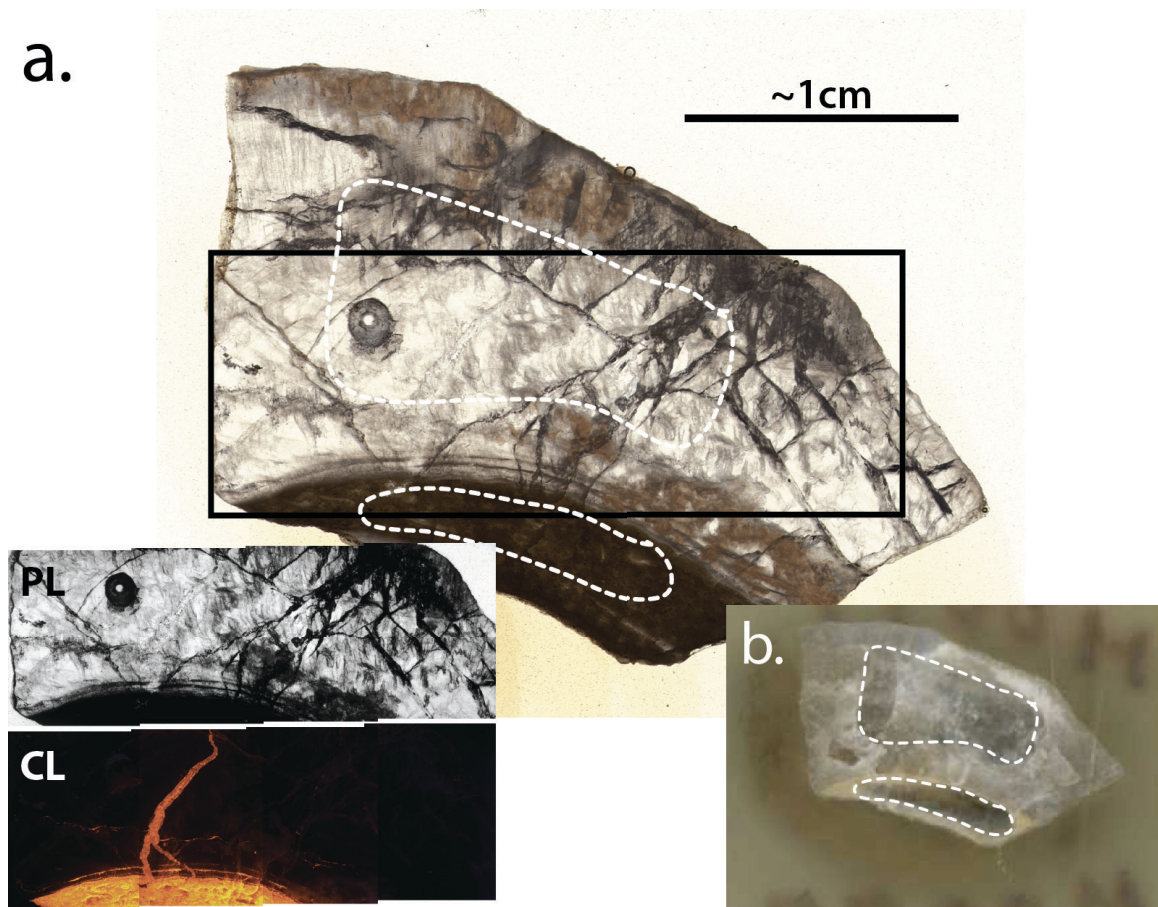


Figure A3.4. Scanned thin section (a.) and billet (b.) of brachiopod sample MO077 (cross-sectional view). Collection and taxonomic information is listed in Table 3.1. In a. and b. the areas inside the dashed lines are the regions of shell (translucent material) and limestone matrix (opaque material) sub-sampled for carbonate clumped isotope analysis. The black outlined box in a. corresponds to the plane polarized light ('PL') and cathodoluminescence ('CL') photomicrographs shown in the lower left corner. PL and CL are photomicrograph mosaics each composed of 4 overlapping images. The dark, circular area inside the black outlined boxes in a. and in PL is the sub-sampled region of Mii et al. (1999).

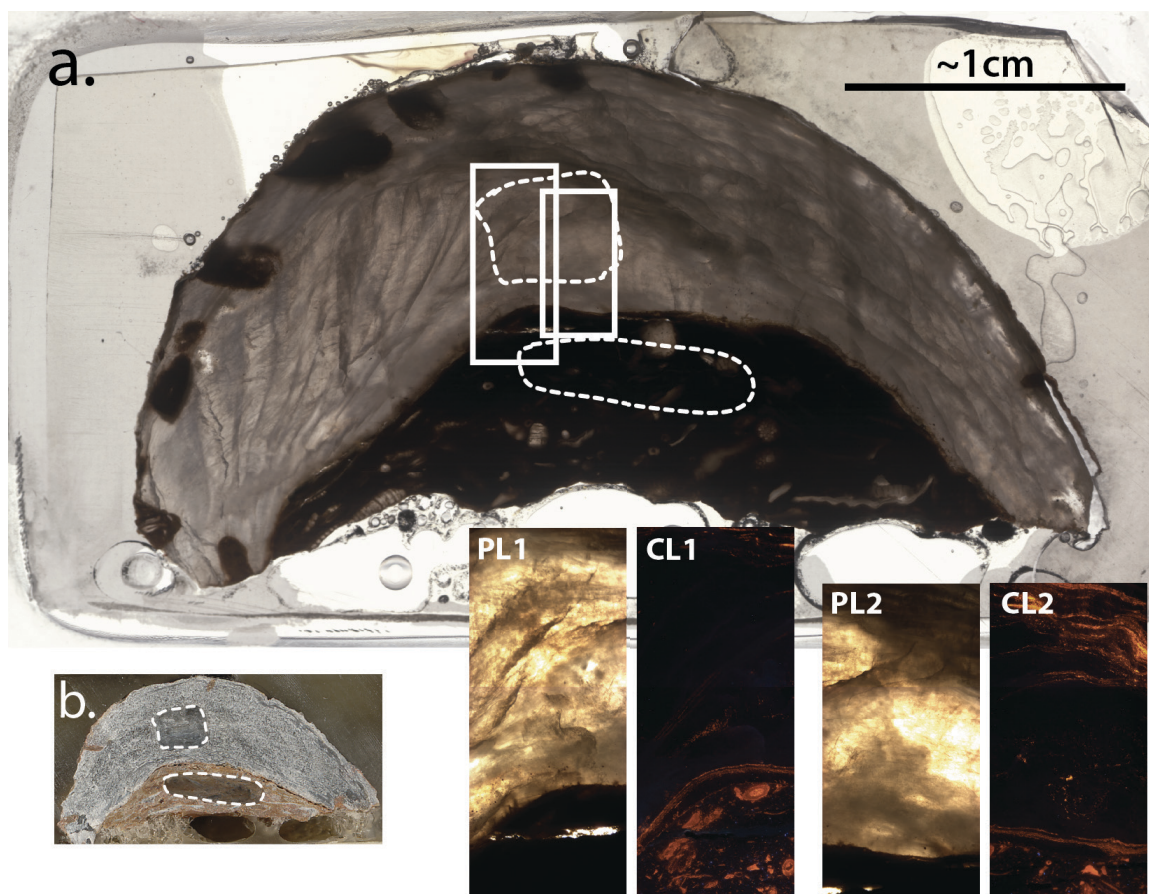


Figure A3.5. Scanned thin section (a.) and billet (b.) of brachiopod sample NV008 (cross-sectional view). Collection and taxonomic information is listed in Table 3.1. In a. and b. the areas inside the dashed lines are the regions of shell (translucent material) and limestone matrix (opaque material) sub-sampled for carbonate clumped isotope analysis. The white boxes in a. correspond to the plane polarized light (‘PL’) and cathodoluminescence (‘CL’) photomicrographs shown in the lower right corner. PL1 and CL1 are photomicrograph mosaics each composed of 3 overlapping images. PL2 and CL2 are also photomicrograph mosaics, but each are composed of only 2 overlapping images.

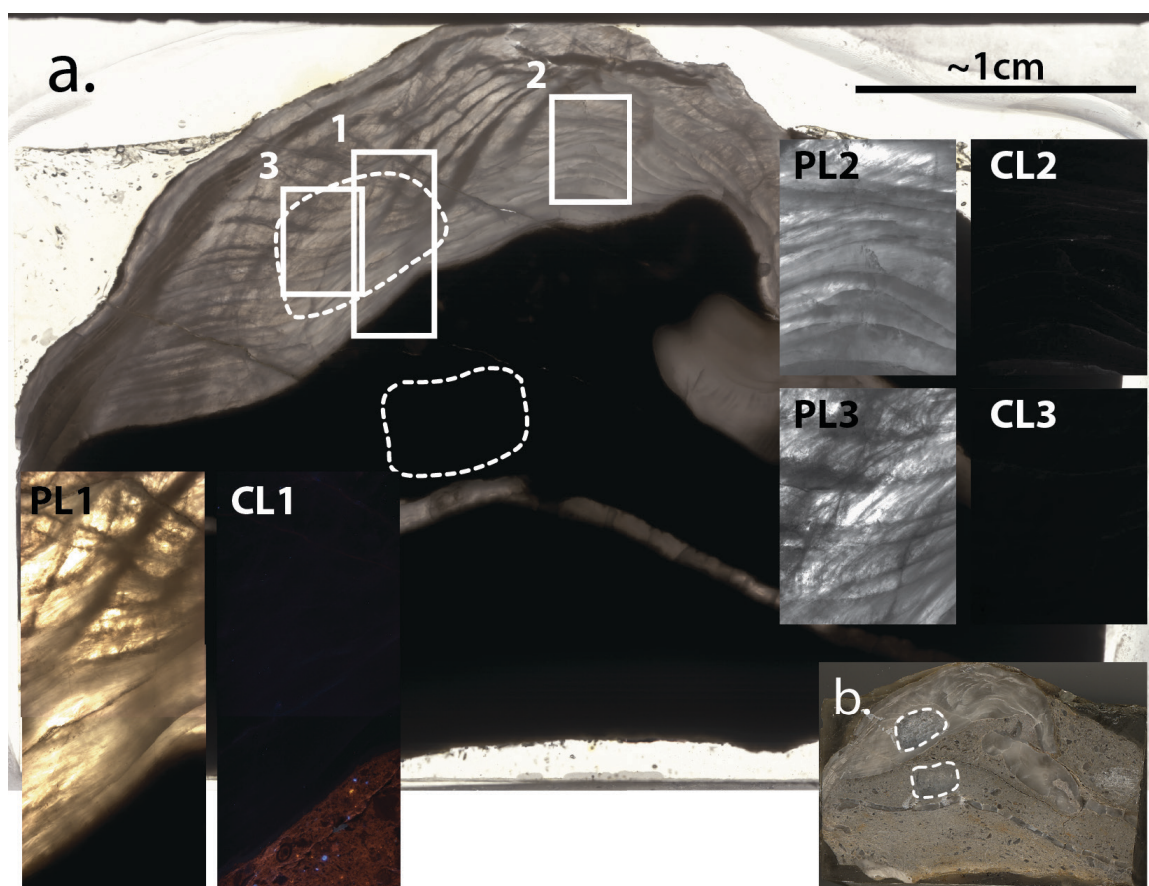


Figure A3.6. Scanned thin section (a.) and billet (b.) of brachiopod sample NV014 (cross-sectional view). Collection and taxonomic information is listed in Table 3.1. In a. and b. the areas inside the white dashed lines are the regions of shell (translucent material) and limestone matrix (opaque material) sub-sampled for carbonate clumped isotope analysis. The white boxes in a. correspond to the plane polarized light (‘PL’) and cathodoluminescence (‘CL’) photomicrographs. PL1 and CL1 are photomicrograph mosaics each composed of 2 overlapping images.

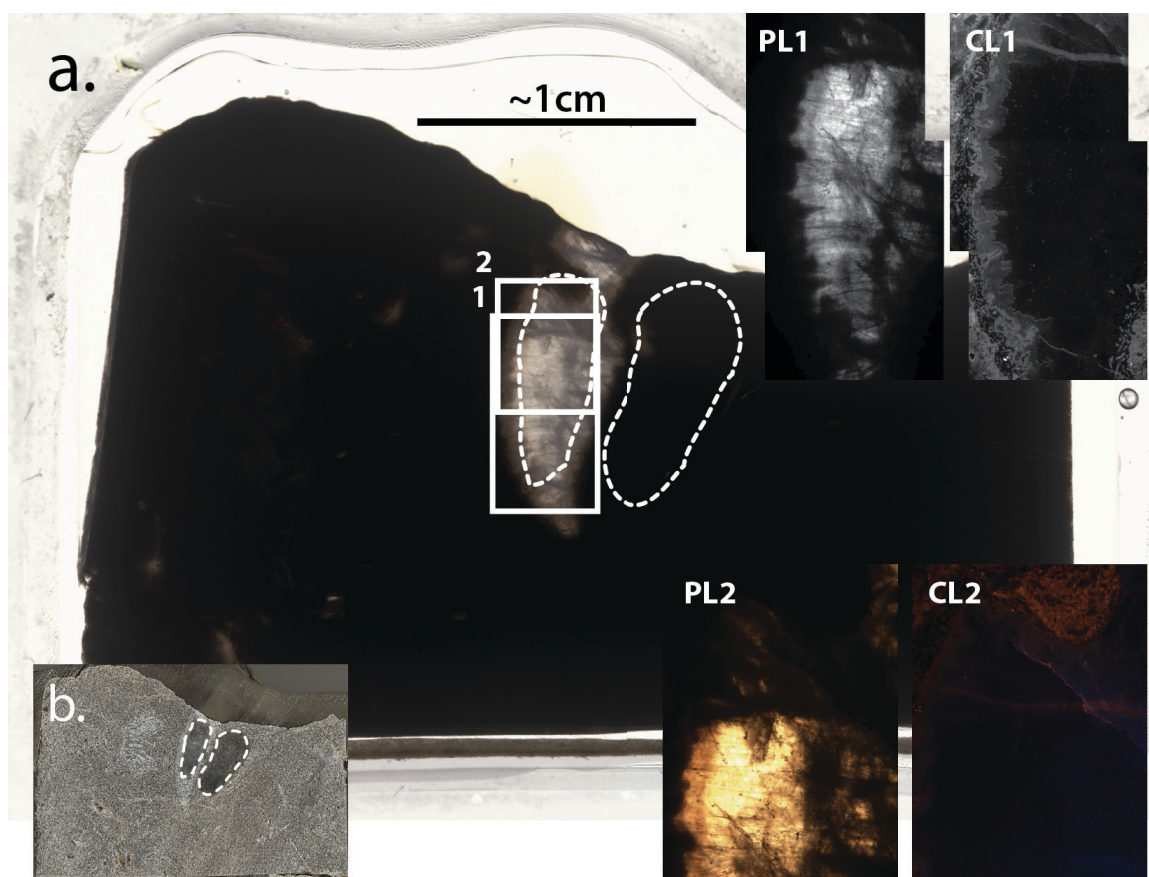


Figure A3.7. Scanned thin section (a.) and billet (b.) of brachiopod sample NV021 (cross-sectional view). Collection and taxonomic information is listed in Table 3.1. In a. and b. the areas inside the dashed lines are the regions of shell (translucent material) and limestone matrix (opaque material) sub-sampled for carbonate clumped isotope analysis. The white boxes in a. correspond to the plane polarized light (‘PL’) and cathodoluminescence (‘CL’) photomicrographs shown in the upper and lower right corners. PL1 and CL1 are photomicrograph mosaics each composed of 2 overlapping images.

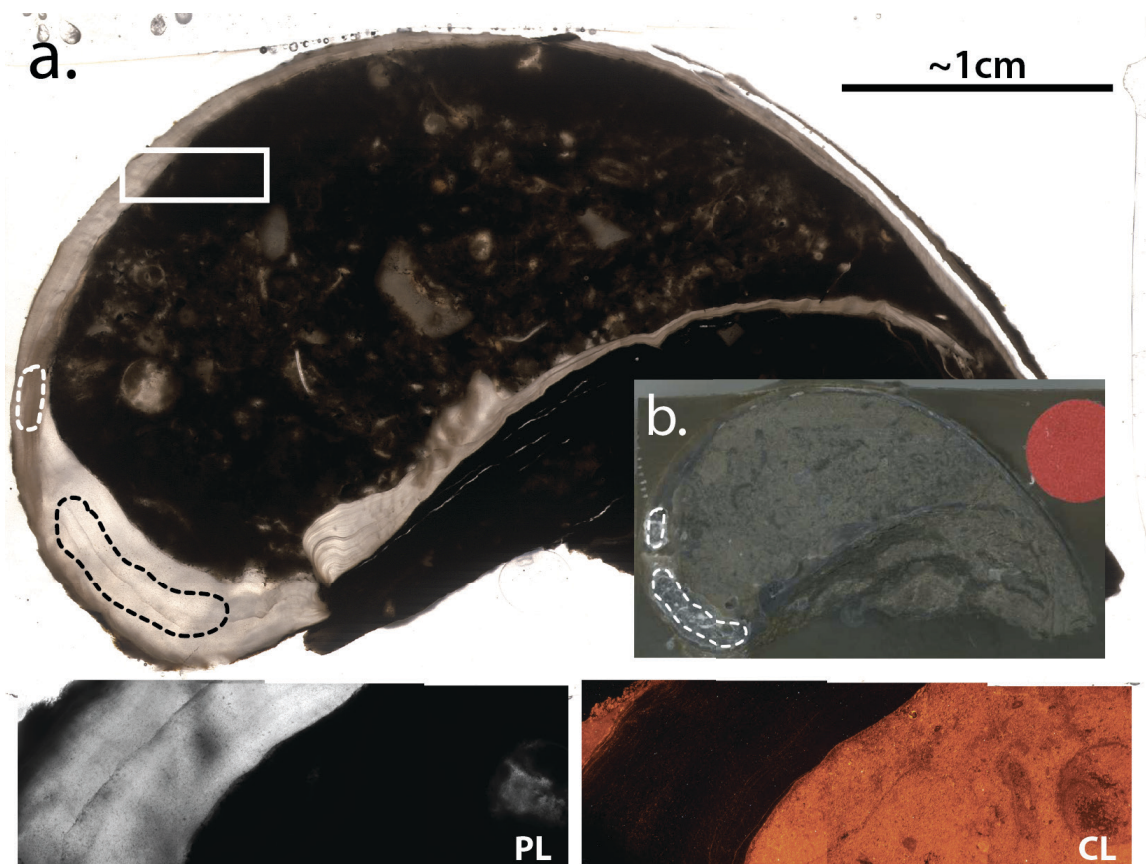


Figure A3.8. Scanned thin section (a.) and billet (b.) of brachiopod sample WP58 Inf-1 (cross-sectional view). Collection and taxonomic information is listed in Table 3.1. In a. and b. the areas inside the dashed lines are the regions of shell (translucent material) subsampled for carbonate clumped isotope analysis. The white box in a. corresponds to the plane polarized light ('PL') and cathodoluminescence ('CL') photomicrographs shown below a. and b. PL and CL are photomicrograph mosaics each composed of 3 overlapping images.

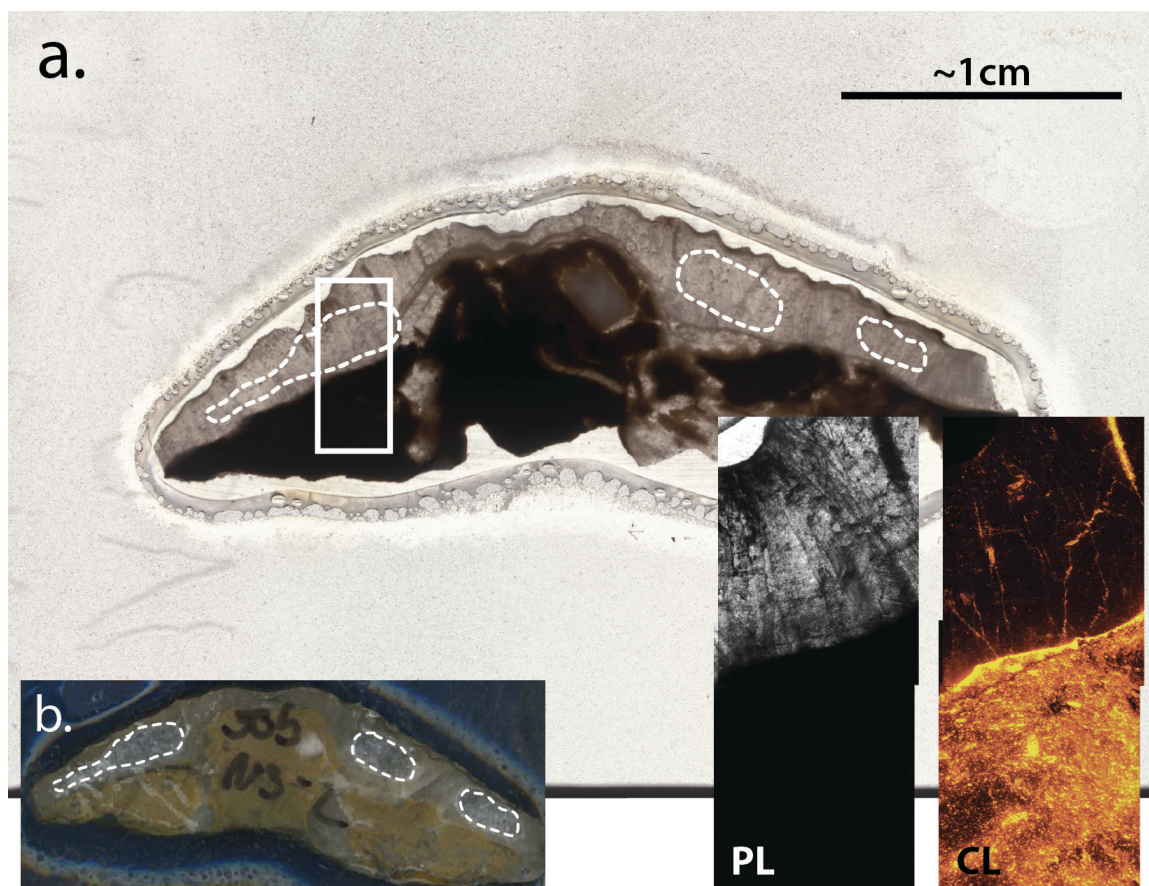


Figure A3.9. Scanned thin section (a.) and billet (b.) of brachiopod sample WP50b NS-1 (cross-sectional view looking across the shell length axis). Collection and taxonomic information is listed in Table 3.1. In a. and b. the areas inside the dashed lines are the regions of shell (translucent material) sub-sampled for carbonate clumped isotope analysis. The white box in a. corresponds to the plane polarized light ('PL') and cathodoluminescence ('CL') photomicrographs shown in the lower right corner. PL and CL are photomicrograph mosaics each composed of 2 overlapping images.

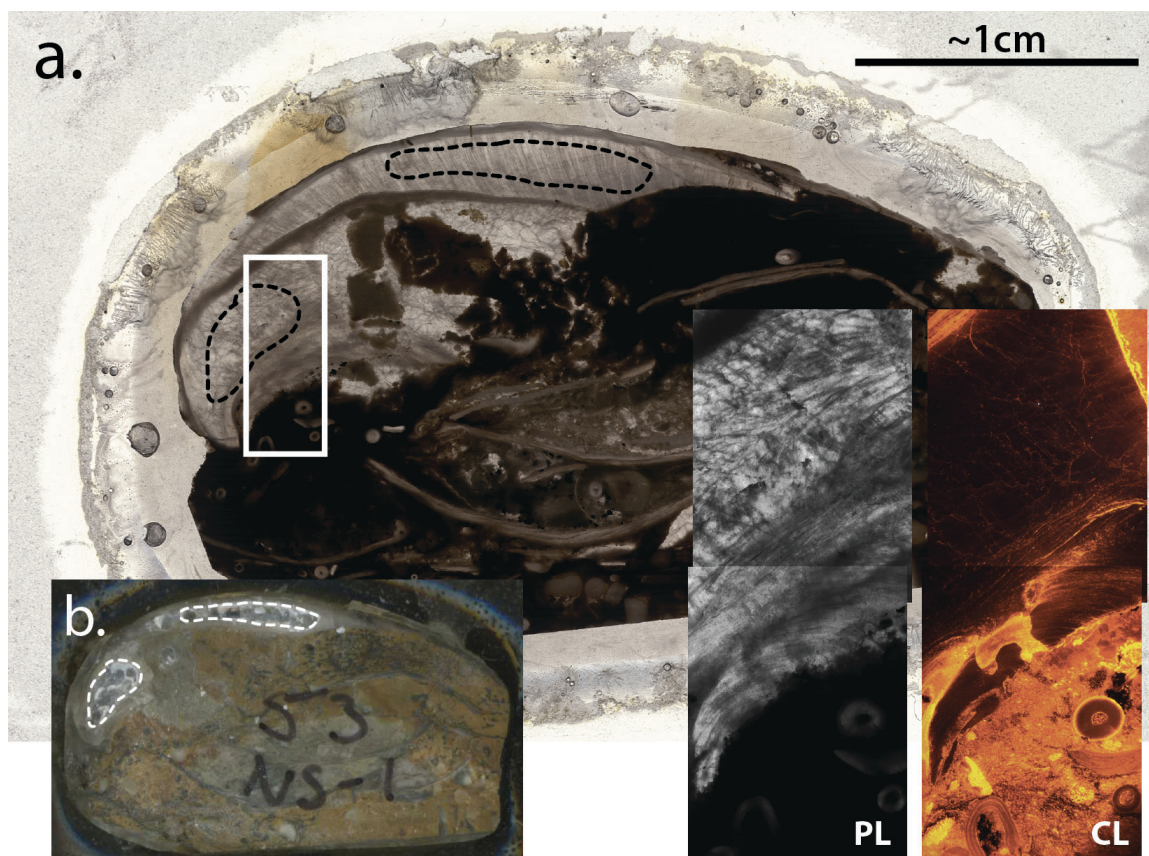


Figure A3.10. Scanned thin section (a.) and billet (b.) of brachiopod sample WP53 NS-1 (cross-sectional view). Collection and taxonomic information is listed in Table 3.1. In a. and b. the areas inside the dashed lines are the regions of shell (translucent material) sub-sampled for carbonate clumped isotope analysis. The white box in a. corresponds to the plane polarized light ('PL') and cathodoluminescence ('CL') photomicrographs shown in the lower right corner. PL and CL are photomicrograph mosaics each composed of 2 overlapping images.

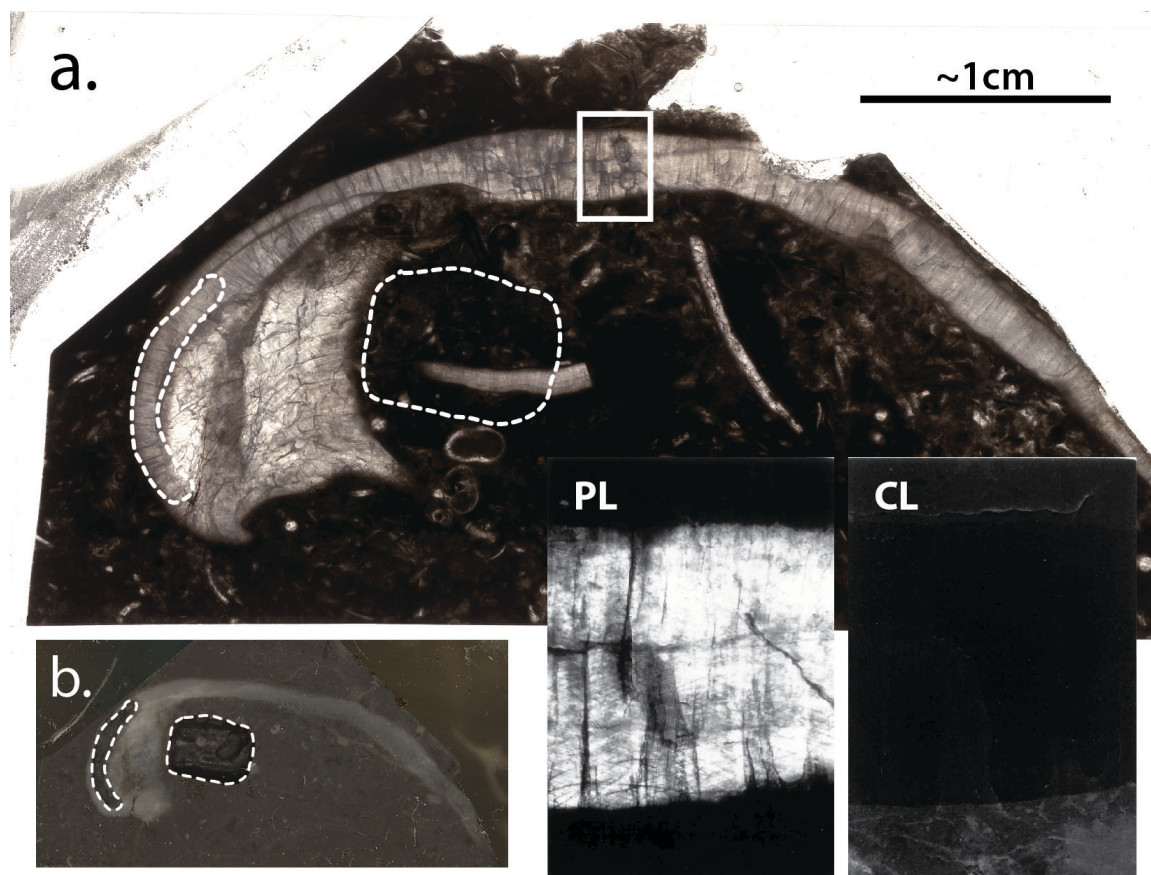


Figure A3.11. Scanned thin section (a.) and billet (b.) of brachiopod sample RU124 (cross-sectional view). Collection and taxonomic information is listed in Table 3.1. In a. and b. the areas inside the white dashed lines are the regions of shell (translucent material) and limestone matrix (opaque material) sub-sampled for carbonate clumped isotope analysis. The white box in a. corresponds to the plane polarized light ('PL') and cathodoluminescence ('CL') photomicrographs from Mii et al. (2001) shown in the lower right corner. PL and CL are photomicrograph mosaics each composed of 2 overlapping images. The dark areas inside the white box in a. are the sub-sampled regions of Mii et al. (2001).

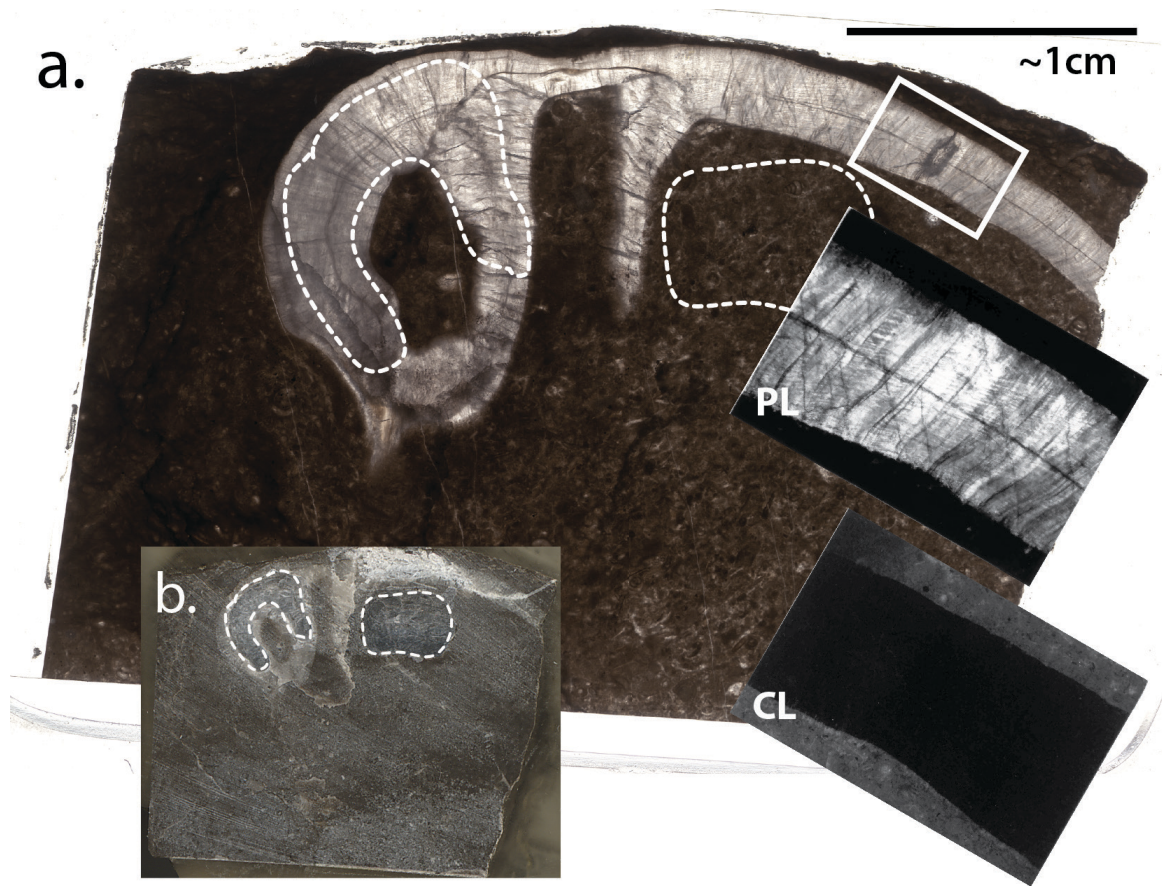


Figure A3.12. Scanned thin section (a.) and billet (b.) of brachiopod sample RU129A (cross-sectional view). Collection and taxonomic information is listed in Table 3.1. In a. and b. the areas inside the white dashed lines are the regions of shell (translucent material) and limestone matrix (opaque material) sub-sampled for carbonate clumped isotope analysis. The white box in a. corresponds to the plane polarized light (‘PL’) and cathodoluminescence (‘CL’) photomicrographs from Mii et al. (2001) shown in the lower right corner. The dark area inside the white box in a. is the sub-sampled region of Mii et al. (2001).

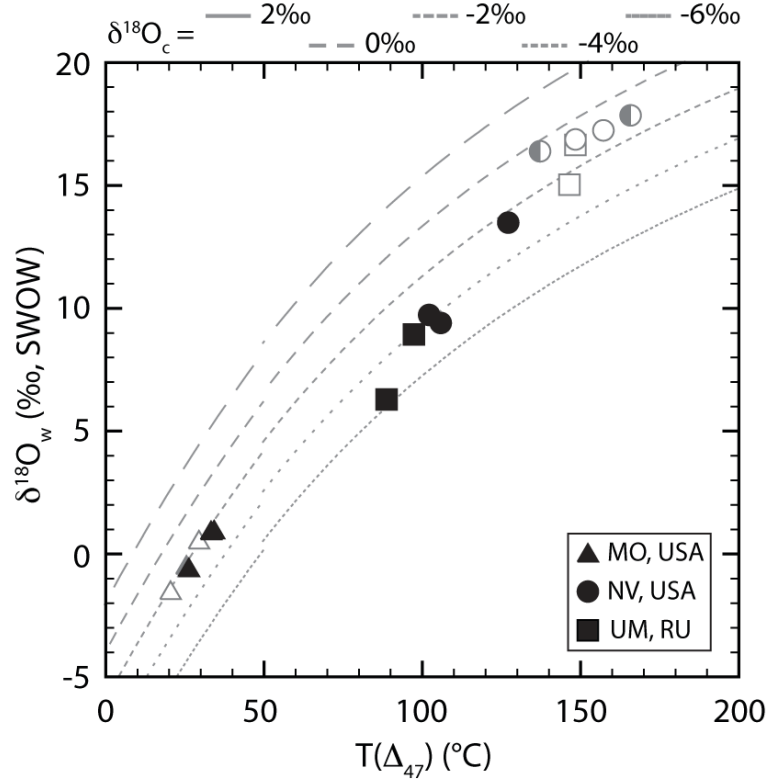


Figure A3.13. Brachiopod-associated matrix carbonate clumped isotope temperatures ($T(\Delta_{47})$) versus calculated water oxygen isotope compositions ($\delta^{18}\text{O}_w$). Water oxygen isotope values were determined from measured carbonate $\delta^{18}\text{O}$ and clumped isotope temperatures using the calcite-water oxygen isotope thermometry equation of Kim and O'Neil (1997). For paleotemperatures $>50^\circ\text{C}$, the equation of O'Neil et al. (1969) was used. Details on the Δ_{47} -temperature relationships used to determine the temperatures are in Table S2. The gray dashed and dotted lines represent solutions to the calcite-water oxygen isotope thermometry equations for constant carbonate $\delta^{18}\text{O}$ values, as noted in the figure. The gray data are the brachiopod calcite data shown in Fig. 3.1, where open and half-filled symbols represent pristine and near-pristine shells, respectively.

A3.4 Supplementary data tables for Carboniferous brachiopod analyses and basin history compilations

Table A3.3. Stable isotope compositions of Carboniferous limestones from North America and Western Russia associated with brachiopods in Table 3.2.

Sample ID	CL Character	<i>n</i>	$\delta^{13}\text{C}$ (‰, VPDB)	$\delta^{18}\text{O}$ (‰, VPDB)	Δ_{47} (‰, CDES)*	Temp. (°C) [#]	$\delta^{18}\text{O}_w$ (‰, VSMOW) [§]
North America							
<i>Fern Glen Formation (upper Mississippi Valley, Missouri, USA), Early Mississippian (348-340 Mya)</i>							
MO074-m	L	3	2.83 ± 0.04	-2.19 ± 0.03	0.655 ± 0.015	34 ± 6	0.97
MO076-m	L	3	2.83 ± 0.02	-2.16 ± 0.02	0.677 ± 0.005	26 ± 2	-0.56
MO077-m	L	2	3.23 ± 0.09	-2.08 ± 0.19	0.657 ± 0.000	33 ± 0	0.94
<i>Bird Spring Formation (Eastern Great Basin province, Nevada, USA), Late Mississippian (333-318 Mya)</i>							
NV008-m	L	2	-0.25 ± 0.11	-4.52 ± 0.00	0.504 ± 0.003	106 ± 2	9.30
NV014-m	L	3	1.50 ± 0.03	-3.83 ± 0.02	0.509 ± 0.007	102 ± 5	9.63
NV021-m	L	3	2.48 ± 0.03	-2.51 ± 0.12	0.474 ± 0.008	127 ± 6	13.37
Western Russia							
<i>Cheremchanskian & Krasnopolyanskian Horizons (Urals Mountains, Russia), Late Pennsylvanian (318 Mya)</i>							
RU124-m	SL	3	3.38 ± 0.09	-4.12 ± 0.05	0.517 ± 0.009	98 ± 5	8.82
RU129A-m	SL	3	3.49 ± 0.74	-5.75 ± 0.32	0.532 ± 0.022	89 ± 12	6.18

Note: Error values are standard error of the mean ($\pm 1\sigma/\sqrt{n}$), where 1σ is the standard deviation of *n* analyses. When *n* = 2 the error value is 1σ (standard deviation).

*Values relative to the ‘carbon dioxide equilibrium scale’ or CDES. An acid correction factor of 0.092‰ was applied to normalize these data to the 25 °C phosphoric acid reaction scale.

[#]Paleotemperatures calculated using linear regressions through the theoretical Δ_{47} -temperature relationship from Schauble et al. (2006) adjusted for the kinetic effects of calcite phosphoric acid reaction (Guo et al., 2009). A regression of model predictions from 50-250 °C ($\Delta_{47} = 41746/T^2 + 0.213$) was used for ‘NV’ and ‘RU’ samples. Error was calculated by propagating the analytical error for Δ_{47} through this equation.

[§]Water isotope compositions calculated using clumped isotope derived paleotemperatures and the calcite oxygen isotope thermometry equation of O’Neil et al. (1969): $1000\ln\alpha = 2.78 \times 10^6/T^2 - 3.39$.

Table A3.4. Minor and trace element contents of reacted and unreacted WA-CB-13 determined from electron microprobe analysis

Reaction ID	<i>n</i>	Temp., Time (°C, min)	MgO (wt. %)	MnO (wt. %)	FeO (wt. %)	CaO (wt. %)	CO ₂ * (wt. %)	Total (wt. %)
unreacted	5	-, -	0.091 ± 0.028	0.012 ± 0.007	0.002 ± 0.002	55.381 ± 0.277	43.971	99.457
SRX013	5	425, 2880	0.146 ± 0.064	0.008 ± 0.004	0.004 ± 0.004	54.790 ± 0.971	43.971	98.919
SRX032	5	450, 90	0.133 ± 0.083	0.007 ± 0.007	0.006 ± 0.006	54.473 ± 0.470	43.971	98.591
SRX022	5	450, 2880	0.129 ± 0.046	0.008 ± 0.009	0.005 ± 0.003	54.22 ± 0.733	43.971	98.334

Note: All ± values are 1σ standard deviation of *n* grains of shell material. 2-4 microprobe spots were analyzed per grain. Analyses were standardized against concurrent analyses of in-house laboratory standards of dolomite, rhodochrosite, siderite, and calcite.

*Weight percent for CO₂ was assigned for calcite.

Table A3.5. Stable isotope compositions of WA-CB-13 calcite heating experiments done under a dry CO₂ atmosphere

Reaction ID	<i>n</i>	Temp. (°C)	Time (min)	δ ¹³ C (‰, VPDB)	δ ¹⁸ O (‰, VPDB)	Δ ₄₇ (‰, CDES)
unreacted	3	-	-	3.75 ± 0.02	-0.66 ± 0.03	0.669 ± 0.010
SRX040	1	385	30	3.80	-0.95	0.650
SRX036	1	385	60	3.78	-0.95	0.637
SRX047	1	385	120	3.76	-0.86	0.629
SRX043	2	385	240	3.77 ± 0.02	-0.97 ± 0.06	0.625 ± 0.009
SRX034	2	385	480	3.76 ± 0.01	-1.00 ± 0.02	0.597 ± 0.021
SRX037	2	385	1450	3.75 ± 0.04	-0.94 ± 0.02	0.564 ± 0.023
SRX042	2	385	4320	3.77 ± 0.05	-0.99 ± 0.03	0.543 ± 0.20
SRX038	1	405	30	3.79	-0.92	0.627
SRX046	2	405	60	3.74 ± 0.00	-0.96 ± 0.01	0.635 ± 0.009
SRX045	1	405	120	3.80	-0.98	0.599
SRX035	2	405	240	3.77 ± 0.02	-0.96 ± 0.02	0.569 ± 0.005
SRX033	1	405	480	3.78	-0.87	0.558
SRX041	1	405	1450	3.73	-1.03	0.521
SRX044	1	405	4320	3.77	-0.96	0.474
SRX007	3	425	30	3.74 ± 0.01	-0.97 ± 0.01	0.588 ± 0.006
SRX010	3	425	60	3.74 ± 0.01	-1.01 ± 0.02	0.562 ± 0.003
SRX009	3	425	90	3.72 ± 0.01	-0.75 ± 0.03	0.557 ± 0.004
SRX008	3	425	120	3.76 ± 0.01	-1.00 ± 0.04	0.554 ± 0.006
SRX006	3	425	240	3.72 ± 0.02	-1.04 ± 0.06	0.534 ± 0.012
SRX011	3	425	480	3.77 ± 0.01	-0.99 ± 0.02	0.496 ± 0.002
SRX014	3	425	1440	3.72 ± 0.02	-1.03 ± 0.02	0.459 ± 0.007
SRX013*	3	425	2880	3.75 ± 0.02	-1.08 ± 0.02	0.419 ± 0.006
SRX012*	3	425	5760	3.75 ± 0.02	-1.00 ± 0.02	0.374 ± 0.008
SRX025	3	450	30	3.79 ± 0.01	-0.92 ± 0.03	0.553 ± 0.005
SRX023	2	450	60	3.72 ± 0.03	-1.06 ± 0.07	0.528 ± 0.014
SRX032	3	450	90	3.76 ± 0.01	-0.99 ± 0.02	0.502 ± 0.002
SRX019	3	450	120	3.72 ± 0.03	-1.06 ± 0.02	0.489 ± 0.008
SRX020*	3	450	240	3.75 ± 0.02	-1.05 ± 0.01	0.463 ± 0.006
SRX031	3	450	1440	3.77 ± 0.02	-1.03 ± 0.02	0.383 ± 0.003
SRX022	3	450	2880	3.75 ± 0.04	-1.10 ± 0.04	0.354 ± 0.007
SRX030*	3	450	5760	3.72 ± 0.02	-1.15 ± 0.03	0.322 ± 0.008
SRX016	3	475	30	3.74 ± 0.02	-1.00 ± 0.04	0.498 ± 0.003
SRX026	3	475	60	3.73 ± 0.00	-0.99 ± 0.02	0.462 ± 0.009
SRX027	3	475	90	3.72 ± 0.02	-1.05 ± 0.02	0.446 ± 0.008
SRX029	3	475	120	3.75 ± 0.01	-1.04 ± 0.02	0.438 ± 0.006
SRX021*	3	475	240	3.78 ± 0.02	-1.01 ± 0.02	0.407 ± 0.009
SRX017	3	475	480	3.70 ± 0.01	-1.08 ± 0.00	0.377 ± 0.004
SRX018	4	475	1450	3.73 ± 0.02	-1.11 ± 0.03	0.344 ± 0.009
SRX024	4	475	2880	3.71 ± 0.00	-1.10 ± 0.04	0.339 ± 0.010
SRX015*	4	475	5760	3.74 ± 0.01	-1.09 ± 0.01	0.331 ± 0.003

Note: Error values are standard error of the mean ($\pm 1\sigma/\sqrt{n}$), where 1σ is the standard deviation of *n* analyses. When *n* = 2 the error value is 1σ (standard deviation).

*Samples in which, during the quench to room temperature, a small amount of condensation was observed on the inside of the quartz reaction tubes.

Table A3.6. Thermal history of Carrara marble from the Alpi Apuane metamorphic core complex in the Northern Apennines, Italy.

Time (Ma)	Temp. (°C)	Temp. Uncertainty (°C)	Justification
30.5	20	± 5	Deposition of ‘pseudomacigno sandstone’ turbidites, the youngest deposits prior to metamorphism; Carmignani and Kligfield (1990) (citing biostratigraphy from Dallan-Nardi (1977)).
26	375	± 25	K-Ar and $^{40}\text{Ar}/^{39}\text{Ar}$ thermochronology of earliest compressive deformation phase (D_1) micas; Kligfield et al. (1986). Uncertainty estimated from the range of values reported by Kligfield et al. (1986).
10	240	± 40	Zircon fission-track thermochronology; Fellin et al. (2007), Bernet (2002) (as reported by Balestrieri et al. (2003)).
7	180	± 20	Zircon U-Th/He thermochronology; Fellin et al. (2007), Balestrieri et al. (2003)
5.5	110	± 20	Apatite fission-track thermochronology; Carmignani and Kligfield (1990), Balestrieri et al. (2003), Fellin et al. (2007)
5	70	± 10	Apatite U-Th/He thermochronology; Fellin et al. (2007)
0	20		Approximate present day temperature

Note: Temperature uncertainty for each thermochronometer estimated from Reiners (2005) based on typical cooling rates and crystal sizes.

Table A3.7. Burial temperature history for Arrow Canyon, Nevada, USA.

Time (Ma)	Temp. (°C)	Temp. Uncertainty (°C)	Justification
318	25	± 5	Approximate age based on biostratigraphy; Bishop et al. (2009, 2010).
311	30		
308	43		
307	50		
305	53		
299	55		
250	135	± 35	Rapid burial in the Antler foreland basin. Temperatures based on sediment decompaction estimates for Pennsylvanian strata and a geothermal gradient of 25 °C/km (Martin et al., 2012). Maximum burial temperature based on conodont CAI in Arrow Canyon (= 2.0-2.5; Martin et al., 2012) ¹ . Values in Martin et al. (2012) cited as personal communication with B. Wardlaw. Timing based on the activation of the Sonoma Orogeny in the eastern Great Basin province (Dickinson, 2006). Temperature uncertainty estimated from interpolation between CAI 2 and CAI 3 in Epstein et al. (1977).
25	42.5	± 12	Basin & range tectonics drove uplift to ~0.5 km burial depths in the eastern Great Basin. Uncertainty estimated assuming ± 0.5 km burial depth. Temperatures calculated using a geothermal gradient of 25 °C/km.
0	21		Present day formation temperature estimated from mean annual air temperature (NOAA, Las Vegas, NV).

¹Garside & Hess (2007) show CAI values of >3 for Carboniferous conodonts in the Arrow Canyon range, which suggest higher burial temperatures ranging from 110-200 °C.

Table A3.8. Burial temperature history for Carboniferous strata in the Uralian foredeep along eastern margin of the Russian Platform, Russia.

Time (Ma)	Temp. (°C)	Temp. Uncertainty (°C)	Justification
315	20	± 5	Age and paleotemperature estimated from Mii et al. (2001) and Grossman et al. (2002).
295	100	± 40	Burial temperatures from Carboniferous CAI values of ~2 and vitrinite reflectance values of ~1% in the southern Uralian foredeep (Matenaar et al., 1999) ¹ . Temperature uncertainty estimated from Arrhenius plots in Epstein et al. (1977).
260	90	± 30	High burial temperatures persisted until at least the Permian based on vitrinite reflectance values of 0.8-0.9% in lower Permian rocks (Matenaar et al., 1999) ¹ . Temperature uncertainty estimated from mean range values presented in Epstein et al. (1977).
210	70	±10	General scheme for post-Uralian Orogeny exhumation (Glasmacher et al. 2002). Temperatures calculated assuming at geothermal gradient of 25 °C/km.
15	60	±10	
0	~5		Present day formation temperature estimated from mean air temperature for Yekaterinburg, Russia.

¹Stratigraphic coherence between the Sokol section, the brachiopod collection locality in this study, and Carboniferous sections in the southern Ural Mountains sampled by Matenaar et al. (1999) is confirmed by Proust et al. (1998).

Table A3.9. Burial temperature histories for mid-Carboniferous strata in the southern Illinois basin, IL, USA

Time (Ma)	Temp. (°C)	Justification
<i>'Burial only' model, Rowan et al., 2002, Fluorspar District</i>		
320	25	Chesterian age for the Grove Church Formation (Flake, 2011) and approximate paleotemperature from Grossman et al. (2008).
310	50	
290	60	Relatively high (0.09-0.14 mm/yr) sedimentation rates were assumed in the model for this interval.
280	100	
270	135	Maximum burial temperature coincident with middle Permian ore deposition. Value in general agreement with the approximate range of fluid inclusion homogenization temperatures (~130-150 °C) and Herrin Coal vitrinite reflectance values.
260	100	Relatively high (0.09-0.14 mm/yr) erosion rates were assumed in the model for this interval.
250	60	
160	50	
0	25	
<i>'Hybrid' (burial +hydrothermal fluid flow) model, Rowan et al., 2002, Fluorspar District</i>		
320	25	Chesterian age for the Grove Church Formation (Flake, 2011) and approximate paleotemperature from Grossman et al. (2008).
300	60	
295	60	During the Permian burial reaching a maximum depth of 1.3 km in the southern parts of the basin. In the model the southern end of the Illinois Basin dwells at this depth until 160 Ma.
290	70	
280	75	
275	95	To simulate the effects of lower Permian magmatism at the southern end of the basin, basal heat flow in the model was increased from 62.5 to 155 W/m ² .
270	175	
265	110	
260	95	
160	95	Fluid flow rates into the Illinois Basin decline after the uplift of the Pascola arch.
60	70	
10	60	
0	25	

Table A3.10. Burial temperature history for upper Pennsylvanian strata in the Appalachian Basin, WV, USA.

Time (Ma)	Temp. (°C)	Temp. Uncertainty (°C)	Justification
305	25	± 5	Virgilian age of the Ames Formation (Flake, 2011 and references therein) and approximate paleotemperature from Grossman et al. (2008).
263	145	± 10	Vitrinite reflectance and fluid inclusion homogenization thermometry from Reed et al. (2005), similar maximum burial temperatures found by Mora et al. (1998). Uncertainty estimated from the range of measured values in Reed et al. (2005).
142	100	± 20	Apatite fission track thermochronology data from Blackmer et al. (1994), reported by Reed et al. (2005).
89	60	± 10	Apatite (U-Th)/He thermochronology data from Reed et al. (2005). Uncertainty estimated from Reiners (2005) based on the published cooling rate and He diffusion domain size in apatite.
0	19		Average present day formation temperature reported by Reed et al. (2005)

Note: This burial temperature history for Pennsylvanian strata in West Virginia generally agrees with the maximum burial depths of Pennsylvanian strata in southwestern Pennsylvania (Blackmer et al., 1994) and eastern Ohio (Caudill et al., 1997).

Table A3.11. Burial temperature history for early Mississippian strata in the U.S. Midcontinent (MO, USA).

Time (Ma)	Temp. (°C)	Temp. Uncertainty (°C)	Justification
345	25	± 5	Age and approximate paleotemperature from Mii et al. (1999).
330	38	± 5	Crystal morphology and geochemistry of early cements suggest burial depths no greater than 0.5 km (Zones II-IV, II'; Kaufman et al. (1988) ¹ .
320	50	± 10	Vitrinite reflectance thermometry from shales in the Burlington-Keokuk Formation, which overlies the lower Osagean carbonates in Missouri, indicates a maximum burial depth of ~1 km ^{1,2} .
305	50	± 10	Coal-rank data from Pennsylvanian coals unconformably overlying the Burlington-Keokuk Formation ² .
0	10		Present day formation temperature estimated from mean annual air temperature (NOAA, Quad Cities, IA/IL).

¹Temperature calculated assuming a geothermal gradient of 25 °C/km, and uncertainty estimated by assuming ± 10 °C/km variation in the geothermal gradient.

²Interpretation from Kaufman et al. (1988) and Banner & Kaufman (1994) but no vitrinite reflectance data are actually presented in these papers. Coal-grade data and a burial history curve are cited as unpublished data by O. Cox.

A3.5 Supplementary data table for Carboniferous brachiopod analyses

(Table A3.12, *see supplemental files*)

A4.1 Brachiopod petrographic screening images

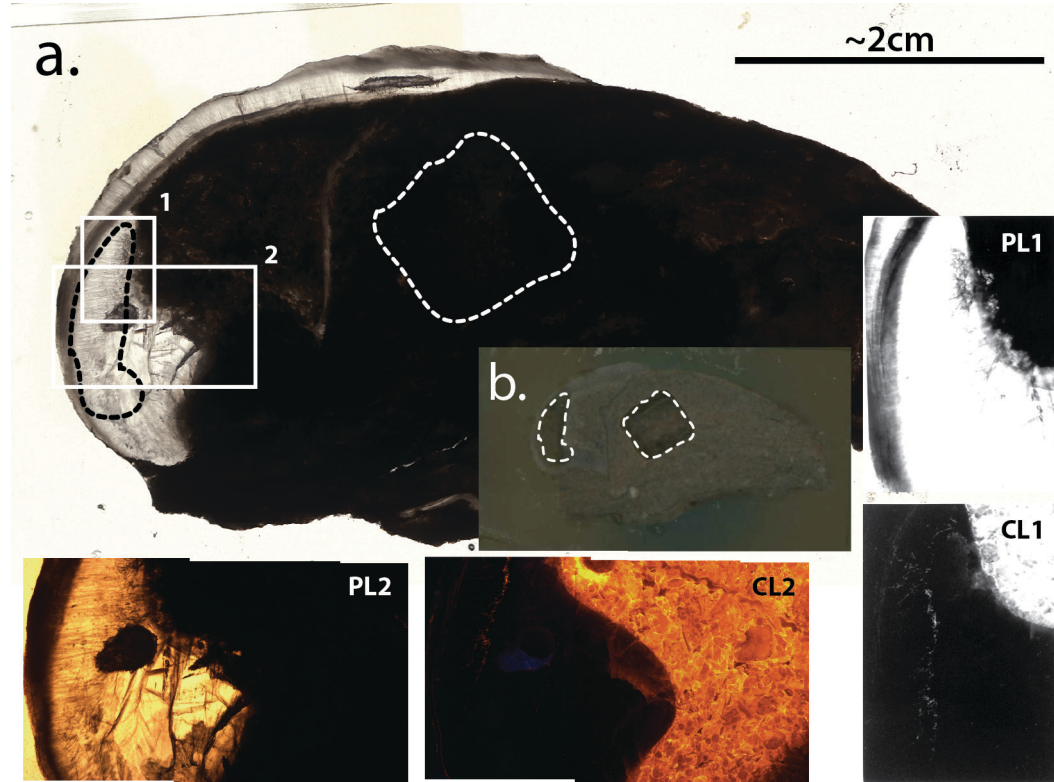


Figure A4.1. Scanned thin section (a) and billet (b) of brachiopod IA115 (cross-sectional perspective). Taxonomic information is listed in Table A4.1. Sample originally collected by Mii et al. (1999). In (a) and (b) the areas inside the dashed lines are regions of shell (translucent material) and limestone matrix (opaque material) sub-sampled for carbonate clumped isotope analysis. The white outlined boxes in (a) correspond to the plane polarized light ('PL') and cathodoluminescence ('CL') photomicrographs from Mii et al. (1999) (PL1 and CL1) and this study (PL2 and CL2). PL2 and CL2 are photomicrograph mosaics each composed of 3 overlapping images and were captured using methods described in Section 3.2.1. The dark, circular area inside the white outlines in (a) is the sub-sampled region of Mii et al. (1999).

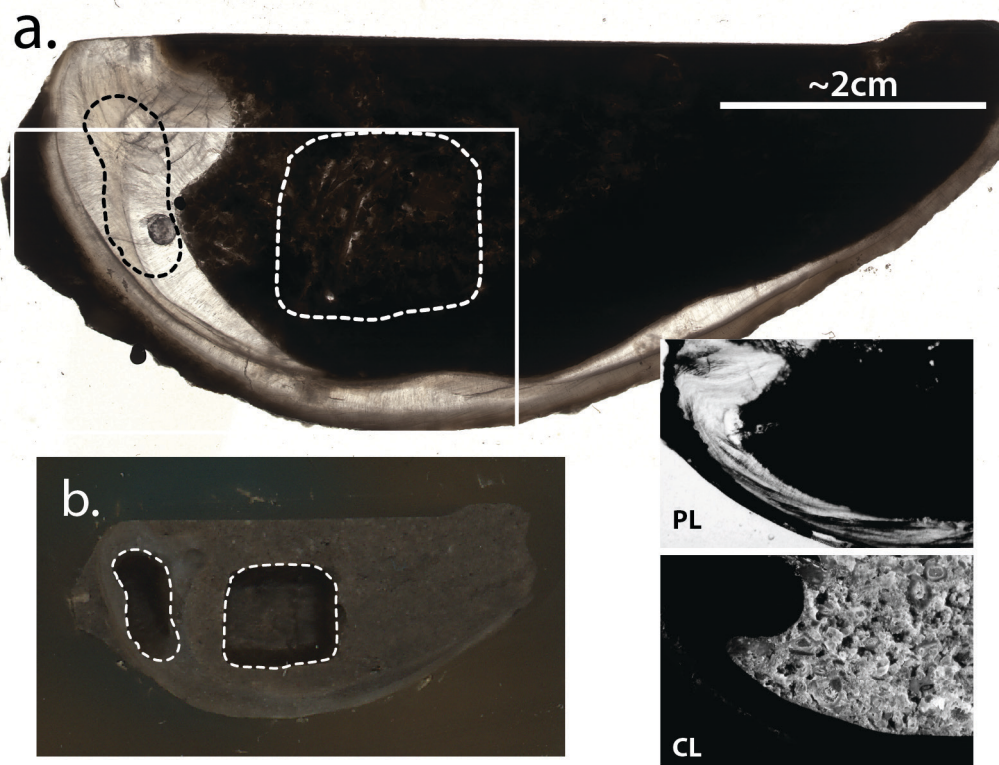


Figure A4.2. Scanned thin section (a) and billet (b) of brachiopod IA144 (cross-sectional perspective). Taxonomic information is listed in Table A4.1. Sample originally collected by Mii et al. (1999). In (a) and (b) the areas inside the dashed lines are regions of shell (translucent material) and limestone matrix (opaque material) sub-sampled for carbonate clumped isotope analysis. The white outlined box in (a) corresponds to the plane polarized light ('PL') and cathodoluminescence ('CL') photomicrographs from Mii et al. (1999). The dark, circular area inside the dashed lines in (a) is the sub-sampled region of Mii et al. (1999).

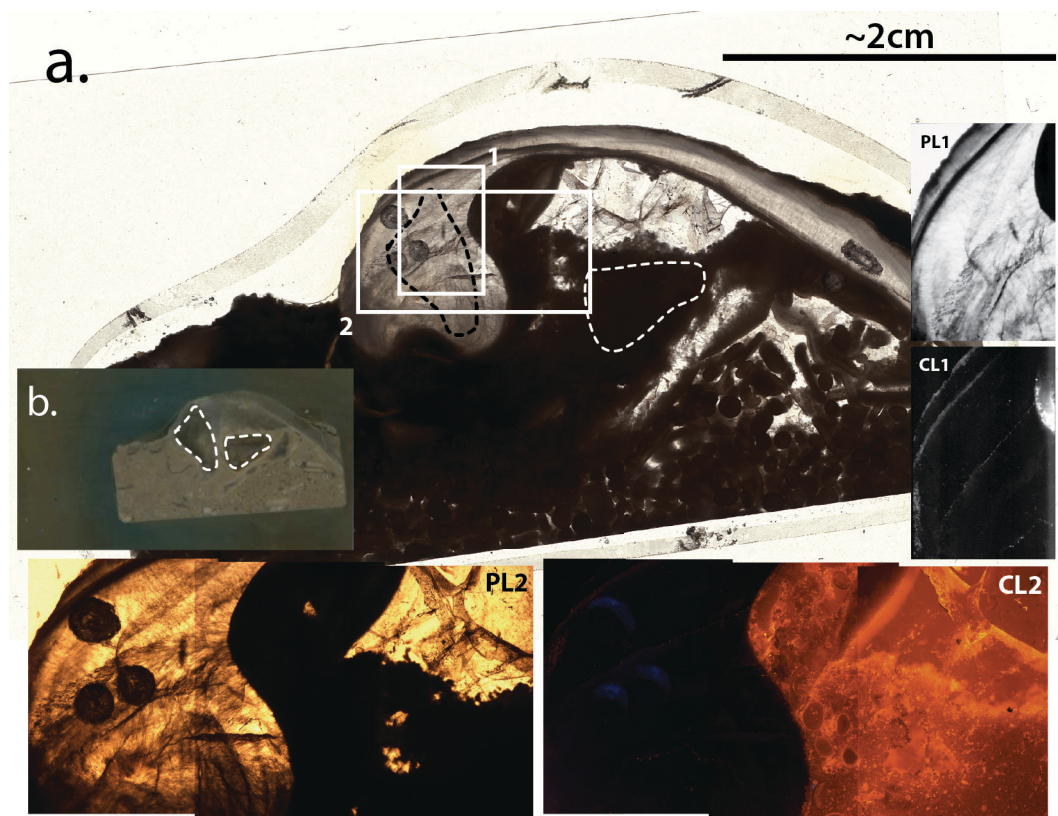


Figure A4.3. Scanned thin section (a) and billet (b) of brachiopod IA146 (cross-sectional perspective). Taxonomic information is listed in Table A4.1. Sample originally collected by Mii et al. (1999). In (a) and (b) the areas inside the dashed lines are regions of shell (translucent material) and limestone matrix (opaque material) sub-sampled for carbonate clumped isotope analysis. The white outlined boxes in (a) correspond to the plane polarized light (‘PL’) and cathodoluminescence (‘CL’) photomicrographs from Mii et al. (1999) (PL1 and CL1) and this study (PL2 and CL2). PL2 and CL2 are photomicrograph mosaics each composed of 3 overlapping images and were captured using methods described in Section 3.2.1. The dark, circular area inside the dashed lines in (a) is the sub-sampled region of Mii et al. (1999).

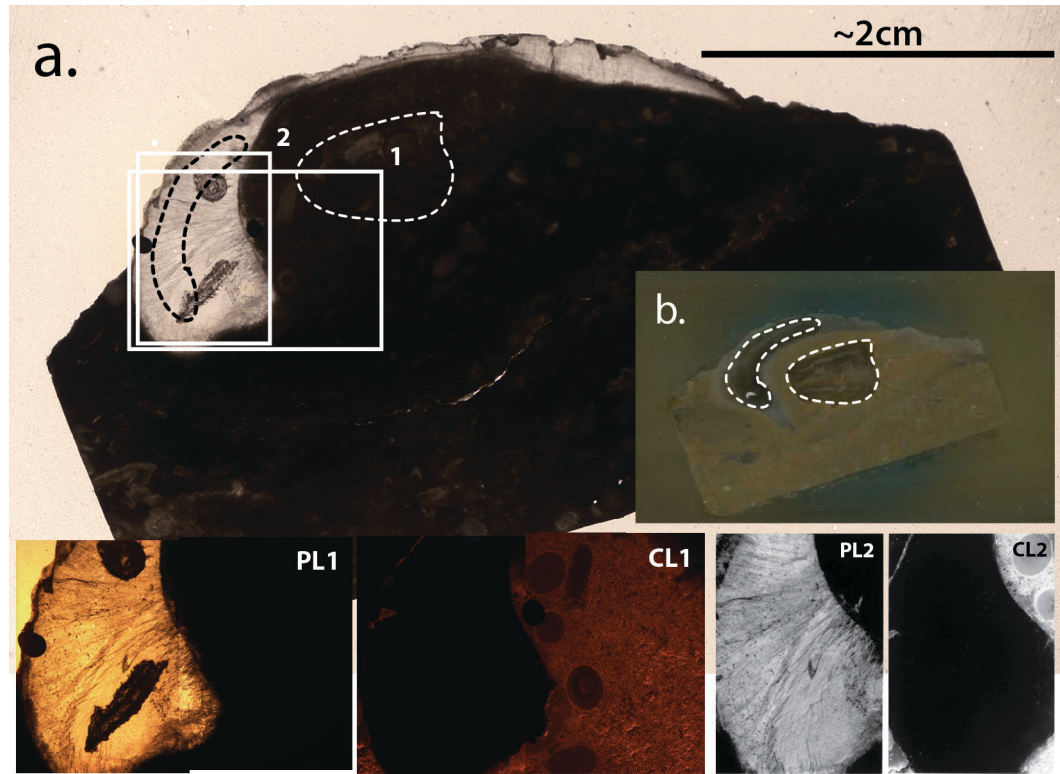


Figure A4.4. Scanned thin section (a) and billet (b) of brachiopod IA197 (cross-sectional perspective). Taxonomic information is listed in Table A4.1. Sample originally collected by Mii et al. (1999). In (a) and (b) the areas inside the dashed lines are regions of shell (translucent material) and limestone matrix (opaque material) sub-sampled for carbonate clumped isotope analysis. The white outlined boxes in (a) correspond to the plane polarized light (‘PL’) and cathodoluminescence (‘CL’) photomicrographs from Mii et al. (1999) (PL1 and CL1) and this study (PL2 and CL2). PL2 and CL2 are photomicrograph mosaics each composed of 2 overlapping images and were captured using methods described in Section 3.2.1. The two dark areas inside the white boxes in (a) are the sub-sampled regions of Mii et al. (1999).

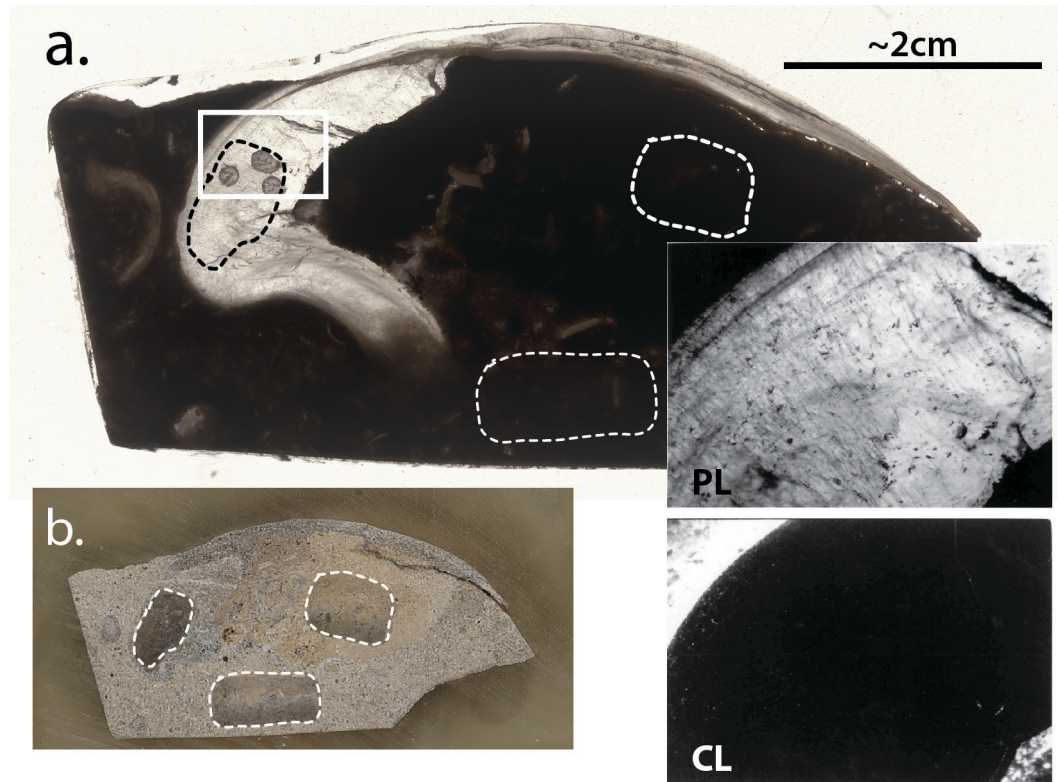


Figure A4.5. Scanned thin section (a) and billet (b) of brachiopod RU001 (cross-sectional perspective). Taxonomic information is listed in Table A4.1. Sample originally collected by Mii et al. (2001). In (a) and (b) the areas inside the dashed lines are regions of shell (translucent material) and limestone matrix (opaque material) sub-sampled for carbonate clumped isotope analysis. The white outlined box in (a) corresponds to the plane polarized light ('PL') and cathodoluminescence ('CL') photomicrographs from Mii et al. (2001). The dark, circular areas inside the white outlines in (a) are the sub-sampled regions of Mii et al. (2001).

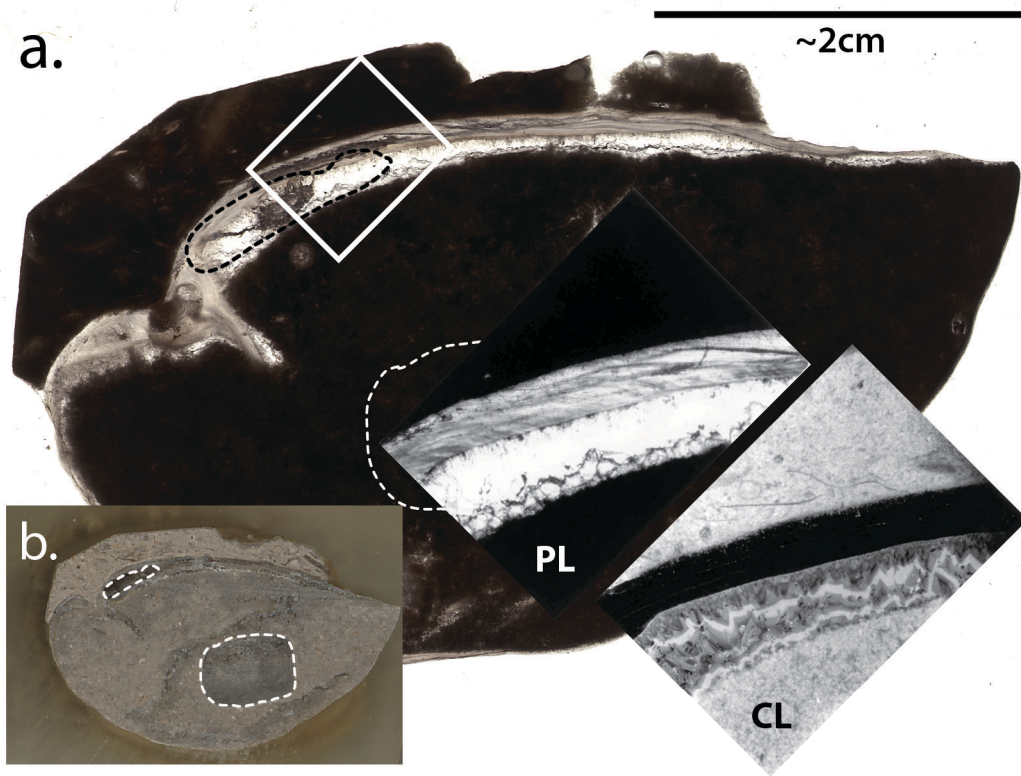


Figure A4.6. Scanned thin section (a) and billet (b) of brachiopod RU010 (cross-sectional perspective). Taxonomic information is listed in Table A4.1. Sample originally collected by Mii et al. (2001). In (a) and (b) the areas inside the dashed lines are regions of shell (translucent material) and limestone matrix (opaque material) sub-sampled for carbonate clumped isotope analysis. The white outlined box in (a) corresponds to the plane polarized light ('PL') and cathodoluminescence ('CL') photomicrographs from Mii et al. (2001). The dark, circular area inside the dashed line in (a) is the sub-sampled region of Mii et al. (2001).

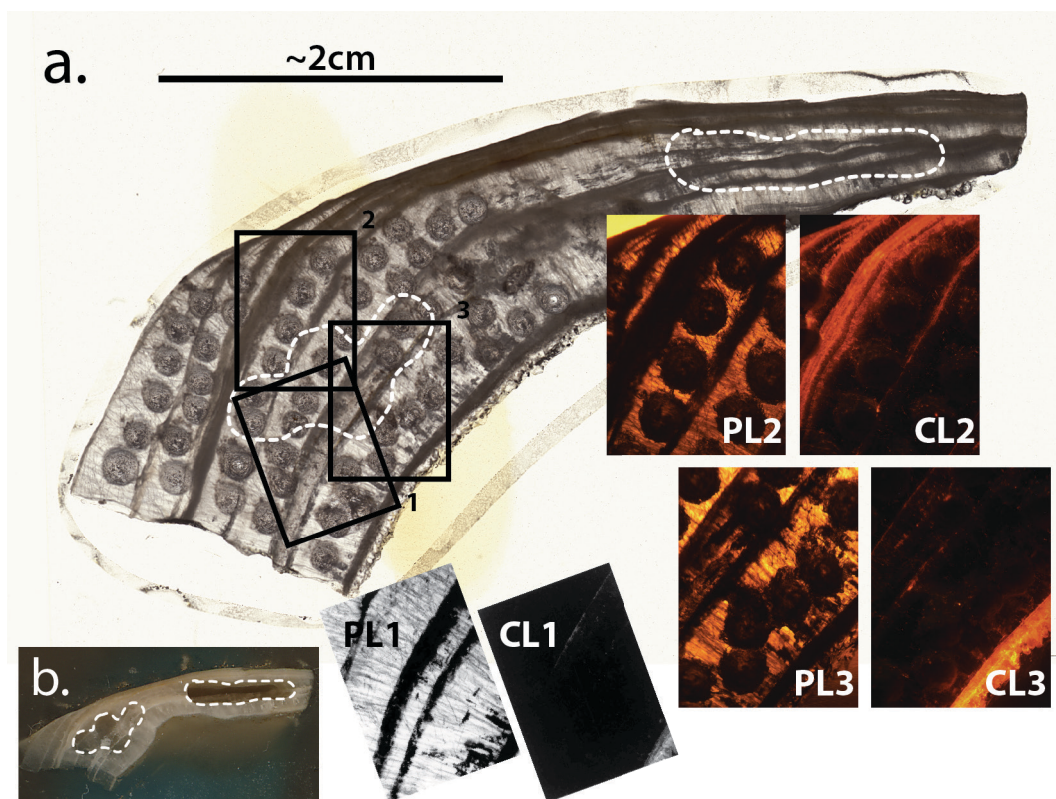


Figure A4.7. Scanned thin section (a) and billet (b) of brachiopod RU053 (cross-sectional perspective). Taxonomic information is listed in Table A4.1. Sample originally collected by Mii et al. (2001). In (a) and (b) the areas inside the dashed lines are regions of shell (translucent material) and limestone matrix (opaque material) sub-sampled for carbonate clumped isotope analysis. The black outlined boxes in (a) correspond to the plane polarized light (‘PL’) and cathodoluminescence (‘CL’) photomicrographs from Mii et al. (1999) (PL1 and CL1) and this study (PL2 and CL2). Photomosaic pairs 2 and 3 were captured using methods described in Section 3.2.1. The dark, circular areas in (a) are the many sub-sampled regions of Mii et al. (2001).

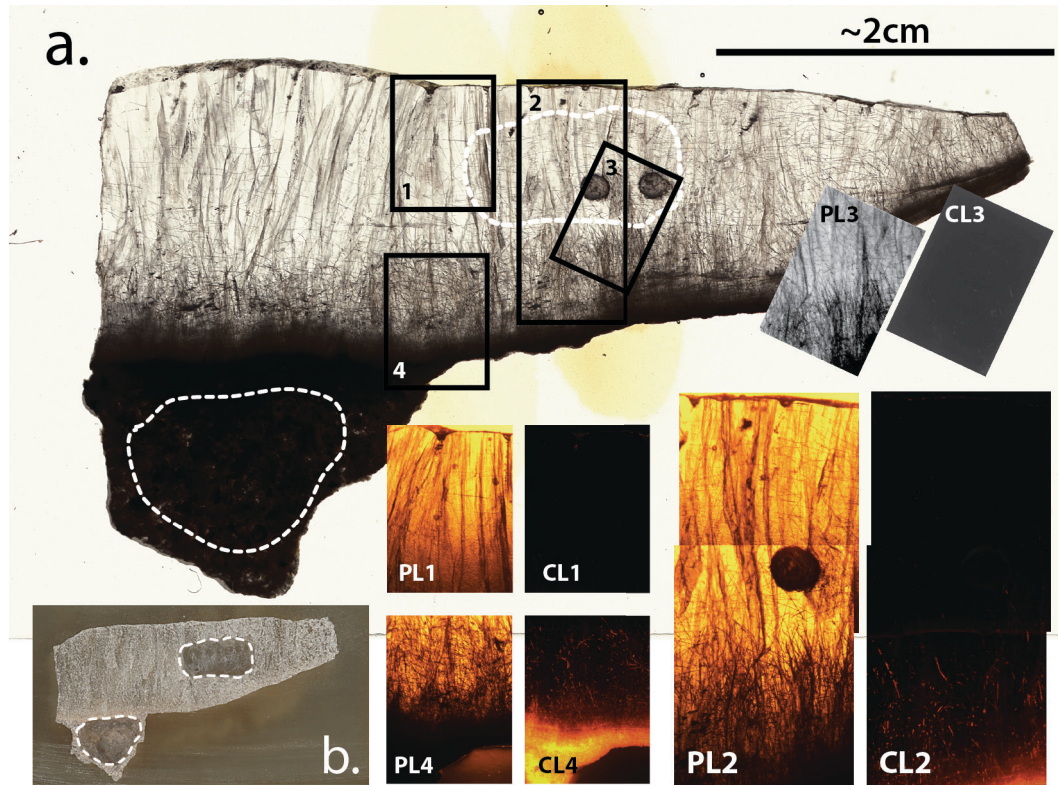


Figure A4.8. Scanned thin section (a) and billet (b) of brachiopod RU054 (cross-sectional perspective). Taxonomic information is listed in Table A4.1. Sample originally collected by Mii et al. (2001). In (a) and (b) the areas inside the dashed lines are regions of shell (translucent material) and limestone matrix (opaque material) sub-sampled for carbonate clumped isotope analysis. The black outlined boxes in (a) correspond to the plane polarized light ('PL') and cathodoluminescence ('CL') photomicrographs from Mii et al. (1999) (PL3 and CL3) and this study (PL1 & CL1, PL2 & CL2, and PL4 & CL4). PL2 and CL2 are photomicrograph mosaics each composed of 2 overlapping images and were captured using methods described in Section 3.2.1. The two dark, circular areas inside the dashed white lines in (a) are the sub-sampled regions of Mii et al. (2001).

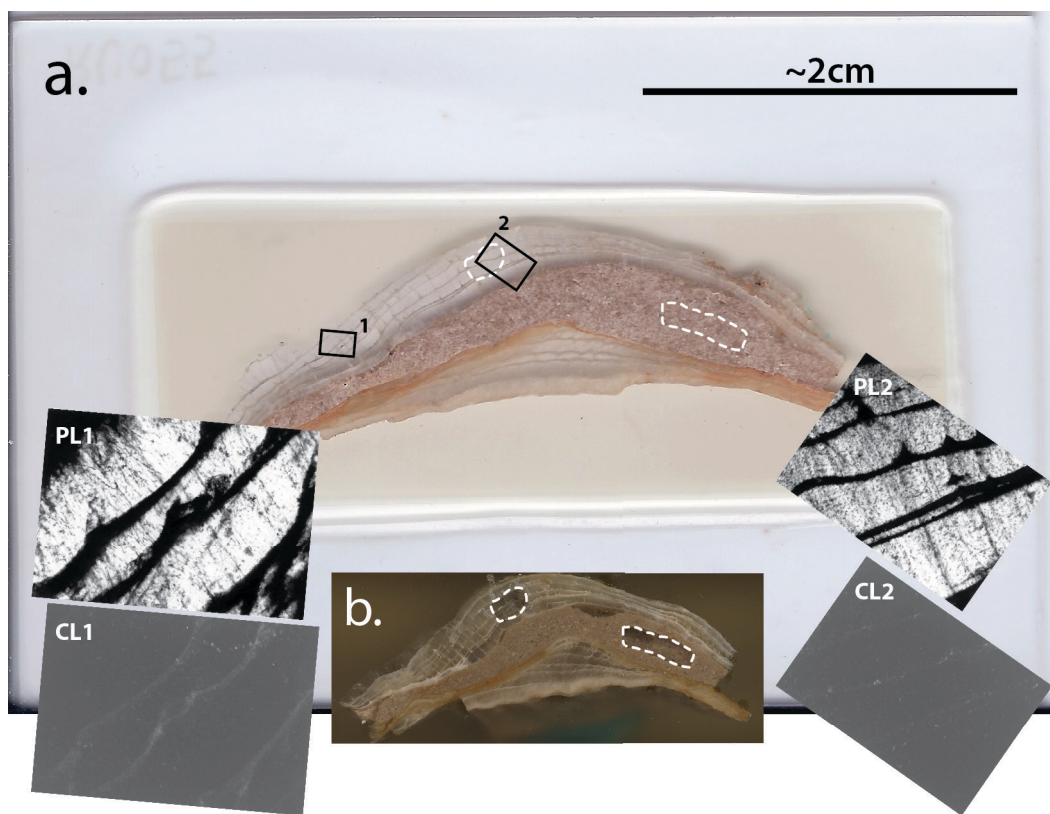


Figure A4.9. Scanned thin section (a) and billet (b) of brachiopod RU055 (cross-sectional perspective). Taxonomic information is listed in Table A4.1. Sample originally collected by Mii et al. (2001). In (a) and (b) the areas inside the dashed lines are regions of shell (translucent material) and limestone matrix (opaque material) sub-sampled for carbonate clumped isotope analysis. The black outlined boxes in (a) correspond to the plane polarized light ('PL') and cathodoluminescence ('CL') photomicrographs from Mii et al. (2001) (PL1 & CL1 and PL2 & CL2).

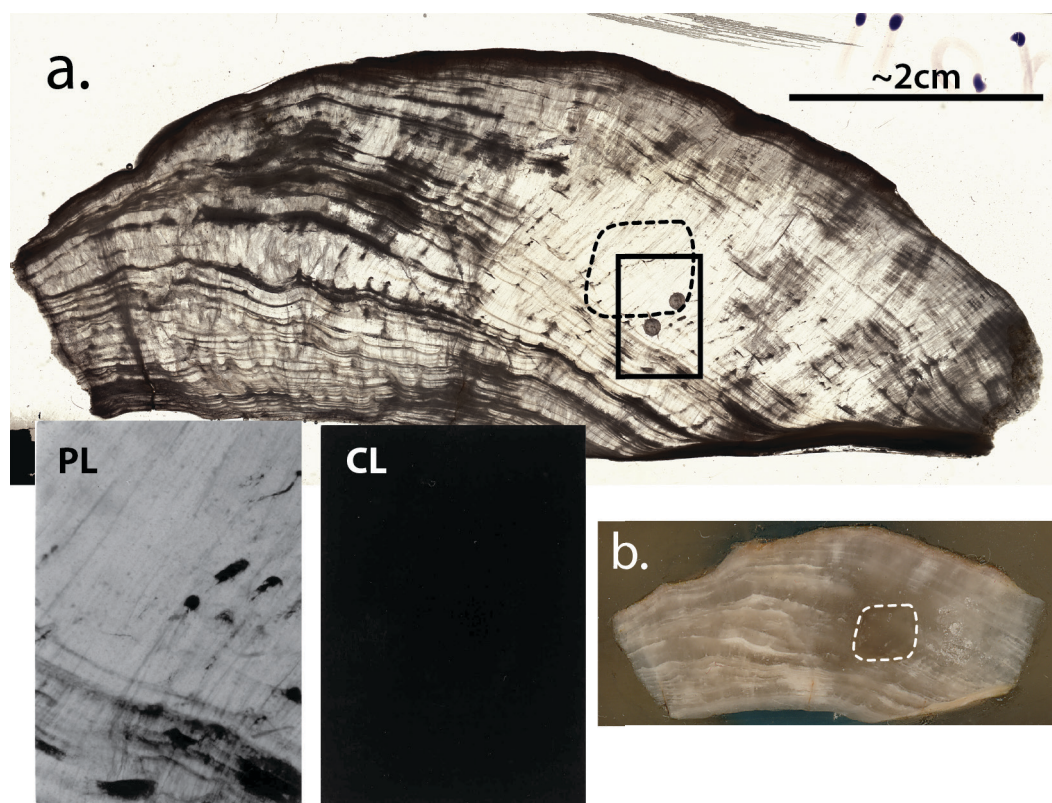


Figure A4.10. Scanned thin section (a) and billet (b) of brachiopod RU071 (cross-sectional perspective). Taxonomic information is listed in Table A4.1. Sample originally collected by Mii et al. (2001). In (a) and (b) the areas inside the dashed lines are regions of shell sub-sampled for carbonate clumped isotope analysis. The black outlined box in (a) corresponds to the plane polarized light ('PL') and cathodoluminescence ('CL') photomicrographs from Mii et al. (2001). The dark, circular areas inside the black outline in (a) are the sub-sampled regions of Mii et al. (2001).

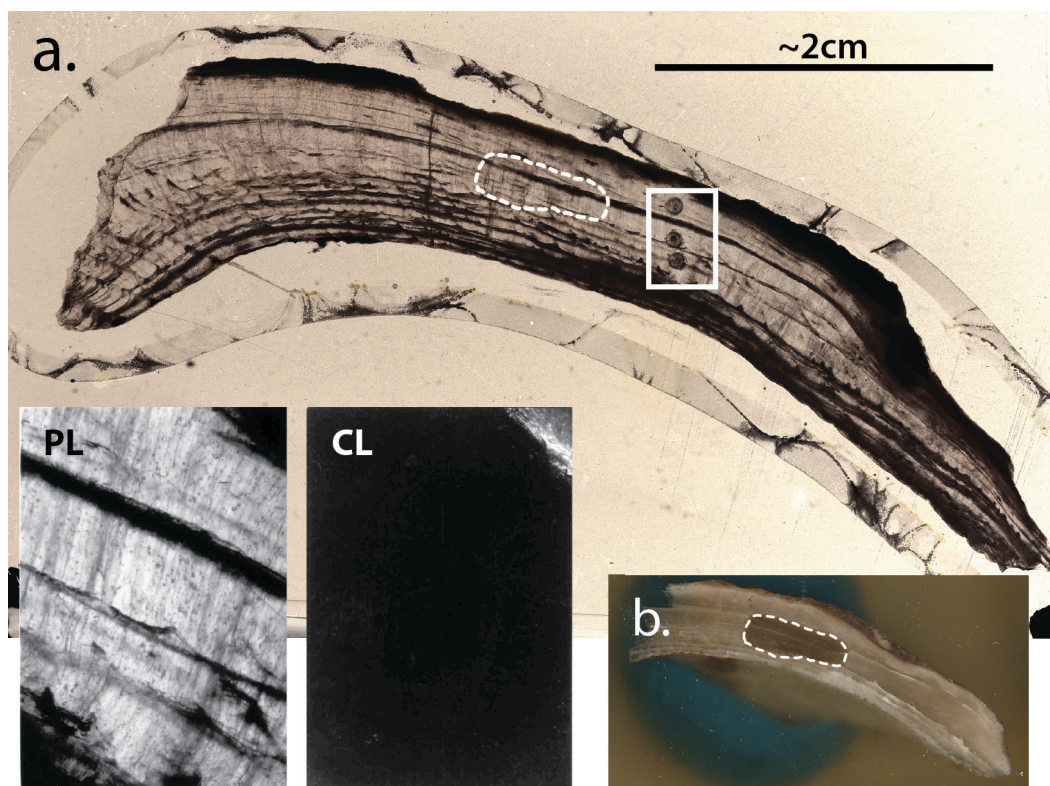


Figure A4.11. Scanned thin section (a) and billet (b) of brachiopod RU073 (cross-sectional perspective). Taxonomic information is listed in Table A4.1. Sample originally collected by Mii et al. (2001). In (a) and (b) the areas inside the dashed lines are regions of shell sub-sampled for carbonate clumped isotope analysis. The white outlined box in (a) corresponds to the plane polarized light (‘PL’) and cathodoluminescence (‘CL’) photomicrographs from Mii et al. (2001). The dark, circular areas inside the white outline in (a) are the sub-sampled regions of Mii et al. (2001).

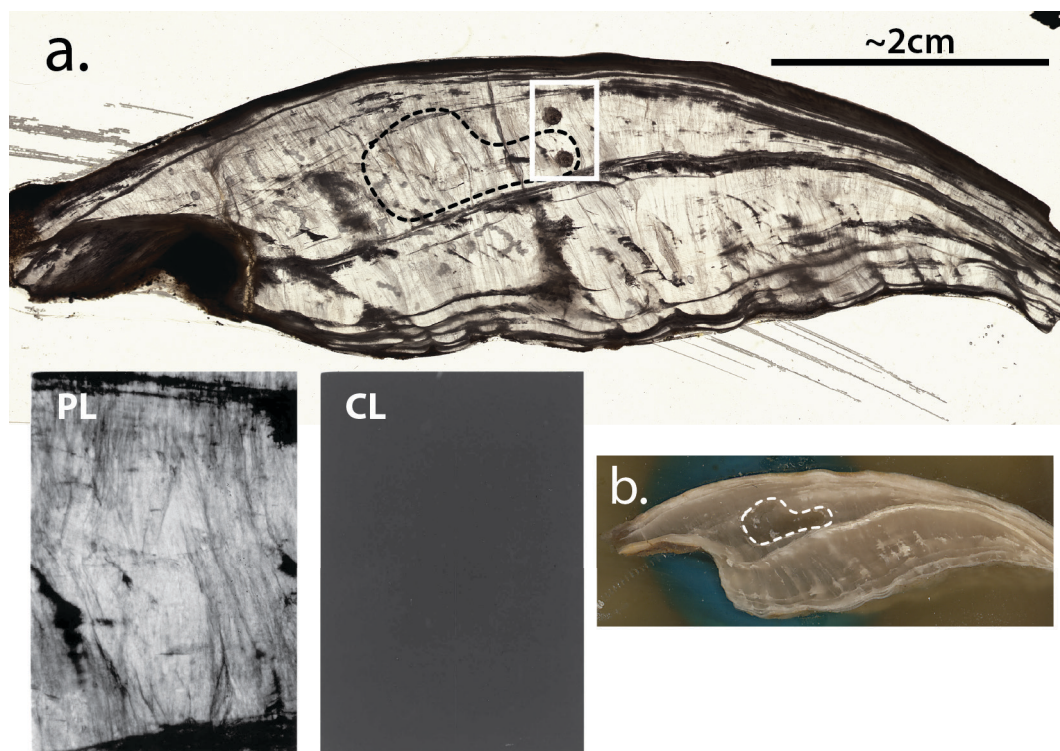


Figure A4.12. Scanned thin section (a) and billet (b) of brachiopod RU071 (cross-sectional perspective). Taxonomic information is listed in Table A4.1. Sample originally collected by Mii et al. (2001). In (a) and (b) the areas inside the dashed lines are regions of shell sub-sampled for carbonate clumped isotope analysis. The white outlined box in (a) corresponds to the plane polarized light (‘PL’) and cathodoluminescence (‘CL’) photomicrographs from Mii et al. (2001). The dark, circular areas inside the white outline in (a) are the sub-sampled regions of Mii et al. (2001).

A4.2 Supplementary data tables for the Phanerozoic carbonate clumped isotope record from brachiopod and mollusk shells

(Tables A4.1, A4.2, and A4.3, *see supplemental files*)

REFERENCES

- Adaddi, L., Raz, S., Weiner, S. (2003). Taking advantage of disorder: amorphous calcium carbonate and its roles in biomineralization. *Adv. Mater.*, 15, 959–970.
- Adlis, D.S., Grossman, E.L., Yancey, T.E., McLerran, R.D. (1998). Isotope stratigraphy and paleodepth changes of Pennsylvanian cyclical sedimentary deposits. *Palaaios*, 3, 487–506.
- Adkins, J.F., Boyle, E.A., Curry, W.B., Lutringer, A. (2003). Stable isotopes in deep-sea corals and a new mechanism for “vital effects”. *Geochim. Cosmochim. Acta*, 67, 1129–1143.
- Affek, H.P., Eiler, J.M. (2006). Abundance of mass 47 CO₂ in urban air, car exhaust, and human breath. *Geochim. Cosmochim. Acta*, 70, 1–12.
- Anderson, T.F. (1969). Self-diffusion of carbon and oxygen in calcite by isotope exchange with carbon dioxide. *J. Geophys. Res.*, 74, 3918–3932.
- Balestreieri M.L., Bernet M., Brandon M.T., Picotti V., Reiners P., Zattin M. (2003) Pliocene and Pleistocene exhumation and uplift of two key areas of the Northern Apennines. *Quatern. Int.*, 101-102, 67-73.
- Banner J.L., Kaufman J. (1994) The isotopic record of ocean chemistry and diagenesis preserved in non-luminescent brachiopods from Mississippian carbonate rocks, Illinois and Missouri. *Geol. Soc. Am. Bull.*, 106, 1074-1082.
- Beck, W.C., Grossman, E.L., Morse, J.W. (2005). Experimental studies of oxygen isotope fractionation in the carbonic acid system at 15°, 25°, and 40°C. *Geochim. Cosmochim. Acta*, 69, 3493–3503.

- Beirne, E.C., Wanamaker, A.D., Jr., Feindel, S.C. (2012). Experimental validation of environmental controls on the $\delta^{13}\text{C}$ of *Arctica islandica* (ocean quahog) shell carbonate. *Geochim. Cosmochim. Acta*, 84, 395–409.
- Bentov, S., Brownlee, C., Erez, J. (2009). The role of seawater endocytosis in the biomineralization process in calcareous foraminifera. *Proc. Natl. Acad. Sci. U.S.A.*, 106, 21500–21504.
- Bernet M. (2002) Exhuming the Alps through time: Clues from detrital zircon fission-track ages, Ph.D. dissertation, Yale University.
- Bishop J.W., Montañez I.P., Gulbranson E.L., Brenckle P.L. (2009) The onset of mid-Carboniferous glacio-eustasy: Sedimentologic and diagenetic constraints, Arrow Canyon, Nevada. *Palaeogeogr. Palaeoclim. Palaeoecol.*, 276, 217-243.
- Blackmer G.C., Omar G.I., Gold D.P. (1994) Post-Alleghanian unroofing history of the Appalachian Basin, Pennsylvania, from apatite fission track analysis and thermal models. *Tectonics*, 13, 1259-1276.
- Boely, T., Gastellu-Etchegorry, J.P., Potier, M., and Nurhakim, S. (1990) Seasonal and interannual variations of the sea surface temperatures (SST) in the Banda and Arafura Sea Area. *Neth. J. Sea Res.*, 25, 425-429.
- Brand, U., Posenato, R., Came, R., Affek, H., Angiolini, L., Azmy, K., Farabegoli, E. (2012). The end-Permian mass extinction: A rapid volcanic CO₂ and CH₄-climatic catastrophe. *Chem. Geol.*, 322–323, 121–144.
- Buening, N., Spero, H.J. (1996). Oxygen- and carbon-isotope analyses of the articulate brachiopod *Laqueus californianus*: a recorder of environmental changes in the subeuphotic zone. *Mar. Biol.*, 127, 105–114.

- Came, R.E., Brand, U., and Affek, H.P. (2014) Clumped isotope signatures in modern brachiopod carbonate. *Chem. Geol.*, 377, 20-30.
- Came, R.E., Eiler, J.M., Veizer, J., Azmy, K., Brand, U., Weidman, C.R.. (2007). Coupling of surface temperatures and atmospheric CO₂ concentrations during the Palaeozoic era. *Nature*, 449, 98–201.
- Carmignani L., Kligfield, R. (1990). Crustal extension in the northern Apennines: The transition from compression to extension in the Alpi Apuane core complex. *Tectonics*, 9, 1275–1303.
- Carpenter, S.L., Lohmann, K.C. (1995). $\delta^{18}\text{O}$ and $\delta^{13}\text{C}$ values of modern brachiopod shells. *Geochim. Cosmochim. Acta*, 59, 3749–3764.
- Carroll, M.L., Ambrose, W.G., Jr., Levin, B.S., Ryan, S.K., Ratner, A.R., Henkes, G.A., Greenacre, M.J.. (2011). Climatic regulation of *Clinocardium ciliatum* (bivalvia) growth in the northwestern Barents Sea. *Palaeogeogr. Palaeoclimatol. Palaeoecol.*, 302, 10–20.
- Castraño, J.R., Sparks, D.M. (1974). Interpretation of vitrinite reflectance measurements in sedimentary rocks and determination of burial history using vitrinite reflectance and authigenic minerals. *Geol. Soc. Am. Spec. Paper*, 153, 31–52.
- Caudill, M. R., Driese S. G., Mora C. I. (1997) Physical compaction of vertic palaeosols: implications for burial diagenesis and palaeo-precipitation estimates. *Sedimentology*, 44, 673-685.
- Chacko, T., Mayeda, T.K., Clayton, R.N., Goldsmith, J.R.. (1991). Oxygen and carbon isotope fractionations between CO₂ and calcite. *Geochim. Cosmochim. Acta*, 55, 2867–2882

- Cohen, A.L., McConnaughey, T.A. (2003). Geochemical perspectives on coral mineralization. Dove, P.M., De Yoreo, J.J., Weiner, S. (Eds.), *Biomineralization*, Reviews in Mineralogy and Geochemistry, Washington, 151–182.
- Cole, D.R., Chakraborty, S. (2001). Rates and mechanisms of isotope exchange. *Rev. Mineral. Geochem.*, 43, 83–223.
- Compston, W. (1960). The carbon isotopic composition of certain marine invertebrates and coals from the Australian Permian. *Geochim. Cosmochim. Acta*, 18, 1–22.
- Crenshaw, M.A. (1972). The inorganic composition of molluscan extrapallial fluid. *Biol. Bull.*, 143, 506–512.
- Criss, R.E. (1999). Principles of stable isotope distribution. Oxford University Press, New York.
- Csank, A.Z., Tripathi, A.K., Patterson, W.P., Eagle, R.A., Rybczynski, N., Ballantyne, A.P., Eiler, J. (2011). Estimates of Arctic land surface temperatures during the early Pliocene from two novel proxies. *Earth Planet. Sci. Lett.*, 304, 291–299.
- Cummins, R.C., Finnegan, S., Fike, D.A., Eiler, J.M., and Fischer, W.W., 2014, Carbonate clumped isotope constraints on Silurian ocean temperature and seawater $\delta^{18}\text{O}$. *Geochim. Cosmochim. Acta*, 140, 241–258.
- Cusack, M., Dauphin, Y., Chung, P., Pérez-Huerta, A., Cuif, J.-P. (2008). Multiscale structure of calcite fibres of the shell of the brachiopod *Terebratulina retusa*. *J. Struct. Biol.*, 164, 96–100.
- Dennis, K.J., Schrag, D.P. (2010). Clumped isotope thermometry of carbonatites as an indicator of diagenetic alteration. *Geochim. Cosmochim. Acta*, 74, 4110–4122.

- Dennis, K.J., Affek, H.P., Passey, B.H., Schrag, D.P., Eiler, J.M. (2011). Defining an absolute reference frame for ‘clumped’ isotope studies of CO₂. *Geochim. Cosmochim. Acta*, 75, 7117–7131.
- Dennis, K.J., Cochran, J.K., Landman, N.H., Schrag, D.P. (2013). The climate of the Late Cretaceous: New insights from the application of the carbonate clumped isotope thermometer to Western Interior Seaway macrofossil. *Earth Planet. Sci. Lett.*, 362, 51–65.
- Dickinson W.R. (2006) Geotectonic evolution of the Great Basin. *Geosphere*, 2, 353–368.
- Dietrich, D., Lampke, T., Rößler, R. (2013) A microstructure study on silicified wood from the Permian petrified forest of Chemnitz. *Paläont. Zeitsch.*, 87, 397–407.
- Dixon, M.D., Haig, D.W. (2004). Foraminifera and their habitats within a cool-water carbonate succession following glaciation, Early Permian (Sakmarian), Western Australia. *J. Foram. Res.*, 34, 308–324.
- Donelick, R.A., O’Sullivan, P.B., Ketcham, R.A. (2005). Apatite fission-track analysis. *Rev. Mineral. Geochem.*, 58, 49–94.
- Douglas, P.M.J., Affek, H.P., Ivany, L.C., Houben, A.J.P., Sijp, W.P., Sluijs, A., Schouten, S., and Pagani, M. (2014) Pronounced zonal heterogeneity in Eocene southern high-latitude seas surface temperatures. *Proc. Natl. Acad. Sci. U.S.A.*, 111, 6582–6587.
- Eagle, E.A., Eiler, J.M., Tripathi, A.K., Ries, J.B., Freitas, P.S., Hiebenthal, C., Wanamaker, Jr., A.D., Taviani, M., Elliot, M., Marensi, S., Nakamura, K., Ramirez, P., and Roy, K. (2013) The influence of temperature and seawater carbonate

- saturation state on ^{13}C - ^{18}O bond ordering in bivalve mollusks. *Biogeosci.*, 10, 4591-4606.
- Eigen, M. (1964). Proton transfer, acid–base catalysis, and enzymatic hydrolysis *Angew. Chem. Int. Ed. Engl.*, 3, 1–19.
- Eiler, J.M. (2011). Paleoclimate reconstruction using carbonate clumped isotope thermometry. *Quater. Sci. Rev.*, 30, 3575–3588.
- Eiler, J.M., Schauble, E.A. (2004). ^{18}O ^{13}C ^{16}O in Earth's atmosphere. *Geochim. Cosmochim. Acta*, 68, 4767–4777.
- Epstein, A.G., Epstein, J.B., Harris, L.D. (1977). Conodont color alteration – an index to organic metamorphism. U.S. Geological Survey Professional Paper 995, Washington, DC.
- Epstein, S., Buchsbaum, R., Lowenstam, H.A., Urey, H.C. (1953). Revised carbonate–water isotopic temperature scale. *Geol. Soc. Am. Bull.*, 64, 1315–1325.
- Erez, J. (2003). The source of ions for biomineralization in foraminifera and their implications for paleoceanographic proxies. Dove, P.M., De Yoreo, J.J., Weiner, S. (Eds.), *Biomineralization*, Reviews in Mineralogy and Geochemistry, Washington, 115–144.
- Farver, J.R.. (1994). Oxygen self-diffusion in calcite: Dependence on temperature and water fugacity. *Earth Planet. Sci. Lett.*, 121, 575–587.
- Fellin, M.G., Reiners, P.W., Brandon, M.T., Wuthrich, E., Balestrieri, M.L., Molli, G. (2007). Thermochronologic evidence for the exhumational history of the Alpi Apuane metamorphic core complex, northern Apennines, Italy. *Tectonics*, 26, TC6015

- Fernandez, A., Tang, J., Rosenheim, B.E. (2014) Siderite ‘clumped’ isotope thermometry: A new paleoclimate proxy for humid continental environments. *Geochim. Cosmochim. Acta*, 126, 411-421.
- Ferry, J.M., Passey, B.H., Vasconcelos, C., Eiler, J.M. (2011) Formation of dolomite at 40-80 °C in the Latemar carbonate buildup, Dolomites, Italy, from clumped isotope thermometry. *Geology*, 39, 571-574.
- Finnegan, S., Bergmann, K., Eiler, J.M., Jones, D.S., Fike, D.A., Eisenman, I., Hughes, N.C., Tripathi, A.K., Fischer, W.W. (2011). The magnitude and duration of late Ordovician-Early Silurian glaciation. *Science*, 331, 903–906.
- Flake, R.C. (2011) Circulation of North American epicontinental seas during the Carboniferous using stable isotope and trace element analyses of brachiopod shells. M.S. Thesis, Texas A&M Univ.
- Forster, A., Schouten, S., Baas, M., and Sinninghe Damsté, J.S. (2007) Mid-Cretaceous (Albian-Santonian) sea surface temperature record of the tropical Atlantic Ocean. *Geology*, 35, 919-922.
- Friedlander, G., Kennedy, J.W., Macias, E.S., Miller, J.M.. (1981). Nuclear and radiochemistry. Wiley, New York.
- Garside L.J., Hess R.H. (2007) Petroleum data map of Nevada. Nevada Bureau of Mines and Geology, Reno, NV.
- Gentry, D.K., Sossian, S., Grossman, E.L., Rosenthal, Y., Hicks, D., Lear, C.H. (2008). Stable isotope and Sr/Ca profiles from the marine gastropod *Conus ermineus*: testing a multiproxy approach for inferring paleotemperature and paleosalinity. *Palaios*, 23, 195–209.

- Ghosh, P., Garzione, C.N., Eiler, J.M. (2006a) Rapid uplift of the Altiplano revealed through ^{13}C – ^{18}O bonds in paleosol carbonates. *Science*, 311, 511–515.
- Ghosh, P., Adkins, J., Affek, H., Balta, B., Guo, W., Schauble, E.A., Schrag, D.P., Eiler, J.M. (2006b). ^{13}C – ^{18}O bond in carbonate minerals: a new kind of paleothermometer. *Geochim. Cosmochim. Acta*, 70, 1439–1456.
- Ghosh, P., Eiler, J., Campana, S.E., Feeney, R.F. (2007). Calibration of the carbonate ‘clumped isotope’ paleothermometer for otoliths. *Geochim. Cosmochim. Acta*, 71, 2736–2744.
- Glasmacher U.A., Wagner G.A., Puchkov V.N. (2002) Thermotectonic evolution of the western fold-and-thrust belt, southern Uralides, Russia, as revealed by apatite fission track data. *Tectonophys.* 354, 25-48.
- Goodwin, D.H., Schöne, B.R., Dettman, D.L. (2003). Resolution and fidelity of oxygen isotopes as paleotemperature proxies in bivalve mollusk shells: models and observations. *Palaaios*, 18, 110–125.
- Gregory, R.T., and Taylor, H.P. (1981) An oxygen isotope profile in a section of Cretaceous oceanic crust, Samail Ophiolite, Oman: Evidence for $\delta^{18}\text{O}$ buffering of the oceans by deep (>5 km) seawater-hydrothermal circulation at mid-ocean ridges. *J. Geophys. Res.*, 86, 2737-2755.
- Grellet-Tinner, G., Murelaga, X., Larrasoaña, J.C., Silveira, L.F., Olivares, M., Ortega, L.A., Trimby, P.W., Pascual, A. (2012). The first occurrence in the fossil record of an aquatic avian twig-nest with Phoenicopteriformes eggs: evolutionary implications *PLOS One*, 7, e46972

- Guo, W. (2009). Carbonate clumped isotope thermometry: application to carbonaceous chondrites and effects of kinetic isotope fractionation. Ph. D. thesis, California Institute of Technology.
- Guo, W., Mosenfelder, J.L., Goddard, III W.A., Eiler, J.M. (2009). Isotopic fractionations associated with phosphoric acid digestion of carbonate minerals: insight from first-principles theoretical modeling and clumped isotope measurements. *Geochim. Cosmochim. Acta*, 73, 7203–7225.
- Guo, W., Kim, S.-T., Yuan, J., Farquhar, J., Passey, B.H. (2012). ^{13}C – ^{18}O bonds in dissolved inorganic carbon: toward a better understanding of clumped isotope thermometer in biogenic carbonates. *Mineral. Mag.*, 76, 1791.
- Grossman, E.L. (2012a). Applying oxygen isotope paleothermometry in deep time. In *Reconstructing Earth's Deep-Time Climate*. Ivany, L., Huber, B. (Eds.), The Paleontological Society Papers, 18, 39–67.
- Grossman, E.L. (2012b) Ch. 10. Oxygen isotope stratigraphy. Gradstein, E.M., Ogg, J.G., Schmitz, M., Ogg, G. (Eds.), *The Geologic Time Scale 2012*, pp. 195–220.
- Grossman E.L., Bruckschen P., Mii H.-S., Chuvashov B.I., Yancey T.E., Veizer J. (2002) Carboniferous paleoclimate and global change: Isotopic evidence from the Russian Platform, in: *Carboniferous stratigraphy and Paleogeography in Eurasia*. Institute of Geology and Geochemistry, Russian Academy of Sciences, Urals Branch, Ekaterinburg, pp. 61-71.
- Grossman, E.L., Yancey, T.E., Jones, T.E., Bruckschen, P., Chuvashov, B., Mazzullo, S.J., and Mii, H.-S. (2008) Glaciation, aridification, and carbon sequestration in the

- Permo-Carboniferous: The isotopic record from low latitudes. *Palaeogeogr. Palaeoclimatol. Palaeoecol.*, 268, 222-233.
- Grossman, E.L., Ku, T.-L. (1986). Oxygen and carbon isotope fractionation in biogenic aragonite: temperature effects. *Chem. Geol.*, 59, 59–74.
- Grossman, E.L., Mii, H.-S., Zhang, C., Yancey, T.E. (1996). Chemical variation in Pennsylvanian brachiopod shells—diagenetic, taxonomic, microstructural, and seasonal effects. *J. Sed. Res.*, 66, 1011–1022
- Guo, W., Mosenfelder, J.L., Goddard, III, W.A., Eiler, J.M. (2009). Isotopic fractionations associated with phosphoric acid digestion of carbonate minerals: Insights from first-principles theoretical modeling and clumped isotope measurements. *Geochim. Cosmochim. Acta*, 73, 7203–7225.
- Harris, C.L., Plueddemann, A.J., Gawarkiewicz, G.G. (1998). Water mass distribution and polar front structure in the western Barents Sea. *J. Geophys. Res.*, 103, 2905–2917.
- Hedges, J.I., Prahl, F.G. (1993) Early diagenesis: Consequences for application of molecular biomarkers. Engel, M.H., Macko, S.A. (Eds.), *Organic Geochemistry*, pp. 237–253.
- Hicks, D.W., McMahon, R.F. (2002) Temperature acclimation of upper and lower thermal limits and freeze resistance in the nonindigenous brown mussel, *Perna perna* (L.), from the Gulf of Mexico. *Mar. Biol.*, 140, 1167-1179.
- Huber, M. (2012) Progress in Greenhouse Climate Modeling In Reconstructing Earth's Deep-Time Climate. Ivany, L., Huber, B. (Eds.), *The Paleontological Society Papers*, 18, 213-262.

- Huber, M., Caballero, R. (2011) The early Eocene equable climate problem revisited. *Climates of the Past*, 7, 603–633.
- Huntington, K.W., Eiler, J.M., Affek, H.P., Guo, W., Bonifacie, M., Yeung, L.Y., Thiagarajan, N., Passey, B.H., Tripathi, A., Daëron, M., Came, R. (2009). Methods and limitations of ‘clumped’ CO₂ isotope (Δ_{47}) analysis by gas-source isotope ratio mass spectrometry. *J. Mass Spectrom.*, 44, 1318–1329.
- Jacob, D.E., Wirth, R., Soldati, A.L., Wehrmeister, U., Schreiber, A. (2011) Amorphous calcium carbonate in the shells of adult Unionoida. *J. Struct. Biol.*, 173, 241–249.
- Jackson, J.B.C., Winston, J.E. (1982). Ecology of cryptic coral reef communities: 1. Distribution and abundance of major groups of encrusting organisms. *J. Exp. Mar. Biol. Ecol.*, 57, 135–147.
- Jaffrés, J.B.D., Shields, G.A., Wallmann, K. (2011) The oxygen isotope evolution of seawater: A critical review of a long-standing controversy and an improved geological water cycle model for the past 3.4 billion years. *Earth-Sci. Rev.*, 83, 83–122.
- Joachimski, M.M., Breisig, S., Buggisch, W., Talent, J.A., Mawson, R., Gereke, M., Morrow, J.R., Day, J., Weddige, K. (2009) Devonian climate and reef evolution: Insights from oxygen isotopes in apatite. *Earth Planet. Sci. Lett.*, 284, 599–609.
- Johannessen, O.M., Foster, L.A. (1978). A note on the topographically controlled oceanic Polar Front in the Barents Sea. *J. Geophys. Res.*, 83, 4567–4571.
- Jones, T.E., Grossman, E.L., Yancey, (2003). T.E. Exploring the stable isotope record of global change and paleoclimate: the mid-Carboniferous GSSP (Arrow Canyon, Nevada) and the Ural Mountains, Russia. *Geol. Soc. Amer. Abs.*, 35, 254.

- Kasting, J.F., Howard, M.T., Wallmann, K., Veizer, J., Shields, G., Jaffrés, J. (2006) Paleoclimates, ocean depth, and the oxygen isotopic composition of seawater. *Earth Planet. Sci. Lett.*, 252, 82-93.
- Kaufman J., Cander H.S., Daniels L.D., Meyers W.J. (1988) Calcite cement stratigraphy and cementation history of the Burlington-Keokuk Formation (Mississippian), Illinois and Missouri. *J. Sediment. Petrol.*, 58, 312-326.
- Keating-Bitonti, C.R., Ivany, L.C., Affek, H.P., Douglas, P., Samson, S.D. (2011). Warm, not super-hot, temperatures in the early Eocene subtropics. *Geology*, 39, 771–774.
- Ketcham, R.A. (2005). Forward and inverse modeling of low-temperature thermochronometry data. *Rev. Mineral. Geochem.*, 58, 275–314.
- Kim, S.-T., O’Neil, J.R.. (1997). Equilibrium and nonequilibrium oxygen isotope effects in synthetic carbonates. *Geochim. Cosmochim. Acta*, 61, 3461–3475.
- Kim, S.-T., O’Neil, J.R., Hillaire-Marcel, C., Mucci, A. (2007). Oxygen isotope fractionation between synthetic aragonite and water: influence of temperature and Mg^{2+} concentration. *Geochim. Cosmochim. Acta*, 71, 4704–4715.
- Kittel, C. (2005). Introduction to Solid State Physics (8th ed.). John Wiley & Sons Inc, New Jersey.
- Kligfield, R., Hunziker, J., Dallmeyer, R.D. (1986). Dating of deformation phases using K–Ar and $^{40}Ar/^{39}Ar$ techniques: results from the Northern Apennines. *J. Struct. Geol.*, 8, 781–798.
- Knudsen, K.L., Eiriksson, J., Jansen, J., Jiang, H., Rytter, F., Gudmundsdottir, E.R. (2004). Paleoceanographic changes off North Iceland through the last 1200 years:

- foraminifera, stable isotope, diatoms, and ice-rafted debris. *Quatern. Sci. Rev.*, 23, 2231–2246.
- Kronenberg, A.K., Yund, R.A., Giletti, B.J. (1984). Carbon and oxygen diffusion in calcite: Effects of Mn content and P_{H_2O} . *Phys. Chem. Minerals*, 11, 101–112.
- Labotka, T.C., Cole, D.R., Fayek, M.T., Chacko, T. (2011). An experimental study of the diffusion of C and O in calcite in mixed CO₂–H₂O fluids. *Am. Mineral.*, 96, 1262–1269.
- Land, L.S.. (1995). Oxygen and carbon isotopic composition of Ordovician brachiopods: implications for coeval seawater: discussion. *Geochim. Cosmochim. Acta*, 59, 2843–2844.
- Land, L.S., Lynch, F.L. (1996) $\delta^{18}O$ values of mudrocks: more evidence for an ^{18}O -buffered ocean. *Geochim. Cosmochim. Acta*, 60, 3347-3352.
- Lasaga, A.C. (1998). Kinetic Theory in the Earth Sciences. Princeton University Press, New Jersey.
- LeGrande, A.N., Schmidt, G.A. (2006). Global gridded data set of the oxygen isotopic composition in seawater. *Geophys. Res. Lett.*, 33, L12604 5pp.
- Lowenstam, H.A., Weiner, S. (1989). On Biomineralization, Oxford University Press, New York, 99–103.
- Nardi L. (1977) Segnalazione di lepidocycline nella parte basale dello “pseudomacigno” delle Alpi Apuane. *Boll. Soc. Geol. Ital.*, 95, 459-477.
- McConnaughey, T.A., Gillikin, D.P. (2008). Carbon isotopes in mollusk shell carbonates. *Geo-Mar. Lett.*, 28, 287–299.

- Martin, L.G., Montanez, I.P., Bishop, J.W. (2012). A paleotropical carbonate-dominated archive of Carboniferous icehouse dynamics, Bird Spring Fm., Southern Great Basin, USA. *Palaeogeogr. Palaeoclimatol. Palaeoecol.*, 329–330, 64–82.
- Matenaar I., Glasmacher U.A., Pickel W., Giese U., Pazukhin V.N., Kozlov V.I., Puchkov V.N., Stroink L., Walter R. (1999) Incipient metamorphism between Ufa and Beloretsk, western fold-and-thrust belt, southern Urals, Russia. *Geol. Rundsch.*, 87, 545-560.
- Mii, H.-S., Grossman, E.L.. (1994). Late Pennsylvanian seasonality reflected in the ^{18}O and elemental composition of a brachiopod shell. *Geology*, 22, 661–664.
- Mii, H.-S., Grossman, E.L., Yancey, T.E.. (1997). Stable carbon and oxygen isotope shifts in Permian seas of West Spitsbergen—global change or diagenetic artifact? *Geology*, 25, 227–230.
- Mii, H.-S., Grossman, E.L., Yancey, T.E.. (1999). Carboniferous isotope stratigraphies of North America: Implications for Carboniferous paleoceanography and Mississippian glaciation. *Geol. Soc. Am. Bull.*, 111, 960–973.
- Mii, H.-S., Grossman, E.L., Yancey, T.E., Chuvashov, B., Egorov, A. (2001). Isotopic records of brachiopod shells from the Russian Platform – evidence for the onset of mid-Carboniferous glaciation. *Chem. Geol.*, 175, 133–147.
- Mook, W.G.. (1986). ^{13}C in atmospheric CO_2 . *Neth. J. Sea Res.*, 20, 211–223.
- Mora C.I., Sheldon B.T., Elliott W.C., Driese S.G. (1998) An oxygen isotope study of illite and calcite in three Appalachian Paleozoic vertic paleosols. *J. Sediment. Res.*, 68, 456-464.

- Mory, A.J., Haig, D.W. (2011). Permian-Carboniferous geology of the Northern Perth and Southern Carnarvon basins, Western Australia – a field guide. Geological Survey of Western Australia, Perth.
- Muehlenbachs, K. (1998) The oxygen isotopic composition of the oceans, sediments and the seafloor. *Chem. Geol.*, 145, 263-273.
- Muehlenbachs, K., Clayton, R.N. (1976) Oxygen isotope composition of the oceanic crust and its bearing on seawater. *J. Geophys. Res.*, 81, 4365-4369.
- Müller, P.J., Kirst, G., Ruhland, G., von Storch, I., Rosell-Melé, A. (1998) Calibration of the alkenone paleotemperature index $U_{37}^{K'}$ based on core-tops from the eastern South Atlantic and the global ocean (60°N-60°S). *Geochim. Cosmochim. Acta*, 62, 1757-1772.
- O’Leary, M.H. (1984). Measurement of the isotope fractionation associated with diffusion of carbon dioxide in aqueous solution. *J. Phys. Chem.*, 88, 823–825.
- O’Neil, J.R., Clayton, R.N., Mayeda, T.K. (1969). Oxygen isotope fractionation in divalent metal carbonates. *J. Chem. Phys.*, 51, 5547–5558.
- Passey, B.H., Henkes, G.A. (2012). Carbonate clumped isotope bond reordering and geospeedometry. *Earth Planet. Sci. Lett.*, 351–352, 223–236.
- Passey, B.H., Levin, N.E., Cerling, T.E., Brown, F.H., Eiler, J.M. (2010). High-temperature environments of human evolution in East Africa based on bond ordering in paleosol carbonates. *Proc. Natl. Acad. Sci. U.S.A.*, 107, 11245–11249.
- Pearson, P.N., van Dongen, B.E., Nicholas, C.J., Pancost, R.D., Schouten, S., Singano, J.M., Wade, B.S. (2007) Stable warm tropical climate through the Eocene epoch. *Geology*, 35, 211-214.

- Pérez-Huerta, A., Cusack, M., England, J. (2007). Crystallography and diagenesis in fossil craniid brachiopods. *Palaeontology*, 50, 757–763.
- Pérez-Huerta, A., Cusack, M., Méndez, C.A. (2012). Preliminary assessment of the use of electron backscatter diffraction (EBSD) in conodonts. *Lethaia*, 45, 253–258
- Popp, B.N., Anderson, T.F., Sandberg, P.A. (1986). Brachiopods as indicators of original isotopic compositions in some Paleozoic limestones. *Geol. Soc. Am. Bull.*, 97, 1262–1269.
- Preston-Thomas, H. (1990). The international temperature scale of 1990 (ITS-90). *Metrologia*, 27, 3–10.
- Price, G.D., Passey, B.H.. (2013). Dynamic polar climate in a greenhouse world: evidence from clumped isotope thermometry of Early Cretaceous belemnites. *Geology*, 41, 923–926.
- Proust J.N., Chuvashov B.I., Vennin E., Boisseau T. (1998) Carbonate platform drowning in a foreland setting: The mid-Carboniferous platform in western Urals (Russia). *J. Sediment. Res.*, 68, 1175-1188.
- Radha, A.V., Forbes, T.Z., Killian, C.E., Gilbert, P.U.P.A., Navrotsky, A. (2010). Transformation and crystallization energetic of synthetic and biogenic amorphous calcium carbonate. *Proc. Natl. Acad. Sci. U.S.A.*, 107, 16438–16443.
- Ravaux, J., Hamel, G., Zbinden, M., Tasiemski, A.A., Boutet, I., Léger, N., Tanguy, A., Jollivet, D., Shillito, B. (2013). Thermal limit for metazoan life in question: In vivo heat tolerance of the Pompeii worm. *PLOS One*, 8, e64074.

- Reed, J.S., Spotila, J.A., Eriksson, K.A., Bodnar, R.J. (2005). Burial and exhumation history of Pennsylvanian strata, central Appalachian basin: an integrated study. *Basin Res.*, 17, 259–268.
- Reis, J.B. (2004) Effect of ambient Mg/Ca ratio on Mg fractionation in calcareous marine invertebrates: A record of the oceanic Mg/Ca ratio over the Phanerozoic. *Geology*, 32, 981-984.
- Rooker, J.R., Dennis, G.D. (1991). Diel, lunar and seasonal changes in a mangrove fish assemblage off southwestern Puerto Rico. *Bull. Mar. Sci.*, 49, 684–698.
- Rowan, E.L., Goldhaber, M.B., Hatch, J.R. (2002). Regional fluid flow as a factor in the thermal history of the Illinois Basin: Constrains from fluid inclusions and the maturity of Pennsylvanian coals. *AAPG Bull.*, 86, 257–277.
- Schauble, E.A., Ghosh, P., Eiler, J.M. (2006). Preferential formation of ^{13}C – ^{18}O bonds in carbonate minerals, estimated using first-principles lattice dynamics. *Geochim. Cosmochim. Acta*, 70, 2510–2529.
- Schrag, D.P., DePaolo, D.J. (1993). Determination of $\delta^{18}\text{O}$ of seawater in the deep ocean during the last glacial maximum. *Paleoceanography*, 8, 1–6.
- Shenton, B.J., Grossman, E.L., Passey, B.H., Henkes, G.A., Becker, T.P., Laya, J.C., Pérez-Huerta, A., Becker, S.P., Lawson, M., *submitted*, Clumped isotope thermometry in deeply buried sedimentary carbonates: The effects of bond reordering and recrystallization. *Geol. Soc. Am. Bull.*
- Sheehan, P.M.. (2001). The late Ordovician mass extinction. *Annu. Rev. Earth Planet. Sci.*, 29, 331–364.

- Skagseth, Ø., Furevik, T., Ingvaldsen, R., Loeng, H., Mork, K.A., Orvik, K.A., Ozhigin, V. (2008). Volume and heat transports to the Arctic Ocean via the Norwegian and Barents Seas. *Arctic–Subarctic Ocean Fluxes: Defining the Role of the Northern Sea in Climate*, Springer, The Netherlands, 45–64.
- Spero, H.J., Bijma, J., Lea, D.W., Bemis, B.E. (1997). Effect of seawater carbonate concentration on foraminiferal carbon and oxygen isotopes. *Nature*, 390, 497–500.
- Suarez, M.B., Passey, B.H., Kaakinen A. (2011). Paleosol carbonate multiple isotopogue signature of active East Asian summer monsoons during the late Miocene and Pliocene. *Geology*, 39, 1151–1154.
- Thiagarajan, N., Adkins, J., Eiler, J. (2011). Carbonate clumped isotope thermometry of deep-sea coral and implications for vital effects. *Geochim. Cosmochim. Acta*, 75, 4416–4425.
- Tripathi, A.K., Eagle, R.A., Thiagarajan, N., Gagnon, A.C., Bauch, H., Halloran, P.R., Eiler, J.M. (2010). ^{13}C – ^{18}O isotope signatures and ‘clumped isotope’ thermometry in foraminifera and coccoliths. *Geochim. Cosmochim. Acta*, 74, 5697–5717.
- Trotter, J.A., Williams, I.S., Barnes, C.R., Lécuyer, C., Nicoll, R.S. (2008). Did cooling oceans trigger Ordovician biodiversification? Evidence from conodont thermometry. *Science*, 321, 550–554.
- Udowski, E., Michaelis, J., Bottcher, M.E., Hoefs, J. (1991). Factors for the oxygen isotope equilibrium fractionation between aqueous and gaseous CO_2 , carbonic-acid, bicarbonate, carbonate, and water (19 °C). *Z. Phys. Chem. Neue Folge*, 170, 237–249.
- Veizer, J. (1995). Oxygen and carbon isotopic composition of Ordovician brachiopods: implications for coeval seawater: Reply. *Geochim. Cosmochim. Acta*, 59, 2845–2846.

- Veizer, J., Fritz, P., Jones, B.. (1986). Geochemistry of brachiopods: oxygen and carbon isotopic records of Paleozoic oceans. *Geochim. Cosmochim. Acta*, 50, 1679–1696.
- Veizer, J., Ala, D., Azmy, K., Bruckschen, P., Buhl, D., Bruhn, F., Carden, G.A.F., Diener, A., Ebner, S., Godderis, Y., Jasper, T., Korte, C., Pawellek, F., Podlaha, O.G., Strauss, H. (2009). $^{87}\text{Sr}/^{86}\text{Sr}$, $\delta^{13}\text{C}$ and $\delta^{18}\text{O}$ evolution of Phanerozoic seawater. *Chem. Geol.*, 161, 59–88.
- Wacker, U., Fiebig, J., Schoene, B.R. (2013) Clumped isotope analysis of carbonates: comparison of two different acid digestion techniques. *Rapid Commun. Mass Spectrom.*, 27, 1631-1642.
- Wanamaker, Jr., A.D., Heinemeier, J., Scourse, J.D., Richardson, C.A., Butler, P.G., Eiriksson, J., Knudsen, K.L. (2008). Very long-lived mollusks confirm 17th century AD tephra-based radiocarbon reservoir ages for North Icelandic Shelf waters. *Radiocarbon*, 50, 399–412.
- Wanamaker, Jr., A.D., Hetzinger, S., Halfar, J. (2011). Reconstructing mid- to high-latitude marine climate and ocean variability using bivalves, coralline algae, and marine sediment cores from the Northern Hemisphere. *Palaeogeogr. Palaeoclimatol. Palaeoecol.*, 302, 1–9.
- Wanamaker, Jr., A.D., Kreutz, K.J., Borns, Jr., H.W., Introne, D.S., Feindel, S., Funder, S., Rawson, P.D., Barber, B.J. (2007). Experimental determination of salinity, temperature, growth and metabolic effects on shell isotope chemistry of *Mytilus edulis* collected from Maine and Greenland. *Paleoceanography*, 22, PA2217, 12 pp.

- Wang, Z., Schauble, E.A., Eiler, J.M. (2004). Equilibrium thermodynamics of multiply substituted isotopologues of molecular gases. *Geochim. Cosmochim. Acta*, 68, 4779–4797.
- Weiner, S., Dove, P.M. (2003). An overview of biomineralization processes and the problem of the vital effect. Dove, P.M., De Yoreo, J.J., Weiner, S. (Eds.), *Biomineralization*, Reviews in Mineralogy and Geochemistry, Washington, 1–29.
- Weiss, I.M., Tuross, N., Addadi, L., Weiner, S. (2002). Mollusc larval shell formation: amorphous calcium carbonate is a precursor phase for aragonite. *J. Exp. Zool.*, 293, 478–491.
- Winter, A., Appeldoorn, R.S., Bruckner, A., Williams, Jr., E.H., Goenaga, C. (1998). Sea surface temperature and coral reef bleaching off La Parguera, Puerto Rico (northeastern Caribbean Sea). *Coral Reefs*, 17, 377–382.
- Zaarur, S., Olack, G., Affek, H.P. (2011). Paleo-environmental implication of clumped isotopes in land snail shells. *Geochim. Cosmochim. Acta*, 75, 6859–6869.
- Zeebe, R.E., Wolf-Gladrow, D. (2001). *CO₂ in seawater: equilibrium, kinetics, isotopes*. Elsevier Oceanography Series, 65, 4–10.
- Zhang, J., Quay, P.D., Wilbur, D.O. (1995). Carbon isotope fractionation during gas-water exchange and dissolution of CO₂. *Geochim. Cosmochim. Acta*, 59, 107–114.
- Zhang, Y. (2010). Diffusion in Minerals and Melts: Theoretical Background. *Rev. Mineral. Geochem.*, 72, 5–59.

CURRICULUM VITAE

Gregory A. Henkes

Department of Earth & Planetary Sciences, The Johns Hopkins University
301 Olin Hall, 3400 N. Charles St., Baltimore, Maryland, 21218
Phone: (410) 516-7135, Fax: (410) 516-7933
Email: ghenkes1@jhu.edu, Website: www.gahenkes.com

Education

- 2014* Doctor of Philosophy in Geochemistry, Johns Hopkins University
 *Expected to be conferred December 2014 and defended September 2014
 Advisor: Benjamin Passey
 Dissertation: Carbonate clumped isotope geochemistry of marine mollusk and brachiopod shells and its application to deep-time paleoclimatology
- 2008 Bachelor of Science in Biology, Bates College
 Advisors: William Ambrose (Biology) and Beverly Johnson (Geology)
 Senior Thesis: Mineral and stable isotope geochemistry evidence for environmental change from the shells of the Smooth Greenland Cockle, *Serripes groenlandicus*, from the Barents Sea
- Fall 2006 Semester in Environmental Science, Marine Biological Laboratory
 Advisor: Kenneth Foreman
 Independent Study: Tracing sources of nitrogen for primary producers in West Falmouth Harbor, MA, by examining the $\delta^{15}\text{N}$ values of macroalgae and nitrates in local groundwaters

Laboratory Experience

- 2010 – Present Research Assistant, Johns Hopkins University
 Carbonate clumped isotope analysis, carbonate heating experiments, triple oxygen isotope analysis of carbonates and waters, electron microprobe analysis, x-ray diffraction analysis, petrographic and cathodoluminescence microscopy of carbonates, operation and maintenance of vacuum line for gas preparation, and wet chemistry.
- 2008 – 2009 Stable Isotope Laboratory Manager, Smithsonian Institution
 Installation and operation of two stable isotope ratio mass spectrometers configured for analysis of $\delta^{13}\text{C}$, $\delta^{15}\text{N}$, $\delta^{18}\text{O}$, and δD in organic matter (animal tissues, soil/sediment, feathers), $\delta^{13}\text{C}$ and $\delta^{18}\text{O}$ in carbonates (shell, plaster), and $\delta^{34}\text{S}$ in sulfide minerals.

Teaching Experience

- 2012, 2014 Teaching Assistant, Johns Hopkins University, Department of Earth & Planetary Sciences
 “Introduction to Global Environmental Change”, “Oceans & Atmospheres”
- 2011 – 2014 Guest Lecturer, Johns Hopkins University, Department of Earth & Planetary Sciences
 “Introduction to Global Environmental Change”, “Isotope Geochemistry”,
 “Climates of the Past”, “Ocean Biogeochemical Cycles”
- 2007 – 2008 Teaching Assistant & Technical Writing Assistant, Bates College,
 Department of Biology
 “Organismal Biology”, “Cellular and Molecular Biology”, “Ecology and Evolution”

Field Experience

- 2011 *Perth and Carnarvon Basins*, Western Australia – collection of Permian and Carboniferous marine invertebrate fossils.
- 2011 *Cape Eleuthera*, The Bahamas – SCUBA survey and collection of warm-water biogenic carbonates.
- 2009 – 2013 *Chesapeake Bay*, Maryland, USA – archaeological excavation of Holocene shell middens and vessel-based sampling of oyster reefs.
- 2005 – 2010 *Gulf of Maine*, Maine, USA – SCUBA sample collection, environmental monitoring, mud-flat ecology field experiments, sediment respiration incubations.
- 2007 *Barents Sea*, Norway – ship-based physical and biological oceanography, benthic trawl collection of marine invertebrates.
- 2006 *Buzzards Bay*, Massachusetts, USA – near-shore sampling of waters and dissolved nitrate and ammonium, aquatic and terrestrial ecological surveys.
- 2006 *Great Bay-Mullica River*, New Jersey, USA – hook-and-line fishing and underwater acoustic telemetry to track fish movement.
- Other Skills: PADI certified Rescue Diver (SCUBA), USCG small passenger vessel safety certification, basic navigation

Awards and Fellowships

- 2012 *Student Travel Grant Award*, V.M. Goldschmidt Conference, Montreal, Canada
- 2010 *Honorable Mention*, National Science Foundation Graduate Research Fellowship
- 2009 – 2010 *Ernst Cloos Memorial Fellow*, Johns Hopkins University
- Summer 2009 *Smithsonian Institution Predoctoral Fellowship*, Museum Conservation Institute
- 2007 *Howard Hughes Summer Research Fellowship*, Bates College
- 2007 *Warren Award for best undergraduate poster*, New England Estuarine Research Society
- 2006 *NSF-REU Internship*, Rutgers University Institute of Marine and Coastal Sciences

Publications

Submitted

Shenton BJ, Grossman EL, Passey BH, **Henkes GA**, Becker TP, Laya JC, Perez-Huerta A, Becker SP, Lawson M. Clumped isotope thermometry in deeply buried sedimentary carbonates: The effects of bond reordering and recrystallization. Submission to *Geological Society of America Bulletin* in July 2014.

Published

12. Passey BH, Hu H, Ji H, Montanari S, Li S, **Henkes GA**, Levin NE. (2014) Triple oxygen isotopes in biogenic and sedimentary carbonates. *Geochimica et Cosmochimica Acta* 141, 1-25.
11. **Henkes GA**, Passey BH, Grossman EL, Shenton B, Pérez-Huerta A, Yancey TE. (2014) Temperature limits for preservation of primary calcite clumped isotope paleotemperatures. *Geochimica et Cosmochimica Acta* 139, 362-382.
10. Rick TC and **Henkes GA** (2014) Radiocarbon variability in *Crassostrea virginica* shells from the Chesapeake Bay. *Radiocarbon* 56, 305-311.
9. Able KW, Grothues TM, Turnure JT, Malone MA, **Henkes GA** (2013) Dynamics of residency and egress in selected estuarine fishes: evidence from acoustic telemetry. *Environmental Biology of Fishes* 97, 91-102.
8. **Henkes GA**, Passey BH, Wanamaker AD, Grossman EL, Ambrose WG Jr., Carroll ML (2013) Carbonate clumped isotope compositions of modern marine mollusk and brachiopod shells. *Geochimica et Cosmochimica Acta* 106, 307-325.
7. Passey BH and **Henkes GA** (2012) Carbonate clumped isotope bond reordering and geospeedometry. *Earth and Planetary Sciences Letters* 351-352, 223-236.
6. Rick TC, **Henkes GA**, Lowery DL, Colman SM, Culleton BJ (2012) Marine radiocarbon reservoir corrections (ΔR) for Chesapeake Bay and the Middle Atlantic Coast of North America. *Quaternary Research* 77, 205-210.
5. Rick TC, Lowery DL, **Henkes GA**, Wah JS (2011) A late Holocene radiocarbon chronology for the shell middens of Fishing Bay, Maryland. *Archaeology of Eastern North America* 39, 153-167.
4. Carroll ML, Ambrose WG Jr., Levin BS, Locke WL V, **Henkes GA**, Hop H, Renaud PE (2011) Pan-Svalbard growth rate variability and environmental regulation in the Arctic bivalve *Serripes groenlandicus*. *Journal of Marine Systems* 88, 239-251.
3. Carroll ML, Ambrose WG Jr., Levin BS, Ryan SK, Ratner AR, **Henkes GA** (2011) Climatic regulation of *Clinocardium ciliatum* (bivalvia) growth in the northwestern Barents Sea. *Palaeogeography, Palaeoclimatology, Palaeoecology* 302, 10-20.

2. Marra PP, Dove CJ, Dolbeer R, Dahlan NF, Heacker M, Whatton JF, Diggs NE, France C, **Henkes GA** (2009) Migratory Canada geese cause crash of US Airways Flight 1549. *Frontiers in Ecology and the Environment* 7, 297-301.
1. Carroll ML, Johnson BL, **Henkes GA**, McMahon KW, Voronkov A, Ambrose WG Jr., Denisenko SG (2009) Bivalves as indicators of environmental variation and potential anthropogenic impacts in the southern Barents Sea. *Marine Pollution Bulletin* 59, 193-206.

Reviewer for *Marine Biology*, *Geochimica et Cosmochimica Acta* (2), *American Chemical Society-Petroleum Research Fund*

Conference Abstracts

(*upcoming*) December 2014, *American Geophysical Union Fall Meeting, San Francisco, CA, USA*
Invited talk: “Preservation of primary carbonate clumped isotope temperatures: Recrystallization vs. bond reordering” with BH Passey and EL Grossman.

(*upcoming*) August 2014, *4th International Workshop on Clumped Isotopes, Zurich, Switzerland*
Talk: “Cool high-latitude temperatures for the Early Permian based on carbonate clumped isotope paleotemperatures from shallowly buried brachiopod shells” with BH Passey, EL Grossman, BJ Shenton, and TE Yancey.

December 2013, *American Geophysical Union Fall Meeting, San Francisco, CA, USA*
Invited talk: “Constraints on Phanerozoic paleotemperature and seawater oxygen isotope evolution from the carbonate clumped isotope compositions of Late Paleozoic marine fossils” with BH Passey, EL Grossman, A Pérez-Huerta, B Shenton, and TE Yancey.

April 2013, *Society for American Archaeology 78th Annual Meeting, Honolulu, HI, USA*
Invited talk: “Carbonate clumped isotope thermometry of archaeological shell from the Chesapeake Bay” with TC Rick and BH Passey.

January 2013, *3rd International Workshop on Clumped Isotopes, Cambridge, MA, USA*
Talk: “Empirical and experimental evidence of ¹³C-¹⁸O bond reordering in Paleozoic brachiopod shells” with BH Passey, EL Grossman, TE Yancey, and B Shenton.

June 2012, *The 22nd V.M. Goldschmidt Conference, Montreal, Canada*
Talk: “Clumped isotope thermometry of Carboniferous brachiopods and the effects of burial heating” with EL Grossman, TE Yancey, and BH Passey.

July 2011, *The XVII International Congress on the Carboniferous and Permian, Perth, Australia*
Poster: “Clumped isotope geochemistry of Carboniferous brachiopods: Early lessons from a novel paleothermometer” with BH Passey, EL Grossman, and TE Yancey.

December 2010, *American Geophysical Union Fall Meeting, San Francisco, CA, USA*

Invited talk: “Clumped isotope thermometry of modern and early Cretaceous molluscan carbonate from high-latitude seas” with GD Price, WG Ambrose Jr., ML Carroll, and BH Passey.

December 2007, *American Geophysical Union Fall Meeting, San Francisco, CA, USA*

Poster: “Tracing environmental variation of the past 130 years in the Barents Sea: Mineral ratio (Mg/Ca, Sr/Ca, Ba/Ca, Mn/Ca) evidence in shells of the circumpolar Greenland cockle, *Serripes groenlandicus*” with WG Ambrose Jr., BJ Johnson, ML Carroll, KW McMahon, SG Denisenko, TR Thorrold.

July 2007, *1st International Sclerochronology Conference, St. Petersburg, FL, USA*

Poster: “Environmental conditions in a Norwegian high-Arctic fjord: Evidence from *Serripes groenlandicus* (Bivalvia) growth rates and shell organic carbon isotope compositions” with BJ Johnson, WG Ambrose Jr., KW McMahon, ML Carroll, and H Hop.

Spring 2007, *New England Estuarine Research Society Spring Meeting, Boothbay, ME, USA*

Poster: “Annual growth variations and shifts in the $\delta^{13}\text{C}$ signal in shell organic matter of the Greenland cockle, *Serripes groenlandicus*”, an indicator of changing primary productivity in the Arctic Ocean?” with BJ Johnson, WG Ambrose Jr., KW McMahon, ML Carroll, and H Hop.

Invited Seminars

2014 University of Georgia, Center for Applied Isotope Studies

2014 Carnegie Institution of Washington, Geophysical Laboratory, *informal talk*

2014 National Institute of Standards and Technology, Gas Metrology Group

2014 Texas A&M University, Department of Geology & Geophysics, *informal talk*

Professional Memberships

American Geophysical Union, Geochemical Society, American Association of Petroleum Geologists, Society for American Archaeology